Downloaded from UvA-DARE, the institutional repository of the University of Amsterdam (UvA)
http://dare.uva.nl/document/72835

File ID 72835
Filename Thesis

SOURCE (OR PART OF THE FOLLOWING SOURCE):
Type Dissertation
Title Charged Current Cross Section Measurement at HERA
Author S.J.L.A. Grijpink
Faculty Faculty of Science
Year 2004
Pages 163

FULL BIBLIOGRAPHIC DETAILS:
http://dare.uva.nl/record/170668

Copyright

It is not permitted to download or to forward/distribute the text or part of it without the consent of the author(s) and/or copyright holder(s), other than for strictly personal, individual use.

UvA-DARE is a service provided by the library of the University of Amsterdam (http://dare.uva.nl)

Charged Current Cross Section Measurement at HERA

Sjors Grijpink

Charged Current Cross Section Measurement at HERA

Charged Current Cross Section Measurement at HERA

ACADEMISCH PROEFSCHRIFT

TER VERKRIJGING VAN DE GRAAD VAN DOCTOR
AAN DE UNIVERSITEIT VAN AMSTERDAM
OP GEZAG VAN DE RECTOR MAGNIFICUS
PROF.MR. P.F. VAN DER HEIJDEN
TEN OVERSTAAN VAN EEN DOOR HET COLLEGE VOOR PROMOTIES
INGESTELDE COMMISSIE, IN HET OPENBAAR TE VERDEDIGEN
IN DE AULA DER UNIVERSITEIT
OP 7 APRIL 2004, TE 14:00 UUR

door

Sjors Johannes Louis Assuerus Grijpink

geboren te Tiel

Promotor: Prof.Dr. J.J. Engelen
Co-promotor: Dr. E. de Wolf

Faculteit der Natuurwetenschappen, Wiskunde en Informatica

The work described in this thesis is part of the research programme of 'het Nationaal Instituut voor Kernfysica en Hoge–Energie Fysica (NIKHEF)' in Amsterdam, the Netherlands. The author was financially supported by 'de Stichting voor Fundamenteel Onderzoek der Materie (FOM)', which is funded by 'de Nederlandse Organisatie voor Wetenschappelijk Onderzoek (NWO)'.

La dernière chose qu'on trouve en faisant un ouvrage, est de savoir celle qu'il faut mettre la première. [The last thing one knows in constructing a work is what to put first.]

- *Pensées* (1670), Blaise Pascal

aan mijn ouders

Contents

Introduction

The twentieth century has truly been a glorious time for physics. At the turn of the century two major breakthroughs in the understanding of physics were made. In 1900 Max Planck introduced the theory of quantum physics [1], which was the basis for the development of quantum mechanics. Around the same time Einstein also formulated his theory of relativity [2]. Experimentally, physics was dominated by the investigation of radioactivity. And in 1909 Rutherford provided the start of particle physics as we know it today by, for the first time, using a particle beam to investigate matter. He and his collaborators Geiger and Marsden allowed a beam of α-particles to hit a target composed of a gold foil. Analysis of the scattering angle distribution showed that the atom was not a uniformly filled object, but in fact contained a charged nucleus which had a radius of less than a $1/10000^{\text{th}}$ of the radius of the atom [3]. The atom was mostly void! This experiment inspired Niels Bohr to formulate his model of the atom [4]: A highly positively charged nucleus with electrons orbiting around. The discovery of the neutron in nuclear fission [5] prompted the idea that the nucleus was built up of protons and neutrons held together by a new force, the nuclear force or strong interaction.

Many years and significant world events passed, until in the 50's technology had advanced sufficiently to allow the first particle accelerators to be built. Using a beam of electrons McAllister and Hofstadter managed to measure the shape of the proton, the so called form factor [6]. This experiment showed that the proton was an extended object, unlike the electron which even today behaves like a point-like particle.

The year 1969 saw the first deep inelastic scattering, DIS, experiment. Here the word deep indicates that the energies were so high as to probe the proton structure with a resolution of a fraction of the radius of the proton. The word inelastic indicates that the proton breaks up and other particles are produced. The experiment took electrons that had been accelerated to 7 GeV and brought them into collision with a hydrogen target. In the same way as the Rutherford experiment showed a small hard structure in the atom, this experiment showed that the proton was not an extended object with uniform charged density, but an object composed of point-like charged particles [7]. Feynman immediately explained the results with a model where the proton was built up of point-like particles and antiparticles, named partons. These partons were later identified with the quarks, Gell-Mann had introduced several years before to explain the increasing number of particles found in particle beam experiments [8].

Quarks have never been observed as free particles and this among other things was incorporated in the gauge theory of strong interactions, quantum chromo dynamics, QCD. The mediators of the strong force are the gluons. This helped explain why in the deep inelastic scattering experiments it was observed that only half of the momentum of the proton was carried by the charged quarks. Evidence for the existence of the gluon was obtained in 1979 when in e^-e^+ scattering events were observed with three distinct jets of particles: a quark, an antiquark and a gluon jet [9].

So far we have concentrated on the electromagnetic interaction between charged particles such as electrons with quarks and the strong interaction between quarks. There is however a third interaction, the weak interaction. This interaction mediates for instance nuclear β-decay. In 1932 Fermi was the first to attempt an explanation of this phenomenon [10]. He described this by the transition of a neutron into a proton an electron and a massless neutral particle for which the name neutrino was coined. This theory was at first very successful, but ran into some difficulty. The interaction did not conserve parity: an interaction viewed in a mirror does not occur in nature, whereas the original does. Lee and Yang suggested that this might be the case by studying the mathematics of the theory [11]. The experimental evidence for parity violation was given by Wu by studying angular asymmetries in the β-decay of polarised ^{60}Co nuclei [12]. To incorporate parity violation in the Fermi model, Glashow, Salam and Weinberg combined the electromagnetic and weak interaction in the electroweak theory [13]. The mediators of the weak force are the neutral Z^0 and the charged $W^\pm$ particles. Due to the high mass of these particles, $M_Z \approx 91\,\mathrm{GeV}$ and the $M_W \approx 80\,\mathrm{GeV}$, it took till 1983 that they were discovered by the CERN $p\bar{p}$ collider experiments [14]. Today, the electroweak theory together with quantum chromo dynamics form the Standard Model, SM, in particle physics.

The first electron/positron-proton collider in the world, HERA, built at the DESY institute in Hamburg, became operational in 1992 and collides electrons/positrons of 27.5 GeV with protons of 920 GeV. It provides an unprecedented resolution for probing the structure of the proton down to $1/1000^{\mathrm{th}}$ of its radius. The work presented in this thesis has been performed with the

ZEUS detector, one of the colliding beam experiments situated at HERA. The high energy particle beams of HERA allow the exploration of a significant extension of the kinematic phase space in deep inelastic scattering and provide a very clean way of measuring the structure of the proton. With the ZEUS detector, the structure of the proton can be determined from the neutral current DIS cross section measurements. In this case the exchanged particle in the ep interaction is a photon or a Z^0 and all quark and antiquark flavours in the proton contribute to the cross section. In this thesis another measurement, which provides information about the structure of the proton, is described: the measurement of the charged current DIS cross section. In ep charged current DIS the exchanged particle is a $W^{\pm}$ boson providing an excellent way of obtaining information about specific quark and antiquark distributions in the proton. Measuring the cross section at low-x and high-Q^2, where x is the fraction of the proton momentum carried by the struck quark and Q^2 the momentum transferred to the quark from the incoming lepton, provides a very strong test of QCD. At high-x and high-Q^2 in e^-p scattering it gives a direct measurement of the u valence quark distribution and in e^+p scattering a direct measurement of the d valence quark distribution in the proton. Furthermore, according to the electroweak theory, the W boson only couples to left-handed fermions and right-handed antifermions and this can be verified very nicely with the measurement of the charged current deep inelastic scattering cross section.

This thesis is organised as follows. In chapter 1, the theoretical framework of deep inelastic scattering and QCD is given. The experimental set-up, both the accelerator and detector, is described in chapter 2. Detector simulation, needed for a precise measurement, is described in chapter 3. The reconstruction of the measured quantities and their corrections are explained in chapter 4. In chapter 5 the on-line and off-line selection of charged current events is described in great detail. In chapter 6 it is described how the charged current cross sections are determined together with an analysis of the uncertainties on the measurements. Finally, the results of the cross section measurements and a discussion of the results are given in chapter 7.

Chapter 1

Deep Inelastic Scattering

1.1. Introduction

One of the most powerful and cleanest possibilities to investigate the quark/parton substructure of matter is provided by deep inelastic scattering, DIS, of leptons on hadrons [15]. In this chapter the definitions of the DIS kinematic variables and the formulae for the charged current, CC, cross sections are given. The cross sections are given in terms of the structure functions and are put in the context of the quark-parton model. The details of how the expressions are derived can be found elsewhere [16][17][18].

1.2. DIS Kinematics

The basic process for lepton[1]-nucleon deep inelastic scattering is given by

$$lN \rightarrow l'X \tag{1.1}$$

where l and l' represent the incoming and outgoing leptons, N represents the nucleon and X represents the hadronic final state particles. The associated four vectors are k, k' for the incoming and outgoing leptons respectively, and P for the incoming nucleon. The process is mediated by the exchange of a virtual vector boson, V^* (γ, W or Z). Figure 1.1 shows the lowest order Feynman diagram for the process. The four-momentum of the virtual boson is

$$q = k - k', \tag{1.2}$$

and the four-vector P_X of the hadronic final state system X is given by

$$P_X = P + q. \tag{1.3}$$

[1]Lepton is taken to include anti-leptons, unless otherwise stated.

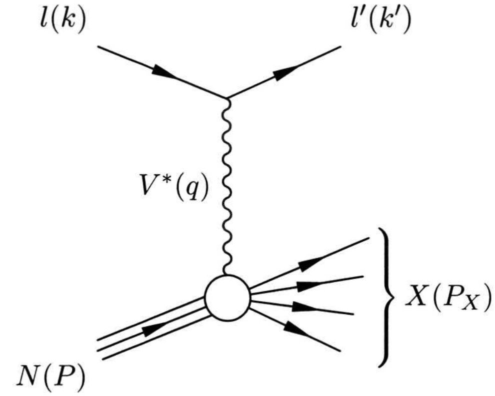

Figure 1.1. Feynman diagrams for lowest order deep inelastic lepton-nucleon scattering, $lN \to l'X$, via the exchange of a Vector-Boson.

Various Lorentz invariant variables which are most commonly used to describe the kinematics of the interaction can be constructed from the four vectors:

- s, the square of the centre-of-mass energy for the lepton-nucleon interaction,
$$s = (P + k)^2, \tag{1.4}$$
- Q^2, the (negative of the) square of the invariant mass of the exchanged virtual boson,
$$Q^2 = -q^2, \tag{1.5}$$
- the Bjorken x variable, which is interpreted in the quark-parton model as the fraction of the four-momentum of the incoming nucleon carried by the struck quark. Hence, it takes a value in the range 0 to 1 and is
$$x = \frac{Q^2}{2P \cdot q}, \tag{1.6}$$
- W, the invariant mass of the hadronic system X determined by
$$W^2 = (P_X)^2 = (P + q)^2, \tag{1.7}$$
- the inelasticity y, the fraction of the energy of the lepton transferred to the nucleon in the rest frame of the nucleon. It takes a value in the range 0 to 1 and is given by
$$y = \frac{P \cdot q}{P \cdot k}. \tag{1.8}$$

At HERA (see Sect. 2.2), an electron-proton collider, the energies of the incoming electron and proton are fixed and thus the centre-of-mass energy is fixed ($\sqrt{s} = 318\,\mathrm{GeV}$). Note that[2]

$$Q^2 = sxy, \tag{1.9}$$

$$W^2 = Q^2\left(\frac{1}{x} - 1\right). \tag{1.10}$$

The DIS kinematics can be described by two independent kinematic variables. Commonly used combinations are x and Q^2 or x and y. The formulae are appropriate for $Q^2, W \gg M_p^2$, where M_p^2 is the proton mass.

1.3. Cross Section and Structure Functions

The double differential charged current cross sections for lepton-nucleon scattering, mediated by a single W boson at high energies, are given in terms of three structure functions, F_2, F_L and xF_3, as

$$\frac{\mathrm{d}^2\sigma^{\mathrm{CC}}(l^\pm N)}{\mathrm{d}x\mathrm{d}Q^2} = \frac{G_F^2}{4\pi x}\left(\frac{M_W^2}{M_W^2+Q^2}\right)^2\left[Y_+F_2(x,Q^2) - y^2F_L(x,Q^2) \mp Y_-xF_3(x,Q^2)\right], \tag{1.11}$$

where $l^\pm$ is the incoming lepton, N the incoming nucleon, M_W the mass of the W boson and G_F the Fermi coupling constant which can be expressed as

$$G_F = \frac{\pi\alpha}{\sqrt{2}\sin^2\theta_W M_W^2}, \tag{1.12}$$

where α is the fine structure constant and θ_W is the Weinberg angle. The kinematic factor, $Y_\pm$, is given by

$$Y_\pm(y) = 1 \pm (1-y)^2. \tag{1.13}$$

The longitudinal structure function, F_L, stems from the exchange of longitudinally polarised gauge bosons. The parity violating structure function, xF_3, arises from the interference between the vector and axial-vector, V-A, couplings of the weak interaction.

[2]Neglecting the masses of the proton and the electron.

With protons as the incoming nucleons, in deep inelastic scattering, the structure function can be interpreted in terms of the parton densities within the proton. Then, using the predictions of zeroth order perturbative quantum chromodynamics, pQCD (see Sect. 1.5), where $F_L = 0$, the differential charged current cross section for electron-proton scattering becomes

$$\frac{\mathrm{d}^2\sigma^{\mathrm{CC}}(e^-p)}{\mathrm{d}x\mathrm{d}Q^2} = \frac{G_F^2}{2\pi x}\left(\frac{M_W^2}{M_W^2+Q^2}\right)^2 \sum_i \left[xq_i(x,Q^2) + (1-y)^2 x\bar{q}_i(x,Q^2)\right] , \tag{1.14}$$

whereas for positron-proton scattering it becomes

$$\frac{\mathrm{d}^2\sigma^{\mathrm{CC}}(e^+p)}{\mathrm{d}x\mathrm{d}Q^2} = \frac{G_F^2}{2\pi x}\left(\frac{M_W^2}{M_W^2+Q^2}\right)^2 \sum_i \left[(1-y)^2 xq_i(x,Q^2) + x\bar{q}_i(x,Q^2)\right] , \tag{1.15}$$

where the sums contain only the appropriate quarks and antiquarks for the charge of the current. The kinematic factor $(1-y)^2$ suppresses the quark (antiquark) contribution to the CC cross section for e^+p (e^-p), due to the V-A nature of the weak interaction. The W boson only couples to left-handed fermions and right-handed antifermions. Therefore the angular distribution of the quark in e^-q scattering and the antiquark in $e^+\bar{q}$ scattering will be isotropic ($l = 0$). On the other hand the distribution of the quark in e^+q scattering and the antiquark in $e^-\bar{q}$ scattering will exhibit a $1/4(1+\cos\theta^*)^2$ behaviour ($l = 1$). The quark scattering angle in the electron quark centre-of-mass, θ^*, is related to y through $(1-y) = 1/2(1+\cos\theta^*)$.

So, specifying the flavours entering into the quark sums, the structure functions for $e^-p \to \nu X$ can be expressed as

$$F_2 = 2x\left(u(x,Q^2) + c(x,Q^2) + \bar{d}(x,Q^2) + \bar{s}(x,Q^2)\right) , \tag{1.16}$$

$$xF_3 = 2x\left(u(x,Q^2) + c(x,Q^2) - \bar{d}(x,Q^2) + \bar{s}(x,Q^2)\right) . \tag{1.17}$$

For $e^+p \to \bar{\nu}X$ the structure functions can be expressed as

$$F_2 = 2x\left(d(x,Q^2) + s(x,Q^2) + \bar{u}(x,Q^2) + \bar{c}(x,Q^2)\right) , \tag{1.18}$$

$$xF_3 = 2x\left(d(x,Q^2) + s(x,Q^2) - \bar{u}(x,Q^2) + \bar{c}(x,Q^2)\right) . \tag{1.19}$$

The assumption is made that there is no significant top or bottom quark content in the proton and that the energies considered are above the threshold for the production of charmed quarks in the final state[3].

In an analogous way to the charged current cross section (1.11), the cross section for the neutral current, NC, DIS process, $l^{\pm}N \to l^{\pm}X$ can be given in terms of three structure functions, $F_2^{\rm NC}$, $F_L^{\rm NC}$, $xF_3^{\rm NC}$, as

$$\frac{{\rm d}^2\sigma^{\rm NC}(l^{\pm}N)}{{\rm d}x{\rm d}Q^2} = \frac{2\pi\alpha^2}{Q^4 x}\left[Y_+F_2^{\rm NC}(x,Q^2) - y^2F_L^{\rm NC}(x,Q^2) \mp Y_- xF_3^{\rm NC}(x,Q^2)\right], \quad (1.20)$$

where $l^{\pm}$ is the incoming lepton, N the incoming nucleon, α is the electromagnetic coupling constant, $F_L^{\rm NC}$ the longitudinally structure function and $xF_3^{\rm NC}$ the parity violating structure function arising mainly from the γZ^0 interference. Hence, for $Q^2 \ll M_Z^2$, $xF_3^{\rm NC}$ is negligible and the structure functions, $F_2^{\rm NC}$ and $F_L^{\rm NC}$ are given purely by γ^* exchange. Note that in zeroth order pQCD, where $F_L^{\rm NC} = 0$, in the region dominated by pure γ^* exchange the differential NC cross section and the structure function $F_2^{\rm NC}$ are directly related by the simple relationship

$$\frac{{\rm d}^2\sigma^{\rm NC}(ep)}{{\rm d}x{\rm d}Q^2} = \frac{2\pi\alpha^2}{Q^4 x}Y_+F_2^{\rm NC}(x,Q^2), \quad (1.21)$$

The lepton-nucleon scattering process has been used extensively to measure quark distribution functions, and to investigate their Q^2 dependence. Note that in the NC structure function the coupling e^2, the quark charge squared, is included, whereas in CC it is not.

1.4. The Quark-Parton Model

In 1969 R.P. Feynman formulated the quark-parton model [19], QPM, in order to provide a physical picture of the scaling that had been predicted by Bjorken [20] and was observed in the first high energy physics, HEP, DIS experiments at SLAC [21], where $F_2^{\rm NC}$ was observed to be independent of Q^2 for x values around $x \sim 0.3$.

In the QPM the nucleon is treated as an object full of point-like non-interacting scattering centres, partons. The lepton-nucleon scattering cross section is approximated by an incoherent sum of elastic lepton-parton scattering cross

[3]Below the charm threshold, one has to multiply d by $\cos^2\theta_c$ and s by $\sin^2\theta_c$ in (1.16) and (1.17) and $\bar{d}$ by $cos^2\theta_c$ and $\bar{s}$ by $\sin^2\theta_c$ in (1.18) and (1.19), where θ_c is the Cabibbo mixing angle.

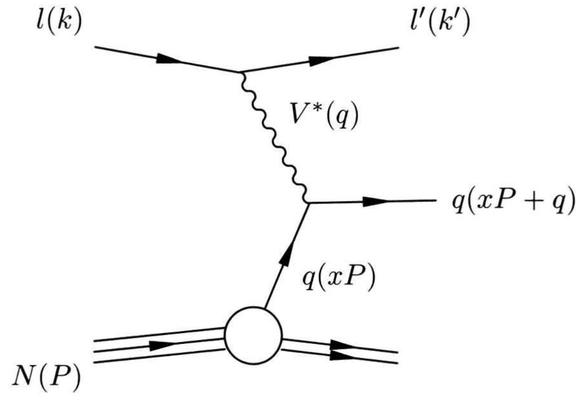

Figure 1.2. Schematic view of lepton-nucleon scattering in the quark-parton model.

sections, see Fig. 1.2. In the infinite momentum frame the Bjorken scaling variable x is then identified with the fraction of the nucleon's momentum involved in the hard scattering. This can be shown by denoting the momentum fraction of the parton to be η. Then, after the elastic electron-parton scattering, the parton has a four-momentum of $q' = \eta P + q$, where

$$q'^2 = (\eta P + q)^2, \tag{1.22}$$
$$= \eta^2 m_N^2 + 2\eta P \cdot q - Q^2, \tag{1.23}$$
$$= m_q^2. \tag{1.24}$$

In the infinite momentum frame, neglecting the parton and nucleon masses, m_q and m_N, this leads to

$$\eta = \frac{Q^2}{2P \cdot q} = x. \tag{1.25}$$

Hence, the momentum distribution of the partons in a nucleon can be expressed as $xq(x)$, where $q(x)$ is the parton density function, PDF, which gives the distribution of the partons in the nucleon.

Note, that in the QPM the structure function F_2^{NC} is simply given by the sum of the quark-antiquark momentum distributions, weighted by the square of the quark charges

$$F_2^{\mathrm{NC}}(x) = \sum_q e_q^2 (xq(x) + x\bar{q}(x)). \tag{1.26}$$

In the static quark model a nucleon and other baryons are pictured as made of three constituent quarks which give them their flavour properties. To incorporate this picture in the QPM, the QPM identifies the constituent quarks as valence quarks, giving the nucleon its flavour, but adds a sea of quark-antiquark pairs to the nucleon, with no overall flavour. Both the valence quarks and the sea quarks and antiquarks are then identified as partons. The antiquark distributions within a nucleon are purely sea distributions, whereas the quark distributions have both valence and sea contributions. Consequently, for the proton to ensure the quantum numbers are correct, i.e. the quantum numbers of the *uud* combination, in the realm of the QPM the number of quarks need to satisfy the following sum rules:

$$\int_0^1 (u(x) - \bar{u}(x))\mathrm{d}x = 2, \quad \int_0^1 (d(x) - \bar{d}(x))\mathrm{d}x = 1, \quad \int_0^1 (s(x) - \bar{s}(x))\mathrm{d}x = 0, \tag{1.27}$$

giving the proton charge +1, baryon number 1 and strangeness 0. A sum rule can also be applied to the sum over the momenta of all types of quarks and antiquarks in the proton. Denoting the distribution by

$$x\Sigma(x) = x(u(x) + \bar{u}(x) + d(x) + \bar{d}(x) + s(x) + \bar{s}(x) + c(x) + \bar{c}(x)), \tag{1.28}$$

the momentum sum rule, MSR, should hold

$$\int_0^1 x\Sigma(x)\mathrm{d}x = 1, \tag{1.29}$$

if quarks and antiquarks carry all of the momentum of the proton. This was not confirmed; measurements showed that only half of the momentum of the proton was contributed by the quarks and antiquarks. This can be explained in the framework of QCD, where the missing momentum is carried by the gluons.

1.5. Q^2 Dependence: QCD Evolution

The QPM model must be modified to allow interactions between quarks. This is accomplished in QCD, a non-Abelian gauge theory of the strong interaction between quarks and gluons, which combines short distance freedom with long distance confinement, due to the variable strength of the strong interaction.

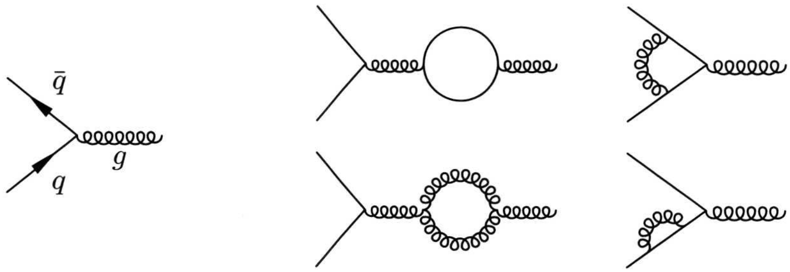

Figure 1.3. Schematic diagram of the $q\bar{q}g$ vertex diagram plus virtual loop corrections.

1.5.1. Running Coupling Constant

The strong coupling "constant", $\bar{g}$, is defined as the value of the coupling at the $q\bar{q}g$ vertex. In the calculation of $\bar{g}$ all virtual loop diagrams have to be included (see Fig. 1.3), causing infinities which are controlled by a renormalisation procedure. In this procedure the coupling is defined to be finite at some scale μ^2, and $\bar{g}(Q^2)$ is expressed in terms of this fixed value at any other scale. The one-loop solution is usually expressed in terms of the "running coupling constant", $\alpha_s(Q^2) = \bar{g}^2(Q^2)/(4\pi)$, as

$$\alpha_s(Q^2) = \frac{4\pi}{\beta_0 \ln(Q^2/\Lambda^2)}, \tag{1.30}$$

where Λ is a parameter of QCD, which depends on the renormalisation scale and scheme and also on the number of active flavours, n_i, at the scale Q^2 and $\beta_0 = 11 - 2n_i/3$ [22].

Note that the dependence of the coupling constant on the external scale Q^2 is true for all field theories including Quantum Electro Dynamics, QED, where it manifests itself as charge screening. Whereas, in QCD, due to the non-Abelian nature of the gluon-gluon coupling, it manifests itself as anti-screening, i.e. the closer one probes the less strong the charge appears. Hence, when Q^2 is fairly large, e.g. $Q^2 > 4\,\mathrm{GeV}^2$ for DIS, α_s is small and the quarks are "asymptotically free". In this region perturbation theory can be used to perform calculations within QCD. To perform calculations in the region of low Q^2, the coupling constant is high and non perturbative techniques are needed (the description of these techniques is outside the scope of this thesis).

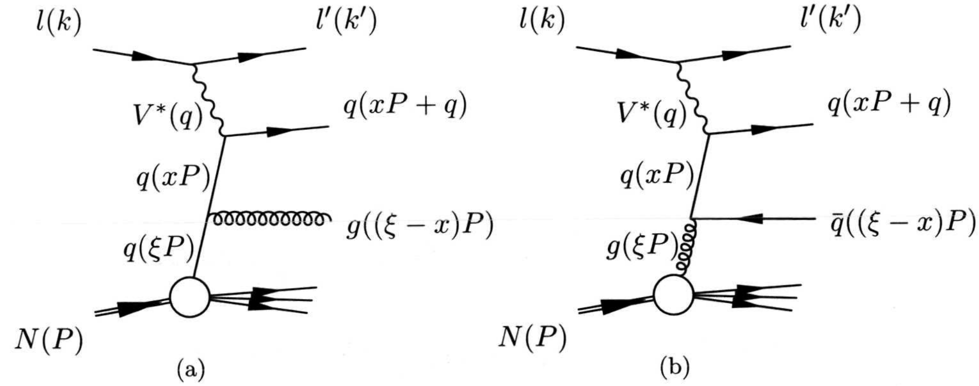

Figure 1.4. Schematic view of leading order extension diagrams to the QPM: (a) the QCD Compton process and; (b) the boson-gluon fusion process.

1.5.2. Q^2 Dependence of Parton Distribution Functions

As a consequence of the quark-gluon couplings in QCD, the quark momentum distribution, and thus the structure functions, depend on (evolve with) Q^2. Before a quark in the nucleon interacts with the vector boson, it could radiate a gluon as in Fig. 1.4(a) (the QCD Compton process). Therefore, although the quark which is struck has momentum fraction x, the quark originally had a larger momentum fraction $\xi > x$. Alternatively, as in Fig. 1.4(b), it may be that a gluon with momentum fraction ξ produced a $q\bar{q}$ pair and one of these became the struck quark with momentum fraction x (the boson-gluon fusion process). Thus the quark distributions, $q(\xi, Q^2)$ for all momentum fractions ξ such that $x < \xi < 1$, contribute to the process shown in Fig. 1.4(a), and the gluon distribution $g(\xi, Q^2)$, for all momentum fractions ξ such that $x < \xi < 1$, contributes to the process shown in Fig. 1.4(b).

So, the parton being probed may not be the "original" constituent, but may arise from the strong interactions within the nucleon. The smaller the wavelength of the probe (i.e. the larger the scale Q^2), the more of such quantum fluctuations can be observed and hence the amount of $q\bar{q}$ pairs and gluons in the partonic sea increases. Although these sea partons carry only a small fraction of the nucleon momentum, their increasing number leads to a softening of the valence quark distribution as Q^2 increases. Consequently, the structure function F_2^{NC}, containing both valence and sea quark distributions, rises with Q^2 for low values of x, where sea quarks dominate, and falls with Q^2 at large values of x, where valence quarks dominate (see Fig. 1.5).

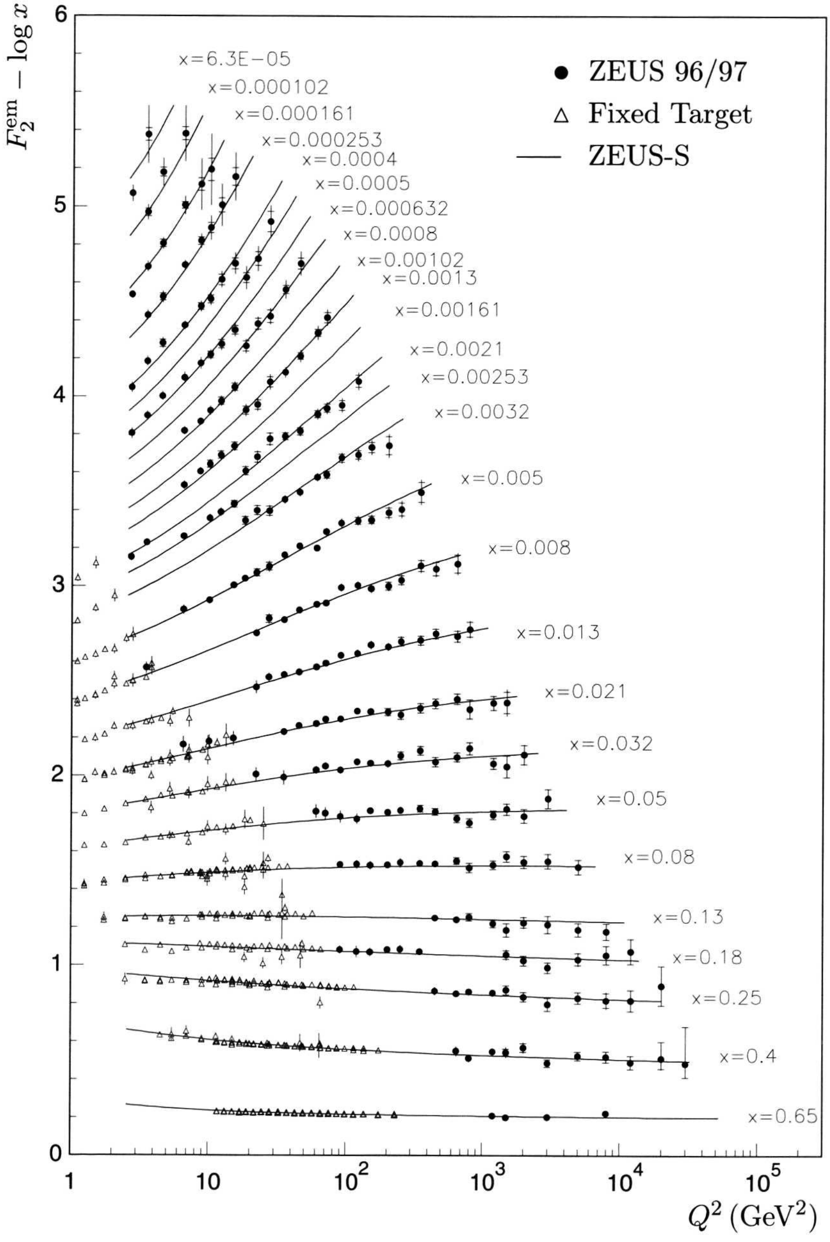

Figure 1.5. The results for F_2^{em} (points) versus Q^2 are shown for fixed x. The fixed target results from NMC, BCDMS and E665 (triangles) and the ZEUS-S fit, see Sect. 7.3, (curve) are also shown.

The Dokshitzer-Gribov-Lipatov-Altarelli-Parisi, DGLAP [23], formalism can be used to quantify these effects and expresses the evolution of the quark distribution by

$$\frac{\mathrm{d}q_i(x,Q^2)}{\mathrm{d}\ln Q^2} = \frac{\alpha_s(Q^2)}{2\pi}\int_x^1 \frac{\mathrm{d}\xi}{\xi}\left[\sum_j q_j(\xi,Q^2)P_{q_i,q_j}\left(\frac{x}{\xi}\right) + g(\xi,Q^2)P_{q_i,g}\left(\frac{x}{\xi}\right)\right], \quad (1.31)$$

and the corresponding evolution of the gluon distribution by

$$\frac{\mathrm{d}g(x,Q^2)}{\mathrm{d}\ln Q^2} = \frac{\alpha_s(Q^2)}{2\pi}\int_x^1 \frac{\mathrm{d}\xi}{\xi}\left[\sum_j q_j(\xi,Q^2)P_{g,q_j}\left(\frac{x}{\xi}\right) + g(\xi,Q^2)P_{g,g}\left(\frac{x}{\xi}\right)\right], \quad (1.32)$$

where $P_{ij}(z)$ are the "splitting functions" representing the probability of a parton j emitting a parton i with momentum fraction z of that of the parent parton, when the scale changes from $\ln Q^2$ to $\ln Q^2 + \mathrm{d}\ln Q^2$. These splitting functions contribute to the evolution of the parton distributions at order α_s, α_s^2, etc. e.g. for $P_{qq}(z)$

$$P_{qq}(z) = P_{qq}^0(z) + \frac{\alpha_s(Q^2)}{2\pi}P_{qq}^1(z) + \cdots \quad (1.33)$$

The above specified evolution of the parton distributions can be related to the measurable cross sections and structure functions. Analogous to (1.26), the F_2^{NC} structure function in first order pQCD can then be written as

$$\frac{F_2(x)}{x} = \sum_{q,\bar{q}} e_q^2\left[q(x) + \Delta q(x,Q^2)\right] = \sum_{q,\bar{q}} e_q^2 q(x,Q^2), \quad (1.34)$$

where the Q^2 dependence in the parton cross section, due to the additional $q\bar{q}g$ vertex contribution, is transferred into the parton distribution function $q(x) \to q(x,Q^2)$.

In second order QCD, this absorption of the Q^2 dependence into the parton distribution function, cannot be maintained. The equations which identify the structure functions as sums over quark distributions have to be modified accordingly to give expressions like [18]

$$\frac{F_2^{\mathrm{NC}}(x,Q^2)}{x} = \int_x^1 \frac{d\xi}{\xi}\left[\sum_i C_2\left(\frac{x}{\xi},\alpha_s\right) q_i(\xi,Q^2) + C_g\left(\frac{x}{\xi},\alpha_s\right) g(\xi,Q^2)\right], \quad (1.35)$$

where the sum denotes the appropriate quark flavours and the coefficient functions, C, represent the appropriate parts of the V^*-parton scattering cross section

$$C_2\left(\frac{x}{\xi},\alpha_s\right)=\sigma_2\left(\frac{x}{\xi},\alpha_s\right)=e_i^2\left[\delta\left(1-\frac{x}{\xi}\right)+\alpha_s(Q^2)f_2\left(\frac{x}{\xi}\right)\right], \tag{1.36}$$

and

$$C_g\left(\frac{x}{\xi},\alpha_s\right)=\sigma_g\left(\frac{x}{\xi},\alpha_s\right)=\left[\alpha_s(Q^2)f_g\left(\frac{x}{\xi}\right)\right]. \tag{1.37}$$

Similar expressions can be obtained for xF_3 in terms of f_3, but in this case the gluon makes no contribution. As a consequence of the fact that at second order the gluon radiation can no longer be accounted for by making the quark distributions scale-dependent, the nucleon can no longer be pictured purely as a sum of spin 1/2 quarks and thus the Callan-Gross relationship, $2xF_1 = F_2$, is violated at second order. A consequence of this violation is that the longitudinal structure function, F_L, is no longer zero.

1.6. Electroweak Radiative Corrections

The cross sections as described in the previous sections are referred to as the "Born" level cross sections, due to the absence of higher-order electroweak effects, radiative effects, in their description. The cross section including radiative effects is related to the Born cross section by

$$\frac{\mathrm{d}\sigma_{\mathrm{rad}}}{\mathrm{d}\mathbf{v}}=\int \mathrm{d}\mathbf{v}' K(\mathbf{v},\mathbf{v}')\frac{\mathrm{d}\sigma_{\mathrm{Born}}}{\mathrm{d}\mathbf{v}'} \tag{1.38}$$

where $\mathbf{v}$ and $\mathbf{v}'$ are two-dimensional vectors representing the kinematic variables (x, Q^2), and $K(\mathbf{v},\mathbf{v}')$ is the radiative kernel describing the transition from phase space $\mathbf{v}'$ to $\mathbf{v}$. In order to unfold the Born level cross section electroweak radiative corrections of order $\mathcal{O}(\alpha_{\mathrm{em}})$ have to be taken into account:

- pure QED corrections. Radiation of photons can shift reconstructed kinematic variables, e.g. from large to small values of x inducing additional enhancement factors [24];

- purely weak one-loop corrections.

Processes contributing to the QED corrections come from initial state radiation, ISR, from the incoming electron and quark, photon emission from the exchanged W boson and final state radiation, FSR, from the outgoing quark. The processes contributing to the weak one-loop corrections come from W self energy, lepton vertex loops and two boson exchange. These contributions can be organised in terms contributing to the complete cross section according to their dependence on the electric charge of the incoming particles: "leptonic", "interference" and "quarkonic" contribution terms [25][26].

The presently available numerical programs for the calculation of the CC cross section do not all take into account the complete set of $\mathcal{O}(\alpha)$ electroweak radiative corrections. Two programs which do include the complete set of corrections, DISEPW [27][4] and **epcctot** [29], have been compared [24] and are found to agree well. However, these programs are not suited for use in a realistic experimental analysis. They do not allow for application of experimental cuts and they are restricted to the use of the kinematic variables reconstructed from the leptons whereas experiments, in the case of the CC cross section measurement, have to determine kinematic variables from the hadronic final state. The Monte Carlo, MC, event generator HERACLES/DJANGOH (see Sect. 3.1) circumvents these two restrictions. However, it has the CC radiative corrections implemented in an approximation where the quarkonic and interference contributions are neglected. From comparisons made between DJANGOH and **epcctot** [25] it can be concluded that neglecting quarkonic and interference contributions in the implementation of QED corrections in DJANGOH is justified as long as measurements do not require an accuracy of better than 2%.

1.7. Summary

In this chapter the theoretical framework which was used in the measurements presented in this thesis has been given. The much more formal description of QCD derived from the Operator Product Expansion and the Renormalisation Group Equation to give predictions in terms of the moments of the structure functions can be found elsewhere [17][22]. In the next chapters the measurement of the cross section of $e^{-}p$ and $e^{+}p$ charged current interactions will be described. In the last chapter a comparison between the measurements and the predictions from QCD will be presented.

[4] A branch of HECTOR [28].

Chapter 2

ZEUS a Detector for HERA

2.1. Introduction

The charged current *ep* cross section presented in this thesis was measured using the ZEUS detector. The ZEUS detector is one of four detectors situated at the HERA accelerator, at the DESY laboratory located in Hamburg, Germany. In this chapter the HERA accelerator and the ZEUS detector will be described. The description of the ZEUS detector will focus on the sub-detectors most relevant for the measurement of the charged current *ep* cross section. A detailed description of the ZEUS detector can be found in [30].

2.2. The HERA Accelerator

The Hadron Elektron Ring Anlage, HERA, is the first and currently the only accelerator which allows for deep inelastic electron [1]-proton colliding beam experiments. The electrons are accelerated to an energy of 27.5 GeV. Until 1998 protons were accelerated to 820 GeV. Later the energy of the proton beam was increased to 920 GeV providing a centre-of-mass energy of $\sqrt{s} = 2\sqrt{E_e E_p} =$ 318 GeV. Four experiments use the HERA facility (see Fig. 2.1). Two of them use both beams: the H1 experiment, located at the North Hall, and the ZEUS experiment, located at the South Hall. The main objective of these two experiments is to measure the parton distributions inside the proton, using the electrons in the electron beam as probes. The other two experiments only use one of the beams provided by HERA. In the East Hall the polarised electron beam collides with various polarised and unpolarised targets of the HERMES detector. The HERMES experiment measures the spin structure of the nucleon. HERA-B, at the West Hall, uses the interactions of the halo of the proton

[1] Electron can be read as positron, unless otherwise stated.

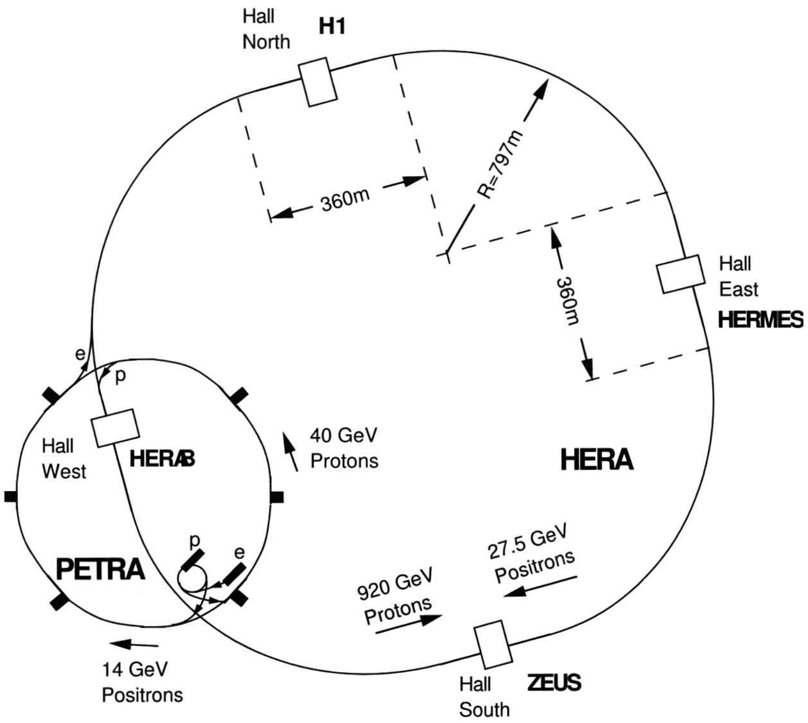

Figure 2.1. Schematic view of the HERA accelerator together with the injection system PETRA and the four experiments using the HERA beams.

beam with a wire target to measure J/ψ production originating from b-decays to measure CP violation in the b-system.

The HERA accelerator is situated in Hamburg, Germany, and was constructed by the Deutsches Elektron Synchroton laboratory, DESY, together with international collaborators. The HERA tunnel has a circumference of 6336 m and was finished in 1987. In 1990 the accelerator was installed, and first collisions were observed in October 1991.

The beams for HERA are provided by a chain of pre-accelerators. The protons are obtained from a surface-plasma magnetron source generating H^- ions which are accelerated by several radio frequency, RF, cavities in the linear collider, LINAC III [31], to 50 MeV for injection in DESY III. In the DESY III accelerator the H^- ions are accelerated to 7.5 GeV in 11 bunches with 96 ns bunch spacing and subsequently the two electrons are stripped off the H^- ions

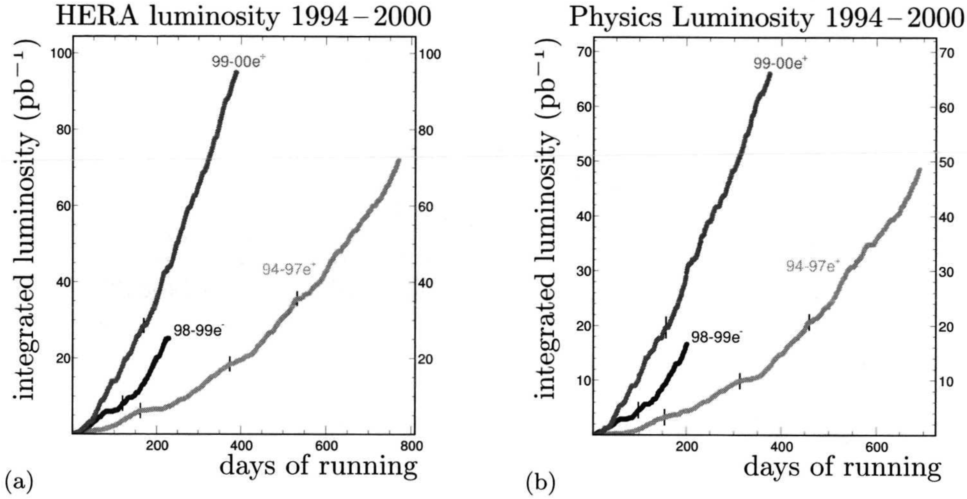

Figure 2.2. Integrated luminosity versus days of running: (a) delivered by HERA; (b) gated by ZEUS and suitable for physics analysis. The figures show the integrated luminosity collected during the years 1994 to 2000.

by passing through a gold foil. The protons are then passed to the Positron Elektron Tandem Ring Anlage, PETRA, where they are accelerated in 70 bunches, again with 96 ns bunch spacing, to the HERA proton injection energy of 40 GeV.

The electrons and positrons are obtained by conversion of photons produced by bremsstrahlung in an electron beam. The electrons (positrons) are accelerated in LINAC I (LINAC II) to an energy of 220 MeV (450 MeV) before being injected into DESY II which increases the electron and positron energy to 7.5 GeV. The electrons (positrons) are then injected into PETRA II which accelerates 70 bunches of the leptons, with 96 ns bunch spacing, to the HERA lepton injection energy of 14 GeV. Figure 2.1 shows a schematic overview of the HERA accelerator together with the injection system PETRA.

The luminosity provided by HERA has steadily increased over the years. Figure 2.2(a) shows the integrated luminosity delivered by HERA as a function of days of running and Fig. 2.2(b) shows the integrated luminosity collected by ZEUS. In the first three years of HERA operation, electrons were used for the lepton beam. Due to various problems (e.g. bad vacuum) the lifetime of the electron beam was very short ($\sim$ 3 hours) and in 1994 HERA switched to a positron beam which had a longer lifetime ($\sim$ 8 hours). To collect a comparable amount of e^-p and e^+p data, HERA switched in 1998 to an electron beam. At the same time the proton beam energy was increased from 820 GeV to 920 GeV, providing an extension of the kinematic range covered by HERA. Due to still bad electron beam conditions HERA switched back to positrons again in 1999. Hence, the integrated luminosity delivered in the running period 1998 – 1999 was rather low ($\mathcal{L} = 25.2\,\mathrm{pb}^{-1}$ of which $16.7\,\mathrm{pb}^{-1}$ was collected by ZEUS and used for physics analysis). HERA ran with a positron beam until the upgrade shutdown in 2000 and delivered in that period, 1999 – 2000, an integrated luminosity of $94.9\,\mathrm{pb}^{-1}$ of which $66.3\,\mathrm{pb}^{-1}$ was collected by ZEUS and could be used for physics analysis. The various configurations per running period are listed in Table 2.1 together with the collected luminosity.

Table 2.1. Overview of the various run configurations of HERA over the years together with the luminosity collected by ZEUS. The data collected in the period 1998 – 2000 *was used for the analysis described in this thesis.*

year	mode	E_e(GeV)	E_p(GeV)	$\mathcal{L}(\mathrm{pb}^{-1})$	$\delta\mathcal{L}/\mathcal{L}(\%)$
1993	e^-p	26.7	820	0.55	—
1994	e^-p	27.5	820	0.28	1.5
1994 – 1997	e^+p	27.5	820	48.3	1.5
1998 – 1999	e^-p	27.5	920	16.7	1.8
1999 – 2000	e^+p	27.5	920	66.3	2.25

2.3. The ZEUS Detector

In this section the components of the ZEUS detector most relevant for the analysis described in this thesis will be described briefly. A detailed description of the ZEUS detector can be found elsewhere [30][32]. The ZEUS detector is a general purpose detector with nearly hermetic calorimeter coverage. A cross sectional view of the detector is presented in Fig. 2.3.

The ZEUS detector is an asymmetrical detector, since the centre-of-mass system does not coincide with the laboratory system due to the proton colliding with the much lighter lepton. Therefore, particles in the final state generally will be boosted in the forward direction[2] where the detector is made thicker in

[2]The ZEUS coordinate system is a right-handed Cartesian system, with the Z axis pointing

order to fully contain the hadronic final state.

From the inside out, the detector consists of tracking chambers inside a superconducting solenoid magnet, $B-$field $= 1.43\,\mathrm{T}$, surrounded by electromagnetic, EM, and hadronic calorimeters and muon chambers. The most important detector parameters are given in Table 2.2.

Table 2.2. The most important ZEUS central detector parameters

component	parameter	value
UCAL	angular coverage	$2.6° < \theta < 178.4°$
	$\sigma(E)/E$ (EM shower)	$0.18/\sqrt{E(\mathrm{GeV})} \oplus 0.02$
	$\sigma(E)/E$ (hadronic shower)	$0.35/\sqrt{E(\mathrm{GeV})} \oplus 0.03$
	position resolution (hadrons)	$\sim 1\,\mathrm{cm}$
	time resolution	$< 1\,\mathrm{ns}$
CTD	angular coverage	$15° < \theta < 164°$
	$\sigma(P_T)/P_T$	$0.0058 P_T(\mathrm{GeV}) \oplus 0.0065$ $\oplus\, 0.0014/P_T$
	Z-vertex resolution	$0.4\,\mathrm{cm}$
	$R-\phi$ vertex resolution	$0.1\,\mathrm{cm}$

2.3.1. Tracking Detectors

In the centre of the ZEUS detector the vertex detector, VXD [33], was located. The VXD was removed at the end of the 1995 running period, and has been replaced by the micro vertex detector, MVD, during the upgrade in 2001. The central tracking detector, CTD, is surrounding the VXD. The very forward region is covered by the forward detector, FDET, the very backward region by the rear tracking detector, RTD.

Central Tracking Detector

The main tracking detector of ZEUS is the central tracking detector, CTD [34]. The CTD is a 205 cm long cylindrical drift chamber with inner and outer radii of 18.2 cm and 79.4 cm, respectively, covering the polar angle region of $15° < \theta < 164°$. It is composed of 72 concentric layers of sense wires, evenly divided into

in the proton beam direction, referred to as the "forward direction", and the X axis pointing left towards the centre of HERA. The coordinate origin is at the nominal interaction point.

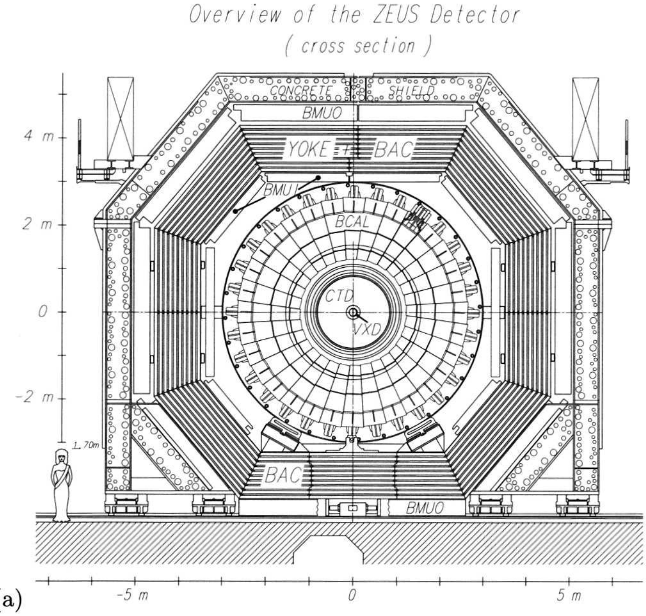

(a)

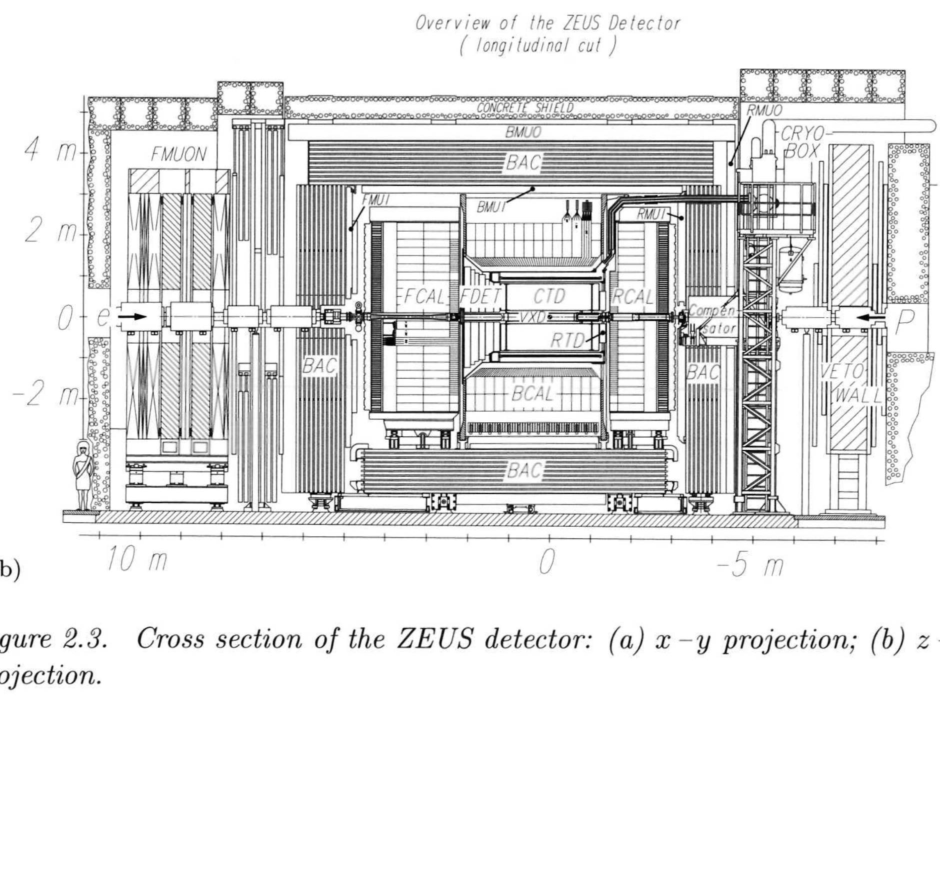

(b)

Figure 2.3. Cross section of the ZEUS detector: (a) $x-y$ projection; (b) $z-y$ projection.

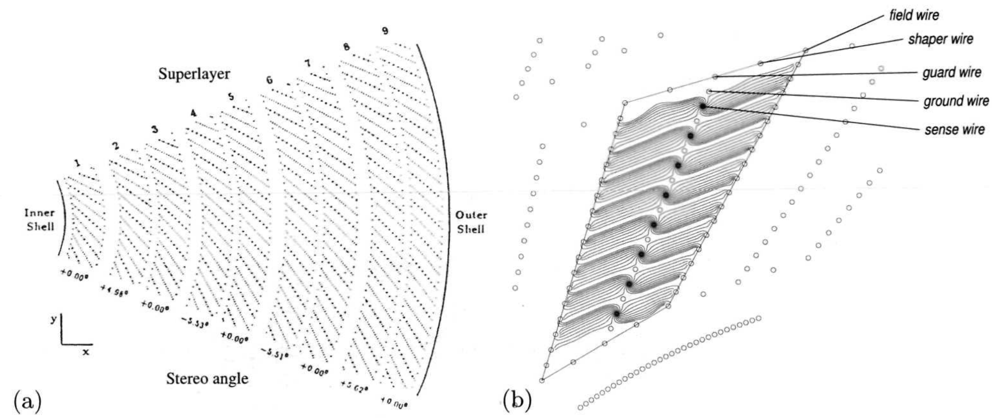

Figure 2.4. Layout of: (a) the wires in one octant of the CTD. The larger (smaller) dots indicate the sense (ground) wires. The wire positions are shown at the end plates; (b) an expanded single drift cell.

9 superlayers. Five superlayers have wires parallel to the Z axis, axial wires, while the remaining four superlayers have wires with a small stereo angle of $\sim 5^\circ$ with respect to the Z axis. This allows for both an $R-\phi$ and a Z coordinate measurement. Figure 2.4(a) shows one octant of the CTD, together with the values of the stereo angle of the wires in the superlayers. The superlayers are divided into cells of eight sense wires orientated at an angle of 45° with the radial direction to produce drift lines approximately tangential to the chamber azimuth in the 1.43 T magnetic field provided by the superconducting solenoid magnet surrounding the CTD. This orientation also ensures that at least one layer in the superlayer will have a drift time shorter than the bunch crossing time of 96 ns. Figure 2.4(b) shows an expanded single drift cell.

Superlayers 1, 3 and 5 can provide a so called flight-by-timing vertex. This vertex is used in the trigger decision and has a resolution of $\sim$ 5 cm in Z. In the final event reconstruction more advanced methods are used in track reconstruction and vertex determination, and the interaction vertex is measured with a typical resolution of 0.4 cm in the Z direction and 0.1 cm transverse to the beam direction. The resolution of the transverse momentum for tracks passing at least three superlayers is: $\sigma(P_T)/P_T = 0.0058 P_T(\mathrm{GeV}) \oplus 0.0065 \oplus 0.0014/P_T$ [35].

Forward and Rear Tracking Detectors

To track particles going into the very forward direction, the forward detector, FDET, consisting of the forward tracking detector, FTD, and the transition radiation detector, TRD, could be used. The FTD consists of three planar drift chambers, and covers a polar angle region in the forward direction of $7.5^\circ < \theta < 28^\circ$. The TRD, a detector to separate electrons from hadrons, is situated between the FTD chambers. During the upgrade of the detector in 2001 the TRD has been replaced by the straw tube tracker, STT. To track particles going into the very rear direction, the rear tracking detector, RTD, could be used. The RTD consists of one plane of drift chambers, covering the polar angle region of $160^\circ < \theta < 170^\circ$.

In the analysis described in this thesis, the information from these tracking detectors was used only by the muon identification program MUFFIN and in the process of scanning for events containing halo and cosmic muons (see Sect. 5.9.1).

2.3.2. Calorimeters

The ZEUS tracking detectors are surrounded by a high resolution uranium-scintillator sampling calorimeter which on its turn is surrounded by the backing calorimeter, BAC.

Uranium Calorimeter

The ^{238}U-scintillator sampling calorimeter, UCAL or CAL [36], is composed of alternating plates of scintillator material and depleted uranium. The calorimeter is nearly hermetic, with a solid angle coverage of 99.8% in the forward region, and 99.5% in the rear region. The calorimeter consists of a forward part, FCAL, a barrel part, BCAL, and a rear part, RCAL[3]. Figure 2.5 gives a schematic overview of the CAL and its angular coverage. The FCAL and BCAL (RCAL) are divided into an electromagnetic section, EMC, and two (one) hadronic sections, HAC1 and HAC2. Perpendicular to this division these sections are divided into cells, of which the sizes are determined by the scintillator tiles. In the electromagnetic section of the FCAL and BCAL, FEMC and BEMC, cells have transverse dimensions of $5 \times 20\,\mathrm{cm}^2$ while the cells in the hadronic section are larger from $20 \times 20\,\mathrm{cm}^2$ (HAC1) to $24.4 \times 35.2\,\mathrm{cm}^2$ at the front face

[3]The regions between the various parts are indicated by super crack regions.

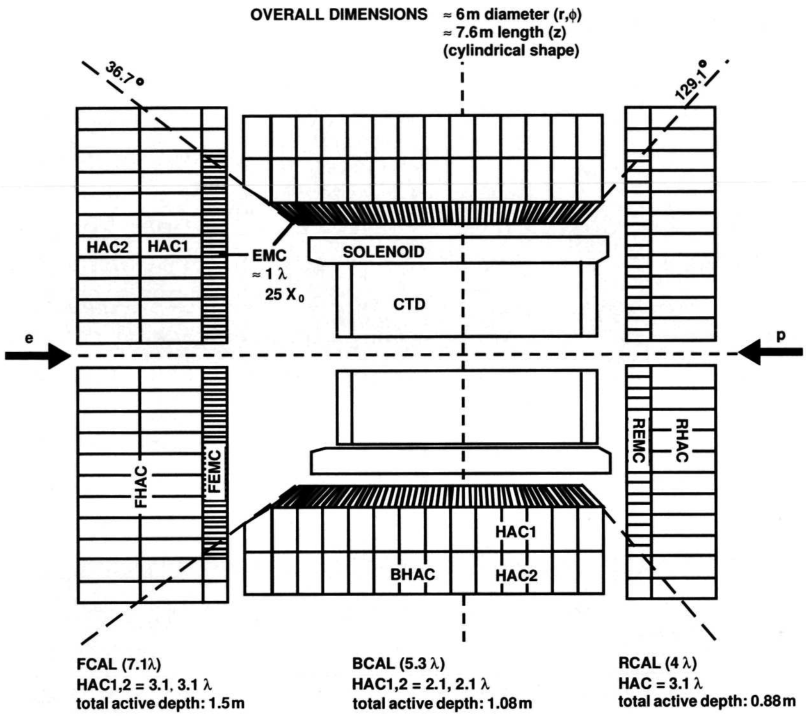

Figure 2.5. Schematic view of the UCAL

of a BCAL HAC2, BHAC2, cell. The cells in the electromagnetic section of the RCAL, REMC, have transverse dimensions of $10 \times 20\,\mathrm{cm}^2$. The BEMC cells are wedge shaped and point towards the interaction point. The light produced in the scintillator material by particles in the shower, is collected by wavelength shifter bars on either side of the cell, and converted into electronic signals by two photomultiplier tubes, PMTs. The dual readout of a cell increases the measurement precision and prevents "dead" cells when one of the PMTs fails. Also timing information is provided for energy deposits. The resolution of the timing is better than 1 ns, for energy deposits greater than 4.5 GeV.

Particle energies are determined from the energy deposits in the active material of the particle shower induced by the traversing particle. An electron or photon initiates an electromagnetic shower in the calorimeter which consists of low energetic e^-e^+ pairs and bremsstrahlung photons. Hadrons entering the calorimeter will interact strongly with the absorber material, and initiate had-

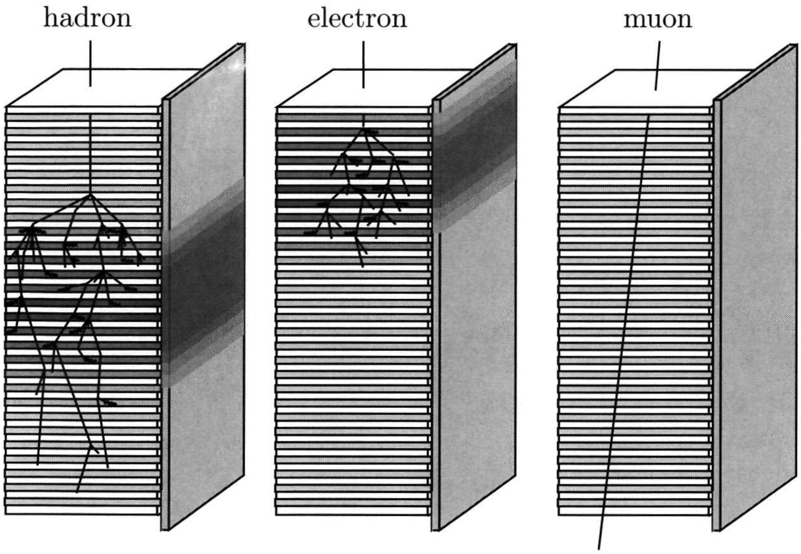

Figure 2.6. Typical shower profiles of hadrons, electrons and muons in the CAL.

ronic showers, generally broader than EM showers and peaking at larger depth. Muons with energies typical for HERA act as minimum ionising particles, MIPs, distributing their energy equally of the whole trajectory. Figure 2.6 shows the shower development for the different particles. In general, the measured energy in a purely electromagnetic shower (e) will be greater than in a purely hadronic shower (h) of the same energy. The major factors contributing to this difference, are energy loss to nuclear recoil and nuclear breakup energy. As a hadron interaction deposits its energy partly through electromagnetic interaction and partly in purely hadronic interaction, where the actual em fraction varies significantly, the varying sensitivity will cause a deterioration of the hadronic energy resolution. By choosing depleted Uranium as absorber and judiciously choosing the thickness of absorber and scintillator, it has been possible to create a calorimeter with equal sensitivity to hadronic and electromagnetic showers ($e/h = 1$) [37]. Using this technique of compensating calorimetry, energy resolutions of $\sigma(E)/E = 0.18/\sqrt{E} \oplus 0.02$ for electrons and $\sigma(E)/E = 0.35/\sqrt{E} \oplus 0.03$ for hadrons (E in GeV) have been achieved. Furthermore, the activity of the uranium provides a calibration and monitoring signal for the CAL. Calibration between cells of the calorimeter is possible at the level of 1% by setting the gains of the PMTs in such a way as to equalise the uranium signal [30].

Backing Calorimeter

The CAL is surrounded by the backing calorimeter, BAC [38], which is integrated with the iron yoke that is used as a path for the solenoid flux return. The BAC consists of 40000 proportional tubes and 1700 pad towers, and can be used to measure energies of particle showers not fully contained within the CAL. The BAC also serves as a muon filter. The energy resolution for hadrons is $\sigma(E)/E = 1.2/\sqrt{E}$ with E in GeV. The BAC has been used in this analysis as a systematic check for energy leakage out of the CAL (see Sect. 6.5.7), and in the process of event scanning for muon identification.

2.3.3. Muon Chambers

The outer part of the ZEUS detector is composed of muon detectors. The muon detector consists of a forward muon detector, FMUON, barrel muon detector, BMUON, and a rear muon detector, RMUON [39]. The forward muon detector consists of four layers of limited streamer tubes, LSTs, and four drift chambers. One LST and one drift chamber are mounted on the inner surface of the yoke, FMUI, while the other LSTs and drift chambers are mounted on a toroidal 1.7 T magnet residing outside the yoke, FMUO. The polar angular coverage of the FMUON is $6° < \theta < 32°$. The BMUON and RMUON are somewhat smaller. The barrel muon detector consists of LSTs placed on the inside of the BAC, BMUI, and LSTs placed on the outside, BMUO, and has a polar angular coverage of $34° < \theta < 135°$. The rear muon detector also consists of LSTs placed on the inside of the BAC, RMUI, and LSTs placed on the outside, RMUO, and has a polar angular coverage of $134° < \theta < 171°$. The BMUON does not have a fully azimuthal coverage, i.e. $-55° < \varphi < 235°$, as there is no bottom octant. The momentum resolution is designed to be $\sim 20\%$ for muons up to 10 GeV in the BMUON and RMUON, and for muons up to 100 GeV in the FMUON.

In the analysis described in this thesis the muon detectors have been very valuable in the identification of halo and cosmic muons by MUFFIN, and in the process of scanning the events by eye.

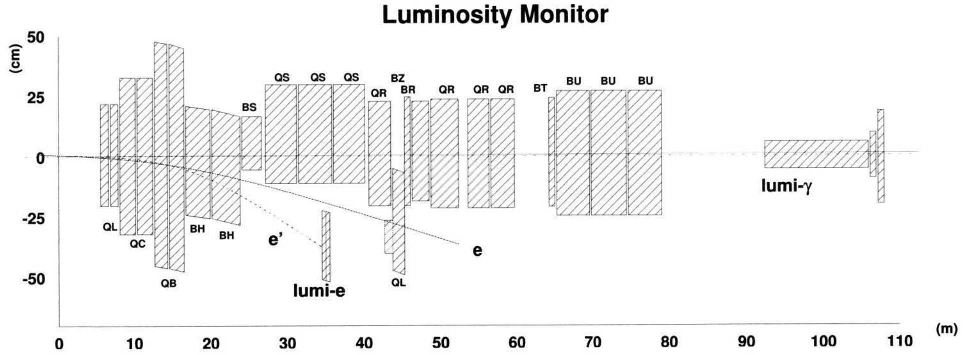

Figure 2.7. Layout of the ZEUS luminosity monitor.

2.3.4. C5 Counter

The C5 counter [40] is positioned at $z = -315\,\mathrm{cm}$, directly behind the RCAL. It is an assembly of four scintillation counters arranged in two planes around the HERA beampipe, separated by 0.3 cm of lead. It records separately the arrival times of the protons and electrons in the beams and is used to reject events due to upstream beam-gas interactions.

2.3.5. Luminosity Monitor

The luminosity is measured with the luminosity monitor, LUMI, via the bremsstrahlung reaction: $ep \to ep\gamma$ [41]. The cross section for this reaction, the Bethe-Heitler process [42], is very precisely known [43] and therefore forms an excellent way by which the luminosity can be measured. The LUMI consists of two sampling lead-scintillator calorimeters: a photon detector, LUMI-γ, located at $Z = -107\,\mathrm{m}$ near the proton beam pipe, and an electron detector, LUMI-e, located at $Z = -35\,\mathrm{m}$ near the electron beam, both shown in Fig. 2.7. The energy resolution for both detectors is $\sigma(E)/E = 0.18/\sqrt{E(\mathrm{GeV})}$. However, a carbon-lead filter in front of the LUMI-γ, installed to shield it from synchrotron radiation, reduces its resolution to $\sigma(E)/E = 0.25/\sqrt{E(\mathrm{GeV})}$. Due to poor understanding of the LUMI-e only the LUMI-γ is used to measure the luminosity, while the LUMI-e is used only for additional systematic checks. The luminosity is then determined from the ratio of the number of measured bremsstrahlung photons divided by the cross section. The largest uncertainties in the luminosity measurement come from the uncertainty in the calibration of the LUMI-γ and the photon acceptance. The measured luminosity and its uncertainty for each run period are listed in Table 2.1.

2.3.6. Trigger

The bunch spacing time in the HERA accelerator is 96 ns, leading to a bunch crossing rate within the ZEUS detector of 10.4 MHz. Since the rate of non-*ep* events is about 3 – 5 orders of magnitude larger than the rate of *ep* interactions, most of the events detected by ZEUS are background events. An advanced trigger system is needed to select the interesting *ep* physics events and reject the background events in order to bring the event rate down to a level acceptable for data storage. The ZEUS detector has a three level trigger system [44] which reduces the final event rate to an acceptable level of $\sim$ 5 Hz. Figure 2.8 gives a schematic view of the data acquisition chain, DAQ, together with the trigger system.

First Level Trigger

The ZEUS first level trigger, FLT, is based on hardware (ASIC, FPGA) processors, and reduces the rate from 10.4 MHz to about 300 – 500 Hz. Each component stores its event information in a pipeline of 46 bunch crossings deep, running synchronously with the HERA clock. Hence, the FLT decision to keep or discard the event has to reach the components front-end electronics within 4.4 μs. The components participating in the FLT decision, perform their calculations in parallel on a subset of their data, using rough, but fast algorithms. The outcome of the calculation of each component is passed to the global first level trigger, GFLT, within $\sim$ 2.5 μs. The GFLT combines the information from the different components and issues a decision to keep or discard the event within $\sim$ 2 μs.

Second Level Trigger

If the GFLT issues the decision to keep the event, the detector components transport the detector data from the pipeline to event buffers for processing by the second level trigger, SLT, which reduces the output rate to 50 – 70 Hz. The SLT is a software trigger, based on a set of parallel processing transputers. As with the FLT, each component participating in the SLT decision process, processes its own data, which is then passed to the global second level trigger, GSLT, which decides to keep or discard the event. Due to more time available at the SLT level, the components can use more sophisticated algorithms, i.e.

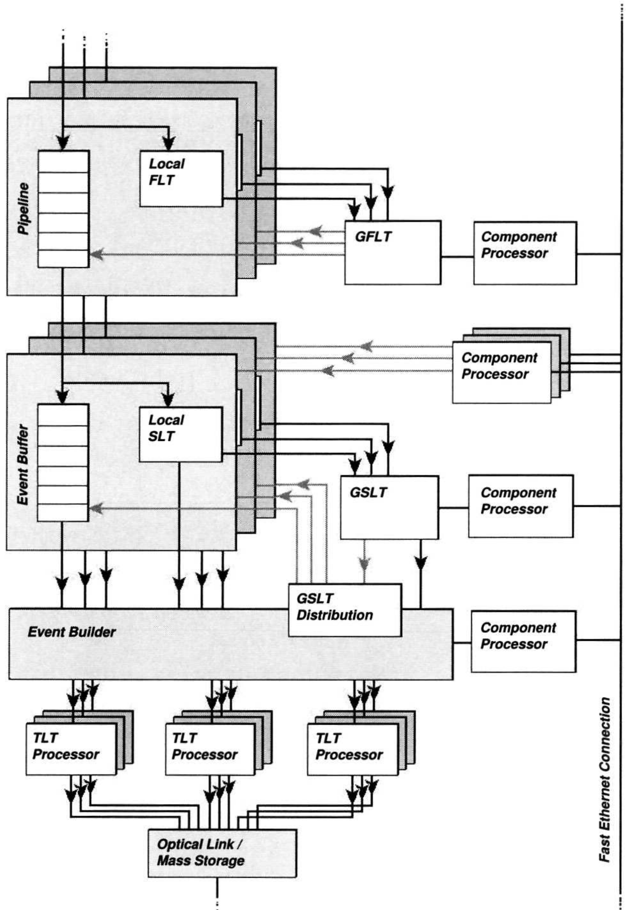

Figure 2.8. A schematic overview of the ZEUS trigger and DAQ chain.

track reconstruction, for processing the available data of better precision that at the FLT.

Third Level Trigger

If the GSLT accepts the event, all components pass their data to the event builder, EVB, which assembles the data into events which are passed to the third level trigger, TLT. The TLT is a cluster of Silicon Graphics workstations, SGIs, which were upgraded to a cluster of Linux machines after the upgrade in 2001. The TLT runs a reduced version of the off-line analysis programs for full event reconstruction, and applies similar event selection algorithms as used in the off-line analysis. The TLT reduces the rate by an additional factor of $5-10$. The event data is transmitted to DESY central data storage via an optical fibre link, FLINK, for storage at $5-14\,\mathrm{Hz}$.

2.4. Data Samples

The charged current cross section measurements described in this thesis are based on data collected in the running period 1998 – 2000. HERA delivered $25.2\,\mathrm{pb}^{-1}$ of e^-p data in the period 1998 – 1999 of which $16.4\,\mathrm{pb}^{-1}$ was collected with the ZEUS detector and passed the data quality monitoring. This sample has been used for the cross section measurement of $e^-p \to \nu_e X$. In the running period 1999 – 2000 HERA delivered $66.41\,\mathrm{pb}^{-1}$ of e^+p data of which $60.9\,\mathrm{pb}^{-1}$ has been used for the cross section measurement of $e^+p \to \bar{\nu}_e X$.

Chapter 3

Event Simulation

The experimentally measured charged current events need to be converted into cross sections. This requires corrections for finite detector efficiencies, resolutions and acceptances. A chain of computer programs were used to simulate the physics processes and correct for these effects. Moreover, the simulation of background physics processes mimicking CC events were used to correct the final measurement. For the simulation of the physics processes Monte Carlo, MC, simulation programs were used. The generation of events is performed in three main steps:

- hard *ep* scattering process;
- QCD cascades;
- hadronisation.

In this chapter an overview will be presented of the MC programs used to simulate the various physics processes.

Figure 3.1 shows a diagram of the ZEUS off-line software chain. The events from the MC event generators are passed, using the ZDIS interface, to the full detector simulation program, MOZART [30], which is based on GEANT 3.13 [45]. The MOZART program, which contains a detailed description of the material composition and geometry of the detector, simulates the passage of all the particles in the event through the various subdetectors. The simulated data created by MOZART are passed to the data acquisition chain and trigger system simulation, performed by the computer program ZGANA [46]. The simulated data is reconstructed by ZEPHYR and stored in the same data format as the events measured by the ZEUS detector, and can be further processed with off-line tools like EAZE, for analysis, and ZEVIS [47], for event visualisation.

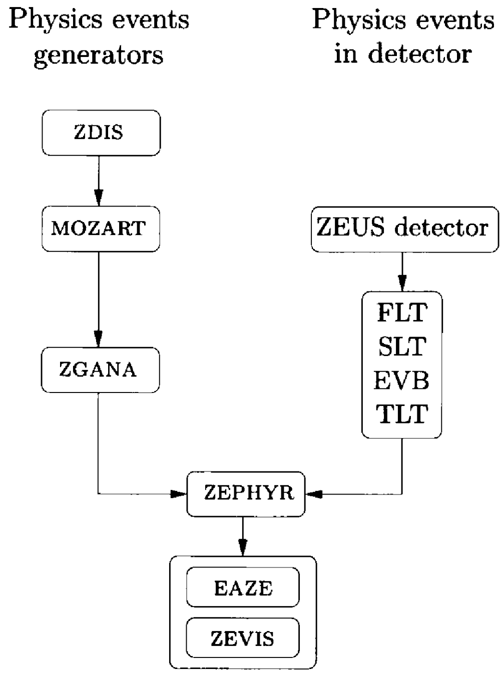

Figure 3.1. Schematic diagram of the ZEUS off-line software chain.

3.1. Signal Monte Carlo

The charged current events were simulated using DJANGOH 1.1 [48] which interfaces HERACLES 4.6.1 [49] to LEPTO 6.5 [50]. The computer program LEPTO was used to simulate the hard *ep* scattering process and HERACLES was used to include the radiative corrections, comprising single photon emission from the lepton as well as self energy corrections and the complete set of one-loop weak corrections. The mass of the W boson was calculated using the values for the fine structure constant, the Fermi constant, the mass of the Z boson and the mass of the top quark published by the Particle Data Group [51], PDG, and with the Higgs boson mass set to 100 GeV. The parametrisation of the parton distribution functions, PDFs, of CTEQ5D [52] were used by LEPTO in the hard scattering processes. The QCD cascade was simulated by the colour dipole model, CDM, of ARIADNE 4.10 [53]. The QCD cascade was modelled by ARIADNE by emitting gluons from a chain of independently radiating dipoles spanning colour connected partons. Monte Carlo events generated with the QCD cascading

Table 3.1. Generated Monte Carlo samples of charged current events.

Monte Carlo samples		$e^-p \to \nu_e X$		$e^+p \to \bar{\nu}_e X$	
		σ(pb)	$\mathcal{L}$(pb^{-1})	σ(pb)	$\mathcal{L}$(pb^{-1})
$Q^2 > 10\,\mathrm{GeV}^2$		78.943	316.01	45.202	553.07
$Q^2 > 100\,\mathrm{GeV}^2$		72.778	343.41	39.774	628.56
$Q^2 > 100\,\mathrm{GeV}^2$	$x > 0.1$	28.201	354.28	9.6417	1037.2
$Q^2 > 100\,\mathrm{GeV}^2$	$x > 0.3$	5.6590	882.31	1.2716	3932.1
$Q^2 > 5000\,\mathrm{GeV}^2$		14.445	1037.4	3.1998	4687.8
$Q^2 > 10000\,\mathrm{GeV}^2$		5.3854	1856.9	0.6828	7322.8
$Q^2 > 20000\,\mathrm{GeV}^2$		1.1339	8819.1	0.0619	80775.4

model of LEPTO, the matrix element parton shower, MEPS, model, instead of the CDM of ARIADNE were used as a systematic check for the model dependence of the QCD cascade, see Sect. 6.5.2. Finally, the hadronisation was simulated using the Lund string model as implemented in JETSET 7.4 [54].

The CC DIS ep cross section falls rapidly with increasing Q^2 and x. Hence, different samples of CC events were generated with increasing thresholds in Q^2 and x in order to have sufficient numbers of events to make the statistical uncertainties arising from the MC simulation negligible compared to those of the data. The thresholds in Q^2 and x were defined from the incoming and outgoing lepton. The various samples were merged and normalised to the data luminosity. In Table 3.1 the CC DIS MC samples generated with ARIADNE CDM are listed. Equivalent samples were generated with the MEPS model.

3.2. Background Monte Carlo

Various processes can form a background in the charged current event sample. The MC programs used to generate these background events, and the samples used to estimate the background will be discussed now.

3.2.1. Neutral Current DIS

Neutral current, NC, events can form a background when the energy of the scattered electron is not fully measured, i.e. when the electron goes into the crack region of the calorimeter, or due to fluctuations in the energy measurement. The NC MC events were generated with the same MC programs as used for the generation of the CC MC events, using CDM of ARIADNE for the QCD cascade. They are listed in Table 3.2 together with the corresponding luminosity. The minimum generated Q^2 is $Q^2 = 100\,\mathrm{GeV}^2$. Although it is possible that NC events with lower Q^2 can also form a background it is very hard to produce NC MC events samples with $Q^2 < 100\,\mathrm{GeV}^2$ with a luminosity comparable to the data luminosity, since the number of events which has to be generated becomes very large.

Table 3.2. Generated Monte Carlo samples of neutral current events.

Monte Carlo samples	$e^-p \to e^-X$		$e^+p \to e^+X$	
	$\sigma(\mathrm{pb})$	$\mathcal{L}(\mathrm{pb}^{-1})$	$\sigma(\mathrm{pb})$	$\mathcal{L}(\mathrm{pb}^{-1})$
$Q^2 > 100\,\mathrm{GeV}^2$	$8.16{\cdot}10^3$	$4.66{\cdot}10^1$	$8.12{\cdot}10^3$	$1.16{\cdot}10^2$
$Q^2 > 400\,\mathrm{GeV}^2$	$1.20{\cdot}10^3$	$5.01{\cdot}10^1$	$1.17{\cdot}10^3$	$1.03{\cdot}10^2$
$Q^2 > 1250\,\mathrm{GeV}^2$	$2.17{\cdot}10^2$	$1.15{\cdot}10^2$	$1.98{\cdot}10^2$	$2.53{\cdot}10^2$
$Q^2 > 2500\,\mathrm{GeV}^2$	$7.18{\cdot}10^1$	$1.67{\cdot}10^2$	$5.89{\cdot}10^1$	$4.07{\cdot}10^2$
$Q^2 > 5000\,\mathrm{GeV}^2$	$2.17{\cdot}10^1$	$5.54{\cdot}10^2$	$1.48{\cdot}10^1$	$1.62{\cdot}10^3$
$Q^2 > 10000\,\mathrm{GeV}^2$	$5.36{\cdot}10^0$	$2.24{\cdot}10^3$	$2.79{\cdot}10^0$	$8.59{\cdot}10^3$
$Q^2 > 20000\,\mathrm{GeV}^2$	$8.47{\cdot}10^{-1}$	$1.42{\cdot}10^4$	$3.10{\cdot}10^{-1}$	$7.74{\cdot}10^4$
$Q^2 > 30000\,\mathrm{GeV}^2$	$1.85{\cdot}10^{-1}$	$3.24{\cdot}10^4$	$5.44{\cdot}10^{-2}$	$2.20{\cdot}10^5$
$Q^2 > 40000\,\mathrm{GeV}^2$	$4.26{\cdot}10^{-2}$	$1.41{\cdot}10^5$	$1.09{\cdot}10^{-2}$	$1.10{\cdot}10^6$
$Q^2 > 50000\,\mathrm{GeV}^2$	$9.19{\cdot}10^{-3}$	$6.53{\cdot}10^5$	$2.12{\cdot}10^{-3}$	$5.66{\cdot}10^6$

3.2.2. Photoproduction

Neutral current interactions with $Q^2 \sim 0\,\mathrm{GeV}^2$ are categorised as photoproduction, php, interactions. Typically php events are multi-jet events with low missing transverse momentum and a scattered electron that escapes undetected through the rear beampipe. Since the cross section of php is much larger than the charged current cross section, php interactions can form a serious background when the energy of the jets produced in the events is not fully measured, i.e. due to fluctuations in the energy measurement for events with a large transverse energy, $E_T = \sum_i E_i \sin\theta_i$, or due to particles produced in the interaction not (fully) measured by the detector (neutrinos, muons).

Two types of photoproduction interactions were simulated. The first type is direct photoproduction. Here the incoming photon acts as a point-like particle in the interaction with the quarks of the proton. Figures 3.2(a) and 3.2(b)

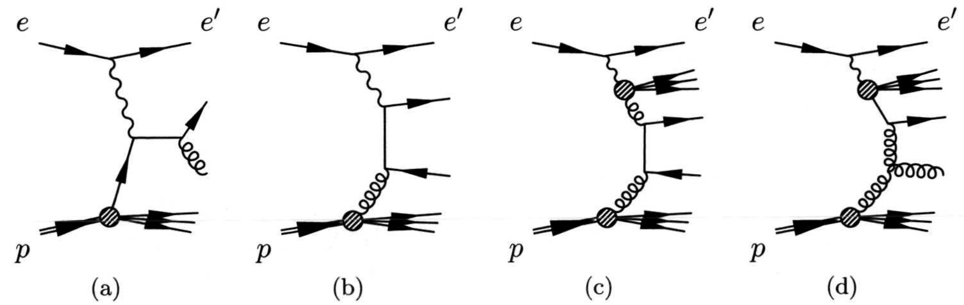

Figure 3.2. Leading order direct photoproduction processes: (a) QCD Compton and (b) boson gluon fusion. Examples of resolved photoproduction processes: (c) and (d).

show two diagrams contributing to the direct php process. The second type is resolved photoproduction, where the incoming photon acts as a source of quarks and gluons interacting with the quarks and gluons of the proton. Figures 3.2(c) and 3.2(d) show two diagrams contributing to the resolved php process.

The php events were generated with the HERWIG 5.9 [55] MC program. Since the php cross section is very large, only events that could mimic a charged current events were selected by requirements on $P_{T,\mathrm{h}}$ and $E_{T,\mathrm{h}}$ at the physics generator level. $P_{T,\mathrm{h}}$ and $E_{T,\mathrm{h}}$ are the vector sum and scalar sum of the transverse energy of the generated final state particles that are not neutrinos and have $0.038 < \theta < 3.081$ (i.e. excluding particles leaving through the beampipe). The generated php MC samples are listed in Table 3.3 together with their $P_{T,\mathrm{h}}$ and $E_{T,\mathrm{h}}$ selection thresholds. It has been verified that events with lower $P_{T,\mathrm{h}}$ or $E_{T,\mathrm{h}}$ do not form a background in the CC event sample.

Table 3.3. Generated Monte Carlo samples of direct and resolved photoproduction events.

Monte Carlo Samples		$\sigma(\mathrm{pb})$	$\mathcal{L}(\mathrm{pb}^{-1})$
direct php	$P_T > 6\,\mathrm{GeV}$ OR $E_T > 18\,\mathrm{GeV}$	$2.17{\cdot}10^4$	4.60
direct php	$P_T > 6\,\mathrm{GeV}$ OR $E_T > 20\,\mathrm{GeV}$	$1.56{\cdot}10^4$	35.9
direct php	$P_T > 6\,\mathrm{GeV}$ OR $E_T > 30\,\mathrm{GeV}$	$3.62{\cdot}10^3$	331.5
resolved php	$P_T > 6\,\mathrm{GeV}$ OR $E_T > 18\,\mathrm{GeV}$	$1.16{\cdot}10^5$	3.03
resolved php	$P_T > 6\,\mathrm{GeV}$ OR $E_T > 20\,\mathrm{GeV}$	$7.92{\cdot}10^4$	22.7
resolved php	$P_T > 6\,\mathrm{GeV}$ OR $E_T > 30\,\mathrm{GeV}$	$1.19{\cdot}10^4$	302.5

3.2.3. Charged Lepton Production

Charged lepton production in ep interactions can form a background in the CC event sample when a $\mu^+\mu^-$ pair, di-muon, or $\tau^+\tau^-$ pair, di-tau, is created via the process shown in Figure 3.3(a). In the case of di-muon production, the muons act as MIPs in the calorimeter and can leave the calorimeter without being stopped, giving rise to a missing transverse momentum in the event. In di-tau production, $P_{T,\mathrm{miss}}$ can be caused by neutrinos from the τ decay leaving the detector undetected. The GRAPE–Dilepton [56] MC generator was used to generate samples of both di-muon and di-tau events. In order to cover the whole kinematic region events were generated in three categories: elastic, quasi-elastic and DIS processes. In Table 3.4 the generated di-lepton event samples with their luminosity are listed.

Table 3.4. Generated Monte Carlo samples of di-lepton events.

Monte Carlo samples		$e^-p \to e^-l^+l^-X$		$e^+p \to e^+l^+l^-X$	
		σ(pb)	$\mathcal{L}$(pb^{-1})	σ(pb)	$\mathcal{L}$(pb^{-1})
$\mu^+\mu^-$	elastic	10.1	1078.66	10.1	2059.26
$\mu^+\mu^-$	quasi-elastic	5.13	19012.1	5.13	20018.5
$\mu^+\mu^-$	DIS	19.2	5934.24	19.2	8635.92
$\tau^+\tau^-$	elastic	6.34	1024.26	6.34	2048.52
$\tau^+\tau^-$	quasi-elastic	3.66	29809.4	3.66	30792.3
$\tau^+\tau^-$	DIS	7.71	13352.9	7.70	14404.5

No e^+e^- pairs, di-electrons, were generated. Di-electron production does not form a background in the CC event sample since the electrons are fully contained within the detector.

3.2.4. Single W Production

Electron-proton interactions in which a real W boson is produced are indicated as single W production. The dominant process for single W production is shown in Fig. 3.3(b). Single W production can form a background in the CC event sample, when the W decays semi-leptonically into a lepton and a neutrino, and the neutrino leaves the detector undetected giving rise to $P_{T,\mathrm{miss}}$.

In an analogous way as for php, two categories are distinguished; resolved and DIS single W production. In resolved W production the incoming photon

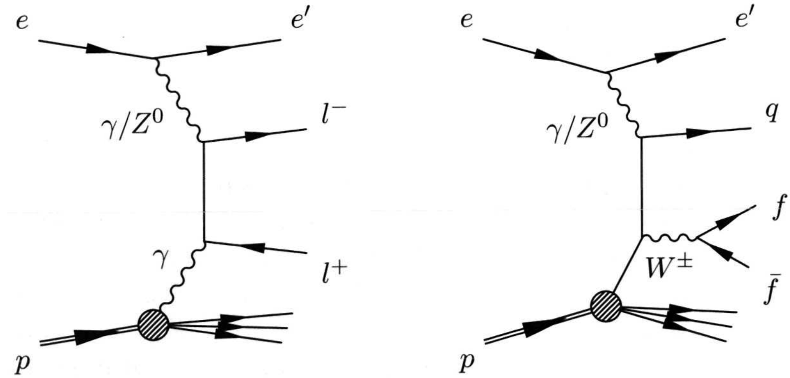

(a) (b)

Figure 3.3. Example diagrams of: (a) di-lepton production via a two photon interaction and (b) single W production. The W can decay to a quark-antiquark pair or a lepton-antilepton pair.

acts as a source of quarks and gluons interacting with the proton. Then the W production can be thought of as $q\bar{q} \to W$, where one of the quarks is regarded as a constituent of the photon [57]. In DIS W production, the photon acts as a point-like particle. In Table 3.5 the samples of single W production events are listed with the corresponding luminosity, which were generated with the EPVEC [58] MC generator.

Table 3.5. Generated Monte Carlo samples of direct and resolved single W events.

Monte Carlo Samples	resolved		DIS	
	σ(pb)	$\mathcal{L}$(pb^{-1})	σ(pb)	$\mathcal{L}$(pb^{-1})
$e^-p \to e^-W^-X$	0.0262	$3.82{\cdot}10^5$	0.0883	$1.13{\cdot}10^5$
$e^-p \to e^-W^+X$	0.0329	$3.04{\cdot}10^5$	0.1036	$9.65{\cdot}10^4$
$e^+p \to e^+W^-X$	0.0262	$3.82{\cdot}10^5$	0.0871	$1.15{\cdot}10^5$
$e^+p \to e^+W^+X$	0.0329	$3.04{\cdot}10^5$	0.1061	$9.43{\cdot}10^4$

Chapter 4

Event Reconstruction

4.1. Introduction

The charged current cross section measurements described in this thesis are expressed in the kinematic variables of DIS interactions. Therefore it is necessary that the kinematic variables are accurately reconstructed from the information provided by the ZEUS detector. In this chapter the reconstruction method for the kinematic variables, the hadronic energy flow and the event vertex will be discussed.

4.2. Kinematics Reconstruction

The kinematic variables describing a DIS interaction in terms of the four-momenta of the partons participating in the hard scattering process have been described in Sect. 1.2. A DIS event can be described with two kinematic variables. Common choices are any pair of x, y or Q^2, which are related through[1]

$$Q^2 = sxy, \tag{4.1}$$

where s is the square of the centre-of-mass energy of the ep system, $s = 4E_eE_p$, with E_e the electron beam energy and E_p the proton beam energy.

Two independent variables which are traditionally used to reconstruct the kinematics of DIS events are the measured energy, E'_e, and polar angle, θ_e, of the scattered electron (see Fig. 4.1). The kinematics are then determined by (using (1.2) and (1.8))

$$y_e = 1 - \frac{E'_e}{2E_e}(1 - \cos\theta_e), \tag{4.2}$$

$$Q_e^2 = \frac{E_e^2 \sin^2\theta_e}{1 - y_e}, \tag{4.3}$$

[1]Neglecting the mass of the electron and proton.

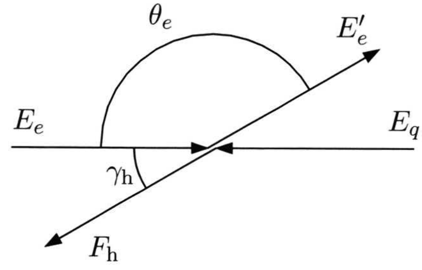

Figure 4.1. Schematic illustration of a DIS interaction showing the quantities used in the reconstruction of the event kinematics, E'_e, θ_e, F_h and γ_h. In this illustration an electron with energy E_e comes from the left and a quark inside the proton with energy E_q comes from the right.

where E_e is the energy of the incoming electron. x_e can be obtained from (4.1). Within the ZEUS collaboration this method is known as the 'Electron-Method'.

Since the ZEUS detector is an almost fully hermetic detector, also the information from the final hadronic system can be used to reconstruct the kinematic variables, where the hadronic final state consists of all particles produced in the *ep* interaction except the scattered electron. Then, the independent variables which can be used to reconstruct the event kinematics are the transverse momentum of the hadronic final state, $P_{T,\mathrm{h}}$, defined as

$$P_{T,\mathrm{h}} = \sqrt{\left(\sum_i P_{X,i}\right)^2 + \left(\sum_i P_{Y,i}\right)^2} = \sqrt{P^2_{X,\mathrm{h}} + P^2_{Y,\mathrm{h}}}, \tag{4.4}$$

and

$$\delta_{\mathrm{h}} = \sum_i (E_i - P_{Z,i}) = E_{\mathrm{h}} - P_{Z,\mathrm{h}}. \tag{4.5}$$

The index i runs over all calorimeter cells with energy deposits from particles in the hadronic final state. E_{h} is the sum of all hadronic energy deposits in the event, and $P_{X,\mathrm{h}}$, $P_{Y,\mathrm{h}}$, $P_{Z,\mathrm{h}}$ are the sums of the projections of the hadronic energy deposits in the X, Y and Z directions. The variables $P_{T,\mathrm{h}}$ and δ_{h} give information about the direction and energy of the hadronic system and can be rewritten to

$$\cos\gamma_{\mathrm{h}} = \frac{P_{T,\mathrm{h}}^2 - \delta_{\mathrm{h}}^2}{P_{T,\mathrm{h}}^2 + \delta_{\mathrm{h}}^2}, \tag{4.6}$$

$$F_{\mathrm{h}} = \frac{P_{T,\mathrm{h}}^2 + \delta_{\mathrm{h}}^2}{2\delta_{\mathrm{h}}}. \tag{4.7}$$

In the naive quark-parton model the angle γ_{h} and the energy F_{h} represent the angle and energy of the scattered quark (see Fig. 4.1).

Since no information about the scattered lepton is available in CC DIS interactions - it leaves the detector as an undetected neutrino - the kinematic variables have to be reconstructed using the information of the hadronic final state only. In analogy with the Electron-Method, and considering the hadronic final state as a single system, of which the internal structure is not important, the kinematic variables can be determined by (or in terms of $P_{T,\mathrm{h}}$ and δ_{h})

$$y_{\mathrm{JB}} = \frac{F_{\mathrm{h}}}{2E_e}(1 - \cos\gamma_{\mathrm{h}}) = \frac{\delta_{\mathrm{h}}}{2E_e}, \tag{4.8}$$

$$Q_{\mathrm{JB}}^2 = \frac{F_{\mathrm{h}}^2 \sin^2\gamma_{\mathrm{h}}}{1 - y_{\mathrm{JB}}} = \frac{P_{T,\mathrm{h}}^2}{1 - y_{\mathrm{JB}}}. \tag{4.9}$$

The x_{JB} of the event can be obtained from (4.1). This reconstruction method is known as the 'Jacquet-Blondel Method' [59].

The uncertainty of the kinematic variables is due to measurement errors on the detector observables, i.e. $P_{T,\mathrm{h}}$ and δ_{h}. The kinematic variables are related to the detector observables via the reconstruction methods. Hence, a measurement error on the detector observables results in a different resolution of the kinematic variables for different regions in the $(x,\ Q^2)$ phase space. Figure 4.2 shows the isolines for some detector observables in the $(x,\ Q^2)$ phase space. The isolines of the observables in the $(x,\ Q^2)$ phase space imply a good intrinsic resolution if they are close together. For these dense isolines, measurement errors on the detector observables lead to small uncertainties on x and Q^2. The intrinsic resolution is worse for isolines that are far apart because then a small measurement error on the detector observables corresponds to a large volume in the $(x,\ Q^2)$ phase space. Figure 4.2(a) shows the isolines for $P_{T,\mathrm{h}}$. At low y the isolines of $P_{T,\mathrm{h}}$ run almost parallel to the x axis. Therefore, by measuring $P_{T,\mathrm{h}}$ at low y the value of Q^2 is almost fixed and nearly independent of y, whereas, the measurement contains minimal information on x. In the very high y region of the (x, Q^2) phase space the isolines of $P_{T,\mathrm{h}}$ and δ_h run almost parallel to each other. This implies a large uncertainty on both x and Q^2; a very precise measurement of the hadronic energy flow would be necessary to obtain a reasonable resolution of x and Q^2. Hence, events with $y > 0.9$ are excluded from the final CC DIS event sample.

The measurement errors on $P_{T,\mathrm{h}}$ and δ_h are related to the accuracy by which the energy of the hadronic system can be measured. The largest negative effect on the energy measurement is caused by the dead material in front of the calorimeter. The corrections applied to the energy measurements to correct for this inactive material will be discussed in Sect. 4.3.3. Other effects affecting the energy measurements are energy leakage through the calorimeter and, since the detector is only almost fully hermetic, particle losses through the forward/backward beampipe. The effect of energy leakage through the calorimeter is included in a systematic study described in Sect. 6.5.7. Furthermore, both $P_{T,\mathrm{h}}$ and δ_h are rather insensitive to particle losses through the forward beam pipe, since very forward particles generally carry not much P_T and their E_h and $P_{Z,\mathrm{h}}$ cancel in δ_h. Particle losses through the backward beam pipe are not an issue, since the direction of the particles in the hadronic system is mostly very forward; this is due to the large difference in energy between the electron and proton beam.

In NC DIS events information is available from both the scattered electron and the hadronic final state, whereas in CC DIS only information of the hadronic part is available. Various methods have been developed to reconstruct the kinematic variables by combining information from the scattered electron and the hadronic final state, and applying energy and momentum conservation. Therefore, these methods are less sensitive for energy losses. Examples of these methods are the 'Double Angle Method' [60], the 'Σ-Method' [61] and the 'P_T-Method' [62].

4.3. Hadronic Energy

The detector observables used in the reconstruction of the kinematic variables are determined from the energy measurement of the CAL. The energy measured in a cell in the CAL is determined from

$$E_{\mathrm{cell}} = E_{\mathrm{PMT},1} + E_{\mathrm{PMT},2}, \tag{4.10}$$

where $E_{\mathrm{PMT},1}$ and $E_{\mathrm{PMT},2}$ are the signals measured by the two PMTs of the cell. The signals from the PMTs also provide a timing signal. The timing

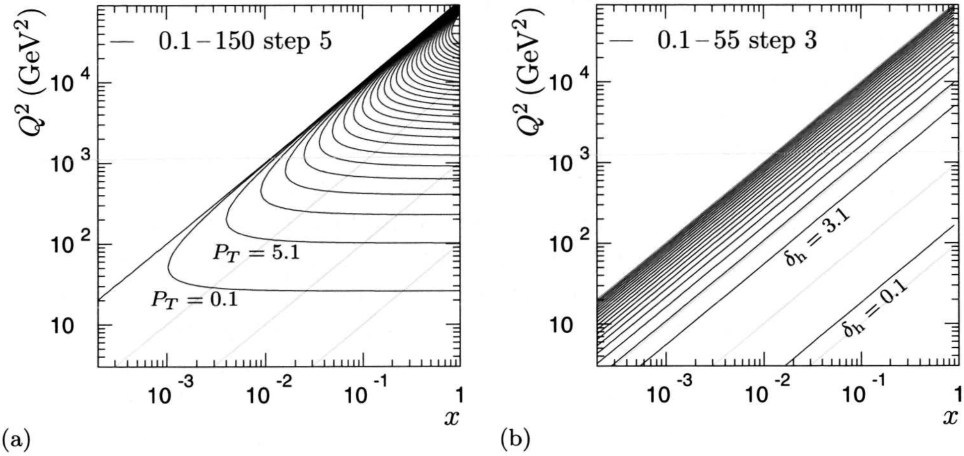

Figure 4.2. Isolines in the (x, Q^2) phase space of: (a) the transverse hadronic energy, $P_{T,h}$, (b) the $E_h - P_{Z,h}$, δ_h, (c) the hadronic angle, γ_h and (d) the energy of the struck quark F_h.

resolution of the cell is optimised with the use of the weighted average of the timing signals of the PMTs

$$t_{\text{cell}} = \frac{\frac{1}{\sigma_1^2} t_{\text{PMT},1} + \frac{1}{\sigma_2^2} t_{\text{PMT},2}}{\frac{1}{\sigma_1^2} + \frac{1}{\sigma_2^2}}, \tag{4.11}$$

where $t_{\mathrm{PMT},1}$ and $t_{\mathrm{PMT},2}$ are the times measured by the two PMTs and σ_i is the PMT timing resolution, parameterised as

$$\sigma_i(\mathrm{ns}) = 0.4 + \frac{1.4}{E_{\mathrm{PMT},i}^{0.65}}, \tag{4.12}$$

where $E_{\mathrm{PMT},i}$ is the energy measured by the i-th PMT of the cell in GeV.

Several corrections are applied in order to improve the energy measurement. They will be discussed in the next sections.

4.3.1. Noise Suppression

The reconstruction of the kinematic variables can be affected by noise in the calorimeter. Especially at low y, i.e. low δ_{h}, a noisy cell in the rear of the detector can change the measured value of y considerably. Noise in the calorimeter originates from natural radioactivity of the depleted uranium, used as the absorber material in the CAL, malfunctioning of the bases of the PMTs and readout electronics.

The uranium noise, UNO, forms a constant background in the CAL for which can be corrected by subtracting the average value. Effects of fluctuations can further be reduced by discarding EMC cells with energy deposits less than 60 MeV, and HAC cells with energy deposits less than 110 MeV. For isolated cells, i.e. cells with no neighbouring cells with an energy deposit, these thresholds were increased to 80 MeV for EMC cells and 140 MeV for HAC cells; these cuts are referred to as "zero suppression cuts". Also "mini-sparks cells" were removed. These are cells of which only one of the PMTs produced a small signal. The imbalance, imb, is defined as the difference in energy measured by the two PMTs

$$\mathrm{imb} = E_{\mathrm{PMT},1} - E_{\mathrm{PMT},2}. \tag{4.13}$$

The ratio $\mathrm{imb}/E_{\mathrm{cell}}$ for mini-sparks is close to ± 1 and they were removed by [63]

$$\left|\frac{\mathrm{imb}}{E_{\mathrm{cell}}}\right| > 0.49 E_{\mathrm{cell}} + 0.03 \texttt{ AND } E_{\mathrm{cell}} < 1\,\mathrm{GeV}. \tag{4.14}$$

Finally, "hot" cells, cells which fire much more often than expected, were removed. These cells were identified by an analysis [64] of samples of random trigger events, N_{rand}. Random trigger events or FLT pass-through events are events without an ep interaction in the detector. These samples consist of about 500 events collected at the beginning of each run. Additional quality

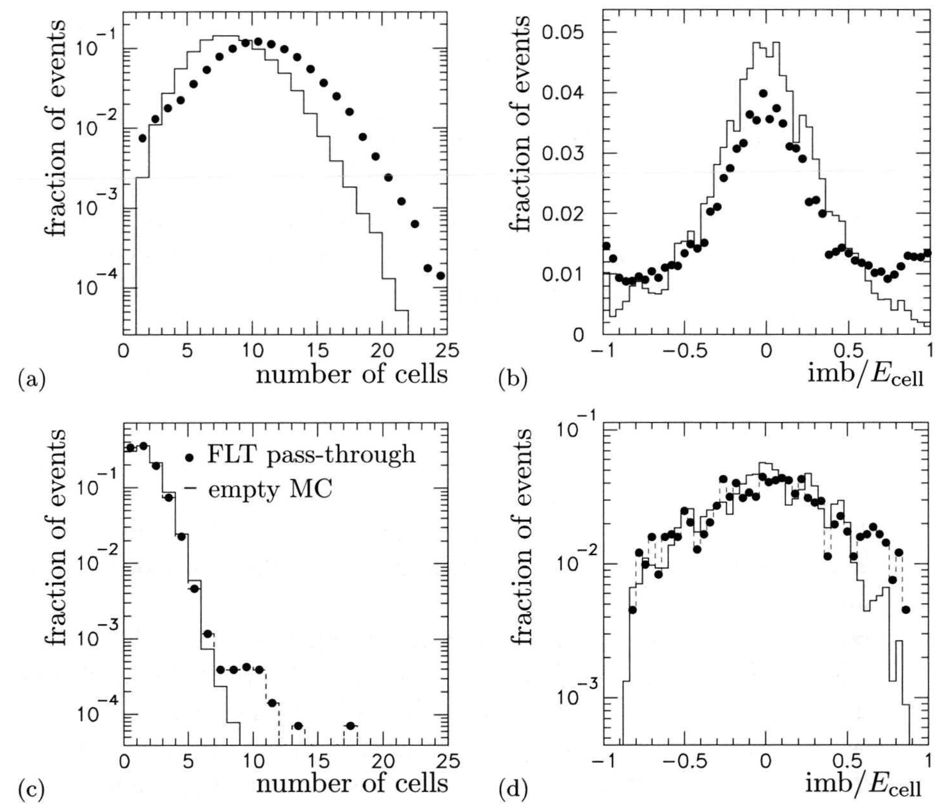

Figure 4.3. The effect of the noise suppression on the number of and the imbalance of cells with measured energy in empty events. (a) and (b) show the distributions before and (c) and (d) show the distributions after the noise suppression. The data (dots) and MC (line) are normalised to the number of events.

cuts remove beam-gas and cosmic muon events to ensure that energy deposits measured in the CAL cells originate from other sources than particle showers. A separate list of noisy cells was produced by a run-by-run three-steps procedure for each part (FCAL, BCAL and RCAL) and section (EMC, HAC1 and HAC2) of the CAL separately. The procedure was as follows:

1. Appearance cut: cells which appear more than 10 times in the sample of N_{rand} events and with total appearance greater than the mean appearance of a cell + 3σ are stored in the noisy cell candidate list and removed for

the next step;

2. Appearance after imbalance cut: cells which appear more than 10 times in the sample after the imbalance cut (4.14) has been applied and with total appearance greater than the mean appearance of a cell + 3σ (after (4.14)) are stored in the noisy cell candidate list and removed for the next step;

3. Energy cut: cells with mean energy deposit, $\langle E \rangle_{\text{cell}}$, greater than the mean energy of a cell + 3σ are stored in the noisy cell candidate list. The mean energy of a cell was defined as: $\langle E \rangle_{\text{cell}} = \sum E_{\text{cell}}/N_{\text{rand}}$, where the sum runs over all events in the sample of N_{rand} events.

Cells enter the final hot cell list if they are classified as noisy in more than two runs. The information stored in the final noisy cell list is the maximum energy, $E^{\text{max}}_{\text{cell}}$, the mean energy, $\langle E \rangle_{\text{cell}}$, the error on the mean energy, $\sigma_{\text{cell}}(E)$, and a tag indicating a high or low appearance of the cell together with the running period during which the cell was noisy. In order to avoid possible bias due to the presence of beam-gas events, the cells belonging to the first two rings around the beam-pipe (both in RCAL and FCAL) are removed from the list. In the event reconstruction, the final noisy cell list is applied as follows:

- Cells without imbalance
  - high appearance (more than 50 times): the cell is removed if its energy is less than $\langle E \rangle_{\text{cell}} + 3\sigma_{\text{cell}}(E)$;
  - low appearance (less than 50 times): the cell is removed if its energy is less than $E^{\text{max}}_{\text{cell}}$;
- Cells with imbalance
  the PMT with the largest energy deposit is considered noisy. Hence, the cell energy is corrected by: $E_{\text{cell}} = E_{\text{cell}} - |\text{imb}|$.

Figure 4.3 shows the effect of the noise suppression on the number of cells with energy deposits and the imbalance of these cells, measured in empty events. Empty MC events were generated using the full detector simulation without *ep* interactions. Hence, the measured cell energies in the MC originates from the UNO simulation. Figure 4.3 shows a good agreement between data and MC after application of the noise suppression.

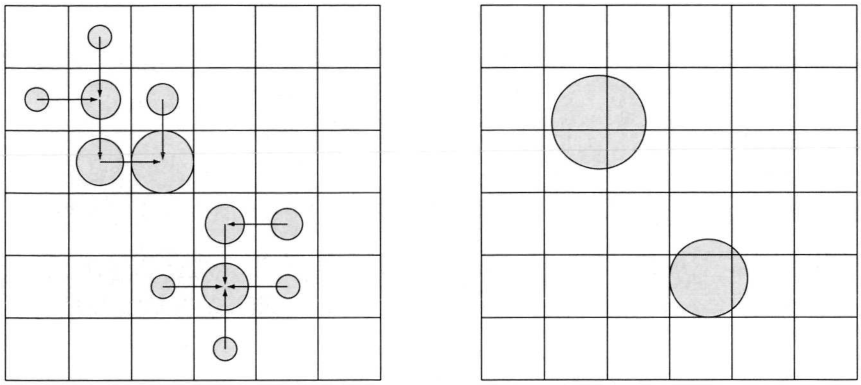

(a) (b)

Figure 4.4. Schematic drawing of cells clustering into cell islands. The squares represent the CAL cells; (a) the size of the filled circles is a measure for the amount of energy deposited in a cell. The clusters are formed by connecting the cells to their nearest neighbour with the highest energy; (b) shows the cell-islands. The size of the filled circles represents the energy of the deposited energy by the particles which entered the CAL.

4.3.2. Clustering

The detector observables could be measured by summing the energy deposits of all calorimeter cells. A better way is to cluster the cells into several groups, cone islands, which belong to the shower of the particle entering the CAL. In this way the energy measurement is corrected for the granularity effects of the calorimeter. Furthermore, the energy correction for dead material can be performed on these cone islands.

The CAL cells are clustered into cone islands in two steps [65]. In the first step, two dimensional objects, cell islands, are created for each part, FCAL, BCAL and RCAL, and section, EMC, HAC1 and HAC2, of the CAL, separately. The cell islands are formed using a nearest neighbour connecting algorithm, connecting cells to the adjacent cell with the highest energy. Figure 4.4(a) shows a schematic drawing of the algorithm used to form cell islands of CAL cells.

In the next step, the cell islands are connected to form three dimensional objects, cone islands. The cone islands are formed from the outside of the

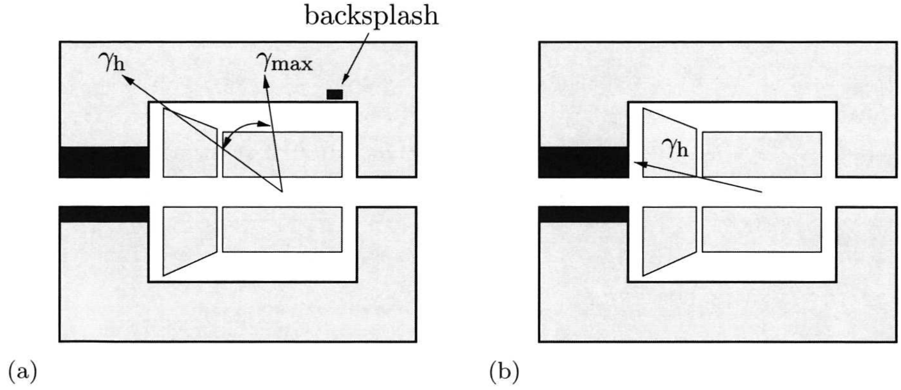

Figure 4.5. Schematic view of the ZEUS detector showing the effect on the angle of the hadronic system, γ_h, of energy deposits in the rear part of detector not originating from the hard interaction, backsplash; (a) before the backsplash correction; (b) after the backsplash correction.

CAL inwards; starting with the connection of HAC2 cell islands with HAC1 cell islands according to a merging probability. This merging probability was determined from a study based on single pion MC simulation, and was parameterised as a function of the opening angle between the examined pair of cell islands. If possible, HAC2 cell islands with a low merging probability are connected directly to EMC cell islands. In the same manner the HAC1 cell islands are connected to the EMC cell islands. The position of the obtained cone islands is determined by the logarithmically weighted centre-of-gravity of the shower [66].

4.3.3. Corrections for the Hadronic Final State

The distribution of the measured kinematic variables reconstructed with cone islands, in short islands, instead of CAL cells, still shows differences with the distribution of the true values from Monte Carlo simulation. The next sections contain an overview of the corrections applied to the hadronic system to correct for the effects of backsplash and dead material which cause these differences.

Backsplash Corrections

In this analysis, the kinematic variables are reconstructed using the Jacquet-Blondel method (see Sect. 4.2). Small energy deposits at a large polar angle have a large effect on the reconstruction of δ_h and thus on the angle of the hadronic system, γ_h, at small y_{JB}. An overestimate of γ_h or δ_h is observed at small y ($y < 0.3$) in events with a large Q^2 [67]. This is caused by energy deposits far away from the impact point of the particle. These energy deposits are caused by two mechanisms:

- backsplash from the calorimeter. Neutral particles, e.g. photons or neutrons, with low energy can escape from a large shower in the CAL (albedo effect) and traverse the detector;
- scattering or showering in the material in front of the calorimeter, e.g. beampipe or CTD inner wall.

The effects can cause an additional contribution to δ_h of the order of 1 GeV which becomes significant for small values of y_{true}.

A method was developed to remove backsplash using a Monte Carlo sample of NC DIS events with $Q^2 > 400\,\text{GeV}$. Islands were identified and removed as backsplash islands if they satisfy

$$E_{isl} < 3\,\text{GeV} \quad \texttt{AND} \quad \theta_{isl} > \gamma_{max},$$

where E_{isl} is the energy of the island and θ_{isl} is the polar angle. The threshold polar angle, γ_{max}, depends on γ_h as follows:

$$\gamma_{max} = \begin{cases} 1.372 \cdot \gamma_h + 0.151, & \gamma_h < 1.95, \\ 0.259 \cdot (\gamma_h - 1.95) + 2.826, & \gamma_h > 1.95. \end{cases}$$

These functions were determined using high Q^2 events of two Monte Carlo samples, one with and one without backsplash events. For each γ_h value a γ_{max} threshold was determined at which the backsplash is removed such that no more than 1% of islands in the event sample without backsplash events is excluded. Subsequently two linear functions were fitted to determine the γ_{max} dependence on γ_h. A detailed description of the fit procedure can be found elsewhere [68].

To reconstruct γ_h the values for γ_{max} were determined iteratively, starting from γ_h as given by all islands and using the resulting γ_h after applying the cut as input for the next iteration until the relative difference in γ_h between two iterations was less than 1%. A schematic view of the ZEUS detector and the effect on γ_h of the removal of backsplash is shown in Fig. 4.5. Figures 4.6 and 4.7 show the effect of the backsplash removal on the bias and resolution of the kinematic variables reconstructed with the Jacquet-Blondel method. A large improvement of the bias in y at low-y_{true} is clearly observed in Fig. 4.7(a).

Energy Corrections

Besides the backsplash correction, also energy corrections were applied for the following effects [68]:

- energy loss in inactive material between the interaction vertex and the surface of the detector;
- overestimate of the energy of hadrons at low energy;
- energy loss for particles entering the (super)crack regions between the F/BCAL and B/RCAL.

Corrections for the first two effects were derived from MC simulation, by comparing the reconstructed island energy, E_{isl}, with the true island energy, $E_{\mathrm{isl}}^{\mathrm{true}}$. A distinction was made between electromagnetic islands, $f_{\mathrm{EMC}} = E_{\mathrm{isl}}^{\mathrm{EMC}}/E_{\mathrm{isl}} = 1$, and hadronic islands, $f_{\mathrm{EMC}} < 1$. A correction function for the energy loss in inactive material was obtained by a fit of the ratio $E_{\mathrm{isl}}/E_{\mathrm{isl}}^{\mathrm{true}}$ for electromagnetic islands at all energies and hadronic islands at $E_{\mathrm{isl}}^{\mathrm{true}} > 7\,\mathrm{GeV}$ as a function of the radiation length, X_0, of the material in front of the CAL. For low energy hadrons the energy loss by ionisation (before initiating a shower) cannot be neglected [69]. This effect resulted in the need for an extra energy correction for hadronic islands with energy below 7 GeV. The correction was obtained by a comparison of the energy of the islands corrected for energy loss in the inactive material with $E_{\mathrm{isl}}^{\mathrm{true}}$ in different bins of f_{EMC}.

The first two corrections were determined with the exclusion of the super crack regions in the CAL, since the simulation of the energy losses in those regions is not in good agreement with the data. Hence, the energy correction for losses in the crack region was determined for data and MC separately without the use of true information provided by the MC simulation. The correction for loss in super cracks was derived using the ratio of the measured energy of the hadronic system and the energy calculated using the Double Angle method, $F_{\mathrm{h}}/F_{\mathrm{DA}}$, as a function of the hadronic angle, γ_{h}, in NC events. The measured

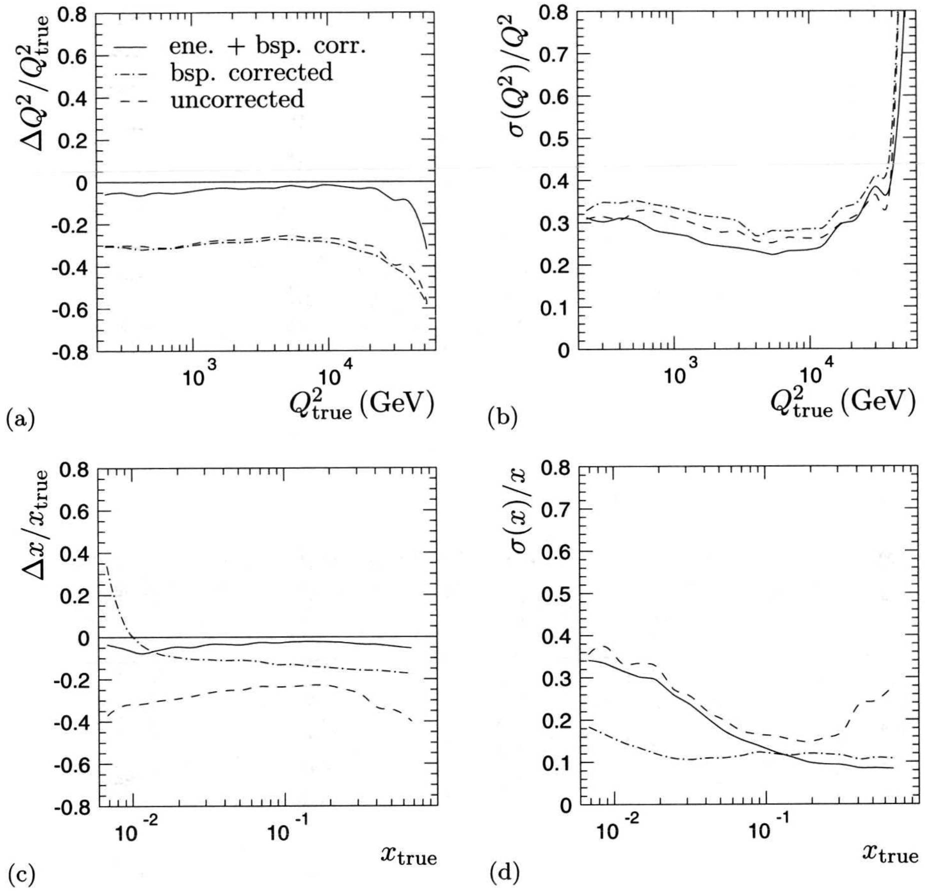

Figure 4.6. The performance of the hadronic reconstruction method (solid lines), compared to the hadronic reconstruction method with only the backsplash, bsp, corrections (dashed dotted lines) and to the hadronic reconstruction without backsplash or energy corrections (dashed lines). (a) The bias in the reconstruction of $Q^2_{\rm JB}$; (b) the resolution of $Q^2_{\rm JB}$; (c) the bias in the reconstruction of $x_{\rm JB}$; (d) the resolution of $x_{\rm JB}$.

energy of the hadronic system, $F_{\rm h}$, was obtained from Equation (4.7) and $F_{\rm DA}$ from

$$F_{\rm DA} = \frac{P_{T,{\rm DA}}}{\sin\gamma_{\rm h}} = \frac{\sqrt{Q^2_{\rm DA}(1-y_{\rm DA})}}{\sin\gamma_{\rm h}}, \tag{4.15}$$

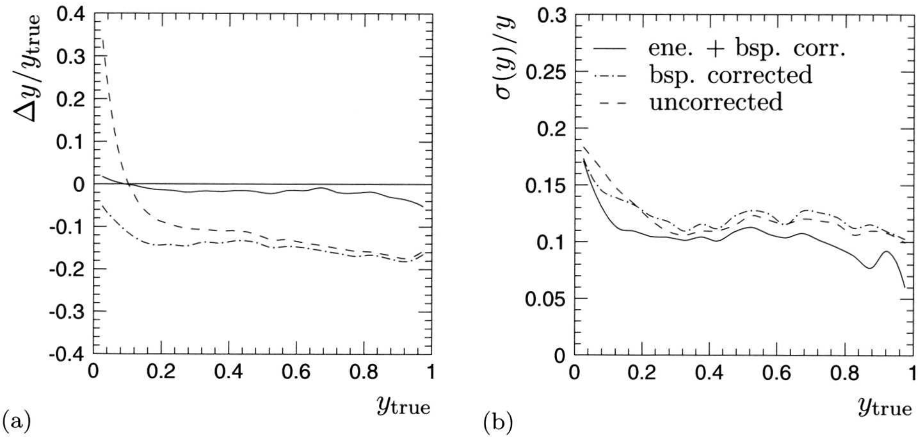

Figure 4.7. The performance of the hadronic reconstruction method (solid lines), compared to the hadronic reconstruction method with only the backsplash, bsp, corrections (dashed dotted lines) and to the hadronic reconstruction without backsplash or energy corrections (dashed lines). (a) The bias in the reconstruction of y_{JB}; (b) the resolution of y_{JB}.

where F_{DA} was used as the "true" energy of the hadronic system and y_{DA} and Q^2_{DA} are the double angle variables

$$y_{\mathrm{DA}} = \frac{\sin\theta_e(1-\cos\gamma_{\mathrm{h}})}{\sin\gamma_{\mathrm{h}} + \sin\theta_e - \sin(\gamma_{\mathrm{h}}+\theta_e)} \tag{4.16}$$

$$Q^2_{\mathrm{DA}} = 4E_e^2\frac{\sin\gamma_{\mathrm{h}}(1+\cos\theta_e)}{\sin\gamma_{\mathrm{h}} + \sin\theta_e - \sin(\gamma_{\mathrm{h}}+\theta_e)}, \tag{4.17}$$

Good agreement was observed between the true F_{h} from MC simulation and F_{DA} [70]. Corrections were obtained for the super crack regions F/BCAL and B/RCAL separately as a function of γ_{h}.

Figures 4.6 and 4.7 show the effect of the energy corrections on the relative resolution and bias of the kinematic variables reconstructed with the Jacquet-Blondel method. The bias is the mean of a Gaussian distribution fitted to the distribution of, e.g. Q^2

$$\frac{\Delta Q^2}{Q^2_{\mathrm{true}}} = \frac{Q^2_{\mathrm{JB}} - Q^2_{\mathrm{true}}}{Q^2_{\mathrm{true}}}, \tag{4.18}$$

in different bins of Q^2_{true}. The resolution is the standard deviation of the fitted Gaussian distribution. Large improvements in the bias of the kinematic variables are observed for all kinematic variables.

4.4. Interaction Vertex Measurement

The beams provided by HERA consisted of bunches of protons and electrons crossing every 96 ns. The length of the proton bunches is about 15 – 20 cm in Z; therefore not every interaction between a proton and an electron takes place at the same place in Z. For electron-proton collisions with a proton at the beginning of the proton bunch, the interaction vertex has a positive Z coordinate. For interactions with a proton at the end of the bunch the Z coordinate of the vertex is negative. In order to reconstruct the kinematic variables accurately it is important to measure the vertex position precisely.

The primary subdetector of ZEUS for measuring the vertex position is the CTD. The vertex position from the CTD is obtained by a fit to the reconstructed tracks. The vertex fit provides both a primary vertex (interaction vertex) and secondary vertices. The primary vertex is obtained from a fit with a constraint on "the diffuse pseudo-proton": the beam spot with beam spread errors. A detailed description of the fit can be found in [71]. The Z position of the interaction vertex can be reconstructed with a resolution of about 1 cm in CC events. (For NC events the presence of a high P_T scattered electron track improves the resolution of the Z position of the interaction vertex to about 0.4 cm.) The resolution of the X and Y position of the vertex is about 0.1 cm. The transverse sizes of the beams are smaller than the CTD vertex resolution in X and Y. Furthermore, the average transverse displacement of the vertex, as measured by the CTD, from its nominal position was also smaller than the resolution. Hence, the X- and Y-vertex positions were set to zero, their nominal position.

The distribution of the Z position of the vertex changes with time, due to changing beam conditions. For the acceptance calculation used in this analysis, the underlying Z-vertex distribution in the MC simulation must be the same as that in the data. (A Z-vertex distribution in the MC simulation which is not the same as that in the data can cause large migration effects in the (x, Q^2) phase space.) The underlying Z-vertex distribution which was used in the MC simulation was determined from event samples with an unbiased vertex distribution [72]. These samples corresponded to the selected run periods of the data.

The probability to find a vertex in an event depends on the number of charged

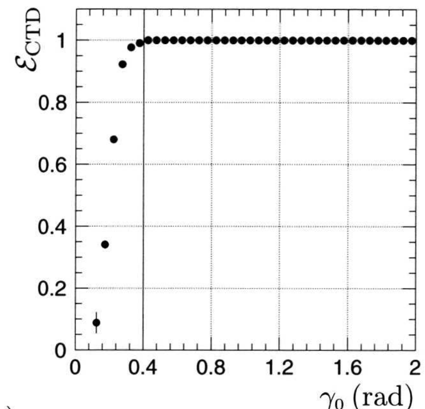

(a)

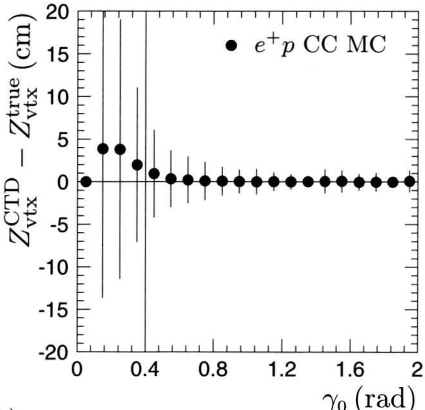

(b)

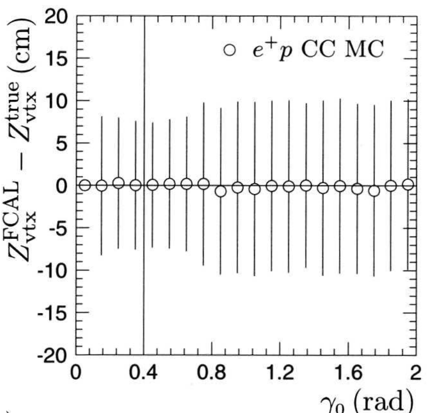

(c)

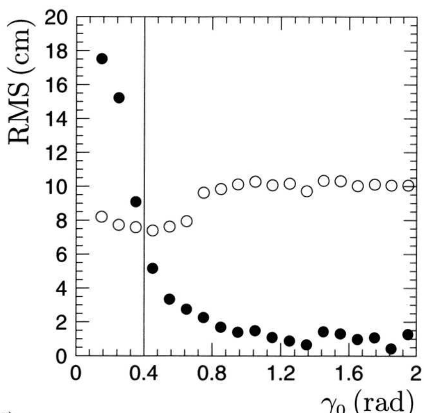

(d)

Figure 4.8. The CTD and FCAL*-timing vertex reconstruction as a function of γ_0 for e^+p charged current Monte Carlo: (a) the CTD vertex finding efficiency, $\mathcal{E}_{CTD}$, (b) the difference between the Z-vertex position measured with the CTD and the true Z-vertex position, $Z^{CTD}_{\mathrm{vtx}} - Z^{\mathrm{true}}_{\mathrm{vtx}}$, (c) the difference between the Z-vertex position measured with the* FCAL*-timing information and the true Z-vertex position, $Z^{\mathrm{FCAL}}_{\mathrm{vtx}} - Z^{\mathrm{true}}_{\mathrm{vtx}}$, and (d) the RMS of $Z^{CTD}_{\mathrm{vtx}} - Z^{\mathrm{true}}_{\mathrm{vtx}}$, solid points, and of $Z^{\mathrm{FCAL}}_{\mathrm{vtx}} - Z^{\mathrm{true}}_{\mathrm{vtx}}$, open points.*

particles in the acceptance region of the CTD. An observable highly correlated with the number of particles in an angular region of the detector is the angle of the hadronic system, γ_{h}. Figure 4.8(a) shows the vertex finding efficiency for e^+p CC MC as a function of γ_0, the angle of the hadronic system measured with respect to the nominal interaction point. For $\gamma_0 > 0.4\,\text{rad}$ (high-γ_0) the vertex finding efficiency is about 100%, whereas for $\gamma_0 < 0.4\,\text{rad}$ (low-γ_0) the efficiency falls rapidly to zero. Figure 4.8(b) shows the difference between the vertex measured with the CTD and the true vertex from the MC as a function of γ_0. For events with $\gamma_0 < 0.4\,\text{rad}$ the Z-vertex position measured with the CTD is biased towards the forward direction and the spread becomes large. These events occupy the high-x region in the $(x,\, Q^2)$ phase space. Instead of using the CTD to measure the vertex of these events the FCAL-timing information was used.

The calorimeter measures the arrival time of the particles entering it. Hence the FCAL can be used to measure the Z-position of the vertex for events with a low number of particles in the CTD (events with low-γ_0).

The time of an ep interaction, t_{vtx}, can be determined from

$$t_{\text{vtx}} = \frac{1}{c}(Z_{\text{int}} - Z_{\text{vtx}}) + t_{\text{int}}, \tag{4.19}$$

where c is the speed of light and Z_{int} and t_{int} are the nominal Z-vertex position and the nominal interaction time. The Z_{int} and t_{int} are obtained by the information from the C5 detector (see Sect. 2.3.4). The nominal vertex position is the point where the electron bunch crosses the middle of the proton bunch. Note that the nominal vertex position does not have to be the same point as the nominal interaction point, which is defined as the centre of the ZEUS detector. The time measured by an FCAL cell of a particle entering the cell with the speed of light from the interaction vertex should be equal to

$$t_{\text{cell}} = t_{\text{vtx}} + cD_{\text{vtx}} - cD_{\text{nom}}, \tag{4.20}$$

where D_{vtx} is the distance between the cell position and the interaction vertex position, $(0, 0, Z_{\text{vtx}})$, and D_{nom} is the distance between the cell position and the nominal interaction point, $(0, 0, 0)$. The time measured by cells in the calorimeter is shifted by the time of flight from the nominal interaction point, the last term in (4.20). The Z-vertex position measured by a cell, $Z_{\text{vtx}}^{\text{cell}}$, can then be obtained by combining (4.11) and (4.20). The FCAL-timing Z-vertex position, $Z_{\text{vtx}}^{\text{FCAL}}$, of an event can now be determined from the weighted sum

$$Z_{\text{vtx}}^{\text{FCAL}} = \frac{\sum_i \frac{1}{\sigma_i^2} Z_{\text{vtx},i}^{\text{cell}}}{\sum_i \frac{1}{\sigma_i^2}}, \tag{4.21}$$

where i runs over all FCAL cells with an imbalance less than 0.5 and energies larger than 0.5 GeV for EMC cells and larger than 1.0 GeV for HAC cells; σ_i denotes the timing resolution (see (4.12)) of the i-th cell.

The FCAL-timing vertex was calibrated with a sample of neutral current DIS events [73]. The calibration was obtained on a run by run basis by comparing the FCAL-timing vertex with the CTD vertex, reconstructed using the high P_T scattered electron track. The resolution of the FCAL-timing vertex improves with increasing energy in the FCAL. For events with an energy deposit in the FCAL larger than 10 GeV the resolution of the FCAL-timing Z-vertex position is about 9 cm and improves to 7 cm for events with energy deposits larger than 100 GeV. The CAL timing in the MC simulation is not very well simulated. Hence, the vertex reconstruction method using the FCAL-timing described here is not applicable to the MC simulation. Therefore, using NC DIS data, the FCAL-timing vertex resolution was parameterised as function of the number of cells which were used in the vertex reconstruction. The FCAL-timing vertex in the MC was simulated by smearing the generated MC vertex with this function.

Figure 4.8(c) shows the difference between the vertex measured with the FCAL and the true vertex from the MC as function of γ_0. No bias in the Z-vertex position is observed for $\gamma_0 < 0.4$ rad, and the spread on the FCAL-timing vertex position becomes better than the spread on the CTD vertex position (see Fig. 4.8(d)) for small γ_0 values. Hence, for events with low-γ_0 the Z-vertex position is reconstructed using the FCAL-timing and for events with high-γ_0 the Z-vertex position is reconstructed using the reconstructed tracks in the CTD.

4.5. Summary

In this chapter the reconstruction of the event and the kinematic variables was discussed. An overview was given of the various kinematic reconstruction methods applicable for ep interactions with the ZEUS detector together with a discussion of the intrinsic resolution the Jacquet-Blondel method. This was followed by a discussion on the measurement of the kinematic variables of the hadronic system in the final state using the measured energy deposits in the CAL and it was shown how the noise from the CAL was suppressed. The cell clustering algorithm was discussed followed by a description of corrections on the measured energy for various effects. In the last part of this chapter it was discussed how the vertex position was determined from reconstructed tracks and the calorimeter timing information.

In the next chapter the selection of charged current deep inelastic scattering events used for the measurements of the cross sections will be discussed.

Chapter 5

Event Selection

In this chapter the selection of charged current deep inelastic scattering events will be discussed. The main characteristic of CC DIS events in the ZEUS detector is the absence of balancing transverse momentum in the calorimeter. The missing transverse momentum, $P_{T,\mathrm{miss}}$, is carried by the final state neutrino which leaves the ZEUS detector undetected and is defined as

$$P_{T,\mathrm{miss}}^2 = P_X^2 + P_Y^2 = \left(\sum_i E_i \sin\theta_i \cos\phi_i\right)^2 + \left(\sum_i E_i \sin\theta_i \sin\phi_i\right)^2 \quad (5.1)$$

where the sum runs over all calorimeter cells, E_i is the energy deposited in a calorimeter cell, θ_i is the polar angle at the Z position of the primary vertex of the event, and ϕ_i is the azimuthal angle with respect to the beam axis. Other types of processes (both ep, and non-ep interactions) can also have $P_{T,\mathrm{miss}}$, and have the signature of a genuine CC DIS event. Due to the much higher event rates for some of these processes, the removal of these background events is an important issue in the charged current event selection procedure.

The same selection cuts were applied on both the e^-p and the e^+p data samples. A few additional cuts were necessary in the analyses of the e^-p data sample in order to remove background of beam-gas events, which was much less severe in the e^+p data sample.

5.1. Trigger and Preselection

The majority of interactions which leave a signal in the ZEUS detector are not ep interactions. The total interaction rate is dominated by interactions of the proton beam with the residual gas in the beampipe, beam-gas interactions, with a rate in the order of $10-100\,\mathrm{kHz}$ whereas the rate for "interesting" ep physics events is only a few Hertz. Section 2.3.6 gives a general description of the trigger layout used by the ZEUS detector. In this section, the specific charged current trigger filters will be discussed which led to the data sample used in the unfolding of the charged current cross sections.

5.1.1. First Level Trigger

The first level trigger, FLT, accepts an event as a charged current event when it passes at least one out of six different filters, trigger slots. In total 64 slots are defined at the FLT were the most important CC trigger slot is `slot60`. Its logic can be expressed as an `OR` of the following criteria:

- $P_{T,\mathrm{miss}}^{\mathrm{FLT}} > 5\,\mathrm{GeV}$ `AND` $E_T^{\mathrm{FLT}} > 5\,\mathrm{GeV}$ `AND` $N_{\mathrm{good\_trk}}^{\mathrm{FLT}} \geq 1$;
- $P_{T,\mathrm{miss}}^{\mathrm{FLT}} > 8\,\mathrm{GeV}$ `AND` $N_{\mathrm{trk}}^{\mathrm{FLT}} \geq 1$;
- $P_{T,\mathrm{miss}}^{\mathrm{FLT}} > 8\,\mathrm{GeV}$ `AND` $E_{\mathrm{FCAL(\text{-}2ir)}}^{\mathrm{FLT}} \geq 10\,\mathrm{GeV}$;

where $P_{T,\mathrm{miss}}^{\mathrm{FLT}}$ and E_T^{FLT} are vector and scalar sums of the transverse energies deposited in the CAL cells, respectively, and $E_{\mathrm{FCAL(\text{-}2ir)}}^{\mathrm{FLT}}$ the total energy deposited in the FCAL. Both E_T^{FLT} and $E_{\mathrm{FCAL(\text{-}2ir)}}^{\mathrm{FLT}}$ are reconstructed without the energy deposited in the cells of the two inner rings of the FCAL. The $P_{T,\mathrm{miss}}$ in beam-gas interaction generally originates from energy deposits in the cells of the inner rings of the FCAL. Excluding these cells in the reconstruction of the detector observables allows for lower cut values, while maintaining a high selection efficiency for charged current events and keeping the trigger rates manageable by rejecting beam-gas events. $N_{\mathrm{trk}}^{\mathrm{FLT}}$ is the total number of tracks in the CTD and $N_{\mathrm{good\_trk}}^{\mathrm{FLT}}$ is the number of CTD tracks at the FLT that point towards the nominal interaction point.

In addition to `slot60`, five other trigger slots were used to increase the charged current event selection efficiency:

41) $E_T^{\mathrm{FLT}} > 20\,\mathrm{GeV}$;

42) $N_{\mathrm{good\_trk}}^{\mathrm{FLT}} \geq 1$ `AND` ($E_{\mathrm{CAL}}^{\mathrm{FLT}} > 15\,\mathrm{GeV}$ `OR` $E_{\mathrm{EMC}}^{\mathrm{FLT}} > 10\,\mathrm{GeV}$ `OR` $E_{\mathrm{BEMC}}^{\mathrm{FLT}} > 3.4\,\mathrm{GeV}$ `OR` $E_{\mathrm{REMC}}^{\mathrm{FLT}} > 2\,\mathrm{GeV}$);

43) $E_T^{\mathrm{FLT}} > 11.5\,\mathrm{GeV}$ `AND` $N_{\mathrm{good\_trk}}^{\mathrm{FLT}} \geq 1$;

44) $E_{\mathrm{BEMC}}^{\mathrm{FLT}} > 4.8\,\mathrm{GeV}$ `AND` ($E_{\mathrm{REMC}}^{\mathrm{FLT}} > 3.4\,\mathrm{GeV}$ `OR` $N_{\mathrm{trk}}^{\mathrm{FLT}} \geq 1$);

61) $P_{T,\mathrm{miss}}^{\mathrm{FLT}} > 3\,\mathrm{GeV}$ `AND` $E_{\mathrm{FCAL(\text{-}1ir)}}^{\mathrm{FLT}} > 1.3\,\mathrm{GeV}$ `AND` $N_{\mathrm{good\_trk}}^{\mathrm{FLT}} \geq 1$;

where $E^{\mathrm{FLT}}_{\mathrm{EMC}}$, $E^{\mathrm{FLT}}_{\mathrm{BEMC}}$ and $E^{\mathrm{FLT}}_{\mathrm{REMC}}$ are the total energy deposited in the EMC cells of the CAL, BCAL and RCAL respectively, and $E^{\mathrm{FLT}}_{\mathrm{CAL}}$ the total energy deposited in the CAL. These trigger slots were also used in the determination of the charged current event selection efficiency of `slot60` [74].

5.1.2. Second Level Trigger

At the second trigger level, SLT, calorimeter timing information is available. This information is used to apply additional cuts to reject cosmic muon events and beam-gas events. Charged current events were selected by the SLT through the `EXO_SLT4` branch, which is defined as an `AND` of the following criteria:

- $|t_{\mathrm{global}}| < 7\,\mathrm{ns}$ `OR` ($N^{\mathrm{SLT}}_{\mathrm{trk}} \geq 1$ `AND NOT CTDBeamGas`);
- `NoOffBeamProton`
- `CC1 OR CC2 OR CC3 OR CC4`;

where t_{global} is the average CAL time and `CTDBeamGas` is a CTD-SLT flag indicating that the event is a beam-gas event [75]. All events were required to have a t_{global} consistent with an ep collision timing.

The `NoOffBeamProton` requirement was defined to remove a background originating from off-beam protons, due to bad beam conditions, entering the CAL at a specific position, and is defined as:

- $|P^{\mathrm{SLT}}_{Y}| > 3\,\mathrm{GeV}$ `OR` $P^{\mathrm{SLT}}_{T,\mathrm{miss}} > 15\,\mathrm{GeV}$ `OR` $P^{\mathrm{SLT}}_{T,\mathrm{CAL(\text{-}1ir)}} > 6\,\mathrm{GeV}$ `OR` $P^{\mathrm{SLT}}_{T,\mathrm{miss}}/P^{\mathrm{SLT}}_{Z} > 0.06$;

The `CC1`, `CC2`, `CC3` and `CC4` requirements are defined as:

$$\texttt{CC1} = P^{\mathrm{SLT}}_{T,\mathrm{miss}} > 6\,\mathrm{GeV}\ \texttt{AND}\ E^{\mathrm{SLT}}_{T,\mathrm{CAL(\text{-}2ir)}} > 6\,\mathrm{GeV}\ \texttt{AND}\ N^{\mathrm{SLT}}_{\mathrm{good\_trk}} \geq 1;$$

$$\texttt{CC2} = P^{\mathrm{SLT}}_{T,\mathrm{miss}} > 9\,\mathrm{GeV}\ \texttt{AND}\ P^{\mathrm{SLT}}_{T,\mathrm{CAL(\text{-}1ir)}} > 8\,\mathrm{GeV}\ \texttt{AND}\ E^{\mathrm{SLT}}_{\mathrm{FCAL}} > 20\,\mathrm{GeV};$$

$$\texttt{CC3} = P^{\mathrm{SLT}}_{T,\mathrm{miss}} > 9\,\mathrm{GeV}\ \texttt{AND}\ \left(P^{\mathrm{SLT}}_{T,\mathrm{miss}}\right)^2/E^{\mathrm{SLT}}_{T} > 2.31\,\mathrm{GeV}\ \texttt{AND}\ E^{\mathrm{SLT}}_{\mathrm{FCAL}} > 80\,\mathrm{GeV};$$

$$\texttt{CC4} = E^{\mathrm{SLT}} - P^{\mathrm{SLT}}_{Z} > 6\,\mathrm{GeV}\ \texttt{AND}\ \left(P^{\mathrm{SLT}}_{T,\mathrm{miss}}\right)^2/E^{\mathrm{SLT}}_{T} > 2.25\,\mathrm{GeV}\ \texttt{AND}\ N^{\mathrm{SLT}}_{\mathrm{good\_trk}} \geq 1;$$

where $N^{\mathrm{SLT}}_{\mathrm{good\_trk}}$ is the number of tracks fitted to a vertex. The -1ir (-2ir) subscript denotes that the energy deposited in the cells in the 1st (2nd) inner ring of the FCAL is not included in the reconstruction of the observables. All CAL variables used in the SLT were calculated assuming the interaction vertex at the nominal position.

5.1.3. Third Level Trigger

After the SLT decision the data of all detector components are passed to the Event Builder, EB, where the full event is reconstructed. The third level trigger, TLT, used the information from all detector components for its decision. Charged current events were selected by the TLT through the branches `EXO_TLT2` or `EXO_TLT6` which aim to trigger events with high-γ_0 and low-γ_0 (see Sect. 5.2) respectively. Both branches further removed cosmic muon events by requiring:

- $|t_{\mathrm{up}} - t_{\mathrm{down}}| < 8\,\mathrm{ns}$;

where t_{up} and t_{down} are the event time obtained from the upper half and lower half of the CAL respectively. Generally cosmic muon events will have an earlier time in the upper half than in the lower half of the detector, since they traverse the detector from top to bottom. The additional criteria imposed by the `EXO_TLT2` branch were:

- $P^{\mathrm{TLT}}_{T,\mathrm{miss}} > 6\,\mathrm{GeV}$;
- $N^{\mathrm{TLT}}_{\mathrm{good\_trk}} \geq 1$;
- $-60\,\mathrm{cm} < Z^{\mathrm{TLT}}_{\mathrm{vtx}} < 60\,\mathrm{cm}$;

where $N^{\mathrm{TLT}}_{\mathrm{good_trk}}$is the number of vertex fitted tracks with $P^{\mathrm{vtx}}_{T,\mathrm{trk}} > 0.5\,\mathrm{GeV}$ and a distance of closest approach of the helix described by the original (not vertex fitted) track to the beam axis less than 1.5 cm. The additional criteria imposed by the `EXO_TLT6` branch were:

- passed the `EXO_SLT4` branch (see Sect. 5.1.2);
- $P^{\mathrm{TLT}}_{T,\mathrm{miss}} > 8\,\mathrm{GeV}$;
- $E^{\mathrm{TLT}}_{\mathrm{FCAL}} > 10\,\mathrm{GeV}$;
- `NOT OffBeamProton`;

where the `OffBeamProton` requirement is defined as:

- $P_{T,\mathrm{CAL(-1ir)}}^{\mathrm{TLT}} < 10\,\mathrm{GeV}$ AND $P_{T,\mathrm{miss}}^{\mathrm{TLT}} > 25\,\mathrm{GeV}$ AND $P_{T,\mathrm{miss}}^{\mathrm{TLT}}/E_T^{\mathrm{TLT}} < 0.7$ AND $E^{\mathrm{TLT}} - P_Z^{\mathrm{TLT}} < 10\,\mathrm{GeV}$ AND $P_{T,\mathrm{miss}}^{\mathrm{TLT}}/P_Z^{\mathrm{TLT}} < 0.08$ AND $|P_Y^{\mathrm{TLT}}| < 4\,\mathrm{GeV}$;

Events that passed all three trigger levels were written to Data Summary Tape, DST. Based on the trigger decisions the online data system categorises events and assigns a DST bit to each category. These bits are accessible when selecting ZEUS data from DST for an off-line analysis. DST bit 34 is reserved for events which passed the trigger criteria outlined above for CC events.

5.1.4. Preselection

For the analysis described in this thesis the ZES facility has been used for the preselection of CC DIS events from DST. The ZES facility is an object-oriented database using Objectivity [76] as the database management system. For each event a number of variables are stored as a tag, to provide a fast and flexible way of selecting events. Its efficient event selection method reduced considerably the number of candidate events passed to the off-line analysis. The following ZES selection criteria were used:

- $P_{T,\mathrm{miss}} > 7\,\mathrm{GeV}$;
- $P'_{T,\mathrm{miss}} > 7\,\mathrm{GeV}$, where $P'_{T,\mathrm{miss}}$ is the missing transverse momentum reconstructed without the information from the FCAL cells closest to the beamhole;
- $P_{T,\mathrm{miss,o}}/\delta_0 > 4.37$ OR $N_{\mathrm{trk}} > 0$, where $P_{T,\mathrm{miss,o}}$ (δ_0) is $P_{T,\mathrm{miss}}$ (δ) calculated assuming the position of the event vertex at the nominal interaction point, $\delta = \sum(E_i - E_i\cos\theta_i) = \sum(E - P_Z)_i$, where the sum runs over all calorimeter cells;
- $E_{\mathrm{BCAL}} < 6\,\mathrm{GeV}$ OR $E_{\mathrm{BHAC}}/E_{\mathrm{BCAL}} < 0.95$;

Figures 5.1(a)–(d) show the distributions of the four most important quantities used in the preselection of charged current events. Each figure shows the e^+p data and Monte Carlo distributions after all the preselection cuts have been applied except for the cut indicated by the vertical line. The Monte Carlo events in the plots were scaled to the luminosity of the data shown, which is a

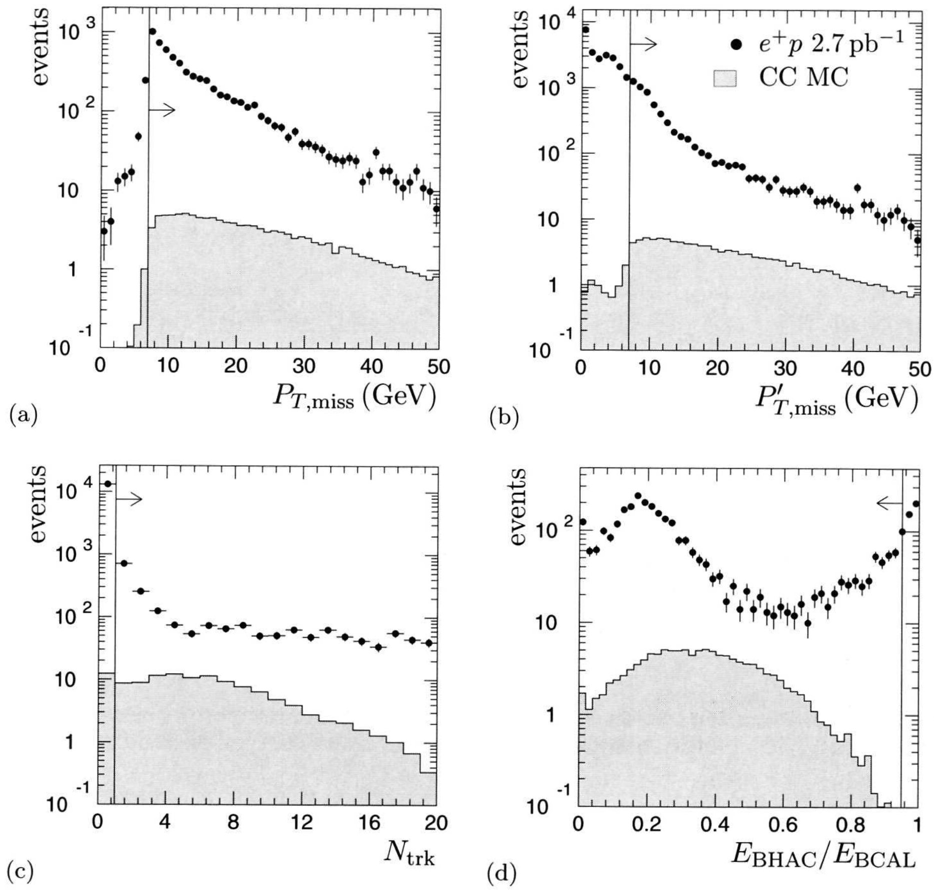

Figure 5.1. The four most important quantities used in the event preselection (see text): (a) the missing transverse momentum, $P_{T,\mathrm{miss}}$; (b) the missing transverse momentum excluding the FCAL inner ring, $P'_{T,\mathrm{miss}}$; (c) the number of tracks per event, N_{trk}; (d) the BHAC energy over the BCAL energy, $E_{\mathrm{BHAC}}/E_{\mathrm{BCAL}}$. The selection cuts applied are shown by the vertical lines in the figures.

fraction (2.66 pb^{-1}) of the full e^+p data sample used in the analysis (60.9 pb^{-1}, See Sect. 2.4). The CC MC distribution shown in Fig. 5.1 is described in Sect. 3.2. It is clear from the figures that there is still a lot of background in the data sample since the preselection cuts were looser than the final charged

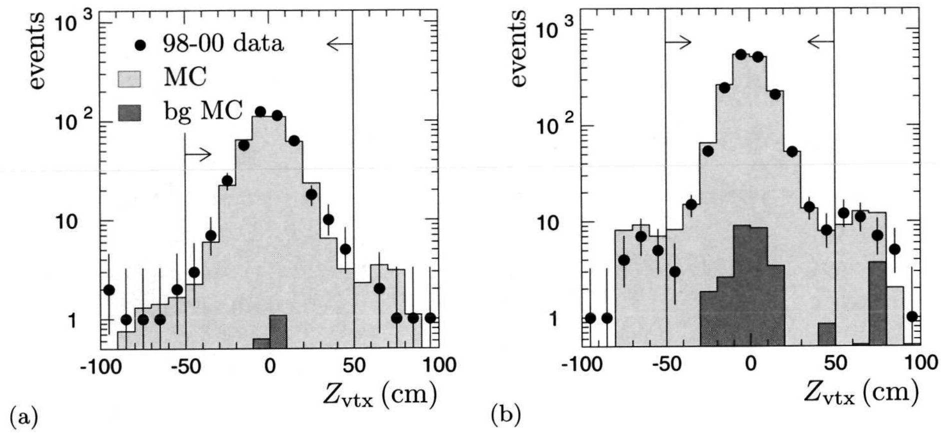

Figure 5.2. The Z position of the vertex reconstructed with: (a) the FCAL timing in the low-γ_0 region; (b) the tracking in the high-γ_0 region. The figures show the event distribution after the final CC selection without the vertex cut, which is indicated by the vertical lines. Both figures show the combined e^-p and e^+p data samples.

current selection cuts, though the amount of data to be analysed is reduced considerably. The same preselection was applied to the e^-p event sample. In the next sections the selection criteria which led to the final CC DIS event sample will be discussed.

5.2. Event Vertex

Depending on the hadronic angle γ_0, the angle of the hadronic system calculated with the vertex at the nominal position, different methods were used to reconstruct the primary vertex of the event. For events with $\gamma_0 > 0.4\,\mathrm{rad}$ (high-γ_0) the CTD was used; for events with $\gamma_0 < 0.4\,\mathrm{rad}$ (low-γ_0) the vertex reconstruction by the CTD became unreliable and in stead the timing information of the FCAL was used to reconstruct the position of the primary vertex. The hadronic angle of the event, γ_h, is reconstructed by

$$\cos\gamma_h = \frac{P_{T,\mathrm{miss}}^2 - \delta^2}{P_{T,\mathrm{miss}}^2 + \delta^2}, \tag{5.2}$$

where $\delta = \sum(E_i - E_i\cos\theta_i) = \sum(E - P_Z)_i$.

Figures 5.2(a) and 5.2(b)[1] show the Z-position of the vertex for low-γ_0 and high-γ_0 events separately. In this plot all charged current selection cuts are applied. The vertical lines indicate the event vertex threshold:

- $-50\,\mathrm{cm} < Z_{\mathrm{vtx}} < 50\,\mathrm{cm}$.

Events with a vertex outside this range originate from interactions of the lepton beam with protons in the satellite bunches. The satellite bunches are formed by protons travelling in the neighbouring bucket of the accelerator radio frequency, RF. These events are genuine ep collisions but are nevertheless removed from the sample. The main reason to remove these events is that the acceptance of the CTD and the calorimeter is best understood for events occurring in the central region of the detector. Furthermore, the vertex determination is more precise in the central region. A minor aspect is that beam-gas events are randomly distributed in Z with the consequence that the fraction of beam-gas events is larger outside the main vertex peak.

5.3. Transverse Momentum and Kinematic Region

In charged current events the incoming lepton exchanges a W boson with one of the (anti)quarks in the proton and changes into a neutrino or antineutrino. The final state (anti)neutrino escaping the detector undetected causes missing transverse momentum, $P_{T,\mathrm{miss}}$. Figures 5.3(a)–(d) show the distributions of the missing transverse momentum for events with low-γ_0 and high-γ_0 separately. To select charged current events the following cuts on $P_{T,\mathrm{miss}}$ have been applied:

- $P_{T,\mathrm{miss}} > 12\,\mathrm{GeV}$, for high-$\gamma_0$ events;
- $P_{T,\mathrm{miss}} > 14\,\mathrm{GeV}$, for low-$\gamma_0$ e^+p events;
- $P_{T,\mathrm{miss}} > 25\,\mathrm{GeV}$, for low-$\gamma_0$ e^-p events.

Since for events with high-γ_0 tracking is possible the cut on missing transverse momentum could be relaxed with respect to events with low-γ_0. The cut value for low-γ_0 e^-p events is larger than for low-γ_0 e^+p events because the background from beam-gas was larger in the e^-p data sample. This background has been removed from the high-γ_0 e^-p data sample with additional cuts which are described in Sect. 5.4.1.

[1]The Monte Carlo distributions shown in the figures are described in Sect. 3.2. This is the case for all figures presented in this chapter, unless stated differently.

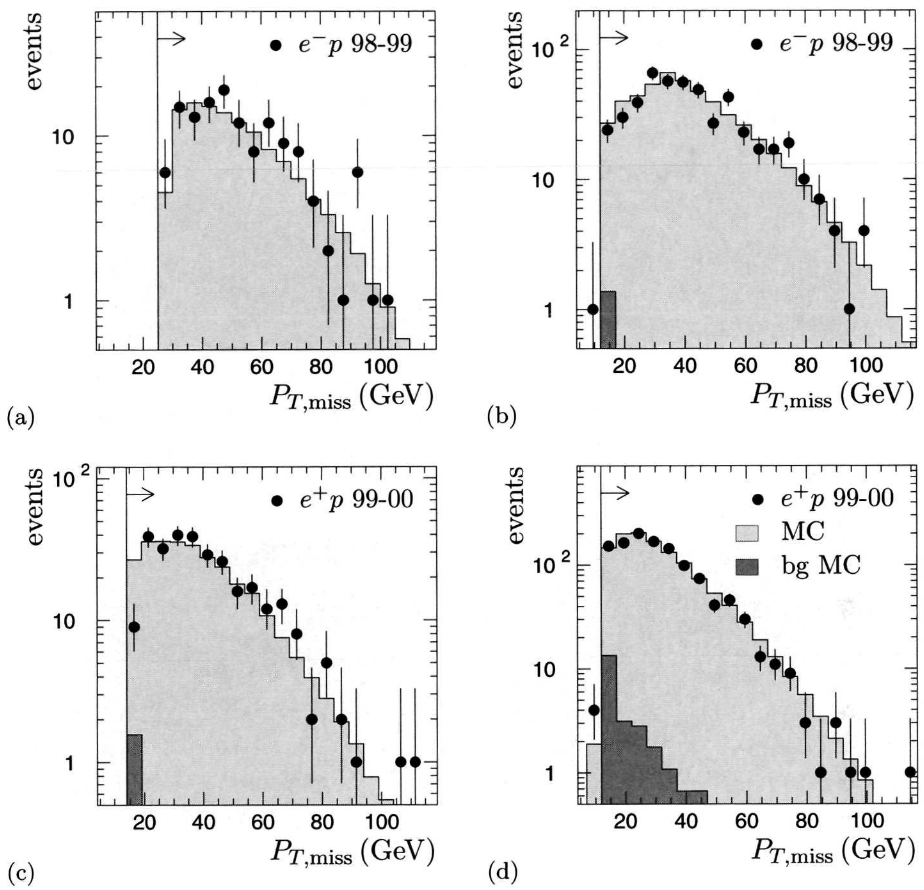

Figure 5.3. The missing transverse momentum distributions for: (a), (c) events with low-γ_0 and; (b), (d)events with high-γ_0. The figures show the event distribution after the final CC selection without the cuts on $P_{T,\mathrm{miss}}$, which are indicated by the vertical lines in the figures.

The transverse momentum of an event is related to Q^2_{JB} by $Q^2_{\mathrm{JB}} = P_T^2/(1 - y_{\mathrm{JB}})$; in Fig. 5.20 and Fig. 5.21 this is shown by the lines in the distribution of x versus Q^2 of the e^-p and e^+p events respectively. Due to this correlation, the applied cuts in $P_{T,\mathrm{miss}}$, results in the following kinematic requirements:

- $Q^2_{\mathrm{JB}} > 200\,\mathrm{GeV}$;
- $y_{\mathrm{JB}} < 0.9$.

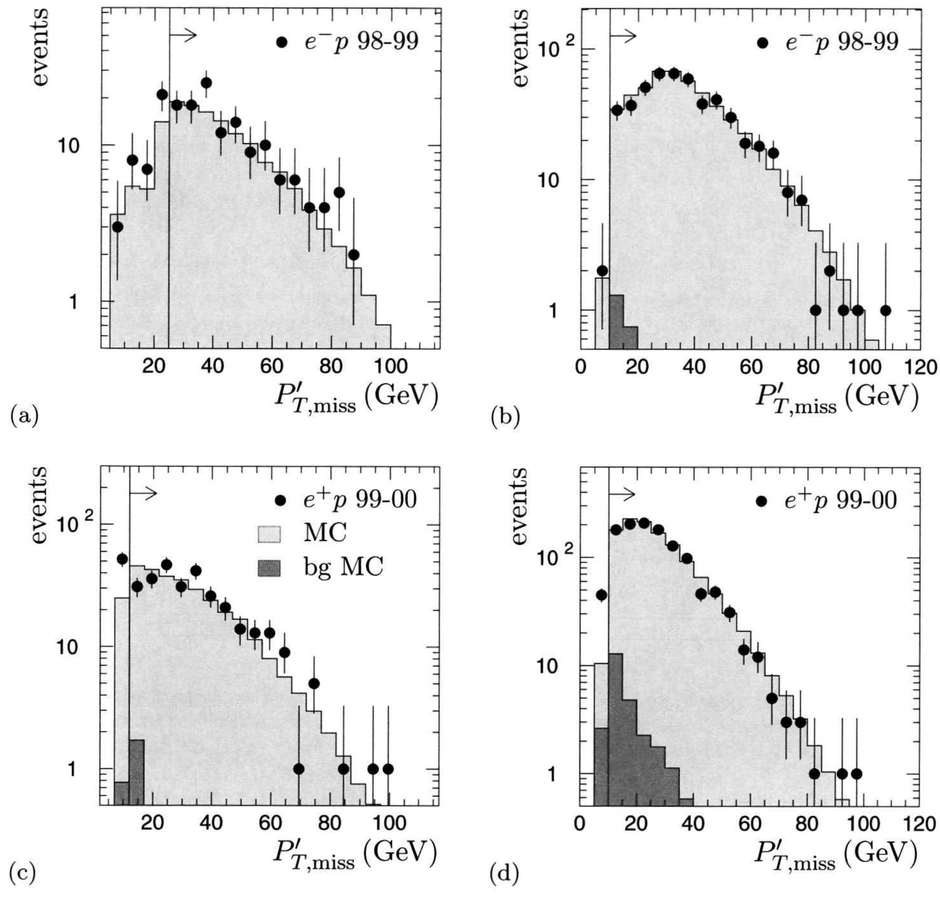

Figure 5.4. The missing transverse momentum reconstructed without the FCAL cells closest to the beamhole, $P'_{T,\mathrm{miss}}$, for: (a), (c) events with low-γ_0 and; (b), (d) events with high-γ_0. The figures show the event distribution after the final CC selection without the cuts on $P'_{T,\mathrm{miss}}$, which are indicated by the vertical lines in the figures.

The cut on y_{JB} has been applied because of the poor resolution in x_{JB} and Q^2_{JB} for high y_{JB} (see Sect. 4.2).

5.4. Beam-gas/pipe Background

Beam-gas events occur when protons in the proton bunch interact with residual gas molecules in the beampipe, whereas beampipe events occur when off-bunch protons interact with the wall of the beampipe. Beampipe events cause $P_{T,\text{miss}}$ in the detector, while beam-gas events generally do not cause $P_{T,\text{miss}}$ in the detector. However, since energy escapes through the beamhole, this could result in a $P_{T,\text{miss}}$ and due to the high occurrences of beam-gas/pipe events they form a severe background in the charged current event sample. Since beam-gas/pipe interactions have a similar signature in the ZEUS detector, the cuts described in this section removed both event types. Typically, beam-gas/pipe interactions show a lot of activity in the forward region of the detector. The $P_{T,\text{miss}}$ of these events originates mainly from energy deposits in the FCAL cells closest to the beamhole. Therefore, for each event the missing transverse momentum has been reconstructed without the information from the cells in the inner ring of the FCAL, cells which are closest to the beamhole, $P'_{T,\text{miss}}$, and the following cuts have been applied to remove the beam-gas/pipe events from the sample:

- $P'_{T,\text{miss}} > 10\,\text{GeV}$, for high-$\gamma_0$ events;
- $P'_{T,\text{miss}} > 12\,\text{GeV}$, for low-$\gamma_0$ e^+p events;
- $P'_{T,\text{miss}} > 25\,\text{GeV}$, for low-$\gamma_0$ e^-p events.

Figures 5.4(a)–(d) show the $P'_{T,\text{miss}}$ distributions for events with high-γ_0 and low-γ_0 separately. The cut values are indicated by the vertical lines.

Beam-gas/pipe events are hadron-hadron collisions with many particles in the final state. For high-γ_0 events a lot of activity in the CTD is expected. Figures 5.5(a) and 5.5(b) show the distribution of N_{trk} versus $N_{\text{trk}}^{\text{good}}$ of measured and simulated e^+p events respectively. N_{trk} is the number of tracks in an event, and $N_{\text{trk}}^{\text{good}}$ is the number of vertex fitted tracks with additional quality criteria:

- $15° < \theta_{\text{trk}}^{\text{vtx}} < 165°$, where $\theta_{\text{trk}}^{\text{vtx}}$ is the polar angle with respect to the beam axis of the vertex fitted track. In this angular range the track passes at least 5 super-layers of the CTD;
- $P_{T,\text{trk}}^{\text{vtx}} > 0.2\,\text{GeV}$, where $P_{T,\text{trk}}^{\text{vtx}}$ is the transverse momentum of the track;
- $\text{DCA}_{\text{trk}}^{\text{vtx}} < 1.5\,\text{cm}$, where $\text{DCA}_{\text{trk}}^{\text{vtx}}$ is the distance of closest approach of the helix described by the original (not vertex fitted) track to the beam line.

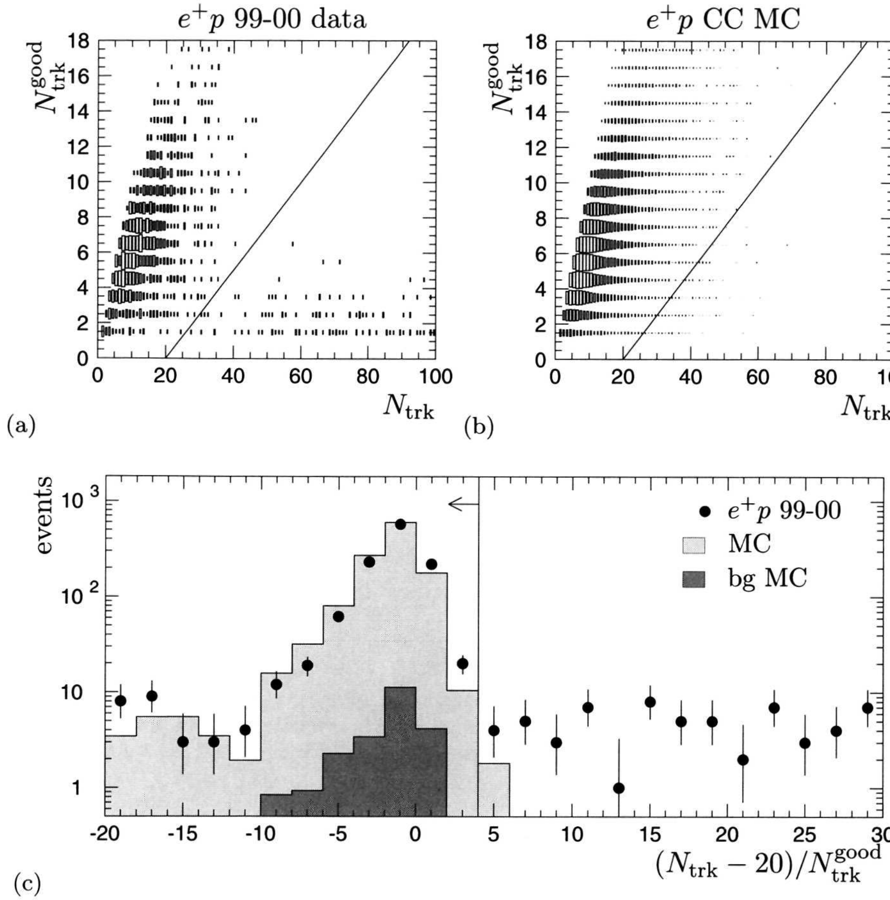

Figure 5.5. Different representations of the tracking cut applied in the analysis: (a) the tracking cut for data and; (b) Monte Carlo; (c) $(N_{trk} - 20)/N_{trk}^{good} < 4$, see text. The figures show the event distribution after the final CC selection without the tracking cut. This cut is only applied for events with high-γ_0.

The beam-gas/pipe events have many tracks but a relatively low number of good tracks, $N_{\rm trk}^{\rm good}$. Using this property, these events were removed from the charged current event sample by the following selection threshold (see Fig. 5.5(c)):

- $(N_{\rm trk} - 20)/N_{\rm trk}^{\rm good} < 4$;

These cuts were sufficient to remove the beam-gas background from the e^+p event sample. Additional cuts were necessary to remove the beam-gas back-

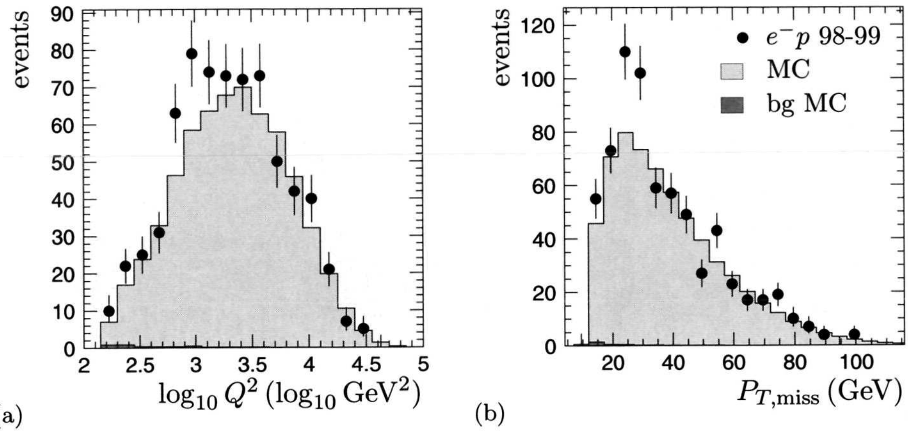

Figure 5.6. Distribution of: (a) Q^2 and; (b) $P_{T,\mathrm{miss}}$ in the e^-p data with the e^+p charged current event selection applied. An excess of data events over MC events is observed.

ground from the e^-p event sample. They will be described in the next section.

5.4.1. Beam-gas Background in the 1998–1999 Data

After four years of running with positrons, and having the beam orbit completely optimised for that, HERA switched in 1998 to electron running. Although the beam conditions allowed ZEUS to take data, the beam-gas background was worse compared to the positron running. Figure 5.6 shows the Q^2 and $P_{T,\mathrm{miss}}$ distributions in the e^-p data with the e^+p charged current event selection applied. As can clearly be observed, there is an excess of data events over Monte Carlo events in the Q^2 range $600-2000\,\mathrm{GeV}$ and in the transverse momentum range of $22-32\,\mathrm{GeV}$.

Due to the higher beam-gas interaction rate in the $98-99$ e^-p data, beam-gas events overlap with "genuine" ep interactions. To study these events, the event sample was "enriched" with beam-gas events by the following looser cuts:

- $P_{T,\mathrm{miss}} > 8\,\mathrm{GeV}$;
- $P'_{T,\mathrm{miss}} > 8\,\mathrm{GeV}$;
- $Q^2 > 50\,\mathrm{GeV}$;

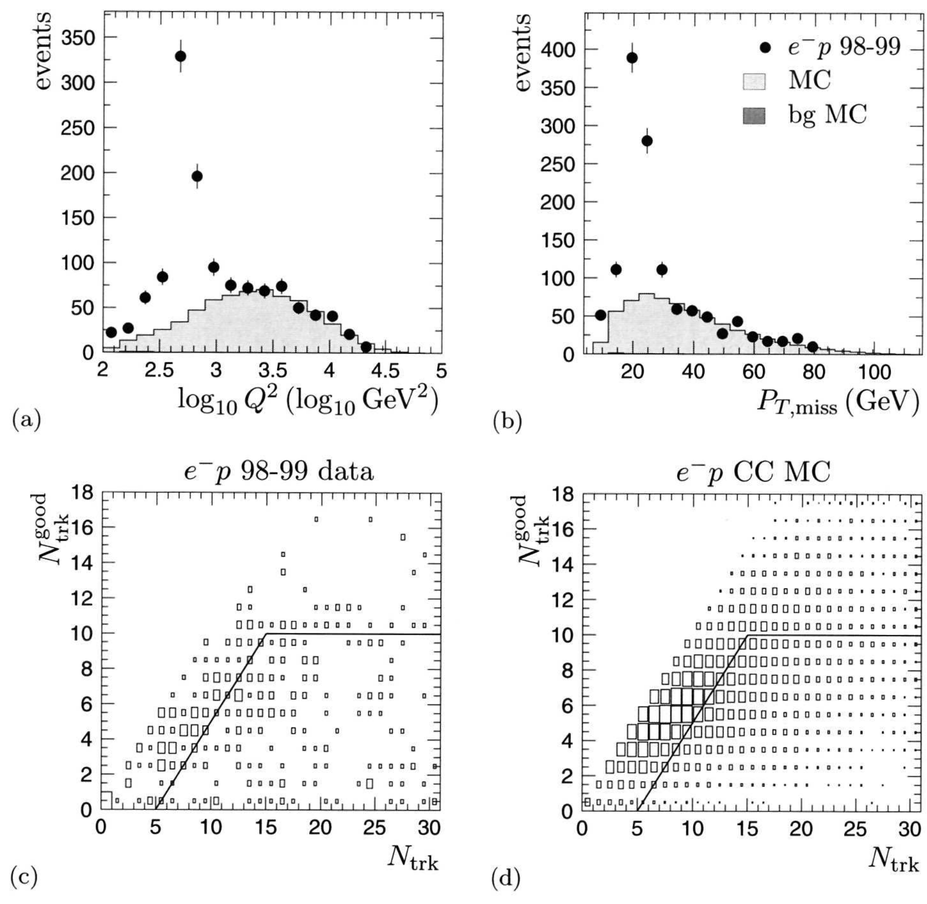

Figure 5.7. Distribution of: (a) Q^2; (b) $P_{T,\text{miss}}$ and N_{trk} versus N_{trk}^{good} of; (c) data events and (d) Monte Carlo events in the e^-p data with an enhanced beam-gas background. The solid lines in the two dimensional histograms shows the additional selection threshold for removing the beam-gas background in the e^-p data.

- No tracking cuts as described in Sections 5.4 and 5.5.

A large enhancement of the excess of data events over MC events is observed in the Q^2 and $P_{T,\text{miss}}$ distribution shown in Figs. 5.7(a) and 5.7(b). Figures 5.7(c) and 5.7(d) show the distribution of N_{trk} versus $N_{\text{trk}}^{\text{good}}$ of measured and simulated e^-p events for the beam-gas "enriched" event sample in data and Monte Carlo.

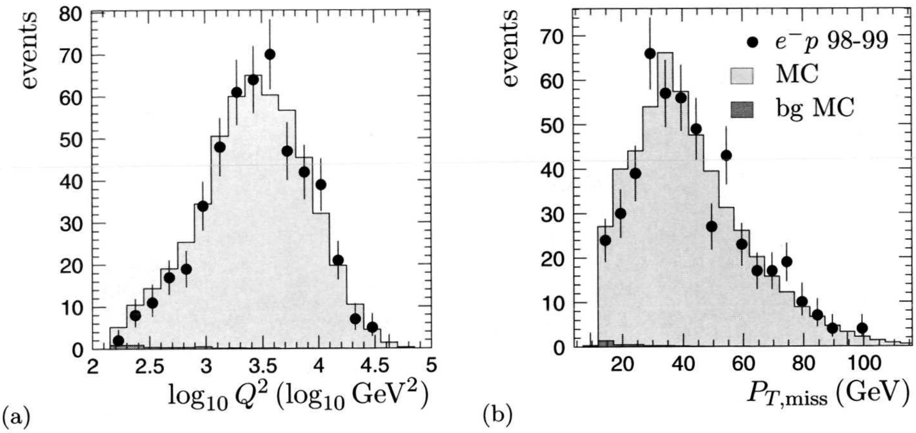

Figure 5.8. Distribution of: (a) Q^2 and; (b) $P_{T,\text{miss}}$ in the e^-p data after all charged current event selection criteria were applied.

The data distribution shows an excess of events with a large number of tracks and a relatively low number of good tracks over the Monte Carlo simulation. To remove these events the following cut, indicated by the solid lines in the figure, was applied:

- $N_{\text{trk}}^{\text{good}} > N_{\text{trk}} - 5$ OR $N_{\text{trk}}^{\text{good}} > 10$.

This cut removed the beam-gas background events in the e^-p event sample for events with high-γ_0. Figure 5.8 shows the Q^2 and $P_{T,\text{miss}}$ distributions after all selection cuts have been applied. Since no tracking information is available for events with low-γ_0, the beam-gas events with low-γ_0 were removed by raising the $P_{T,\text{miss}}$ and $P'_{T,\text{miss}}$ selection threshold values as described in Sects. 5.3 and 5.4.

5.5. Additional Selection Thresholds Based on Tracking

In events with high-γ_0 the current jet is within the angular acceptance of the CTD. Hence tracks should be apparent in the event, and additional tracking requirements in the selection of charged current events were set:

- $N_{\text{trk}} > 0$;
- $N_{\text{trk}}^{\text{good}} > 0$;

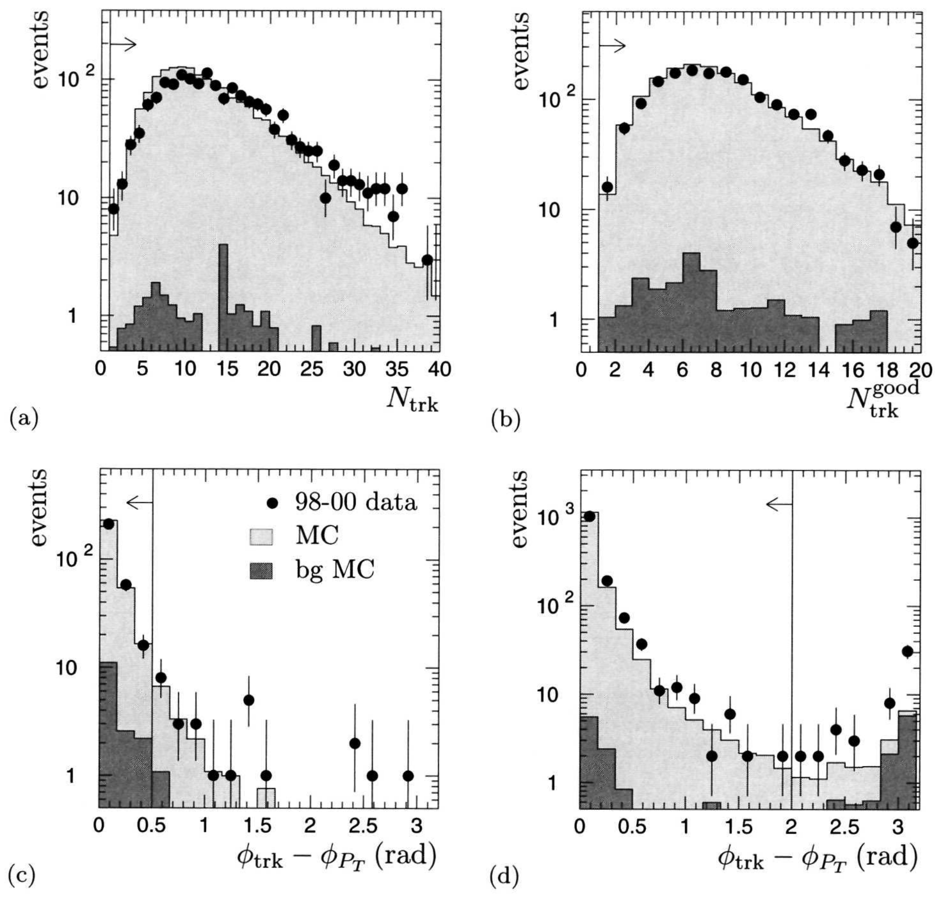

Figure 5.9. Distribution of: (a) the number of all tracks reconstructed using only the CTD, N_{trk}; (b) the number of good tracks, N_{trk}^{good}; (c) $|\phi| = \phi_{trk} - \phi_{P_T}$ (see text) for $P_{T,\mathrm{miss}} < 20$ GeV and; (d) $|\phi|$ for $P_{T,\mathrm{miss}} > 20$ GeV. The figures show the event distribution after the final CC selection without the cut shown by the vertical lines. All figures show the combined e^-p and e^+p data samples.

where $N_{\rm trk}$ is the total number of tracks in the event and $N_{\rm trk}^{\rm good}$ is described in Sect. 5.4. Figures 5.9(a) and 5.9(b) show the distributions of $N_{\rm trk}$ and $N_{\rm trk}^{\rm good}$, respectively. In charged current events, the difference in azimuthal angle from the P_T calculated with the calorimeter and the P_T calculated from tracks, $|\phi| = \phi_{\rm trk} - \phi_{P_T}$, should be very small, since they are highly correlated. This is not

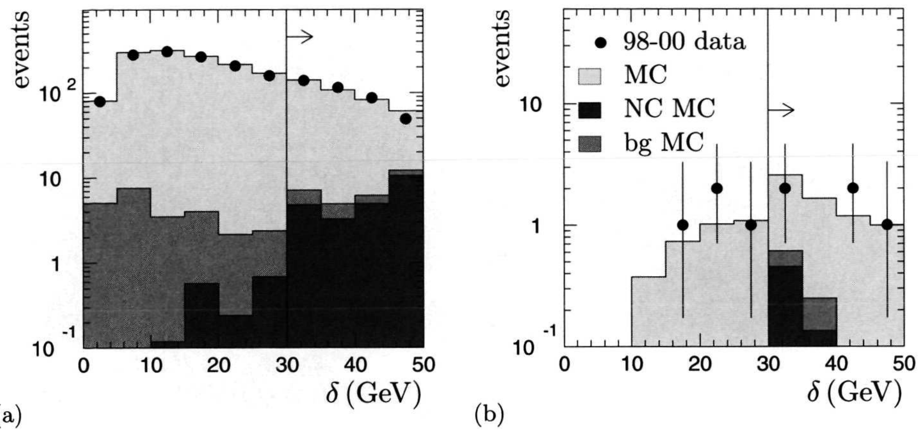

Figure 5.10. Distribution of $\delta = \sum(E - P_Z)_i$ for; (a) all events passing the CC event selection with an enhanced NC background by omitting all NC rejection cuts and; (b) the δ distribution with the final CC selection without the NC rejection cuts shown in the figures by the vertical line. Both figures show the combined e^-p and e^+p data samples.

the case for events other than charged current interactions with $P_{T,\mathrm{miss}}$, where the missing transverse momentum is due to particles leaving tracks in the CTD, but incompletely measured by the CAL (e.g. due to the super crack region). Figure 5.9(c) shows the distribution of $|\phi|$ for $P_{T,\mathrm{miss}} < 20\,\mathrm{GeV}$ and Fig. 5.9(d) shows it for $P_{T,\mathrm{miss}} > 20\,\mathrm{GeV}$. The following cuts have been applied:

- $|\phi| < 0.5\,\mathrm{rad}$, for $P_{T,\mathrm{miss}} < 20\,\mathrm{GeV}$;
- $|\phi| < 2.0\,\mathrm{rad}$, for $P_{T,\mathrm{miss}} > 20\,\mathrm{GeV}$.

5.6. Neutral Current Background

Over a large range in Q^2 the neutral current, NC, *ep* cross section is orders of magnitude larger than the charged current cross section. Usually NC events do not pass the cuts on missing transverse momentum, since the final state scattered electron[2] balances the event in P_T, and $\delta = \sum(E - P_Z)_i = 55\,\mathrm{GeV}$. However, due to energy loss in the final state, e.g. fluctuations in the energy

[2]Note that in this section the scattered electron can be replaced by the scattered positron.

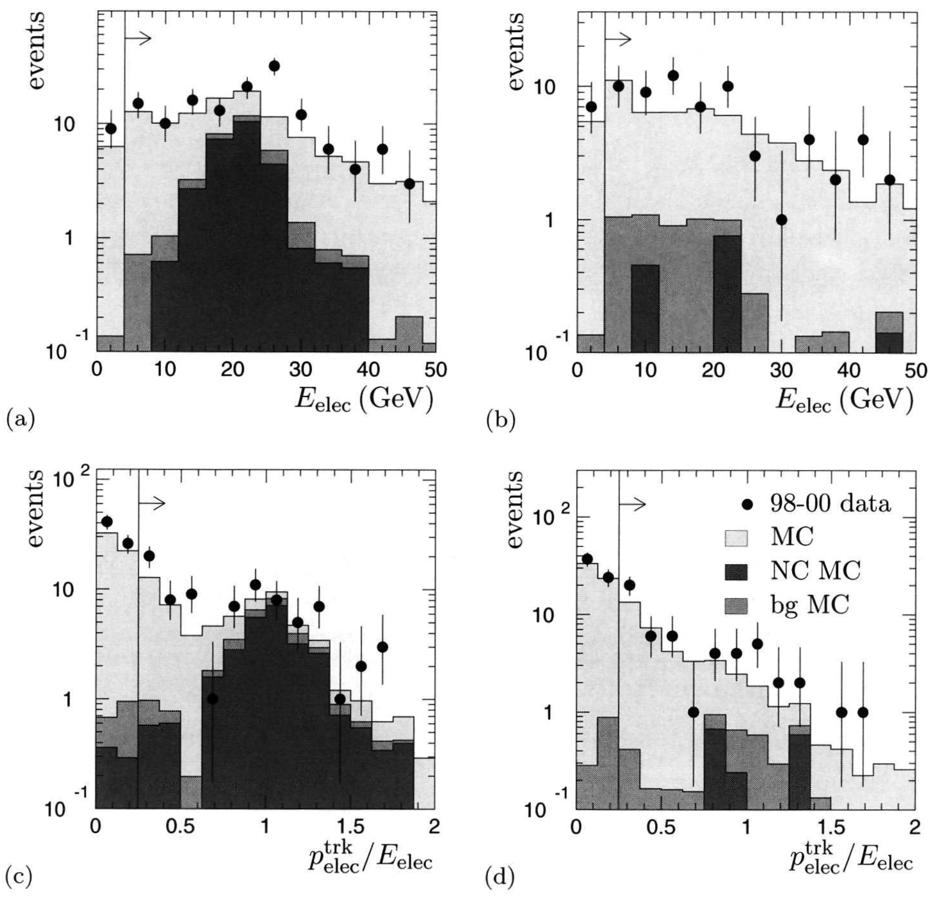

Figure 5.11. Distributions of two quantities used in the selection and rejection of neutral current events from the charged current event sample: (a) and (b) the energy of the electron, E_{elec}; (c) and (d) the ratio of the momentum of the track associated with the electron and the energy of the electron from the calorimeter, p^{trk}_{elec}/E_{elec}. Figures (a) and (c) show the distributions with an enhanced NC background by omitting all NC rejection cuts. Figures (b) and (d) show the distributions with the final CC selection without the NC rejection cuts shown in the figures by the vertical line. All figures show the combined e^-p and e^+p data samples.

measurement, or mismeasurement of the energy of the scattered electron, NC events can have $P_{T,\mathrm{miss}}$. Notice that the rejection of NC events from the CC sample is based on the selection of NC events in the event sample. The main characteristic of a NC DIS event is the presence of a scattered electron. A scattered electron hitting the calorimeter deposits most of its energy in the electromagnetic part of the calorimeter and very little energy in the hadronic part. In addition, electrons have different shower profiles in the calorimeter than other particles. These features were used by a neural network, SINISTRA95 [77], to identify isolated electromagnetic clusters in the calorimeter as candidate scattered electrons in *ep* interactions. Events with a candidate scattered electron were tagged as candidate NC events when they satisfied the following conditions:

- $\mathcal{P}_{\mathrm{elec}} > 0.9$, where $\mathcal{P}_{\mathrm{elec}}$ is the probability of the most likely electron candidate calculated by the neural network;
- $E_{\mathrm{elec}} > 4\,\mathrm{GeV}$, where E_{elec} is the electron energy;
- $E^{\mathrm{cone}} - E_{\mathrm{elec}} < 5\,\mathrm{GeV}$, a criterion for the isolation of the electron; E^{cone} is the energy contained in a cone with $R = \sqrt{(\Delta\phi)^2 + (\Delta\eta)^2} = 0.8$ around the electron, excluding the energy of the electron itself;
- $\theta_{\mathrm{elec}} > 15^\circ$, to ensure that the electron is within the acceptance of the calorimeter.

Candidate neutral current events with the scattered electron in the rear direction outside the angular acceptance of the CTD, going towards the RCAL, were rejected from the event sample if they satisfied the following conditions:

- $E_{T,\mathrm{elec}} < 2\,\mathrm{GeV}$, where $E_{T,\mathrm{elec}}$ is the transverse energy of the electron;
- $P_{T,\mathrm{miss}} < 30\,\mathrm{GeV}$ `AND` $\delta > 30\,\mathrm{GeV}$.

For candidate NC events with the polar angle of the scattered electron within the angular acceptance of the CTD, a track was matched to the electromagnetic cluster of the electron by requiring:

- $\mathrm{DCA}^{\mathrm{trk}}_{\mathrm{elec}} < 15\,\mathrm{cm}$, where $\mathrm{DCA}^{\mathrm{trk}}_{\mathrm{elec}}$ is the distance of closest approach between the track extrapolated to the CAL surface and the electron cluster centre;
- $15^\circ < \theta^{\mathrm{trk}}_{\mathrm{elec}} < 165^\circ$, track passed at least 5 super layers of the CTD;

- $p_{\mathrm{elec}}^{\mathrm{trk}}/E_{\mathrm{elec}} > 0.25$

Candidate NC events with the polar angle of the scattered electron within the angular acceptance of the CTD were rejected from the event sample if they satisfied the following conditions:

- a scattered electron with matching track was found;
- $P_{T,\mathrm{miss}} < 30\,\mathrm{GeV}$ AND $\delta > 30\,\mathrm{GeV}$.

Figures 5.10 and 5.11 show a number of quantities which were used in the selection and later rejection of NC events. It was not necessary to look for NC events with a scattered electron in the FCAL since the Q^2 of these events is very high and therefore the NC cross section, with a Q^2 dependence $\propto 1/Q^4$, is very low. All NC rejection cuts discussed in this section were applied to high-γ_0 events. For low-γ_0 events, it is easily shown that $\delta < 0.2P_T$ using Equation (5.2). Hence, for $P_{T,\mathrm{miss}} < 30\,\mathrm{GeV}$, δ must be less than $6\,\mathrm{GeV}$. No NC events enter this region, and hence no cuts were required.

5.7. Photoproduction Background

In the case that a proton interacts with an almost real photon ($Q^2 \approx 0\,\mathrm{GeV}^2$), one speaks of photoproduction (γp) interactions. The photon with which the proton interacts originates from an incoming electron, which escapes the detector undetected through the beampipe. In resolved photoproduction one of the quarks in the photon interacts with one of the quarks in the proton, whereas in direct photoproduction the photon interacts directly with one of the quarks in the proton. Both types of photoproduction were treated in the same way, since they have an identical signature in the detector. In photoproduction events the P_T of the event is balanced. So the $P_{T,\mathrm{miss}}$ requirements described in Sect. 5.3 removed most photoproduction events from the CC sample. However, due to energy loss in the final state (e.g. fluctuations in the energy measurement for events with high E_T or events with a jet going into the crack region), photoproduction events can have $P_{T,\mathrm{miss}}$. The rejection of photoproduction events from the event sample was based on the energy distribution in the calorimeter. In photoproduction events the energy is usually less localised in the calorimeter, and the ratio $P_{T,\mathrm{miss}}/E_T$ will be smaller than in the case of charged current events where the energy is more collimated in the direction of P_T. The background from photoproduction events decreases rapidly with increasing Q^2, and

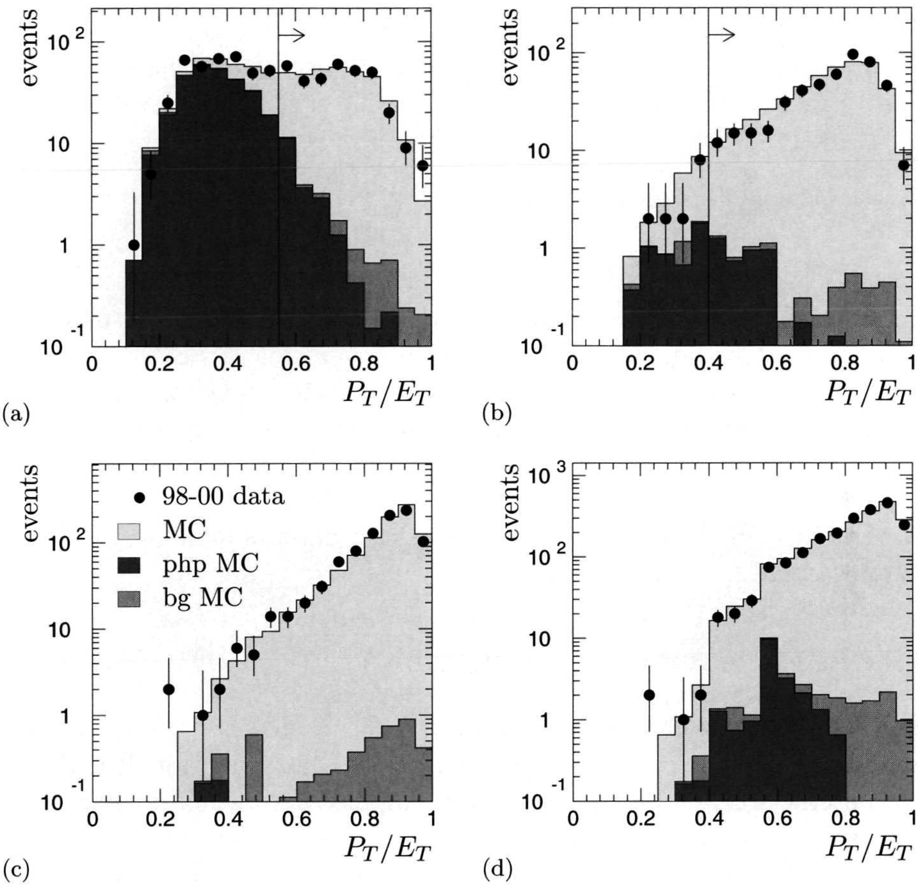

Figure 5.12. Distributions of P_T/E_T for events with: (a) $P_{T,\mathrm{miss}} < 20\,GeV$; (b) $20 < P_{T,\mathrm{miss}} < 30\,GeV$; (c) $P_{T,\mathrm{miss}} > 30\,GeV$; (d) the charged current sample after all selection cuts are applied. Figures 5.12(a)–(c) show the P_T/E_T distributions for events with high-γ_0, without any photoproduction rejection cuts applied. The vertical lines show the photoproduction rejection cuts. All figures show the combined e^-p and e^+p data samples.

therefore with increasing $P_{T,\mathrm{miss}}$. Two different $P_{T,\mathrm{miss}}/E_T$ selection cuts were applied:

- $P_{T,\mathrm{miss}}/E_T > 0.55$, for $P_{T,\mathrm{miss}} < 20\,\mathrm{GeV}$;
- $P_{T,\mathrm{miss}}/E_T > 0.4$, for $20 < P_{T,\mathrm{miss}} < 30\,\mathrm{GeV}$.

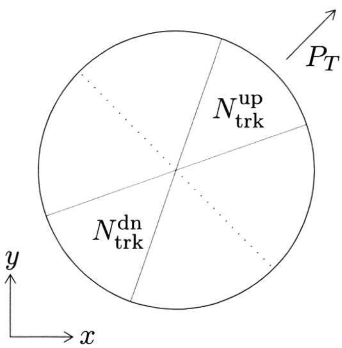

Figure 5.13. Schematic view of the regions in (x, y) of N^{up}_{trk}, N^{dn}_{trk} (see text) and the corresponding direction of P_T.

For $P_{T,\rm miss} > 30\,\rm GeV$ no $P_{T,\rm miss}/E_T$ cut was applied since no photoproduction events enter this region. The selection cuts were applied only for events with high-γ_0. Figures 5.12(a)–5.12(d) show the $P_{T,\rm miss}/E_T$ distributions for the different $P_{T,\rm miss}$ regions.

In dijet photoproduction events missing transverse momentum can be caused by one of the particle jets going into a crack region in the calorimeter. In that case the direction of the P_T is opposite the direction of the poorly measured jet. Tracks in these events point in the direction of the P_T, but also in the direction of the poorly measured jet. In CC events tracks point only in the direction of the P_T. This feature has been used to apply the following selection criteria for events with $P_{T,\rm miss} < 20\,\rm GeV$:

- $N^{dn}_{trk} < 2$;
- $\mathrm{Imb}_{trk} = (N^{up}_{trk} - N^{dn}_{trk})/(N^{up}_{trk} + N^{dn}_{trk}) > 0.7$;

where N^{up}_{trk} (N^{dn}_{trk}) is the number of tracks in the (opposite) direction of P_T. A track is in the (opposite) direction of P_T when the azimuthal angle difference between the track and P_T is less (greater) than 0.5 rad ($\pi - 0.5$ rad), Figure 5.13 gives a schematic view of the regions in $(x,\, y)$ of N^{up}_{trk}, N^{dn}_{trk} and the corresponding direction of P_T.

5.8. Sparks

Not all background is caused by external sources, also malfunctioning of the detector can cause fake charged current events. Especially sparks in the calorimeter can give rise to large $P_{T,\text{miss}}$. Sparks occur when one of the photo-multiplier tubes, PMTs, in a calorimeter cell has a short, hence faking an energy deposit. However, in this case only one of the two PMTs of the cell has a high signal and the imbalance, $\text{Imb}_{\text{cell}} = (E_{\text{PMT}_1} - E_{\text{PMT}_2})/(E_{\text{PMT}_1} + E_{\text{PMT}_2})$, for these cells is very large. Comparing $P_{T,\text{miss}}$ with the missing transverse momentum calculated using only cells with $\text{Imb}_{\text{cell}} < 0.7$, yielded the following selection cut which removed events with sparks:

- $0.5 < P_{T,\text{miss}}^{\text{imb}<0.7}/P_{T,\text{miss}} < 2$.

For events for which the $P_{T,\text{miss}}$ is caused by a spark in a cell of which one of the PMTs is malfunctioning, the imbalance can not be used. For these cells the malfunctioning PMT was ignored and the energy deposit measured by the functioning PMT was doubled and the imbalance of the cell was zero. To remove these events the following cut has been applied:

- $P_T^{\text{cell}}/P_{T,\text{miss}} < 0.5$;

where P_T^{cell} is the P_T of the cell with the highest P_T.

5.9. Cosmic and Halo Muon Background

The contamination of the charged current event sample with events containing cosmic or halo muons was considerable. Cosmic muons are muons produced in cosmic ray showers. Cosmic muons usually do not deposit their energy symmetrically in the detector, therefore producing $P_{T,\text{miss}}$, and consequently enter the CC sample.

Halo muons are muons produced in collisions between protons and residual gas in the beampipe or between protons in the halo of the beam with material upstream in the beampipe. The pions produced in the collisions will decay into muons and follow the beam trajectory in time with the proton bunch at some distance from the beampipe. Halo muons with enough energy can traverse the veto wall, the rear calorimeter, the barrel calorimeter and finally the forward calorimeter depositing a trail of energy. Hence, giving rise to a missing transverse momentum.

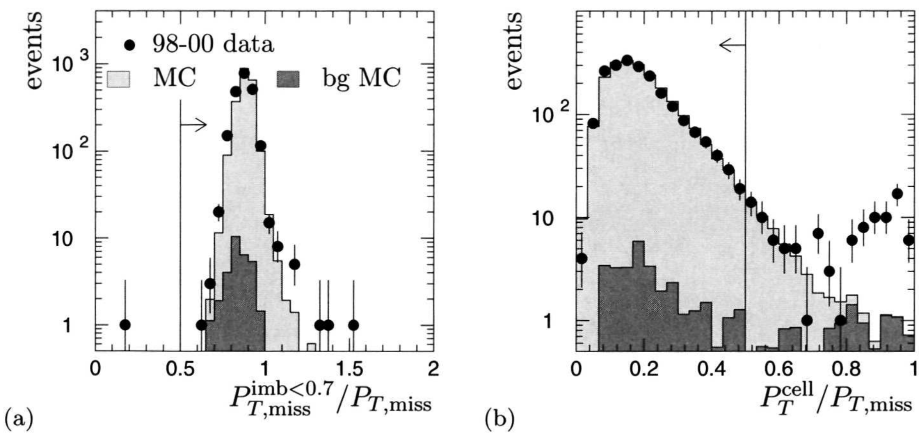

Figure 5.14. Distributions of: (a) the ratio of $P_{T,\mathrm{miss}}$ reconstructed using cells with an imbalance less than 0.7 over $P_{T,\mathrm{miss}}$; (b) ratio of P_T of cells with highest P_T over $P_{T,\mathrm{miss}}$. The figures show the event distribution after the final CC selection without the cuts indicated by the vertical lines.

Muons act as minimum ionising particles in the ZEUS detector. Therefore, the characteristic of muon events is the observation of long and narrow energy deposits in the calorimeter, which corresponds to a straight line trajectory through the detector often in overlap with an *ep* interaction or beam-gas interaction.

5.9.1. MUFFIN

The muon finder program MUFFIN [78, 79] searches for halo and cosmic muons in events which pass the charged current trigger selection. MUFFIN is especially suited to find events with a halo or cosmic muon overlapping with a genuine *ep* interaction or beam-gas interaction. MUFFIN uses the fact that events containing a halo or cosmic muon, pass the CC trigger selection due to the energy deposits in the CAL of the traversing muon creating $P_{T,\mathrm{miss}}$ in the events. Candidate muons are searched for by applying three-dimensional trajectory fits to the CAL clusters in an event. If a muon candidate is found, the CAL cells belonging to that candidate are removed, and the $P_{T,\mathrm{miss}}$ of the event is recalculated. If the $P_{T,\mathrm{miss}}$ is larger than 7 GeV, then the candidate muon is rejected as a halo or cosmic muon and other possible CAL cluster patterns are investigated. If, on

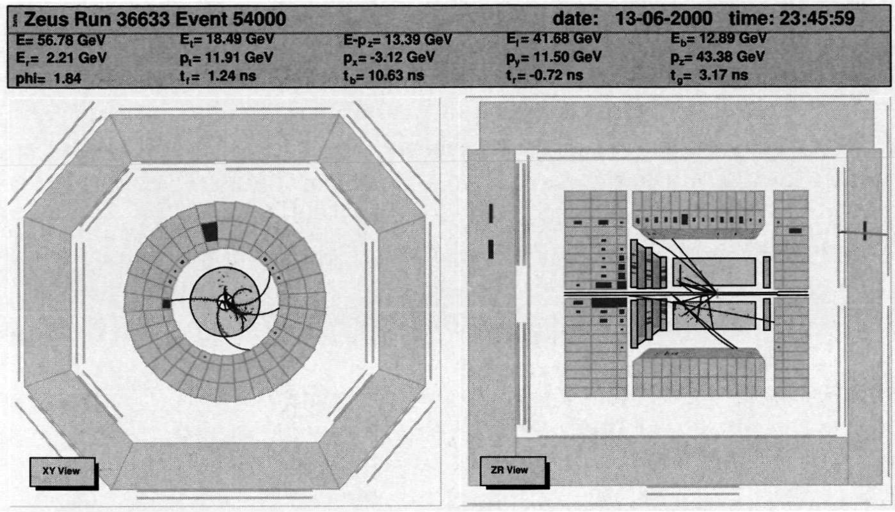

Figure 5.15. The ZEUS event display, ZEVIS, *showing a halo muon event in overlap with a beam-gas interaction. Shown are the $x-y$ projection (left side of the figure) and the $z-r$ projection of the event.*

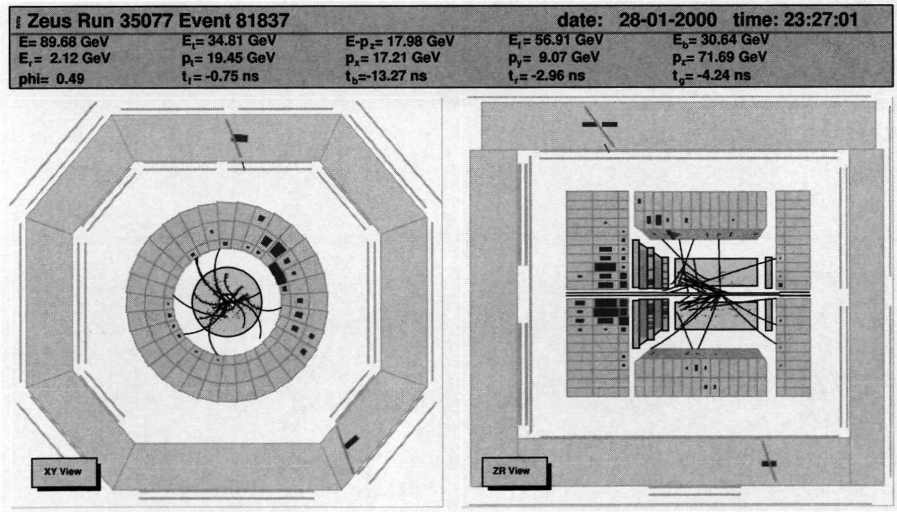

Figure 5.16. The ZEUS event display, ZEVIS, *showing a cosmic muon event traversing the detector in overlap with a beam-gas interaction.*

the other hand, the recalculated $P_{T,\mathrm{miss}}$ is below 7 GeV a more precise line fit is performed and a series of parameters [78] are calculated for the event and the candidate muon trajectory. These parameters are then compared with a list of reference parameters characterising a halo or cosmic muon transversing the detector. If the candidate muon matches the characteristics of a halo or cosmic muon the event was discarded from the CC event sample.

Figures 5.15 and 5.16 show a halo and a cosmic muon event identified as such by MUFFIN from the data sample collected in 2000. Both events passed all CC DIS selection cuts.

5.9.2. Additional Muon Rejection

Additional cosmic muon rejection was required for events with a small angle of the hadronic system. Cosmic muons traversing the forward calorimeter can produce a large bremsstrahlung shower. Typically, those events lose a lot of energy in the HAC section of the FCAL and can contaminate the CC sample. The following cuts were applied to remove these events:

- $E_{\mathrm{FEMC}}/E_{\mathrm{FCAL}} > 0.1$;
- $E_{\mathrm{FHAC1}}/E_{\mathrm{FCAL}} > 0.1$;
- $E_{\mathrm{FHAC2}}/E_{\mathrm{FCAL}} < 0.4$.

In Figs. 5.17(a)–(c) these ratios are shown. Since these events have a small hadronic angle, the cuts were applied only in the low-γ_0 region. In addition the following rejection cut has been applied to remove events with a muon traversing the HAC section of the BCAL:

- $E_{\mathrm{BHAC}}/E_{\mathrm{BCAL}} < 0.9$

This cut has been applied only for events with at least 5 GeV in the BCAL.

Finally nine events containing cosmic or halo muons, which were not removed by the CC event selection or the muon rejection cuts, were rejected by a visual scan from the e^-p data sample and 16 from the e^+p data sample.

5.10. Summary

In this chapter the charged current event selection has been presented. Major background contributions from beam-gas interactions, photoproduction and

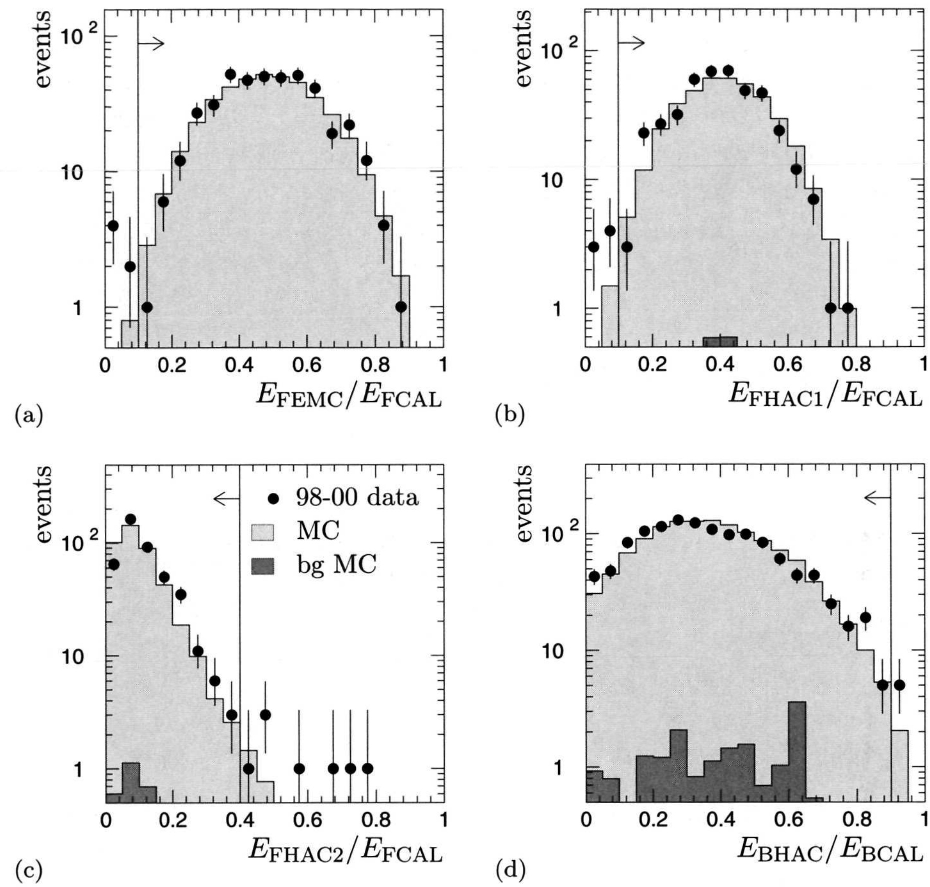

Figure 5.17. Four distributions of calorimeter quantities are shown: (a) $E_{\mathrm{FEMC}}/E_{\mathrm{FCAL}}$; (b) $E_{\mathrm{FHAC1}}/E_{\mathrm{FCAL}}$; (c) $E_{\mathrm{FHAC2}}/E_{\mathrm{FCAL}}$; (d) $E_{\mathrm{BHAC}}/E_{\mathrm{BCAL}}$ for $E_{\mathrm{BCAL}} > 5$ GeV. The figures show the event distribution after the final CC selection without the cuts indicated by the vertical lines. The Figs. 5.17(a)–(c) show only the low-γ_0 region.

cosmic/halo muons, were effectively removed. A summary of the effect of the charged current event selection on data and MC simulation is given in Table 5.1. In the e^-p data a total of 627 data events were left after the charged current event selection compared with 630 Monte Carlo events. In the e^+p data a total of 1456 data events and 1468 of Monte Carlo events were left after the event

Table 5.1. The result of the charged current DIS event selection on data and MC simulation. The second column shows the fraction of the expected number of e⁻p MC events after application of the selection shown in the first column. The third and fourth column show the number of e⁻p data events and the fraction of e⁻p data events after application of the selection shown in the first column, respectively. Column five to seven shows the same for the e⁺p CC DIS selection.

selection	MC (e^-p)	data (e^-p)		MC (e^+p)	data (e^+p)	
	% acc. evts.	acc. evts.	% acc. evts.	% acc. evts.	acc. evts.	% acc. evts.
$Q^2_{\text{gen}} > 10\,\text{GeV}^2$	100.0			100.0		
FLT	91.3			88.5		
SLT	87.4			82.3		
TLT	86.4			81.2		
preselection	82.8	77713	100.0	77.2	93539	100.0
vertex	80.6	45295	58.3	74.3	64018	68.4
$P_{T,\text{miss}}$	68.8	21544	27.7	63.7	24573	26.2
beam-gas/pipe	54.8	2955	3.8	61.7	15461	16.5
additional track	53.8	2600	3.3	59.7	13829	14.7
NC DIS	53.5	2557	3.3	59.4	13666	14.6
photoproduction	51.6	1992	2.6	54.6	8492	9.0
sparks	50.1	854	1.1	53.5	2585	2.7
cosmic/halo muons	50.0	627	0.8	53.3	1456	1.5

selection. The key distributions from which the kinematic variables were determined are presented in Figs. 5.18 and 5.19. The distributions of the various quantities are well reproduced by the Monte Carlo simulation. Figures 5.20 and 5.21 show the final e^-p and e^+p CC events distributed in $(x,\ Q^2)$ phase space.

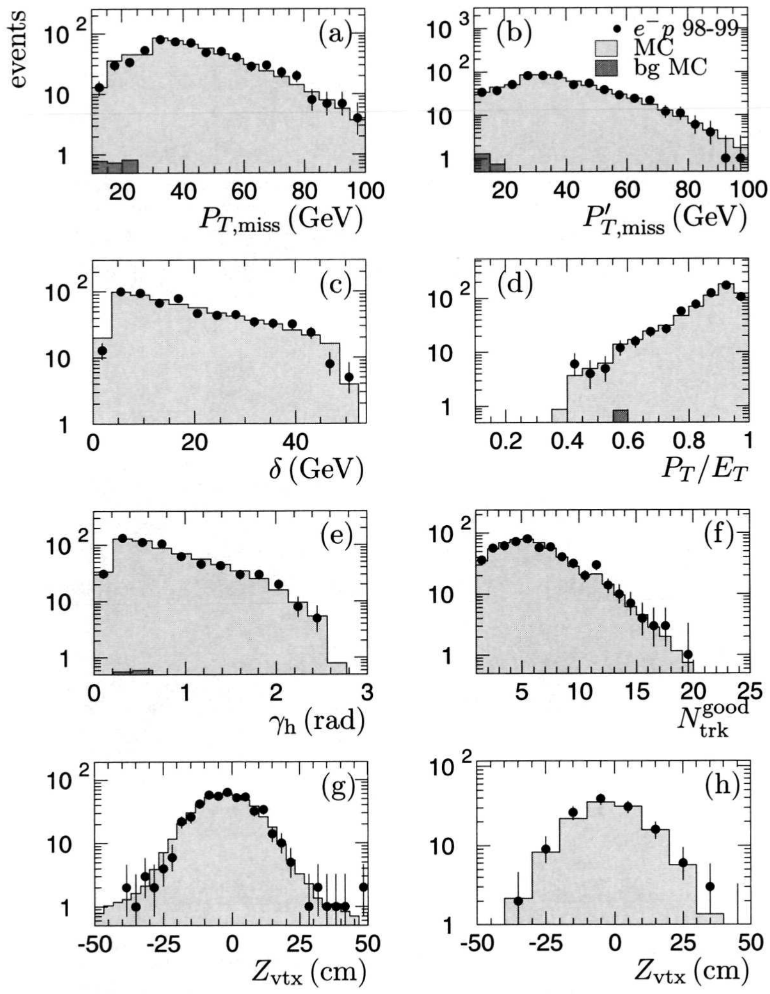

Figure 5.18. Comparison of the final e^-p CC data sample (solid points) with the predictions from the sum of signal Monte Carlo and ep background Monte Carlo (light shaded histogram). The ep background Monte Carlo is shown as the dark shaded histogram. (a) the missing transverse momentum, $P_{T,\mathrm{miss}}$; (b) $P_{T,\mathrm{miss}}$ excluding the very forward cells, $P'_{T,\mathrm{miss}}$; (c) $\delta = \sum(E - P_Z)_i$; (d) the ratio of missing transverse momentum to total transverse energy, $P_{T,\mathrm{miss}}/E_T$; (e) γ_h; (f) the number of good tracks, N_{trk}^{good}; (g) the Z position of the CTD vertex for the high-γ_0 sample and (h) the Z position of the timing vertex for the low-γ_0 sample.

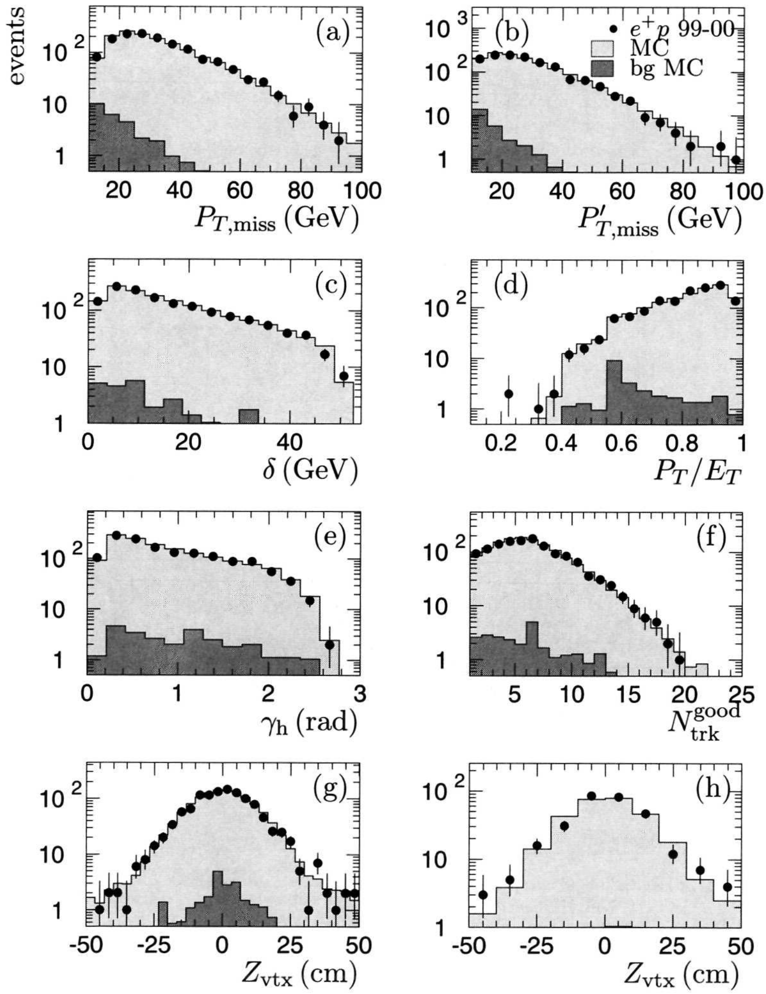

Figure 5.19. Comparison of the final e^+p CC data sample (solid points) with the predictions from the sum of signal Monte Carlo and ep background Monte Carlo (light shaded histogram). The ep background Monte Carlo is shown as the dark shaded histogram. (a) the missing transverse momentum, $P_{T,\mathrm{miss}}$; (b) $P_{T,\mathrm{miss}}$ excluding the very forward cells, $P'_{T,\mathrm{miss}}$; (c) $\delta = \sum(E-P_Z)_i$; (d) the ratio of missing transverse momentum to total transverse energy, $P_{T,\mathrm{miss}}/E_T$; (e) γ_h; (f) the number of good tracks, N_{trk}^{good}; (g) the Z position of the CTD vertex for the high-γ_0 sample and (h) the Z position of the timing vertex for the low-γ_0 sample.

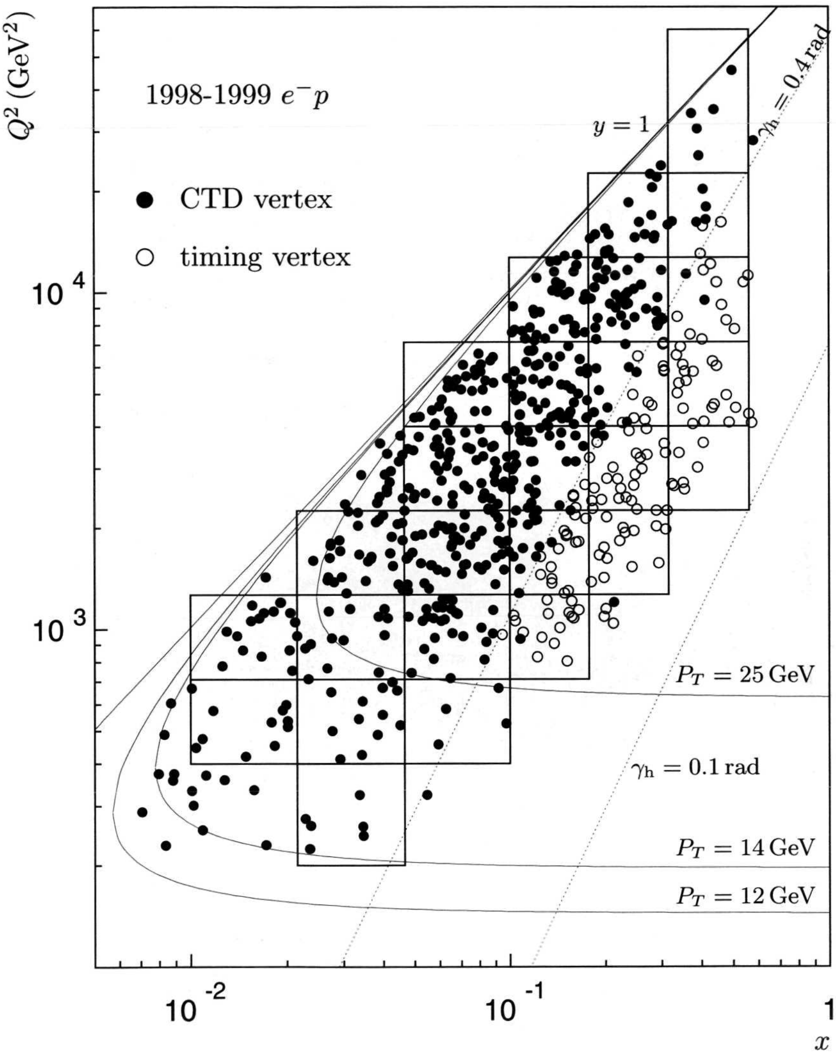

Figure 5.20. Distribution of the final e^-p CC DIS event sample in the (x, Q^2) phase space. The open circles represent the events reconstructed using the FCAL timing vertex ($\gamma_0 < 0.4$ rad). The dots represent the events reconstructed using the CTD tracking vertex ($\gamma_0 > 0.4$ rad). ISO lines for $\gamma_h = 0.1$ rad, $\gamma_h = 0.4$ rad, $P_{T,\mathrm{miss}} = 12$ GeV, $P_{T,\mathrm{miss}} = 14$ GeV and also for $y = 1$ are shown in the figure (note that the ISO lines for γ_h are plotted and not for γ_0).

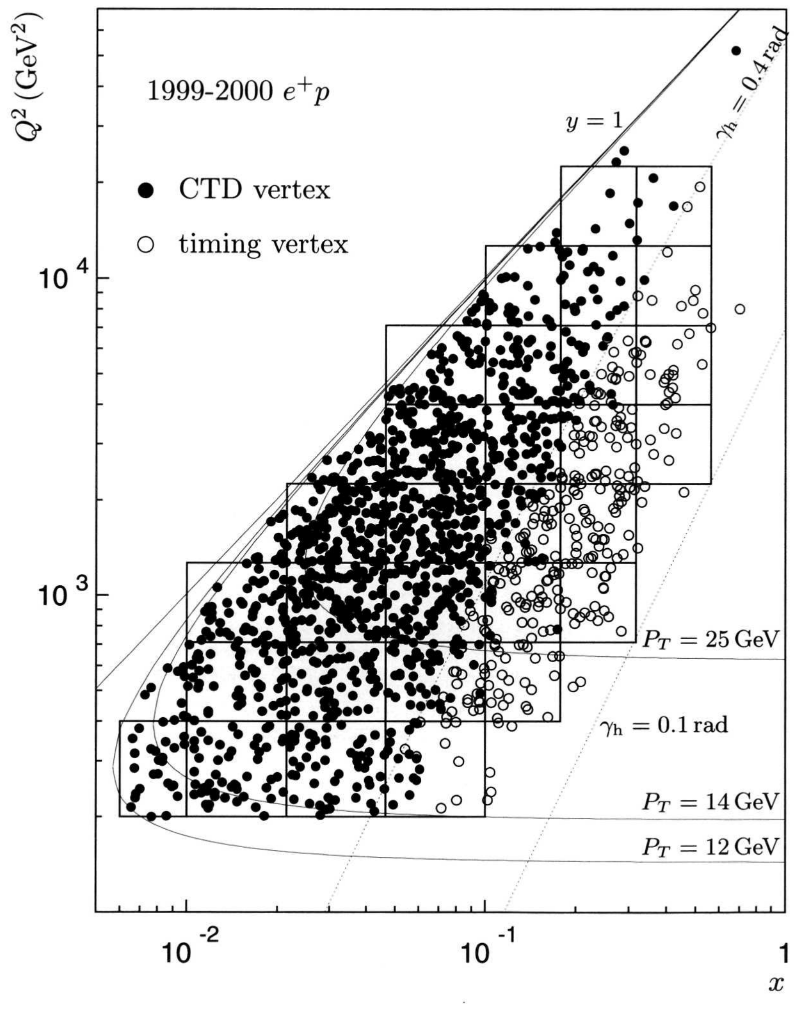

Figure 5.21. Distribution of the final e^+p CC DIS event sample in the $(x,\, Q^2)$ phase space. The open circles represent the events reconstructed using the FCAL timing vertex ($\gamma_0 < 0.4\,rad$). The dots represent the events reconstructed using the CTD tracking vertex ($\gamma_0 > 0.4\,rad$). ISO lines for $\gamma_h = 0.1\,rad$, $\gamma_h = 0.4\,rad$, $P_{T,\mathrm{miss}} = 12\,GeV$, $P_{T,\mathrm{miss}} = 14\,GeV$ and also for $y = 1$ are shown in the figure (note that the ISO lines for γ_h are plotted and not for γ_0).

Chapter 6

Cross Section Measurements

In the previous chapter the selection of charged current DIS events has been presented. In this chapter it will be discussed how this sample of charged current events has been used to measure the charged current ep cross sections. The binning of the kinematic range used in the measurement and the unfolding of the cross section will be discussed, followed by a discussion of the statistical and systematic uncertainties.

6.1. Bin Definitions

In order to measure the differential charged current cross sections the kinematic ranges are divided in bins wide enough to contain a sufficient number of events to measure the cross section in that bin. It is important to use an appropriate binning, since too narrow binning will increase the statistical error and migration effects between neighbouring bins will become too large. On the other hand, too wide binning would result in a measurement which reveals less information than it could have done otherwise. The binning chosen in this analysis ensures that the bin size is several times the resolution of the kinematic variable in which the cross section is unfolded.

The single differential cross section has been unfolded in the kinematic variables Q^2, x and y. For the measurement of the single differential cross section $\mathrm{d}\sigma/\mathrm{d}Q^2$ nine bins were defined in the Q^2 range $200-60000\,\mathrm{GeV}^2$. The Q^2 range $200-22494\,\mathrm{GeV}^2$ has been divided in eight bins with equal width in $\log Q^2$. Since the number of events drops rapidly with higher values of Q^2, the ninth bin had to be made larger and covered the Q^2 range $22494-60000\,\mathrm{GeV}^2$. For the unfolding of the single differential cross section $\mathrm{d}\sigma/\mathrm{d}x$ seven bins were defined in the x range $0.01-1.0$: three bins with equal width in $\log x$ in the x range $0.01-0.1$ and four bins with equal width in $\log x$ in the x range $0.1-1.0$. For the single differential cross section $\mathrm{d}\sigma/\mathrm{d}y$ seven bins were defined in the y range $0.0-0.9$: two bins with equal width in the y range $0.0-0.2$ and five in the y range $0.2-0.9$. For both the e^-p and e^+p data sample the same binning was used for the single differential cross section measurements. Figures 4.6(b), 4.6(d) and 4.7(b) show the resolution in Q^2, x and y, respectively. The resolution in Q^2 is $\sim 30\%$ over the entire Q^2 range. The resolution in x improves from $\sim 30\%$ at low-x to $\sim 10\%$ at high-x. The resolution in y is $\sim 13\%$ over the entire y range.

The binning for the double differential cross section measurements in x and Q^2, $\mathrm{d}^2\sigma/\mathrm{d}x\mathrm{d}Q^2$, was based on the same binning as used in the single differential cross section measurements. The e^-p double differential cross section was measured in 26 bins, whereas in the e^+p data it was measured in 30 bins, in the x range $0.01-0.562$ and the Q^2 range $200-22494\,\mathrm{GeV}^2$. The difference in the number of bins between the e^-p and e^+p data is due to the larger beam-gas background in the e^-p data (see Sect. 5.4.1). Therefore, the cross section could not be measured in a number of low-Q^2 and high-x bins, though an additional bin was defined at high-x and high-Q^2, with Q^2 range $22494-60000\,\mathrm{GeV}$ and x range $0.316-0.562$. For the measurement of $\mathrm{d}^2\sigma/\mathrm{d}x\mathrm{d}Q^2$ in the e^+p data an additional bin was defined at low-x and low-Q^2, with Q^2 range $200-400\,\mathrm{GeV}^2$ and x range $0.006-0.01$. Figures 6.1 and 6.2 show the resolutions of Q^2, x and y respectively for the various $\mathrm{d}^2\sigma/\mathrm{d}x\mathrm{d}Q^2$ bins used in the e^+p data. The same resolutions were observed in the e^-p data.

The cross section measurements were restricted to bins with a high purity, $\mathcal{P}$, and a high acceptance, $\mathcal{A}$. In this way large corrections for detector acceptance and migration effects were avoided. The purity and acceptance of a bin are defined as:

- **purity,** $\mathcal{P}$: the number of events generated and measured in a bin divided by the number of events measured in that bin;

- **efficiency,** $\mathcal{E}$: the number of events generated and measured in a bin divided by the number of events generated in that bin;

- **acceptance,** $\mathcal{A}$: number of events measured in a bin divided by the number of events generated in that bin.

Here "measured in a bin" means that the kinematic variables of the reconstructed event were contained in that bin and that the event met the event selection criteria. Note that with this set of definitions the following relation holds

$$\mathcal{A} = \mathcal{E}/\mathcal{P} \tag{6.1}$$

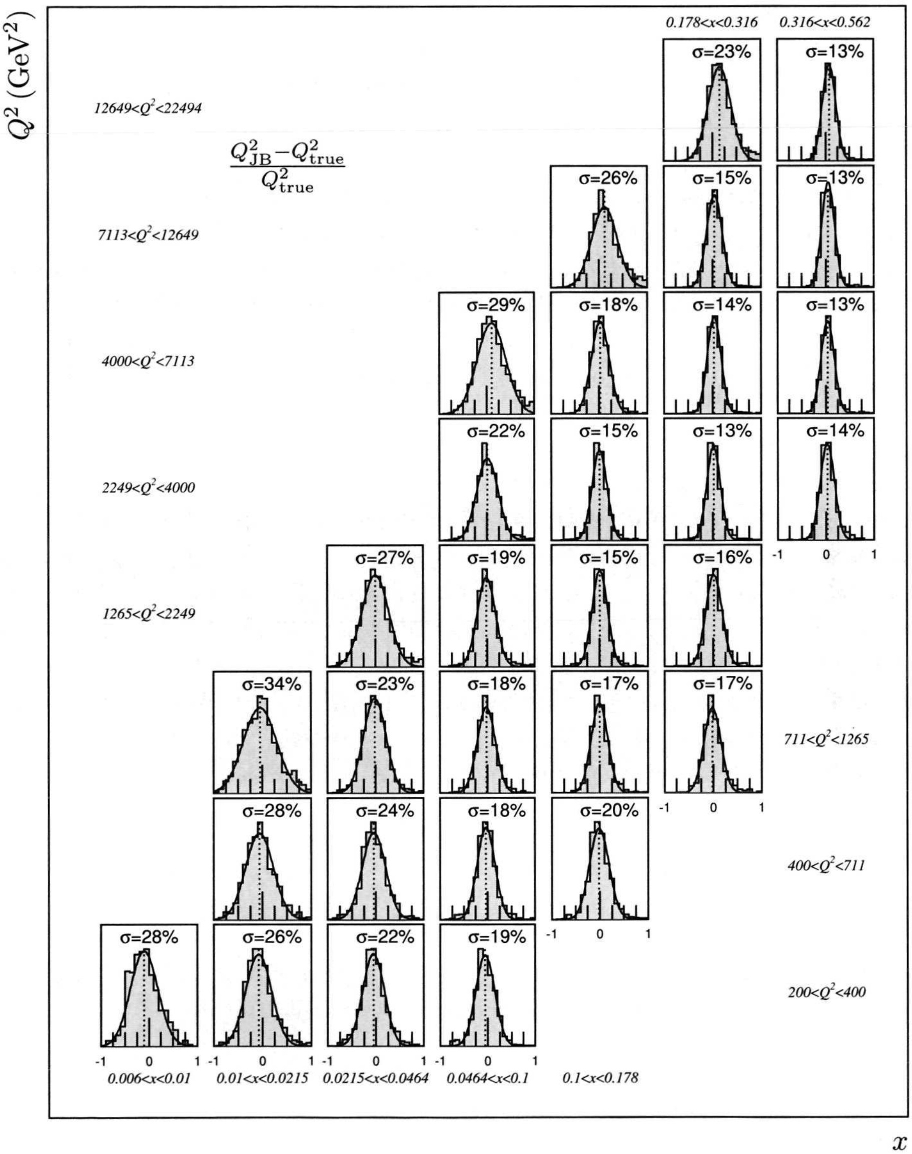

Figure 6.1. Resolution of Q^2 determined from the $(Q^2_{JB}-Q^2_{true})/Q^2_{true}$ distribution, shown for the x, Q^2 bins used in the unfolding of the e^+p double differential cross section. The best resolution are at high-x and high-Q^2.

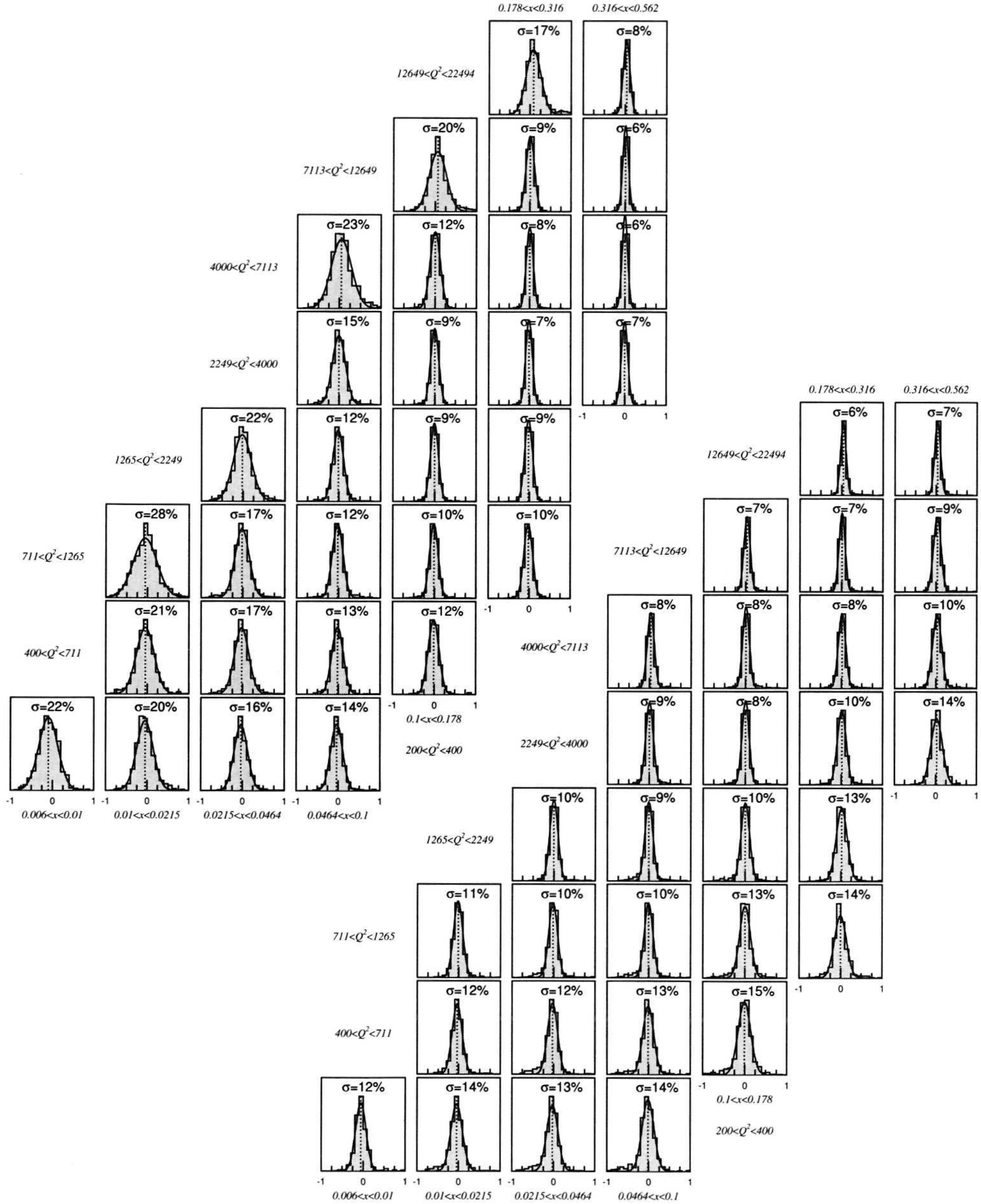

Figure 6.2. Resolutions of x (left), determined from the $(x_{JB} - x_{true})/x_{true}$ distribution, and y (right), determined from the $(y_{JB} - y_{true})/y_{true}$ distribution, shown for the x, Q^2 bins used in the unfolding of the e^+p double differential cross section.

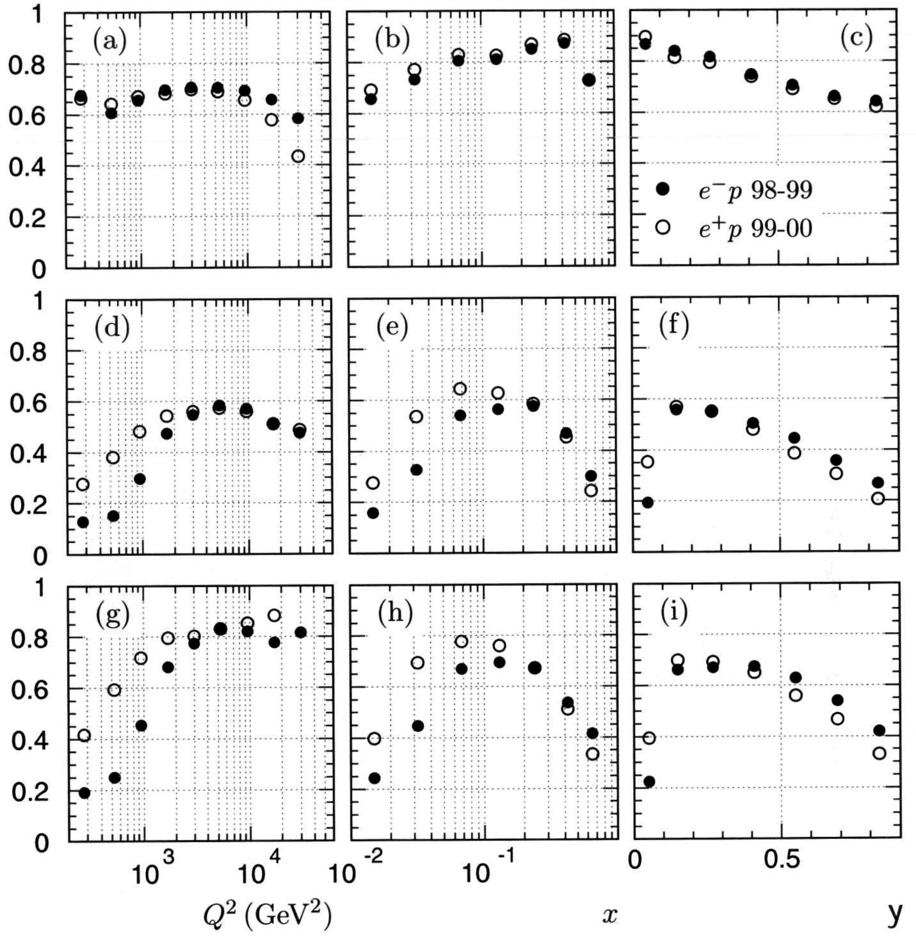

Figure 6.3. Various bin quality variables for the single differential bins in the kinematic variables Q^2, x and y. (a),(b) and (c) the purity $\mathcal{P}$; (d), (e) and (f) the efficiency $\mathcal{E}$; and (g), (h) and (i) the acceptance, $\mathcal{A}$. The solid (open) dots represent the e^-p (e^+p) data.

Figure 6.3 shows the various bin quantities for the different single differential bins in Q^2, x and y, respectively. The acceptance is above 30% for all bins, except for the lowest bins in Q^2,x and y. The purity is well above 50% for all bins, except for the highest bin in Q^2 which has a purity just below 50%. The various bin quantities for all bins used in the analysis are listed in Tab. A.1 to A.8.

6.2. Cross Section Unfolding

The kinematic variables used in the measurement of the cross section are subject to various distortions like smearing effects, detector geometry effects and electroweak radiative effects. Hence, the measured values differ from the true values. The procedure to correct the measurement for these distortions is called unfolding. The cross section is extracted in bins of the various kinematic variables. The integrated cross section including radiative correction in a bin of Q^2 can be written as

$$\sigma_{\rm rad}(\Delta Q^2) = \frac{N_{\rm data} - N_{\rm bg}}{\mathcal{A}\mathcal{L}_{\rm data}}, \tag{6.2}$$

where $\mathcal{L}_{\rm data}$ is the total integrated luminosity. $N_{\rm data}$ is the number of observed data events in the bin that passed the charged current event selection and $N_{\rm bg}$ is the number of background events in the bin, as estimated from MC simulation. The acceptance, $\mathcal{A}$, of the bin which is defined as $\mathcal{A} = N^{\rm MC}_{\rm meas}/N^{\rm MC}_{\rm gen}$, was used to correct for the effects from smearing and detector geometry. Where $N^{\rm MC}_{\rm meas}$ is the observed number of charged current MC events in the bin that passed the CC event selection and $N^{\rm MC}_{\rm gen}$ is the number of CC MC events generated in that bin. Re-weighting $N^{\rm MC}_{\rm meas}$ and $N^{\rm MC}_{\rm gen}$ to the measured luminosity Eq. (6.2) can be rewritten as

$$\sigma_{\rm rad}(\Delta Q^2) = \frac{N_{\rm meas}}{N^{\rm MC}_{\rm meas}} \frac{N^{\rm MC}_{\rm gen}}{\mathcal{L}_{\rm data}} \tag{6.3}$$

$$= \frac{N_{\rm meas}}{N^{\rm MC}_{\rm meas}} \sigma^{\rm MC}_{\rm rad}(\Delta Q^2), \tag{6.4}$$

where $N_{\rm meas} = N_{\rm data} - N_{\rm bg}$ and $\sigma^{\rm MC}_{\rm rad}(\Delta Q^2)$ is the integrated radiative cross section in bin ΔQ^2 evaluated by the CC MC events. To determine the electroweak Born level cross section a correction factor was introduced

$$C_{\rm rad} = \frac{\sigma^{\rm SM}_{\rm Born}(\Delta Q^2)}{\sigma^{\rm SM}_{\rm rad}(\Delta Q^2)}, \tag{6.5}$$

where $\sigma^{\rm SM}_{\rm Born}(\Delta Q^2)$ is the integrated Standard Model, SM, Born level cross section in bin ΔQ^2 and $\sigma^{\rm SM}_{\rm rad}(\Delta Q^2)$ is the integrated SM radiative cross section in bin ΔQ^2. Applying this correction factor, the integrated Born level cross section in bin ΔQ^2 can be obtained from

$$\sigma_{\text{Born}}(\Delta Q^2) = C_{\text{rad}}\sigma_{\text{rad}}(\Delta Q^2), \tag{6.6}$$

$$= \frac{\sigma_{\text{rad}}(\Delta Q^2)}{\sigma^{\text{SM}}_{\text{rad}}(\Delta Q^2)}\sigma^{\text{SM}}_{\text{Born}}(\Delta Q^2), \tag{6.7}$$

where $\sigma^{\text{SM}}_{\text{rad}}(\Delta Q^2)$ was obtained using the same Monte Carlo simulation which had been used to calculate the acceptance, i.e. $\sigma^{\text{SM}}_{\text{rad}}(\Delta Q^2) = \sigma^{\text{MC}}_{\text{rad}}(\Delta Q^2)$. Therefore, combining Eq. (6.4) and Eq. (6.7) the Born level cross section can be written as

$$\sigma_{\text{Born}}(\Delta Q^2) = \frac{N_{\text{meas}}}{N^{\text{MC}}_{\text{meas}}}\sigma^{\text{SM}}_{\text{Born}}(\Delta Q^2). \tag{6.8}$$

To obtain the differential cross section at a specific reference point in the bin, a correction factor was applied. For the differential cross section in Q^2 this bin centring correction factor was defined as

$$C_{\text{centre}} = \frac{\left.\frac{\mathrm{d}\sigma^{\text{SM}}_{\text{Born}}(Q^2)}{\mathrm{d}Q^2}\right|_{Q^2=Q^2_c}}{\sigma^{\text{SM}}_{\text{Born}}(\Delta Q^2)}, \tag{6.9}$$

where $\mathrm{d}\sigma^{\text{SM}}_{\text{Born}}(Q^2)/\mathrm{d}Q^2|_{Q^2=Q^2_c}$ is the SM Born level differential cross section at the reference point Q^2_c. Hence, the Born level differential cross section in Q^2 at the reference point Q^2_c can be obtained from

$$\left.\frac{\mathrm{d}\sigma_{\text{Born}}(Q^2)}{\mathrm{d}Q^2}\right|_{Q^2=Q^2_c} = C_{\text{centre}}\sigma_{\text{Born}}(\Delta Q^2). \tag{6.10}$$

Substituting Eq. (6.8) and (6.9) into Eq. (6.10) the Born level differential cross section can be written as

$$\left.\frac{\mathrm{d}\sigma_{\text{Born}}(Q^2)}{\mathrm{d}Q^2}\right|_{Q^2=Q^2_c} = \frac{N_{\text{meas}}}{N^{\text{MC}}_{\text{meas}}}\left.\frac{\mathrm{d}\sigma^{\text{SM}}_{\text{Born}}(Q^2)}{\mathrm{d}Q^2}\right|_{Q^2=Q^2_c}. \tag{6.11}$$

Finally, the unfolded Born level differential cross section at the reference point Q^2_c was obtained by

$$\left.\frac{\mathrm{d}\sigma_{\text{Born}}(Q^2)}{\mathrm{d}Q^2}\right|_{Q^2=Q^2_c} = \frac{N_{\text{data}} - N_{\text{bg}}}{N^{\text{MC}}_{\text{meas}}}\left.\frac{\mathrm{d}\sigma^{\text{SM}}_{\text{Born}}(Q^2)}{\mathrm{d}Q^2}\right|_{Q^2=Q^2_c}. \tag{6.12}$$

The SM differential cross sections were evaluated in the on-shell scheme [51] using the PDG values for the electroweak parameters and the CTEQ5D [52] parton distribution functions, PDFs. The same unfolding procedure was followed for the single differential cross sections $\mathrm{d}\sigma/\mathrm{d}x$ and $\mathrm{d}\sigma/\mathrm{d}y$ and for the double differential cross sections in bins of x and Q^2, $\mathrm{d}^2\sigma/\mathrm{d}x\mathrm{d}Q^2$.

The reference points in the unfolding of $\mathrm{d}\sigma/\mathrm{d}Q^2$, $\mathrm{d}\sigma/\mathrm{d}x$ and $\mathrm{d}^2\sigma/\mathrm{d}x\mathrm{d}Q^2$ were chosen to be the logarithmic centres of the bins in Q^2 and x, except for the highest Q^2 and highest x bins. The reference point for the highest Q^2 bin was set so that the logarithmic distance to the previous reference point was equal to the logarithmic distances between the other reference points. The reference point in the highest x bin was set at $x_c = 0.65$ [74]. The reference points in the unfolding of $\mathrm{d}\sigma/\mathrm{d}y$ were chosen to be the linear centres of the bins in y. The single differential cross sections in x and y are quoted for $Q^2 > 200\,\mathrm{GeV}$. The calculated SM single differential cross sections in Q^2 and x include the region $y > 0.9$. Hence the acceptance loss by the y selection threshold is corrected and the obtained cross sections were extrapolated to the full y range.

6.3. Background Estimation

Various Monte Carlo samples were used to estimate the number of *ep* interactions other than charged current interactions passing the CC event selection. These background events were subtracted in the cross section unfolding procedure (see (6.12)). The *ep* backgrounds evaluated using MC samples were: NC DIS, photoproduction, charged lepton production and single W production. Section 3.2 gives an overview of the MC programs which were used to generate the background events. Tables A.1 to A.8 list the background contributions from the different *ep* processes in the bins used in the cross section unfolding. The smallest background contribution comes from the NC DIS interactions, whereas the photoproduction background is the largest. Over the full kinematic range the background is well below 2%, except in the lowest Q^2 bins. Here the background contamination is of the order of 5% for e^-p and 10%.for e^+p data.

6.4. Statistical Uncertainties

The quoted statistical uncertainties in the cross section measurements are determined using standard statistical data analysis techniques. The cross section is proportional to the number of events by (see eq. (6.12))

$$\sigma \sim \frac{N_{\text{data}} - N_{\text{bg}}}{N_{\text{MC}}} \tag{6.13}$$

where N_{data} is the total number of observed data events and N_{MC} and N_{bg} are the number of measured charged current and background MC events, respectively. N_{MC} and N_{bg} were obtained by the weighted sum of all the events passing the CC event selection criteria from the various Monte Carlo samples; $N_{\text{MC}} = \sum_i w_{\text{MC},i}$ and $N_{\text{bg}} = \sum_i w_{\text{bg},i}$ where i runs over all events and the weight assigned to each of the generated events is such that the total number of events is normalised to the data luminosity. The statistical error of N_{MC} in a bin is

$$\Delta N_{\text{MC}} = \sqrt{\sum_i w_{\text{MC},i}^2} \tag{6.14}$$

and similarly for N_{bg}: $\Delta N_{\text{bg}} = \sqrt{\sum_i w_{\text{bg},i}^2}$. The weight of the observed data events is one. Therefore, the statistical error of the number of data events in a bin is

$$\Delta N_{\text{data}} = \sqrt{N_{\text{data}}} \tag{6.15}$$

The statistical error of the cross section measurements can now be obtained from

$$\delta_{stat}^i = \sqrt{\frac{(\Delta N_{\text{data}})_i^2 + (\Delta N_{\text{bg}})_i^2}{(N_{\text{data}} + N_{\text{bg}})_i^2} + \left(\frac{\Delta N_{\text{MC}}}{N_{\text{MC}}}\right)_i^2} \tag{6.16}$$

where i denotes the bin number. For bins with less than 12 events a 67% confidence interval was calculated using Poisson statistics; the boundaries of this confidence interval were taken as the statistical uncertainty.

6.5. Systematic Uncertainties

Systematic effects in the measurement can give a bias in the unfolding of the cross section. Various sources of systematic uncertainties have been studied. The most important ones were found to be the energy scale of the calorimeter, QCD cascade models and the effects of the selection thresholds. Other sources of systematic uncertainties which have been studied were: effects of the parton density functions, effects of the NLO QCD corrections, energy leakage, CTD vertex finding efficiency and the MC vertex distribution. The systematic uncertainties have been studied in the same bins as used in the unfolding. The final systematic error will be obtained by the quadratic sum of all the systematic uncertainties.

6.5.1. Calorimeter Energy Scale

A very important systematic uncertainty is the uncertainty of the energy scale of the calorimeter. This energy scale has a direct effect on the reconstruction of the kinematic variables and therefore on the measurement of the cross sections. Especially at high-Q^2 the effect can be relatively large due to the steeply falling of the cross section. The energy scale and the associated uncertainty of the energy scale were determined, using NC DIS events, from the ratios of the total hadronic transverse momentum, $P_{T,\mathrm{h}}$, to $P_{T,\mathrm{DA}}$ and $P_{T,e}$, where $P_{T,\mathrm{DA}} = \sqrt{Q^2_{\mathrm{DA}}(1 - y_{\mathrm{DA}})}$ is the transverse momentum obtained from the double-angle method (see (4.16) and (4.17)) and $P_{T,e}$ is the measured transverse momentum of the scattered electron. In order to restrict the hadronic activity to particular polar regions, a sample of NC DIS events with a single jet was selected. By applying suitable cuts on the location of the current jet and evaluating $P_{T,\mathrm{h}}/P_{T,\mathrm{DA}}$ and $P_{T,\mathrm{h}}/P_{T,e}$ event by event, the hadronic energy scales of the FCAL and BCAL were determined. The responses of the HAC and EMC sections of the individual calorimeters were determined by plotting $P_{T,\mathrm{h}}/P_{T,\mathrm{DA}}$ and $P_{T,\mathrm{h}}/P_{T,e}$ as a function of the fraction of the hadronic energy measured in the EMC section of the calorimeter. In each case, the uncertainty was found by comparing the determinations from data and MC. In order to study the hadronic energy scale in the RCAL, a sample of diffractive DIS events was selected. Such events are characterised by a large gap in the hadronic energy flow between the proton remnant and the current jet. $P_{T,\mathrm{h}}/P_{T,\mathrm{DA}}$ was evaluated event-by-event for events with hadronic activity exclusively in the RCAL and the energy scale and associated uncertainty determined.

The relative uncertainty of the energy scale was determined to be 2% for the RCAL and 1% for the FCAL and BCAL [80]. Varying the energy scale of the calorimeter sections by these amounts in the detector simulation induces small shifts of the kinematic variables. The variations of the energy scale of each of the calorimeters simultaneously up or down by these amounts gave the systematic uncertainty on the total measured energy in the calorimeter. By increasing (decreasing) the FCAL and RCAL energy scales together while the BCAL energy scale was decreased (increased) the uncertainty in the cross sections from the effect of the energy scale on the measurement of γ_{h} was obtained. The uncertainty stemming from the method used to determine the relative uncertainty was determined by simultaneously increasing the energy measured in the EMC section of the calorimeter by 2% and decreasing the energy measurement in the HAC section by 2% and *vice-versa*. This was done separately for each of the calorimeters.

The effect of the uncertainty of the energy scale is maximal in high-Q^2 and high-x bins. These are also the bins with the lowest number of events. Using both data and MC to estimate the systematic uncertainty on the cross section measurement yields an overestimate of the error due to statistical fluctuations in the number of events in these bins. To circumvent this effect only the MC simulation was used to determine the systematic error on the cross section, in the following way:

$$\delta_E^i = \frac{N_{\mathrm{nom}} - N_i}{N_i}, \tag{6.17}$$

where i denotes a particular energy scale variation. N_{nom} is the number of events in the nominal, i.e. not scaled, MC data and N_i is the number of events in the scaled MC data. The systematic error on the cross section, due to the uncertainty of the calorimeter energy scale was obtained by quadratic summation of the three estimates. The uncertainties from this check reach $\sim 15\%$ in the highest Q^2 bins and $\sim 20\%$ in the highest x bins.

6.5.2. QCD Cascade Model

The QCD cascade model used in the Monte Carlo event simulation in this analysis was provided by the colour dipole model, CDM as implemented in the ARIADNE [53] program. As an alternative to the CDM from ARIADNE the matrix element parton shower, MEPS, model as implemented in the LEPTO [50] program can be used for the simulation of the QCD cascade. Both models are successful in describing data from high-Q^2 DIS events [81]. The sensitivity of the cross section measurement to the higher order QCD effects in the hadronic final state was estimated by using the MEPS model from LEPTO instead of the CDM from ARIADNE. The systematic error on the cross section was obtained by the difference in acceptance between the two models

$$\pm\,\delta_{\mathrm{MEPS}} = \pm \left| \frac{\mathcal{A}_{\mathrm{CDM}} - \mathcal{A}_{\mathrm{MEPS}}}{\mathcal{A}_{\mathrm{CDM}}} \right| \tag{6.18}$$

where $+\delta_{\mathrm{MEPS}}$ ($-\delta_{\mathrm{MEPS}}$) is the error in the positive (negative) direction, and $\mathcal{A}_{\mathrm{CDM}}$ and $\mathcal{A}_{\mathrm{MEPS}}$ are the acceptances calculated using the CDM model and MEPS model respectively. The largest uncertainty is found in the e^+p data in the highest Q^2 bin where it reaches $\sim 20\%$ and $\sim 12\%$ in the e^-p. In the highest x bins the uncertainty is $\sim 7\%$.

6.5.3. Selection Thresholds

Many selection thresholds were varied in order to verify the stability of the cross section measurement in terms of efficiency and purity. Generally the selection thresholds for a selection variable were varied by an amount comparable with the resolution of the variable. Furthermore, the thresholds were varied by such an amount that the selection efficiency was still good, and the number of background events, i.e. beam-gas, cosmic muons, etc., did not become too large. Most of the varied selection thresholds did not change the measured cross section, and were therefore not included in the uncertainty [82]. The uncertainty on the cross section due to the selection threshold variation was obtained from the difference between the nominal cross section and the cross section calculated with the threshold variation

$$\delta_{\mathrm{T}}^{i} = \frac{\sigma_i - \sigma_{\mathrm{nom}}}{\sigma_{\mathrm{nom}}} = \frac{N_{\mathrm{data}} - N_{\mathrm{bg}}}{N_{\mathrm{meas}}^{\mathrm{MC}}} \cdot \frac{N_{\mathrm{meas}}^{\mathrm{MC},i}}{N_{\mathrm{data}}^{i} - N_{\mathrm{bg}}^{i}} - 1, \tag{6.19}$$

where i denotes the threshold variation and σ_{nom} the cross section unfolded with the nominal event selection. The selection thresholds which, when shifted, significantly changed the cross section, and for which it was not possible to estimate the uncertainty in an other way, were included in the systematic error. Statistical fluctuations, due to limited statistics in some bins, were suppressed by demanding that changes in $N_{\mathrm{data}} - N_{\mathrm{bg}}$ did not exceed 5%. If so, the uncertainty in the bin for that particular threshold variation was set to zero. In order not to overestimate the uncertainties, the threshold variations were separated in two sets, transverse momentum, T1, and tracking quantities, T2. The largest uncertainty in a set was selected as the uncertainty of the threshold variation for that set.

T1, transverse momentum

The first set of threshold variations, T1, is concerned with the transverse momentum selection cuts:

- $P_{T,\mathrm{miss}} > 12 \pm 1.2\,\mathrm{GeV}$, for high-$\gamma_0$ events;
- $P_{T,\mathrm{miss}} > 14 \pm 1.4\,\mathrm{GeV}$, for low-$\gamma_0$ e^+p events;
- $P_{T,\mathrm{miss}} > 25 \pm 2.5\,\mathrm{GeV}$, for low-$\gamma_0$ e^-p events;
- $P'_{T,\mathrm{miss}} > 10 \pm 1.0\,\mathrm{GeV}$, for high-$\gamma_0$ events;
- $P'_{T,\mathrm{miss}} > 12 \pm 1.2\,\mathrm{GeV}$, for low-$\gamma_0$ e^+p events;
- $P'_{T,\mathrm{miss}} > 25 \pm 2.5\,\mathrm{GeV}$, for low-$\gamma_0$ e^-p events;

where the $P_{T,\mathrm{miss}}$ and $P'_{T,\mathrm{miss}}$ cuts are described in Sect. 5.3 and Sect. 5.4, respectively. The selection thresholds are varied by the resolution of P_T, which is of the order of 10%. The uncertainty arising from these variations are up to $\sim 3\%$ in the lowest-x and highest y bins and up to $\sim 8\%$ in the lowest-Q^2 lowest-x bin of the double differential cross section in the e^+p data.

T2, track quantities

The second set of threshold variations, T2, is concerned with the selection thresholds on tracking variables:

- $\theta_{\mathrm{trk}}^{\mathrm{vtx}} > 15° + 18.5°$;
- $P_{T,\mathrm{trk}}^{\mathrm{vtx}} > 0.2 + 0.02\,\mathrm{GeV}$;
- $N_{\mathrm{trk}}^{\mathrm{good}} > 0.25 N_{\mathrm{trk}} - 5 \pm 1$;
- $N_{\mathrm{trk}}^{\mathrm{good}} > N_{\mathrm{trk}} - 5 \pm 1$, for e^-p events;
- $N_{\mathrm{trk}}^{\mathrm{good}} > 10 \pm 1$, for e^-p events;

The first two thresholds concern the definition of a "good" track and are described in Sect. 5.4. The $\theta_{\mathrm{trk}}^{\mathrm{vtx}}$ threshold is tightened to select only tracks passing six super-layers of the CTD instead of five, and the $P_{T,\mathrm{trk}}^{\mathrm{vtx}}$ thresholds was varied with a somewhat arbitrary 10%. Both the N_{trk} and $N_{\mathrm{trk}}^{\mathrm{good}}$ thresholds are also described in section Sect. 5.4 The additional threshold selection for the e^-p data is described in Sect. 5.4.1. The uncertainty arising from these variations is $\sim 4\%$ in the lowest-x bins. In the e^-p data the uncertainties are $\sim 12\%$ in the lowest-Q^2 bin and up to 17% in the lowest-Q^2 lowest-x bin.

6.5.4. Background Subtraction

The backgrounds discussed in Sect. 6.3 were subtracted in the cross section unfolding procedure. Hence, uncertainties in the normalisation or shapes of these backgrounds can bias the cross section measurement. The largest background contribution came from the direct and resolved photoproduction events. The contribution to the systematic error on the cross section due to the uncertainty of the normalisation is presented in this section.

Figures 6.4(a) and 6.4(c) show the P_T/E_T distribution for high-γ_0 events with $P_T < 20\,\text{GeV}$ for e^-p and e^+p, respectively. The arrows in the figures indicate the selection thresholds as applied in the CC event selection (see Sect. 5.7). Hence, only the background events with $P_T/E_T > 0.55$ were subtracted in the cross section unfolding. Below the P_T/E_T threshold, a large number of photoproduction events is observed in both e^-p and e^+p. The uncertainty in the normalisation of the direct and resolved photoproduction events was obtained by a χ^2 fit, using MINUIT [83], to the total P_T/E_T distribution, with the following function:

$$N_{\text{MC}} = \alpha(\beta f_{\text{dir}} + (1-\beta) f_{\text{res}}) + N_{\text{CC}} + N_{\text{other}} \tag{6.20}$$

where α and β are the fit parameters. Parameter α is the sum of all photoproduction events, i.e. the total photoproduction normalisation, N_{php}; Parameter β is the fraction of direct photoproduction events of the total number of photoproduction events, F_{dir}; N_{CC} is the total number of CC MC events and N_{other} is the sum of all other background MC events (NC DIS, charged lepton production and single W production); f_{dir} and f_{res} are defined as

$$f_{\text{dir},i} \equiv N_{\text{dir},i} / \sum_{i=\text{bin}} N_{\text{dir},i} \qquad f_{\text{res},i} \equiv N_{\text{res},i} / \sum_{i=\text{bin}} N_{\text{res},i}$$

where i denotes the histogram bin number. $N_{\text{dir},i}$ and $N_{\text{res},i}$ are the number of direct and resolved photoproduction events in histogram bin i, respectively. The sum runs over all histogram bins included in the fit. From the above the following χ^2-square definition is obtained

$$\chi^2 = \sum_{i=\text{bin}} \frac{(N_{\text{data},i} - N_{\text{MC},i})^2}{(\delta N_{\text{data},i})^2 + (\delta N_{\text{MC},i})^2} \tag{6.21}$$

where $N_{\text{data},i}$ is the number of data events in histogram bin i, and $N_{\text{MC},i}$ is the sum of the number of events from all MC simulations in histogram bin i, determined from (6.20). $\delta N_{\mathrm{data},i}$ and $\delta N_{\mathrm{MC},i}$ denote the statistical errors on $N_{\mathrm{data},i}$ and $N_{\mathrm{MC},i}$, respectively. (6.20) was chosen as the fit function, since it separates the relative normalisation between the direct and resolved photoproduction MC from the overall photoproduction MC normalisation. Therefore, it was possible to fit the normalisation, N_{php}, and the fraction of direct and resolved photoproduction, F_{dir}, separately.

First a fit was performed to determine N_{php}, with F_{dir} fixed at the values provided by the MC generator; this was followed by a fit of F_{dir} with N_{php} fixed at the fitted value. These fits were performed once in the P_T/E_T range $0.1-1.0$ and once in the range $0.25-0.8$. The results from the fits are listed in Table 6.1, and Figs. 6.4(b) and 6.4(d) show the χ^2/ndf distributions. From these distributions it is clear that no sensitivity for F_{dir} is observed in the P_T/E_T distributions. Hence, no contribution to the systematic error on the cross section measurement was obtained for the fraction of direct and resolved photoproduction.

The fit of N_{php} in both P_T/E_T regions for e^+p, resulted in an uncertainty of the normalisation of $\sim 10\%$. For e^-p, the fit of both N_{php} and F_{dir} failed in the larger P_T/E_T range $0.1-1.0$, due to a lack of statistics. This lack of statistics also influenced the fit for e^-p in the tighter P_T/E_T range $0.25-0.8$, resulting in a large uncertainty of the normalisation of $\sim 25\%$. Since no difference between the photoproduction background in e^-p and e^+p is expected, and the fits of the e^-p data were very much influenced by lack of statistics, the same uncertainty of the normalisation found for e^+p was applied for e^-p. To determine the contribution of the uncertainty on the cross section measurement due to the normalisation of photoproduction, the photoproduction background was varied up and down by 20%, corresponding to twice the value of the uncertainty given by the fit, in both e^-p and e^+p. The systematic error was than obtained by

$$\delta^{\pm}_{\mathrm{php}} = \frac{N_{\mathrm{nom}} - N_{\pm}}{N_{\mathrm{nom}}} \tag{6.22}$$

were N_{nom} is the number of MC events in a sample with the subtracted photoproduction background normalised to the generator cross section. $N_{\pm}$ is the number of MC events with the photoproduction background varied up and down, as described above. The systematic errors were typically less than 1%. Only in one of the lowest-Q^2 bins of the double differential cross section the systematic error was $\sim 4\%$.

The contribution to the cross section measurement from the other backgrounds (NC, charged lepton production and single W production) was very

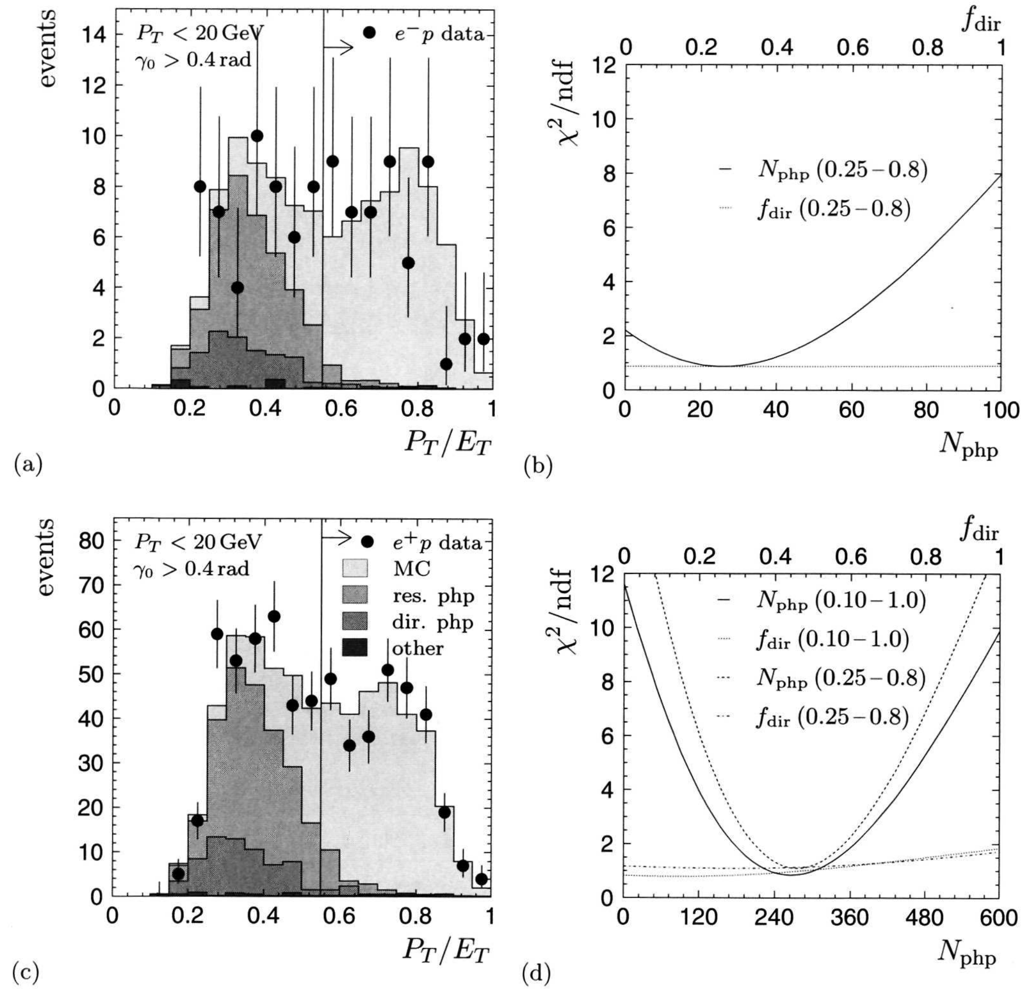

Figure 6.4. (a) The P_T/E_T distribution for events with high-γ_0 and $P_T <$ 20 GeV for e^-p and, (c) for e^+p. (b) The χ^2/ndf distributions of the four fits performed to the P_T/E_T distribution as function of the fraction of direct photoproduction of the fit (upper axis), and as function of the total number of photoprodcution events (lower axis) for e^-p and, (d) for e^+p.

small, and variations of the normalisation of these background by 100% resulted in variations in the cross section well below 0.5% in the full kinematic

Table 6.1. Results for the fit to the P_T/E_T distribution. The numbers for the nominal situation are not fitted but derived from the cross sections given by the MC generator. The fits to N_{php} and f_{dir} are performed separately, e.g. N_{php} is fitted while $f_{dir}$is fixed and vice versa.

fit condition	fit range	N_{php}	F_{dir}	χ^2/ndf
Nominal (e^-p)		38.9 ± 1.4	0.27 ± 0.07	
N_{php} fit	0.25 – 0.8	26.0 ± 6.8	0.27	9.6/11
F_{dir} fit	0.25 – 0.8	26.0	0.16 ± 0.48	9.0/11
Nominal (e^+p)		280.9 ± 7.4	0.31 ± 0.05	
N_{php} fit	0.10 – 1.0	265.8 ± 21.1	0.31	15.2/18
F_{dir} fit	0.10 – 1.0	265.8	0.14 ± 0.17	14.2/18
N_{php} fit	0.25 – 0.8	275.5 ± 22.7	0.31	12.1/11
F_{dir} fit	0.25 – 0.8	275.5	0.28 ± 0.28	12.0/11

range. Therefore the contribution to the total systematic uncertainty from the subtraction of these backgrounds was neglected.

6.5.5. Parton Distribution Functions

The Monte Carlo events used in unfolding the cross section were generated with the CTEQ5D [52] PDFs. The same PDFs were used in the calculation of the bin centring corrections. In this way a consistent unfolding of the cross section was achieved. The influence on the cross section from variations of the PDFs were investigated using the ZEUS-S NLO QCD fit [84] via the difference in acceptance. The Monte Carlo events were re-weighted to the total experimental uncertainty of the prediction of the cross sections evaluated from the ZEUS-S fit. Note that no HERA CC data is included in the fit. The cross sections were unfolded using the re-weighted MC, and compared with the nominal cross sections. The differences in the measured cross sections for the e^-p data were below 0.5% in the full kinematic region, and therefore the contribution to the total systematic error was neglected. For the e^+p data the differences were below 1% except for the highest Q^2 bin where it was −5% and the highest x bin where it was +4%. Hence, the effect of the uncertainty in the PDFs, δ_{PDF}, was included in the total systematic error for the e^+p data.

6.5.6. Effect of NLO QCD Corrections

The computer program DJANGOH [48] does not take into account contributions to the cross section from the longitudinal structure function, F_L, and NLO QCD corrections to xF_3 when generating Monte Carlo events. However, at high-y the contribution of F_L to the cross section is of the order of 10% [18]. In the calculation of the bin centring corrections the contribution of NLO QCD corrections were also neglected, yielding a consistent unfolding of the cross sections, and effects from neglecting the NLO QCD corrections can only originate from differences in the acceptance. The uncertainty is obtained by re-weighting the MC events to the ratio between the cross section calculated with and without NLO QCD corrections. The systematic errors, $\delta_{\rm QCD}$, were typically less than 1% for both e^-p and e^+p. The largest effect was observed in the e^+p data in the highest Q^2 bin where it was $\sim 6\%$ and in the highest x bin where is was $\sim 4\%$.

6.5.7. Energy Leakage

For an accurate measurement of the kinematic variables, it is important that the hadronic system is fully contained within the CAL. Energy leakage of the hadronic system out of the CAL can have an effect on the cross section measurement. The CAL is surrounded by the backing calorimeter, BAC (see Sect. 2.3.2), which was used to measure the effect of energy leakage of the CAL. It was found that 4% of the accepted events had a measurable energy leakage from the CAL into the BAC. The average energy fraction in the BAC w.r.t. to the total energy was 5%. Both the fraction of events with leakage and the average amount of leakage were well modelled by the MC simulation and the effect on the cross section measurement is negligible.

6.5.8. Vertex Finding Efficiency

A difference in the CTD vertex finding efficiency, $\mathcal{E}_{\rm CTD}$, between data and Monte Carlo can bias the measurement of the cross section. To obtain the $\mathcal{E}_{\rm CTD}$ in the γ_0 range of 0.0 – 0.6 rad the CC event selection was redone with the γ_0 threshold set to 0.6 rad (see Sect. 5.2). $\mathcal{E}_{\rm CTD}$ was determined as the ratio of events with a CTD vertex and all events passing the CC event selection (events in the forward direction always have a timing vertex). Figures 6.5(a) and 6.5(b) show the $\mathcal{E}_{\rm CTD}$ for the e^-p and e^+p data and MC as a function of γ_0 . The turn

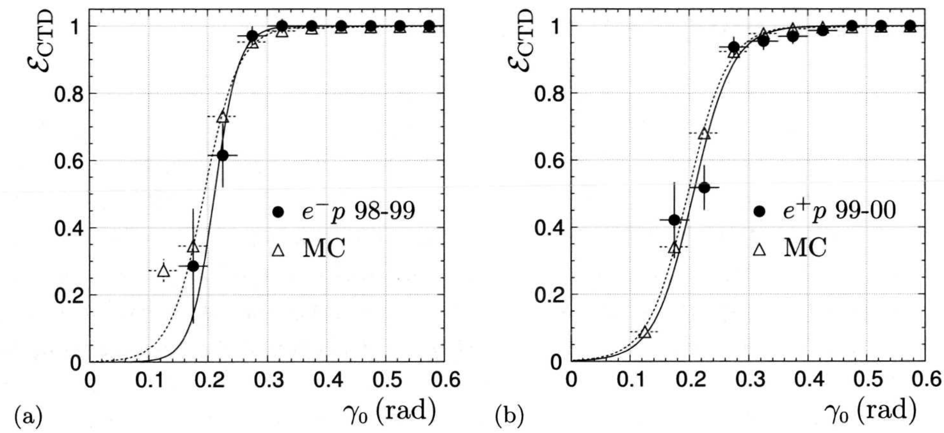

Figure 6.5. The CTD vertex finding efficiency as function of γ_0 for the (a) e^-p and (b) e^+p analysis. The solid dots represent the data events and the open triangles represent the MC events. Also shown are the turn on curves for data (solid line) and MC (dashed line) obtained from a fit.

on curves shown in Fig. 6.5 were obtained by a χ^2 fit to the function

$$\mathcal{E}_{\mathrm{CTD}} = \left(\frac{1}{2}\tanh\left(\frac{\gamma_0 - \alpha}{\beta}\right) + \frac{1}{2}\right)\epsilon, \tag{6.23}$$

with α, β and ϵ as free parameters. Parameter α is the turn on point, β is the slope and ϵ is the saturation value. It can been seen from the figure that good agreement is observed as γ_0 increases towards the 0.4 rad threshold where a CTD vertex is required in this analysis. Also it can be observed from the figure that the efficiency approaches 100% at the threshold of 0.4 rad for both e^-p and e^+p. Hence, the contribution from the CTD vertex finding efficiency to the systematic error is insignificant.

6.5.9. Vertex Distribution in Monte Carlo

The distribution of the Z position of the reconstructed vertex depends on the run period, due to changes of the beam conditions over time. The vertex distributions used in the Monte Carlo samples were corrected for these effects using the method described in Sect. 4.4. Changes in the measured cross section were found to be less than 0.5% and the contribution to the overall systematic uncertainty is insignificant.

6.5.10. Summary of the Systematic Uncertainties

To obtain the total systematic uncertainties the systematic uncertainties from each of the sources described in this section were added in quadrature for the positive and negative deviations from the nominal cross section values separately.

Figures B.1–B.6 show the various systematic checks described in the above sections for the single differential bins. The various systematic errors in all bins used in the analysis are listed in Tab. B.1 to B.8. Table 6.2 shows the systematic errors in the total cross section measurement for e^-p and e^+p charged current DIS in the kinematic region $Q^2 > 200\,\mathrm{GeV}^2$. The largest systematic uncertainty in e^-p came from the selection thresholds based on tracking and in e^+p from the QCD cascade modelling. Note that the largest error on the cross section measurements still came from the limited statistics.

Table 6.2. Uncertainties on the total cross section measurement for e^-p and e^+p charged current deep inelastic scattering in the kinematic region $Q^2 > 200\ GeV^2$.

source	error (%, e^-p)	error (%, e^+p)
calorimeter energy scale	$^{+0.34}_{-0.43}$	$^{+0.48}_{-0.26}$
QCD cascade model	±0.57	±1.08
selection thresholds, T1	±0.65	±0.25
selection thresholds, T2	±0.95	±0.40
php subtraction	$^{+0.18}_{-0.40}$	$^{+0.39}_{-0.68}$
PDF uncertainty	$^{+0.06}_{-0.10}$	±0.50
NLO QCD corrections	-0.57	-0.85
total systematic error	$^{+1.3}_{-1.5}$	$^{+1.4}_{-1.7}$
statistical error	±4.0	±2.6

The uncertainties on the measured total luminosity were 1.8% and 2.25% for the e^-p and e^+p data, respectively, and were not included in the total systematic uncertainty.

6.6. Summary

The binning of the kinematic range used in the measurement of the cross section and the unfolding strategy together with an overview of the various systematic uncertainties were presented in this chapter.

In the next chapter the final results for the charged current cross section for e^-p and e^+p data will be discussed.

Chapter 7

Results

7.1. Introduction

In this chapter the results for the charged current single differential cross section, the reduced cross section and total cross section will be presented for both e^-p and e^+p charged current DIS.

7.2. Total Cross Sections

The total cross sections for e^-p charged current DIS in the kinematic region $Q^2 > 200\,\mathrm{GeV}^2$ is

$$\sigma_{\mathrm{tot}}^{\mathrm{CC}}(Q^2 > 200\,\mathrm{GeV}^2) = 67.2 \pm 2.7\,(\mathrm{stat.})^{+0.9}_{-1.0}\,(\mathrm{syst.})\,\mathrm{pb},$$

and for the total cross section for e^+p CC DIS is

$$\sigma_{\mathrm{tot}}^{\mathrm{CC}}(Q^2 > 200\,\mathrm{GeV}^2) = 34.8 \pm 0.9\,(\mathrm{stat.})^{+0.5}_{-0.6}\,(\mathrm{syst.})\,\mathrm{pb},$$

where the first error is the statistical uncertainty and the second error is the total systematic uncertainty excluding the uncertainty in the measured luminosity of 1.8% (2.25%) for the e^-p (e^+p) data. These results are in good agreement with the SM predictions of $69.0^{+1.6}_{-1.3}\,\mathrm{pb}$ and $37.0^{+1.7}_{-0.8}\,\mathrm{pb}$ for the e^-p and e^+p data, respectively, evaluated using the ZEUS-S fit.

7.3. Single Differential Cross Sections

The charged current single differential cross sections $\mathrm{d}\sigma/\mathrm{d}Q^2$, $\mathrm{d}\sigma/\mathrm{d}x$ and $\mathrm{d}\sigma/\mathrm{d}y$ for the e^-p data and e^+p data for $Q^2 > 200\,\mathrm{GeV}^2$ are shown in Fig. 7.1, 7.2 and 7.3, respectively, and compiled in Table 7.1, 7.2 and 7.3. The Standard Model cross sections derived from (1.11) using the ZEUS-S [84] fit, the CTEQ6D [85] and the MRST(2001) [86] parameterisation of the PDFs are shown, together with the ratios of the measured cross sections and the SM cross section evaluated with the ZEUS-S fit. The PDF uncertainties are estimated from the ZEUS-S fit and are shown as the shaded bands in the figures.

The cross sections $\mathrm{d}\sigma/\mathrm{d}Q^2$ and $\mathrm{d}\sigma/\mathrm{d}x$ both drop by many orders of magnitude due to the effect of the W boson propagator and the decreasing quark density at large x. The ZEUS-S fit was based on fixed target DIS data obtained at low Q^2 ($< 100\,\mathrm{GeV}^2$) and from ZEUS high-Q^2 NC data. Note that no data presented in this thesis was included in the fits. The good description of the data by the SM prediction based on this fit confirms both the decomposition of the proton momentum into different quark flavours, specifically the down-quark contributions, and the evolution of parton distributions towards scales considerably larger than the W boson mass. At very large x and Q^2, the uncertainty in the prediction derived from the ZEUS-S fit, and also the global fits, reflects the lack of data constraining the d quark density.

Table 7.1. Values of the differential cross section, $\mathrm{d}\sigma/\mathrm{d}Q^2$, for the e^-p data and e^+p data. The first error of the measured cross section shows the statistical uncertainty; the second error shows the systematic uncertainty. The Standard Model expectation is evaluated using the CTEQ5D PDFs. Also listed are the value of Q^2 at which the cross sections are quoted.

Q^2_c	$\mathrm{d}\sigma(e^-p)/\mathrm{d}Q^2$ (pb/GeV^2)		$\mathrm{d}\sigma(e^+p)/\mathrm{d}Q^2$ (pb/GeV^2)	
(GeV^2)	measured	SM	measured	SM
280	$2.89 \pm 0.63\,^{+0.41}_{-0.43} \cdot 10^{-2}$	$3.88 \cdot 10^{-2}$	$2.85 \pm 0.22\,^{+0.17}_{-0.18} \cdot 10^{-2}$	$3.07 \cdot 10^{-2}$
530	$2.34 \pm 0.43\,^{+0.15}_{-0.16} \cdot 10^{-2}$	$2.82 \cdot 10^{-2}$	$1.81 \pm 0.13\,^{+0.08}_{-0.07} \cdot 10^{-2}$	$2.07 \cdot 10^{-2}$
950	$2.00 \pm 0.23\,^{+0.12}_{-0.11} \cdot 10^{-2}$	$1.95 \cdot 10^{-2}$	$1.30 \pm 0.08\,^{+0.04}_{-0.05} \cdot 10^{-2}$	$1.29 \cdot 10^{-2}$
1700	$1.18 \pm 0.11\,^{+0.05}_{-0.05} \cdot 10^{-2}$	$1.22 \cdot 10^{-2}$	$7.16 \pm 0.41\,^{+0.15}_{-0.13} \cdot 10^{-3}$	$6.93 \cdot 10^{-3}$
3000	$6.64 \pm 0.57\,^{+0.14}_{-0.16} \cdot 10^{-3}$	$6.68 \cdot 10^{-3}$	$2.90 \pm 0.19\,^{+0.07}_{-0.07} \cdot 10^{-3}$	$3.07 \cdot 10^{-3}$
5300	$3.04 \pm 0.28\,^{+0.11}_{-0.09} \cdot 10^{-3}$	$3.04 \cdot 10^{-3}$	$1.07 \pm 0.09\,^{+0.03}_{-0.03} \cdot 10^{-3}$	$1.02 \cdot 10^{-3}$
9500	$1.24 \pm 0.13\,^{+0.04}_{-0.05} \cdot 10^{-3}$	$1.05 \cdot 10^{-3}$	$2.20 \pm 0.29\,^{+0.16}_{-0.17} \cdot 10^{-4}$	$2.19 \cdot 10^{-4}$
17000	$2.37 \pm 0.45\,^{+0.13}_{-0.13} \cdot 10^{-4}$	$2.55 \cdot 10^{-4}$	$2.05\,^{+0.82}_{-0.61}\,^{+0.26}_{-0.24} \cdot 10^{-5}$	$2.70 \cdot 10^{-5}$
30000	$2.86\,^{+1.54}_{-1.05}\,^{+0.36}_{-0.32} \cdot 10^{-5}$	$3.70 \cdot 10^{-5}$	$2.12\,^{+2.06}_{-1.15}\,^{+0.60}_{-0.59} \cdot 10^{-6}$	$1.48 \cdot 10^{-6}$

Table 7.2. Values of the differential cross section, $\mathrm{d}\sigma/\mathrm{d}x$, for the e^-p data and e^+p data. The first error of the measured cross section shows the statistical uncertainty; the second error shows the systematic uncertainty. The Standard Model expectation is evaluated using the CTEQ5D PDFs. Also listed are the value of x at which the cross sections are quoted.

x_c	$\mathrm{d}\sigma(e^-p)/\mathrm{d}x$ (pb)		$\mathrm{d}\sigma(e^+p)/\mathrm{d}x$ (pb)	
	measured	SM	measured	SM
0.0150	$6.26 \pm 1.05\,^{+0.37}_{-0.38} \cdot 10^2$	$5.97 \cdot 10^2$	$4.58 \pm 0.36\,^{+0.35}_{-0.34} \cdot 10^2$	$4.72 \cdot 10^2$
0.0320	$3.97 \pm 0.45\,^{+0.17}_{-0.17} \cdot 10^2$	$4.60 \cdot 10^2$	$2.92 \pm 0.16\,^{+0.04}_{-0.04} \cdot 10^2$	$3.14 \cdot 10^2$
0.0680	$2.79 \pm 0.22\,^{+0.05}_{-0.05} \cdot 10^2$	$3.00 \cdot 10^2$	$1.59 \pm 0.08\,^{+0.02}_{-0.02} \cdot 10^2$	$1.64 \cdot 10^2$
0.1300	$1.91 \pm 0.15\,^{+0.03}_{-0.03} \cdot 10^2$	$1.76 \cdot 10^2$	$7.22 \pm 0.45\,^{+0.16}_{-0.15} \cdot 10^1$	$7.56 \cdot 10^1$
0.2400	$8.30 \pm 0.75\,^{+0.25}_{-0.25} \cdot 10^1$	$8.22 \cdot 10^1$	$3.01 \pm 0.23\,^{+0.11}_{-0.10} \cdot 10^1$	$2.71 \cdot 10^1$
0.4200	$2.48 \pm 0.35\,^{+0.10}_{-0.11} \cdot 10^1$	$2.36 \cdot 10^1$	$5.98 \pm 0.90\,^{+0.40}_{-0.41} \cdot 10^0$	$5.54 \cdot 10^0$
0.6500	$2.20\,^{+2.14}_{-1.20}\,^{+0.40}_{-0.30} \cdot 10^0$	$2.80 \cdot 10^0$	$4.43\,^{+5.84}_{-2.87}\,^{+1.07}_{-0.82} \cdot 10^{-1}$	$3.78 \cdot 10^{-1}$

Table 7.3. Values of the differential cross section, $\mathrm{d}\sigma/\mathrm{d}y$, for the e^-p data and e^+p data. The first error of the measured cross section shows the statistical uncertainty; the second error shows the systematic uncertainty. The Standard Model expectation is evaluated using the CTEQ5D PDFs. Also listed are the value of y at which the cross sections are quoted.

y_c	$\mathrm{d}\sigma(e^-p)/\mathrm{d}y$ (pb)		$\mathrm{d}\sigma(e^+p)/\mathrm{d}y$ (pb)	
	measured	SM	measured	SM
0.05	$1.34 \pm 0.17\,^{+0.03}_{-0.03} \cdot 10^2$	$1.51 \cdot 10^2$	$7.79 \pm 0.48\,^{+0.27}_{-0.29} \cdot 10^1$	$8.14 \cdot 10^1$
0.15	$1.23 \pm 0.10\,^{+0.03}_{-0.03} \cdot 10^2$	$1.15 \cdot 10^2$	$6.86 \pm 0.37\,^{+0.10}_{-0.10} \cdot 10^1$	$6.55 \cdot 10^1$
0.27	$8.84 \pm 0.73\,^{+0.32}_{-0.33} \cdot 10^1$	$8.64 \cdot 10^1$	$4.46 \pm 0.25\,^{+0.18}_{-0.18} \cdot 10^1$	$4.79 \cdot 10^1$
0.41	$5.76 \pm 0.60\,^{+0.20}_{-0.19} \cdot 10^1$	$6.58 \cdot 10^1$	$3.36 \pm 0.23\,^{+0.04}_{-0.03} \cdot 10^1$	$3.47 \cdot 10^1$
0.55	$5.18 \pm 0.58\,^{+0.12}_{-0.12} \cdot 10^1$	$5.25 \cdot 10^1$	$2.58 \pm 0.21\,^{+0.08}_{-0.08} \cdot 10^1$	$2.63 \cdot 10^1$
0.69	$5.00 \pm 0.62\,^{+0.16}_{-0.21} \cdot 10^1$	$4.35 \cdot 10^1$	$2.15 \pm 0.22\,^{+0.10}_{-0.09} \cdot 10^1$	$2.10 \cdot 10^1$
0.83	$3.20 \pm 0.56\,^{+0.30}_{-0.25} \cdot 10^1$	$3.74 \cdot 10^1$	$1.53 \pm 0.22\,^{+0.12}_{-0.12} \cdot 10^1$	$1.78 \cdot 10^1$

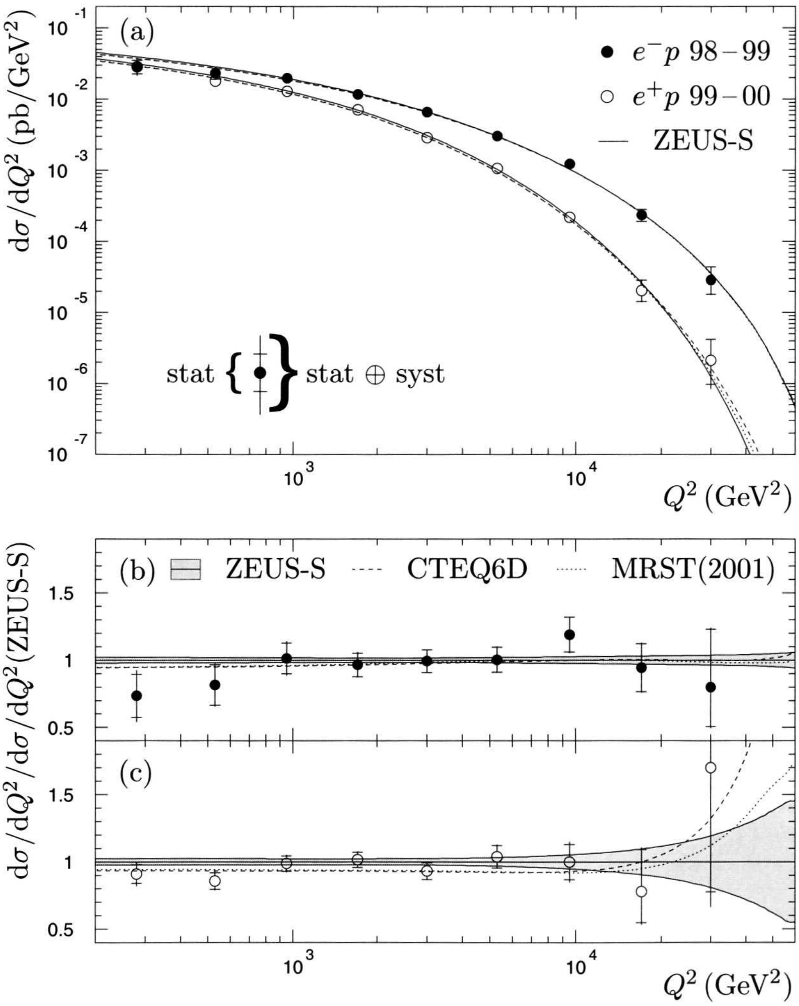

Figure 7.1. (a) The e^-p (solid points) and e^+p (open circles) CC DIS Born cross section, $d\sigma/dQ^2$, for data and the Standard Model expectation evaluated using the ZEUS-S, the CTEQ6D and the MRST(2001) PDFs. The statistical uncertainties are indicated by the inner error bars (delimited by horizontal lines) and the full error bars show the total uncertainty obtained by adding the statistical and systematic contributions in quadrature. (b) The ratio of the measured cross section, $d\sigma/dQ^2$, to the Standard Model expectation evaluated using the ZEUS-S fit for the e^-p data and (c) for the e^+p data. The shaded band shows the uncertainties from the ZEUS-S fit.

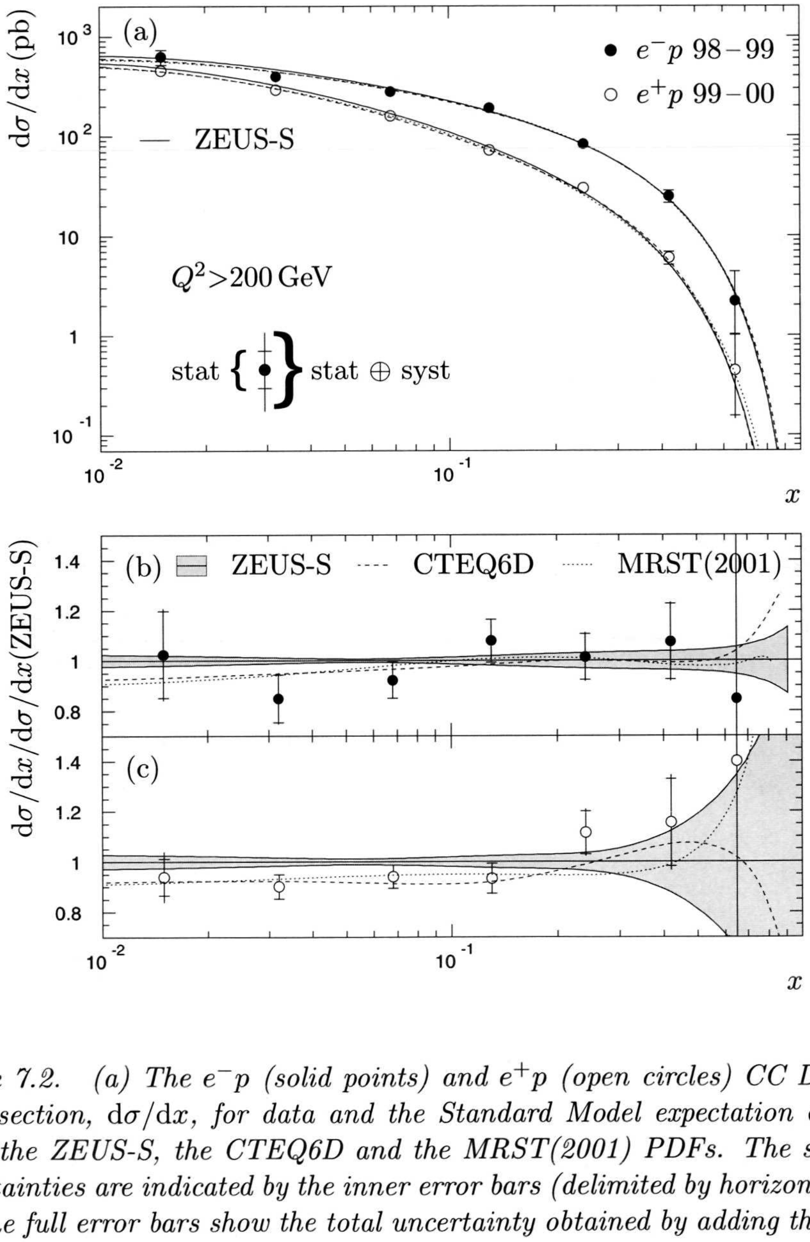

Figure 7.2. (a) The e^-p (solid points) and e^+p (open circles) CC DIS Born cross section, $\mathrm{d}\sigma/\mathrm{d}x$, for data and the Standard Model expectation evaluated using the ZEUS-S, the CTEQ6D and the MRST(2001) PDFs. The statistical uncertainties are indicated by the inner error bars (delimited by horizontal lines) and the full error bars show the total uncertainty obtained by adding the statistical and systematic contributions in quadrature. (b) The ratio of the measured cross section, $\mathrm{d}\sigma/\mathrm{d}x$, to the Standard Model expectation evaluated using the ZEUS-S fit for the e^-p data and (c) for the e^+p data. The shaded band shows the uncertainties from the ZEUS-S fit.

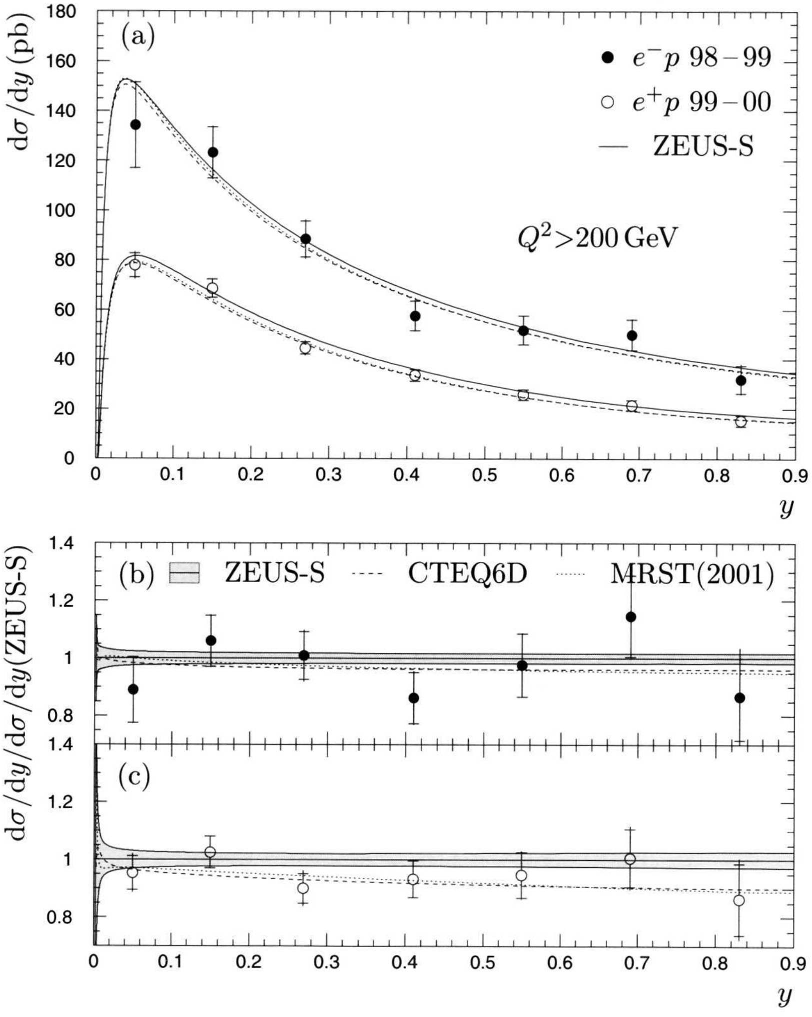

Figure 7.3. (a) The e^-p (solid points) and e^+p (open circles) CC DIS Born cross section, $\mathrm{d}\sigma/\mathrm{d}y$, for data and the Standard Model expectation evaluated using the ZEUS-S, the CTEQ6D and the MRST(2001) PDFs. The statistical uncertainties are indicated by the inner error bars (delimited by horizontal lines) and the full error bars show the total uncertainty obtained by adding the statistical and systematic contributions in quadrature. (b) The ratio of the measured cross section, $\mathrm{d}\sigma/\mathrm{d}y$, to the Standard Model expectation evaluated using the ZEUS-S fit for the e^-p data and (c) for the e^+p data. The shaded band shows the uncertainties from the ZEUS-S fit.

7.4. Reduced Cross Sections

The reduced double differential cross section, $\tilde{\sigma}$, is defined by

$$\tilde{\sigma} = \left[\frac{G_F^2}{2\pi x} \left(\frac{M_W^2}{M_W^2 + Q^2} \right)^2 \right]^{-1} \frac{\mathrm{d}^2\sigma}{\mathrm{d}x\mathrm{d}Q^2}, \qquad (7.1)$$

where M_W is the mass of the W boson and G_F the Fermi coupling constant. At first order in QCD, $\tilde{\sigma}$ for $e^-p \to \nu_e X$ depends on the quark momentum distribution as follows

$$\tilde{\sigma}(e^-p \to \nu_e X) = x \left[u + c + (1-y)^2(\bar{d} + \bar{s}) \right], \qquad (7.2)$$

and for $e^+p \to \bar{\nu}_e X$ as

$$\tilde{\sigma}(e^+p \to \bar{\nu}_e X) = x \left[\bar{u} + \bar{c} + (1-y)^2(d + s) \right], \qquad (7.3)$$

The reduced cross sections are displayed as functions of x for the e^-p data and e^+p data in Figs. 7.4 and 7.5, respectively, as functions of Q^2 for the e^-p data and e^+p data in Figs. 7.6 and 7.7, and are compiled in Table 7.4. The predictions of (1.11), evaluated using the ZEUS-S fit, the CTEQ6D and the MRST(2001) PDFs give a good description of the data. The contributions from the PDF combinations $(u + c)$ and $(\bar{d} + \bar{s})$ to $\tilde{\sigma}(e^-p \to \nu_e X)$ and $(d + s)$ and $(\bar{u} + \bar{c})$ to $\tilde{\sigma}(e^+p \to \bar{\nu}_e X)$, obtained from the ZEUS-S fit, are shown separately in Figs. 7.4 and 7.5, respectively.

7.5. Helicity Study

The W boson couples only to left-handed fermions and right-handed anti-fermions. Therefore the angular distribution of the quark in e^-q scattering and the antiquark in $e^+\bar{q}$ scattering will be isotropic ($l = 0$). On the other hand the distribution of the quark in e^+q scattering and the antiquark in $e^-\bar{q}$ scattering will exhibit a $1/4(1 + \cos\theta^*)^2$ behaviour ($l = 1$). The quark scattering angle in the electron quark centre-of-mass, θ^*, is related to y through $(1-y) = 1/2(1+\cos\theta^*)$. The helicity structure of CC interactions can be illustrated by plotting the reduced double differential cross section of (7.2) and (7.3) versus $(1-y)^2$ in bins of x (see Sect. 1.3). In the region of approximate scaling, i.e. $x \sim 0.1$, this yields a straight line. At leading order in QCD in e^-p CC DIS, the intercept of this line gives the $(u + c)$ contribution, while the slope

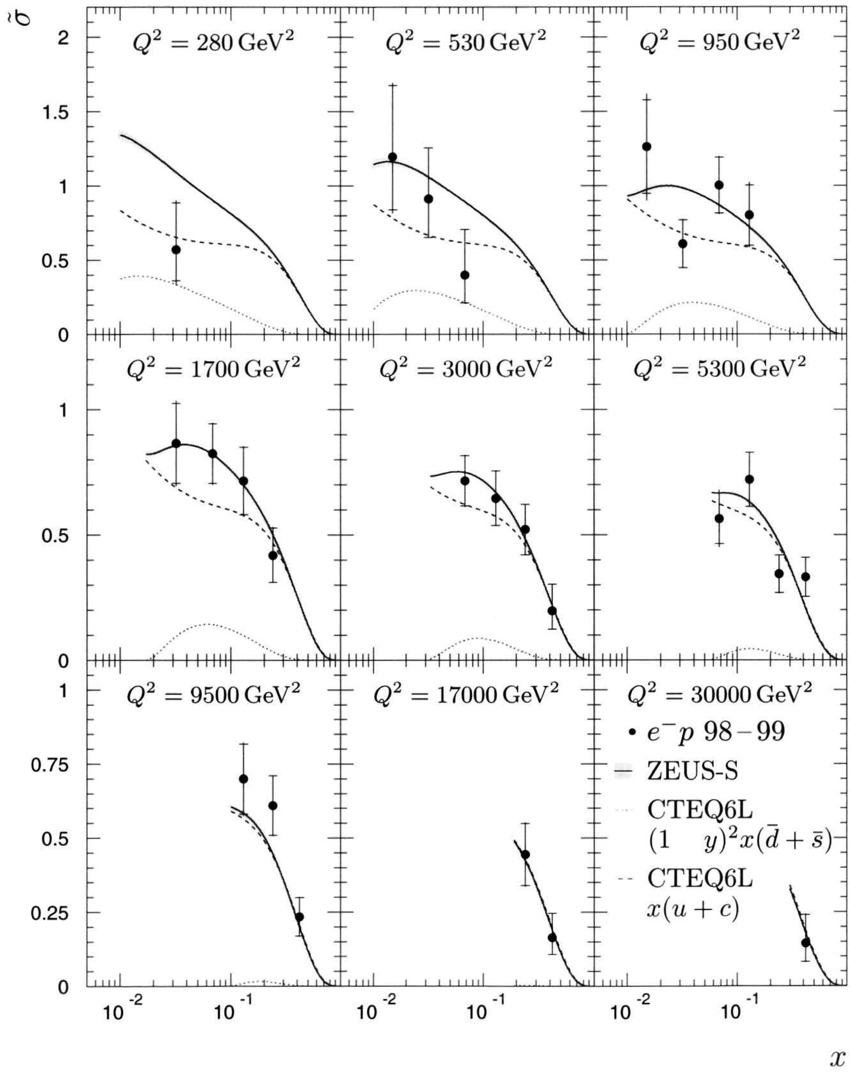

Figure 7.4. The reduced cross section, $\tilde{\sigma}$, as a function of x, for different values of Q^2 for the e^-p data. The data are shown as the filled points, the statistical uncertainties are indicated by the inner error bars (delimited by horizontal lines) and the full error bars show the total uncertainty. The expectation of the Standard Model evaluated using the ZEUS-S fit is shown as a solid line. The shaded band shows the uncertainties from the ZEUS-S fit. The separate contributions of the PDF combinations $(1-y)^2x(\bar{d}+\bar{s})$ and $x(u+c)$, obtained from the CTEQ6L leading order QCD fit, are shown by the dotted and dashed lines, respectively.

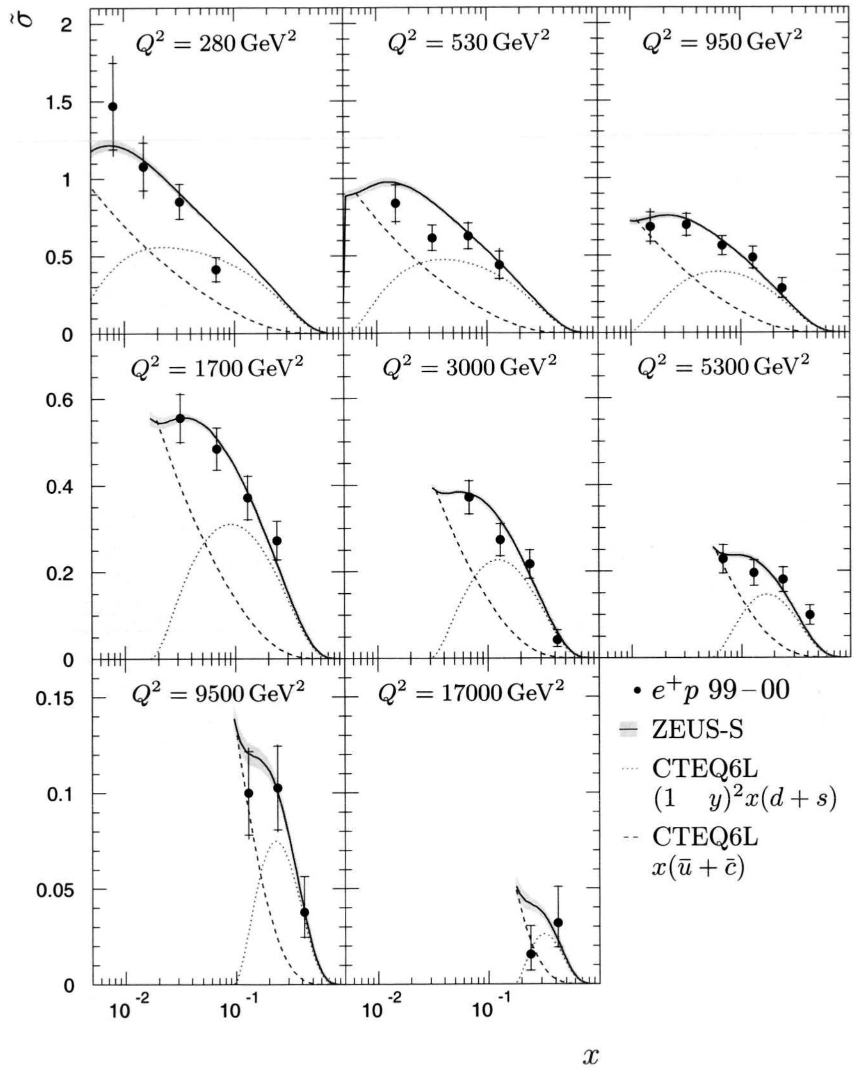

Figure 7.5. The reduced cross section, $\tilde{\sigma}$, as a function of x, for different values of Q^2 for the e^+p data. The data are shown as the filled points, the statistical uncertainties are indicated by the inner error bars (delimited by horizontal lines) and the full error bars show the total uncertainty. The expectation of the Standard Model evaluated using the ZEUS-S fit is shown as a solid line. The shaded band shows the uncertainties from the ZEUS-S fit. The separate contributions of the PDF combinations $(1-y)^2x(d+s)$ and $x(\bar{u}+\bar{c})$, obtained from the CTEQ6L leading order QCD fit, are shown by the dotted and dashed lines, respectively.

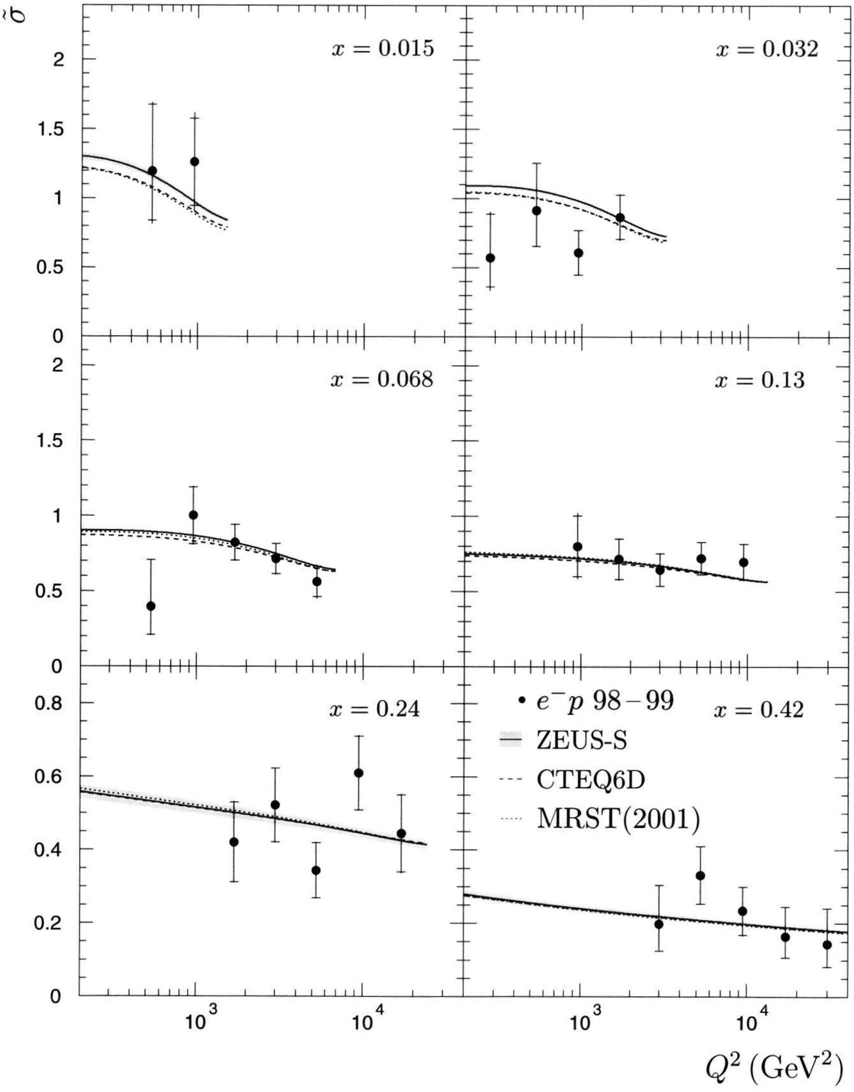

Figure 7.6. The reduced cross section, $\tilde{\sigma}$, as a function of Q^2, for different fixed values of x for the e^-p data. The data are shown as the filled points, the statistical uncertainties are indicated by the inner error bars (delimited by horizontal lines) and the full error bars show the total uncertainty obtained by adding the statistical and systematic contributions in quadrature. The expectation of the Standard Model evaluated using the ZEUS-S, the CTEQ6D and the MRST(2001) PDFs is shown by the solid, dashed and dotted lines, respectively. The shaded band shows the uncertainty from the ZEUS-S fit.

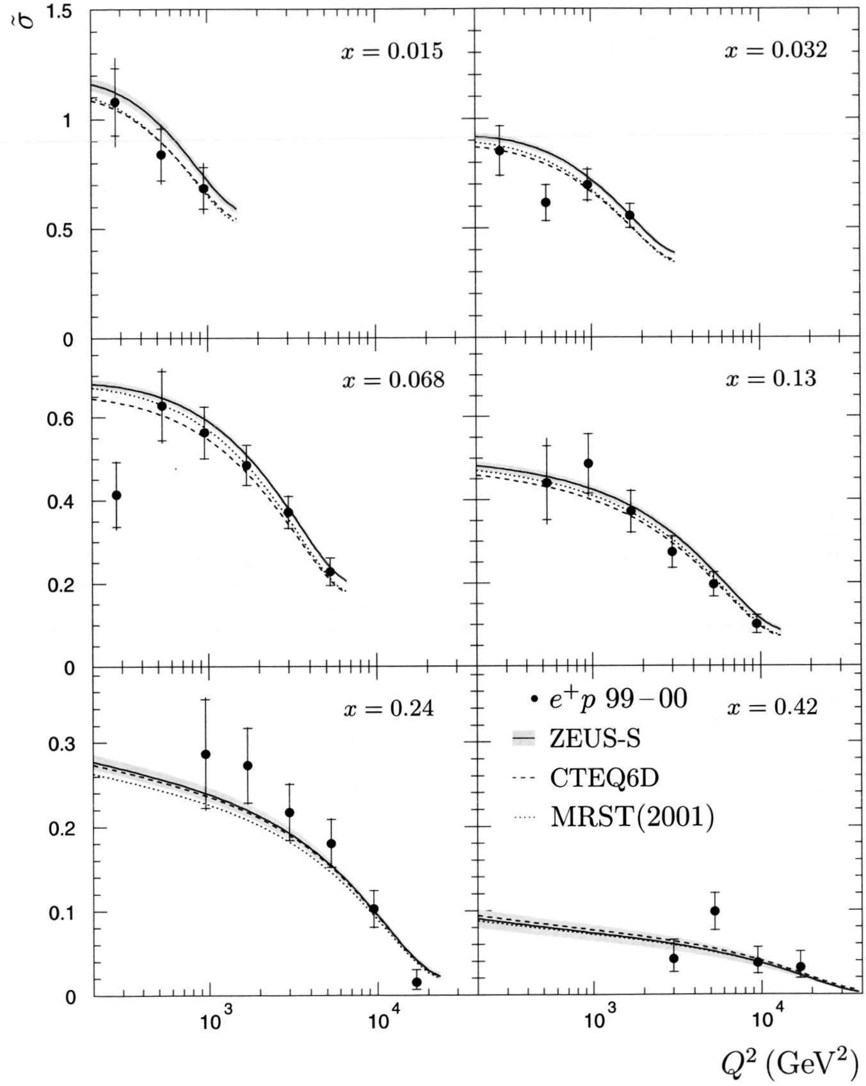

Figure 7.7. The reduced cross section, $\tilde{\sigma}$, as a function of Q^2, for different fixed values of x for the e^+p data. The data are shown as the filled points, the statistical uncertainties are indicated by the inner error bars (delimited by horizontal lines) and the full error bars show the total uncertainty obtained by adding the statistical and systematic contributions in quadrature. The expectation of the Standard Model evaluated using the ZEUS-S, the CTEQ6D and the MRST(2001) PDFs is shown by the solid, dashed and dotted lines, respectively. The shaded band shows the uncertainty from the ZEUS-S fit.

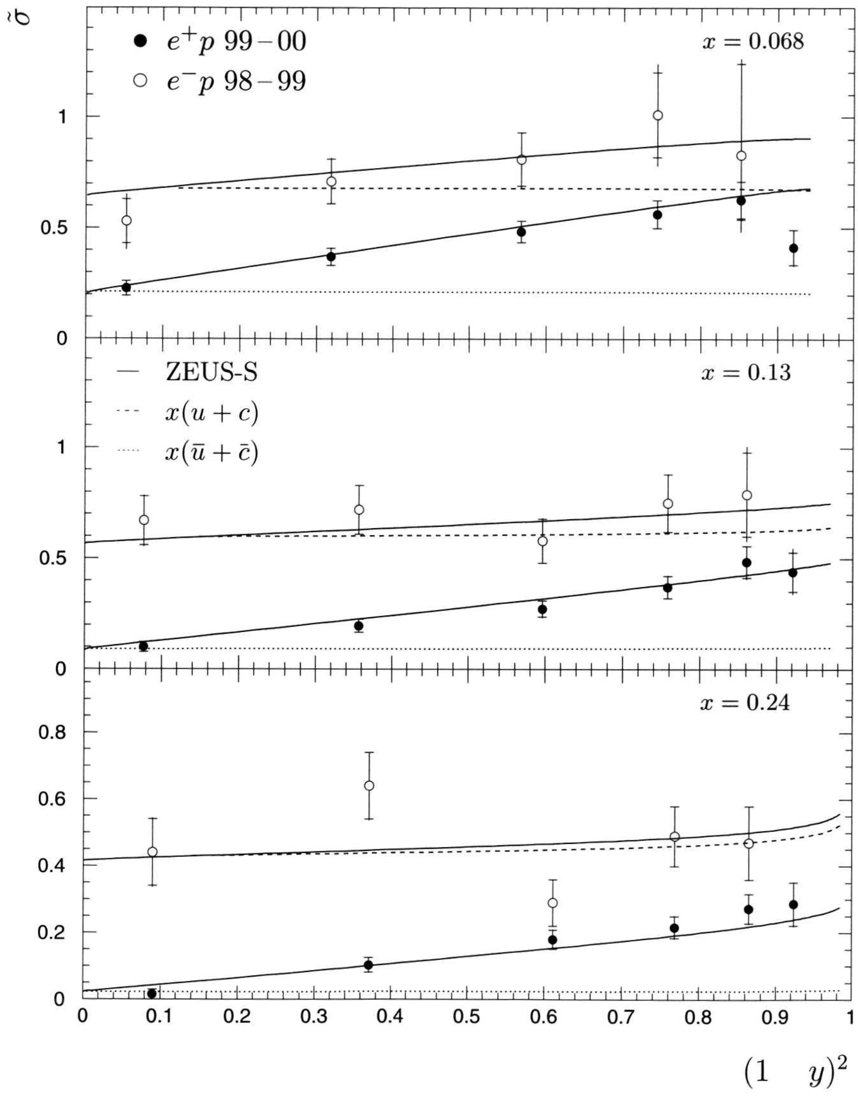

Figure 7.8. The reduced cross section, $\tilde{\sigma}$, as a function of $(1-y)^2$, for different fixed values of x, for e^+p (solid points) and e^-p (open circles) data. The data are shown as the points, the statistical uncertainties are indicated by the inner error bars (delimited by horizontal lines) and the full error bars show the total uncertainty obtained by adding the statistical and systematic contributions in quadrature. The expectation of the Standard Model evaluated using the ZEUS-S fit is shown as a solid line. The contributions of the PDF combinations $x(u+c)$ and $x(\bar{u}+\bar{c})$ are shown by the dashed and dotted lines, respectively

gives the $(\bar{d}+\bar{s})$ contribution, and in e^+p CC DIS, the intercept of this line gives the $(\bar{u}+\bar{c})$ contribution, while the slope gives the $(d+s)$ contribution.

Figure 7.8 shows $\tilde{\sigma}$ as a function of $(1-y)^2$ for the e^-p data, compared to the e^+p data. At large x, e^-p CC DIS is sensitive to the valence part of $u(x, Q^2)$, while e^+p CC DIS is sensitive to the valence part of $d(x, Q^2)$. The data agree with the expectation of the SM evaluated using the ZEUS-S fit.

Note that scaling violation can be observed in the theoretical prediction as $(1-y)^2$ approaches one.

7.6. Conclusions

In this chapter the charged current single differential cross sections were presented for e^-p and e^+p DIS data. In addition, the helicity structure of the weak interaction was verified.

The e^-p CC DIS results presented in this thesis show a large improvement over formerly published results [87] based on $0.82\,\text{pb}^{-1}$. The single differential cross sections are determined in finer bins and both the statistical uncertainties and the total systematic uncertainties were improved at high-Q^2. Furthermore, the differential cross section has been measured in bins of x and Q^2 and the reduced cross section, $\tilde{\sigma}(e^-p)$, was measured for the first time. The e^+p CC DIS results are improved compared to previous results [88] due to the larger data sample and a better analysis of the systematic uncertainties in this measurement. The Standard Model predictions are evaluated using the NLO QCD fits and are in good agreement with the presented measurements.

Recently, the impact of the ZEUS data has been explored by making a fit using ZEUS data only [84]. The ZEUS charged current e^+p data from 1994 – 1997 [89], and the charged and neutral current e^-p data from the 1998 and 1999 runs [90] were used, together with the 1996 and 1997 e^+p neutral current data [91], to make an extraction of the parton density functions independently of other experiments. This fit is called ZEUS-O. Note, that the e^+p charged current measurements presented in this thesis were not used in this fit since the analysis was not finished then.

These high-Q^2 data are very well described by the ZEUS-S fit, as illustrated in Figs. 7.1–7.8. However, in the ZEUS-O fit these additional data sets were used instead of the fixed-target data to constrain the valence distributions. The valence distributions extracted from the ZEUS-O fit are shown in Fig. 7.9(a). They are determined to a precision about a factor of two worse than in the

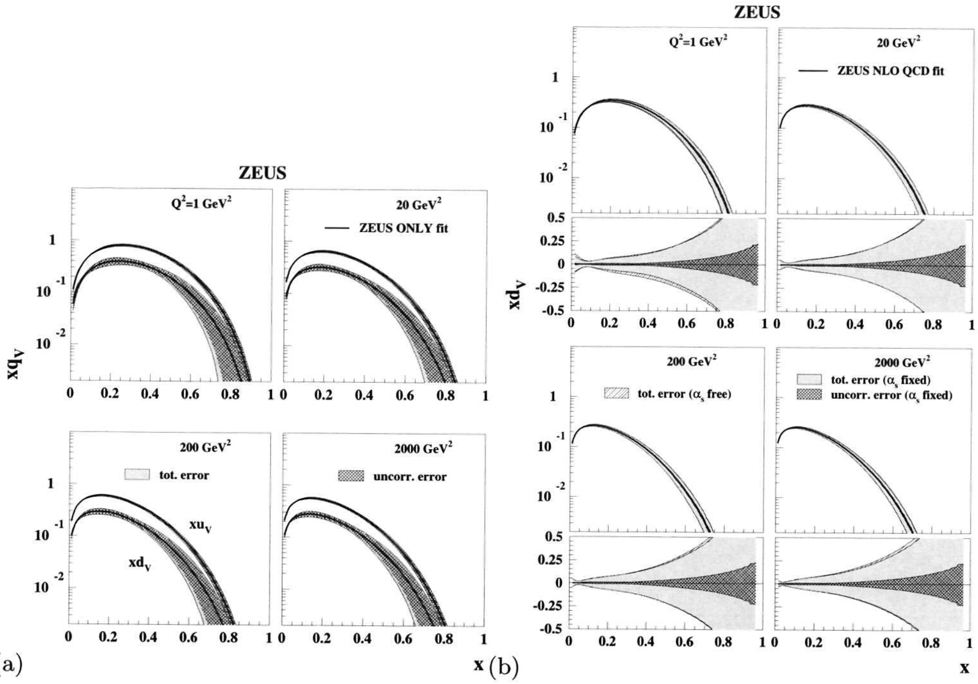

Figure 7.9. (a) The xu_v and xd_v distributions from the ZEUS-O NLO QCD fit in various Q^2 bins. The error bands show the uncertainty from statistical and other uncorrelated sources separately from the total uncertainty including correlated systematic uncertainties. The value of $\alpha_s(M_Z^2) = 0.118$ is fixed. (b) The xd_v distribution from the ZEUS-S NLO QCD fit. The cross-hatched error bands show the statistical and uncorrelated systematic uncertainty, the grey error bands show the total experimental uncertainty including correlated systematic uncertainties (both evaluated from the ZEUS-S fit). The uncertainties on these distributions are shown beneath each distribution as fractional differences from the central value.

ZEUS-S fit. The u-valence distribution is well determined; however, the d-valence distribution is much more poorly determined. In the ZEUS-O fit, the d-valence distribution is determined by the high-Q^2 e^+p charged current data. In contrast in the ZEUS-S fit the d-valence distribution is determined by the deuterium fixed-target data. Recently it has been suggested that such measurements are subject to significant uncertainty from deuteron binding corrections [92]. The ZEUS-O extraction does not suffer this uncertainty. It produces a larger d-valence distribution at high-x than the ZEUS-S fit, as can be seen by comparison with Fig. 7.9(b), but there is no disagreement within the limited statistical precision of the current high-Q^2 data.

In the near future HERA will, after a luminosity upgrade, produce a much larger number of charged current events which will reduce the statistical error considerably, especially in the interesting region of high-Q^2 and high-x. The increase in data and developments in the area of QCD fits provide an excellent basis for a thorough understanding of the proton and QCD in the future.

Table 7.4. Values of the reduced cross section, $\tilde{\sigma}$, for the e^-p data and e^+p data. The first and second errors of the measured cross section show the statistical and systematic uncertainties, respectively. The Standard Model expectation is evaluated using the CTEQ5D PDFs. Also listed are the value of Q^2 and x at which the cross sections are quoted.

Q^2_c	x_c	$\tilde{\sigma}(e^-p)$		$\tilde{\sigma}(e^+p)$	
(GeV^2)		measured	SM	measured	SM
280	0.008			$1.47 \pm 0.28\,^{+0.17}_{-0.16} \cdot 10^{0}$	$1.16 \cdot 10^{0}$
280	0.032	$5.72\,^{+3.15}_{-2.10}\,^{+1.06}_{-1.11} \cdot 10^{-1}$	$1.07 \cdot 10^{0}$	$1.08 \pm 0.15\,^{+0.13}_{-0.14} \cdot 10^{0}$	$1.07 \cdot 10^{0}$
280	0.032			$8.52 \pm 1.12\,^{+0.39}_{-0.34} \cdot 10^{-1}$	$8.78 \cdot 10^{-1}$
280	0.068			$4.14 \pm 0.78\,^{+0.18}_{-0.33} \cdot 10^{-1}$	$6.63 \cdot 10^{-1}$
530	0.015	$1.20\,^{+0.48}_{-0.36}\,^{+0.13}_{-0.14} \cdot 10^{0}$	$1.11 \cdot 10^{0}$	$8.39 \pm 1.18\,^{+0.68}_{-0.67} \cdot 10^{-1}$	$9.22 \cdot 10^{-1}$
530	0.032	$9.13\,^{+3.44}_{-2.58}\,^{+0.25}_{-0.40} \cdot 10^{-1}$	$1.03 \cdot 10^{0}$	$6.15 \pm 0.82\,^{+0.27}_{-0.27} \cdot 10^{-1}$	$8.16 \cdot 10^{-1}$
530	0.068	$3.99\,^{+3.08}_{-1.87}\,^{+0.44}_{-0.46} \cdot 10^{-1}$	$8.81 \cdot 10^{-1}$	$6.28 \pm 0.83\,^{+0.39}_{-0.34} \cdot 10^{-1}$	$6.33 \cdot 10^{-1}$
530	0.130			$4.40 \pm 0.89\,^{+0.62}_{-0.45} \cdot 10^{-1}$	$4.50 \cdot 10^{-1}$
950	0.015	$1.26 \pm 0.31\,^{+0.17}_{-0.18} \cdot 10^{0}$	$9.55 \cdot 10^{-1}$	$6.85 \pm 0.94\,^{+0.68}_{-0.66} \cdot 10^{-1}$	$7.19 \cdot 10^{-1}$
950	0.032	$6.09 \pm 1.62\,^{+0.33}_{-0.23} \cdot 10^{-1}$	$9.59 \cdot 10^{-1}$	$6.97 \pm 0.70\,^{+0.40}_{-0.39} \cdot 10^{-1}$	$7.03 \cdot 10^{-1}$
950	0.068	$1.00 \pm 0.19\,^{+0.06}_{-0.06} \cdot 10^{0}$	$8.55 \cdot 10^{-1}$	$5.63 \pm 0.62\,^{+0.12}_{-0.17} \cdot 10^{-1}$	$5.80 \cdot 10^{-1}$
950	0.130	$8.02 \pm 2.02\,^{+0.92}_{-0.79} \cdot 10^{-1}$	$7.16 \cdot 10^{-1}$	$4.86 \pm 0.71\,^{+0.18}_{-0.35} \cdot 10^{-1}$	$4.21 \cdot 10^{-1}$
950	0.240			$2.87 \pm 0.64\,^{+0.20}_{-0.19} \cdot 10^{-1}$	$2.41 \cdot 10^{-1}$
1700	0.032	$8.66 \pm 1.60\,^{+0.58}_{-0.59} \cdot 10^{-1}$	$8.41 \cdot 10^{-1}$	$5.55 \pm 0.55\,^{+0.19}_{-0.20} \cdot 10^{-1}$	$5.36 \cdot 10^{-1}$
1700	0.068	$8.25 \pm 1.19\,^{+0.36}_{-0.35} \cdot 10^{-1}$	$8.09 \cdot 10^{-1}$	$4.84 \pm 0.48\,^{+0.10}_{-0.05} \cdot 10^{-1}$	$4.93 \cdot 10^{-1}$
1700	0.130	$7.16 \pm 1.34\,^{+0.38}_{-0.49} \cdot 10^{-1}$	$6.93 \cdot 10^{-1}$	$3.71 \pm 0.50\,^{+0.19}_{-0.17} \cdot 10^{-1}$	$3.77 \cdot 10^{-1}$
1700	0.240	$4.20 \pm 1.09\,^{+0.29}_{-0.17} \cdot 10^{-1}$	$5.04 \cdot 10^{-1}$	$2.73 \pm 0.44\,^{+0.10}_{-0.14} \cdot 10^{-1}$	$2.20 \cdot 10^{-1}$
3000	0.068	$7.16 \pm 1.00\,^{+0.29}_{-0.32} \cdot 10^{-1}$	$7.41 \cdot 10^{-1}$	$3.71 \pm 0.39\,^{+0.13}_{-0.13} \cdot 10^{-1}$	$3.67 \cdot 10^{-1}$
3000	0.130	$6.46 \pm 1.08\,^{+0.27}_{-0.22} \cdot 10^{-1}$	$6.64 \cdot 10^{-1}$	$2.73 \pm 0.37\,^{+0.14}_{-0.14} \cdot 10^{-1}$	$3.11 \cdot 10^{-1}$
3000	0.240	$5.22 \pm 1.01\,^{+0.12}_{-0.17} \cdot 10^{-1}$	$4.86 \cdot 10^{-1}$	$2.17 \pm 0.33\,^{+0.11}_{-0.09} \cdot 10^{-1}$	$1.93 \cdot 10^{-1}$
3000	0.420	$1.98\,^{+1.07}_{-0.73}\,^{+0.11}_{-0.10} \cdot 10^{-1}$	$2.24 \cdot 10^{-1}$	$4.24\,^{+2.29}_{-1.57}\,^{+0.23}_{-0.18} \cdot 10^{-2}$	$6.39 \cdot 10^{-2}$
5300	0.068	$5.65 \pm 1.00\,^{+0.58}_{-0.55} \cdot 10^{-1}$	$6.68 \cdot 10^{-1}$	$2.28 \pm 0.33\,^{+0.10}_{-0.11} \cdot 10^{-1}$	$2.33 \cdot 10^{-1}$
5300	0.130	$7.21 \pm 1.08\,^{+0.25}_{-0.21} \cdot 10^{-1}$	$6.28 \cdot 10^{-1}$	$1.96 \pm 0.29\,^{+0.06}_{-0.04} \cdot 10^{-1}$	$2.19 \cdot 10^{-1}$
5300	0.240	$3.44 \pm 0.75\,^{+0.16}_{-0.18} \cdot 10^{-1}$	$4.69 \cdot 10^{-1}$	$1.80 \pm 0.28\,^{+0.11}_{-0.06} \cdot 10^{-1}$	$1.54 \cdot 10^{-1}$
5300	0.420	$3.32 \pm 0.79\,^{+0.15}_{-0.12} \cdot 10^{-1}$	$2.14 \cdot 10^{-1}$	$9.85 \pm 2.22\,^{+0.67}_{-0.63} \cdot 10^{-2}$	$5.44 \cdot 10^{-2}$
9500	0.130	$6.99 \pm 1.19\,^{+0.34}_{-0.36} \cdot 10^{-1}$	$5.83 \cdot 10^{-1}$	$9.99 \pm 2.18\,^{+0.94}_{-0.99} \cdot 10^{-2}$	$1.15 \cdot 10^{-1}$
9500	0.240	$6.10 \pm 1.01\,^{+0.23}_{-0.25} \cdot 10^{-1}$	$4.49 \cdot 10^{-1}$	$1.03 \pm 0.22\,^{+0.06}_{-0.07} \cdot 10^{-1}$	$1.01 \cdot 10^{-1}$
9500	0.420	$2.34 \pm 0.65\,^{+0.15}_{-0.20} \cdot 10^{-1}$	$2.05 \cdot 10^{-1}$	$3.78\,^{+1.86}_{-1.31}\,^{+0.34}_{-0.37} \cdot 10^{-2}$	$4.16 \cdot 10^{-2}$
17000	0.240	$4.45 \pm 1.05\,^{+0.29}_{-0.29} \cdot 10^{-1}$	$4.31 \cdot 10^{-1}$	$1.55\,^{+1.49}_{-0.84}\,^{+0.23}_{-0.19} \cdot 10^{-2}$	$4.21 \cdot 10^{-2}$
17000	0.420	$1.64\,^{+0.81}_{-0.57}\,^{+0.11}_{-0.10} \cdot 10^{-1}$	$1.96 \cdot 10^{-1}$	$3.19\,^{+1.91}_{-1.27}\,^{+0.32}_{-0.34} \cdot 10^{-2}$	$2.48 \cdot 10^{-2}$
30000	0.420	$1.44\,^{+0.97}_{-0.62}\,^{+0.18}_{-0.16} \cdot 10^{-1}$	$1.87 \cdot 10^{-1}$		

Appendix A

Bin Property and Background Tables

Table A.1. Bin properties, number of events in data and from MC simulation (signal and background) for $\mathrm{d}\sigma^{\mathrm{CC}}/\mathrm{d}Q^2$ *in* e^-p *interactions.*

Q^2 range (GeV^2)	$\mathcal{P}$	$\mathcal{E}$	$\mathcal{A}$	C_{rad}	N_{data}	$N_{\mathrm{CC}}^{\mathrm{MC}}$	background expectation NC	php	l^+l^-	$W^\pm$	tot
200 – 400	0.67	0.13	0.19	0.97	19	23.8	0.0	1.1	0.1	0.1	1.2
400 – 711	0.61	0.15	0.25	0.98	29	34.4	0.0	0.3	0.1	0.1	0.5
711 – 1265	0.65	0.30	0.45	0.99	79	76.5	0.0	0.4	0.1	0.2	0.7
1265 – 2249	0.70	0.47	0.68	1.00	124	127.3	0.0	0.0	0.0	0.3	0.4
2249 – 4000	0.71	0.55	0.77	1.01	138	138.5	0.0	0.1	0.0	0.2	0.3
4000 – 7113	0.70	0.58	0.83	1.04	118	117.8	0.0	0.0	0.0	0.1	0.2
7113 – 12649	0.69	0.57	0.82	1.06	85	71.9	0.0	0.0	0.0	0.1	0.1
12649 – 22494	0.66	0.51	0.78	1.09	28	30.1	0.0	0.0	0.0	0.0	0.0
22494 – 60000	0.58	0.48	0.82	1.14	7	9.0	0.0	0.0	0.0	0.0	0.0

Table A.2. Bin properties, number of events in data and from MC simulation (signal and background) for $\mathrm{d}\sigma^{\mathrm{CC}}/\mathrm{d}Q^2$ *in* e^+p *interactions.*

Q^2 range (GeV^2)	$\mathcal{P}$	$\mathcal{E}$	$\mathcal{A}$	C_{rad}	N_{data}	$N_{\mathrm{CC}}^{\mathrm{MC}}$	background expectation NC	php	l^+l^-	$W^\pm$	tot
200 – 400	0.66	0.28	0.42	0.98	159	155.7	0.0	13.1	0.9	0.1	14.2
400 – 711	0.64	0.38	0.59	0.99	204	230.0	0.0	1.3	0.9	0.2	2.3
711 – 1265	0.67	0.48	0.72	1.00	306	299.3	0.2	3.2	0.6	0.2	4.2
1265 – 2249	0.68	0.54	0.80	1.02	324	312.4	0.4	0.3	0.3	0.3	1.4
2249 – 4000	0.70	0.56	0.80	1.03	235	247.9	0.2	0.3	0.2	0.2	0.9
4000 – 7113	0.69	0.57	0.83	1.06	155	147.3	0.0	0.0	0.0	0.1	0.2
7113 – 12649	0.66	0.56	0.85	1.09	59	58.5	0.1	0.0	0.0	0.1	0.2
12649 – 22494	0.58	0.51	0.88	1.13	11	14.5	0.0	0.0	0.0	0.0	0.0
22494 – 60000	0.44	0.49	1.12	1.17	3	2.0	0.0	0.0	0.0	0.0	0.0

Table A.3. Bin properties, number of events in data and from MC simulation (signal and background) for $\mathrm{d}\sigma^{\mathrm{CC}}/\mathrm{d}x$ *in* e^-p *interactions.*

x range	$\mathcal{P}$	$\mathcal{E}$	$\mathcal{A}$	C_{rad}	N_{data}	$N_{\mathrm{CC}}^{\mathrm{MC}}$	background expectation				
							NC	php	l^+l^-	$W^\pm$	tot
0.010 – 0.022	0.66	0.16	0.24	1.06	35	32.8	0.0	0.5	0.0	0.1	0.6
0.022 – 0.046	0.73	0.33	0.45	1.06	78	88.9	0.0	0.9	0.1	0.2	1.2
0.046 – 0.100	0.81	0.54	0.67	1.02	167	178.3	0.0	0.2	0.2	0.4	0.8
0.100 – 0.178	0.81	0.56	0.70	0.98	163	150.0	0.0	0.0	0.0	0.3	0.3
0.178 – 0.316	0.85	0.57	0.67	0.93	123	121.6	0.0	0.0	0.0	0.1	0.2
0.316 – 0.562	0.87	0.47	0.54	0.82	51	48.5	0.0	0.0	0.0	0.0	0.0
0.562 – 1.000	0.72	0.30	0.41	0.71	3	3.8	0.0	0.0	0.0	0.0	0.0

Table A.4. Bin properties, number of events in data and from MC simulation (signal and background) for $\mathrm{d}\sigma^{\mathrm{CC}}/\mathrm{d}x$ *in* e^+p *interactions.*

x range	$\mathcal{P}$	$\mathcal{E}$	$\mathcal{A}$	C_{rad}	N_{data}	$N_{\mathrm{CC}}^{\mathrm{MC}}$	background expectation				
							NC	php	l^+l^-	$W^\pm$	tot
0.010 – 0.022	0.69	0.28	0.40	1.05	167	164.1	0.0	7.3	0.3	0.1	7.7
0.022 – 0.046	0.77	0.54	0.69	1.03	351	370.9	0.5	5.0	0.6	0.2	6.2
0.046 – 0.100	0.83	0.64	0.78	1.00	425	434.5	0.2	3.0	1.2	0.4	4.8
0.100 – 0.178	0.83	0.63	0.76	0.93	258	268.9	0.1	0.0	0.6	0.3	0.9
0.178 – 0.316	0.87	0.58	0.67	0.87	173	155.2	0.2	0.0	0.2	0.1	0.5
0.316 – 0.562	0.89	0.45	0.51	0.79	45	41.6	0.0	0.0	0.0	0.0	0.1
0.562 – 1.000	0.73	0.24	0.33	0.65	2	1.7	0.0	0.0	0.0	0.0	0.0

Table A.5. Bin properties, number of events in data and from MC simulation (signal and background) for $\mathrm{d}\sigma^{\mathrm{CC}}/\mathrm{d}y$ *in* e^-p *interactions.*

y range	$\mathcal{P}$	$\mathcal{E}$	$\mathcal{A}$	C_{rad}	N_{data}	$N_{\mathrm{CC}}^{\mathrm{MC}}$	background expectation				
							NC	php	l^+l^-	$W^\pm$	tot
0.00 – 0.10	0.87	0.19	0.22	0.87	60	66.5	0.0	0.6	0.1	0.1	0.9
0.10 – 0.20	0.84	0.56	0.66	0.97	145	134.9	0.0	0.3	0.1	0.3	0.7
0.20 – 0.34	0.82	0.55	0.67	1.02	149	144.9	0.0	0.3	0.1	0.2	0.6
0.34 – 0.48	0.75	0.50	0.67	1.06	94	106.9	0.0	0.2	0.0	0.2	0.4
0.48 – 0.62	0.71	0.44	0.63	1.07	80	80.7	0.0	0.2	0.0	0.1	0.4
0.62 – 0.76	0.66	0.36	0.54	1.07	66	57.2	0.0	0.2	0.0	0.1	0.3
0.76 – 0.90	0.64	0.27	0.42	1.08	33	38.3	0.0	0.1	0.0	0.1	0.2

Table A.6. Bin properties, number of events in data and from MC simulation (signal and background) for $\mathrm{d}\sigma^{\mathrm{CC}}/\mathrm{d}y$ in e^+p interactions.

y range	$\mathcal{P}$	$\mathcal{E}$	$\mathcal{A}$	C_{rad}	N_{data}	$N_{\mathrm{CC}}^{\mathrm{MC}}$	background expectation				
							NC	php	l^+l^-	$W^{\pm}$	tot
0.00 – 0.10	0.90	0.35	0.40	0.87	264	268.6	0.2	5.1	1.5	0.2	7.0
0.10 – 0.20	0.81	0.57	0.70	0.99	360	337.7	0.0	5.2	0.9	0.3	6.3
0.20 – 0.34	0.79	0.55	0.69	1.04	316	335.6	0.0	3.7	0.2	0.2	4.1
0.34 – 0.48	0.74	0.48	0.65	1.05	219	224.5	0.1	1.4	0.2	0.2	1.9
0.48 – 0.62	0.69	0.39	0.56	1.08	146	146.7	0.6	1.5	0.1	0.1	2.3
0.62 – 0.76	0.65	0.30	0.47	1.08	102	98.1	0.0	1.3	0.0	0.1	1.4
0.76 – 0.90	0.62	0.20	0.33	1.08	49	56.6	0.1	0.2	0.1	0.1	0.4

Table A.7. Bin properties, number of events in data and from MC simulation (signal and background) for $\mathrm{d}^2\sigma^{\mathrm{CC}}/\mathrm{d}x\mathrm{d}Q^2$ in e^-p interactions.

Q_c^2 (GeV^2)	x_c	$\mathcal{P}$	$\mathcal{E}$	$\mathcal{A}$	C_{rad}	N_{data}	$N_{\mathrm{CC}}^{\mathrm{MC}}$	background expectation				
								NC	php	l^+l^-	$W^{\pm}$	tot
280	0.032	0.60	0.28	0.47	0.94	6	10.1	0.0	0.5	0.0	0.0	0.5
530	0.015	0.44	0.14	0.32	1.06	11	10.1	0.0	0.1	0.0	0.0	0.1
530	0.032	0.53	0.27	0.50	1.04	12	13.3	0.0	0.1	0.1	0.1	0.2
530	0.068	0.65	0.22	0.34	0.91	4	8.5	0.0	0.0	0.1	0.0	0.1
950	0.015	0.38	0.12	0.32	1.12	16	11.8	0.0	0.3	0.0	0.0	0.3
950	0.032	0.55	0.29	0.52	1.06	14	21.6	0.0	0.1	0.1	0.1	0.2
950	0.068	0.63	0.41	0.65	0.97	29	24.6	0.0	0.0	0.0	0.1	0.2
950	0.130	0.64	0.39	0.61	0.90	16	14.2	0.0	0.0	0.0	0.0	0.0
1700	0.032	0.48	0.27	0.56	1.10	30	29.0	0.0	0.0	0.0	0.1	0.1
1700	0.068	0.62	0.58	0.93	1.01	49	47.9	0.0	0.0	0.0	0.1	0.2
1700	0.130	0.68	0.58	0.85	0.94	29	28.0	0.0	0.0	0.0	0.1	0.1
1700	0.240	0.68	0.53	0.78	0.85	15	17.9	0.0	0.0	0.0	0.0	0.1
3000	0.068	0.60	0.53	0.89	1.05	52	53.7	0.0	0.0	0.0	0.1	0.1
3000	0.130	0.66	0.62	0.94	0.99	36	36.9	0.0	0.0	0.0	0.1	0.1
3000	0.240	0.70	0.61	0.87	0.92	27	25.1	0.0	0.0	0.0	0.0	0.0
3000	0.420	0.74	0.45	0.61	0.79	7	7.9	0.0	0.0	0.0	0.0	0.0
5300	0.068	0.49	0.38	0.77	1.17	32	37.7	0.0	0.0	0.0	0.1	0.1
5300	0.130	0.64	0.57	0.90	1.02	45	39.1	0.0	0.0	0.0	0.1	0.1
5300	0.240	0.72	0.64	0.89	0.94	21	28.6	0.0	0.0	0.0	0.0	0.0
5300	0.420	0.73	0.59	0.81	0.84	18	11.6	0.0	0.0	0.0	0.0	0.0
9500	0.130	0.52	0.43	0.83	1.13	35	29.1	0.0	0.0	0.0	0.1	0.1
9500	0.240	0.67	0.61	0.91	1.01	37	27.2	0.0	0.0	0.0	0.0	0.0
9500	0.420	0.77	0.64	0.83	0.89	13	11.3	0.0	0.0	0.0	0.0	0.0
17000	0.240	0.54	0.44	0.82	1.13	18	17.4	0.0	0.0	0.0	0.0	0.0
17000	0.420	0.69	0.61	0.88	0.96	8	9.5	0.0	0.0	0.0	0.0	0.0
30000	0.420	0.53	0.47	0.89	1.12	5	6.4	0.0	0.0	0.0	0.0	0.0

Table A.8. Bin properties, number of events in data and from MC simulation (signal and background) for $\mathrm{d}^2\sigma^{\mathrm{CC}}/\mathrm{d}x\mathrm{d}Q^2$ *in* e^+p *interactions.*

Q^2_c	x_c	$\mathcal{P}$	$\mathcal{E}$	$\mathcal{A}$	C_{rad}	N_{data}	$N^{\mathrm{MC}}_{\mathrm{CC}}$	background expectation				
(GeV^2)								NC	php	l^+l^-	$W^\pm$	tot
280	0.008	0.40	0.14	0.35	1.07	26	18.4	0.0	2.4	0.1	0.0	2.5
280	0.015	0.48	0.26	0.54	1.03	49	43.3	0.0	5.0	0.2	0.0	5.3
280	0.032	0.59	0.44	0.75	0.95	55	53.2	0.0	3.1	0.2	0.0	3.3
280	0.068	0.65	0.43	0.66	0.89	24	33.8	0.0	2.4	0.4	0.0	2.8
530	0.015	0.48	0.28	0.58	1.06	52	56.6	0.0	0.4	0.0	0.0	0.5
530	0.032	0.53	0.46	0.87	0.99	57	74.7	0.0	0.5	0.2	0.1	0.7
530	0.068	0.60	0.52	0.87	0.92	59	58.8	0.0	0.1	0.5	0.1	0.6
530	0.130	0.60	0.46	0.77	0.83	25	25.3	0.0	0.0	0.2	0.0	0.2
950	0.015	0.43	0.21	0.49	1.09	52	52.5	0.0	1.9	0.1	0.0	2.0
950	0.032	0.57	0.51	0.89	1.04	102	102.0	0.0	0.7	0.0	0.1	0.8
950	0.068	0.63	0.58	0.92	0.96	84	85.7	0.0	0.5	0.2	0.1	0.8
950	0.130	0.66	0.55	0.84	0.88	48	41.3	0.0	0.0	0.2	0.0	0.2
950	0.240	0.67	0.40	0.60	0.82	20	16.5	0.2	0.0	0.0	0.0	0.3
1700	0.032	0.52	0.42	0.82	1.09	105	100.4	0.4	0.3	0.1	0.1	0.9
1700	0.068	0.64	0.59	0.93	1.02	105	106.6	0.0	0.0	0.0	0.1	0.2
1700	0.130	0.68	0.61	0.90	0.92	57	57.6	0.0	0.0	0.1	0.1	0.2
1700	0.240	0.70	0.56	0.81	0.87	39	31.4	0.0	0.0	0.1	0.0	0.1
3000	0.068	0.61	0.53	0.86	1.08	97	95.6	0.2	0.0	0.0	0.1	0.3
3000	0.130	0.69	0.61	0.90	0.98	55	62.5	0.0	0.0	0.1	0.1	0.1
3000	0.240	0.72	0.62	0.87	0.90	44	39.0	0.0	0.0	0.1	0.0	0.1
3000	0.420	0.71	0.51	0.72	0.81	7	10.5	0.0	0.0	0.0	0.0	0.0
5300	0.068	0.50	0.37	0.74	1.15	49	50.1	0.0	0.0	0.0	0.1	0.1
5300	0.130	0.63	0.58	0.93	1.07	45	50.2	0.0	0.0	0.0	0.0	0.0
5300	0.240	0.70	0.65	0.93	0.95	41	35.1	0.0	0.0	0.0	0.0	0.0
5300	0.420	0.74	0.60	0.82	0.85	20	11.0	0.0	0.0	0.0	0.0	0.0
9500	0.130	0.49	0.43	0.89	1.16	21	23.9	0.1	0.0	0.0	0.1	0.1
9500	0.240	0.67	0.60	0.90	1.04	22	21.6	0.0	0.0	0.0	0.0	0.0
9500	0.420	0.74	0.64	0.86	0.92	8	8.8	0.0	0.0	0.0	0.0	0.0
17000	0.240	0.48	0.46	0.95	1.17	3	8.1	0.0	0.0	0.0	0.0	0.0
17000	0.420	0.65	0.62	0.96	1.02	6	4.6	0.0	0.0	0.0	0.0	0.0

Appendix B

Figures and Tables with Uncertainties

B.1. Graphical Representation of the Uncertainties

In Figs. B.1–B.6 the graphical representation of the systematic uncertainties are shown. The figures show the following systematic uncertainties:

(a) calorimeter energy scale (Sect. 6.5.1);

(b) QCD cascade model (Sect. 6.5.2);

(c) selection thresholds, T1 (Sect. 6.5.3);

(d) selection thresholds, T2 (Sect. 6.5.3);

(e) php subtraction (Sect. 6.5.4);

(f) PDF uncertainty (Sect. 6.5.5);

(g) NLO QCD corrections (Sect. 6.5.6) and

(h) the total systematic uncertainty (solid dots) and the statistical uncertainty (open dots).

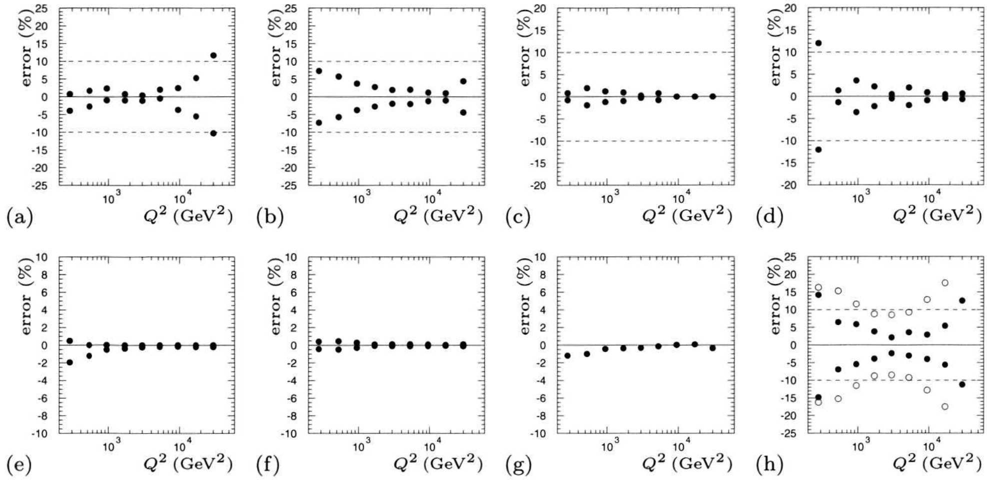

Figure B.1. Graphical representation of the uncertainties on the e^-p $d\sigma^{CC}/dQ^2$ measurement. For a description of the figures see text.

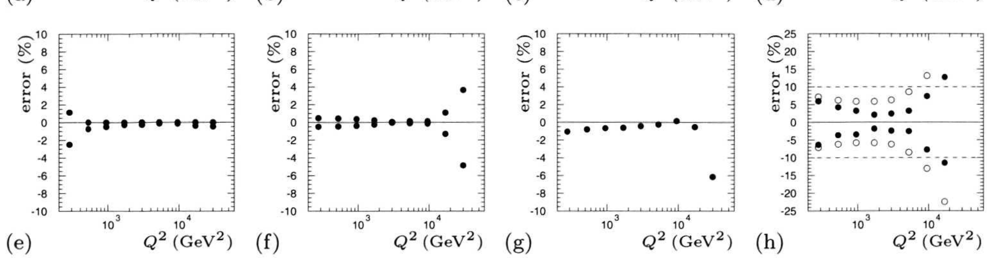

Figure B.2. Graphical representation of the uncertainties on the e^+p $d\sigma^{CC}/dQ^2$ measurement. For a description of the figures see text.

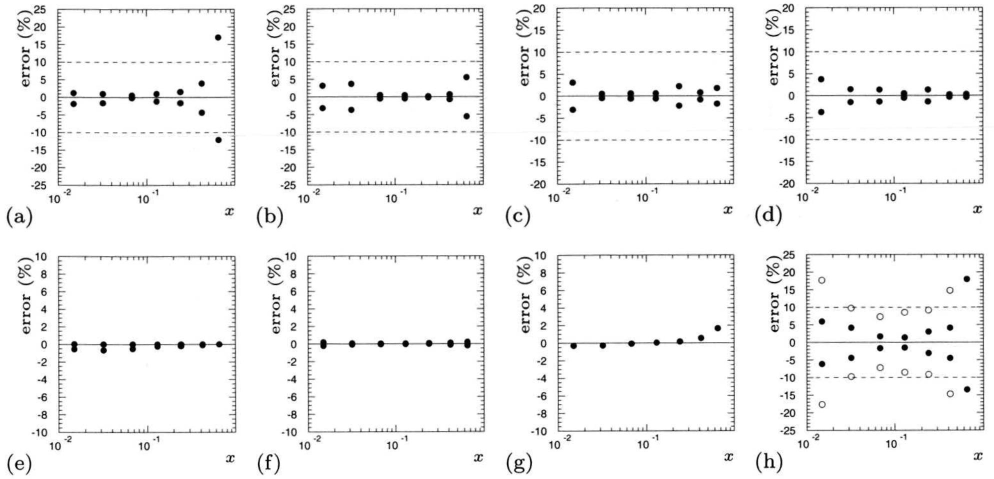

Figure B.3. Graphical representation of the uncertainties on the e^-p $\mathrm{d}\sigma^{\mathrm{CC}}/\mathrm{d}x$ *measurement. For a description of the figures see text.*

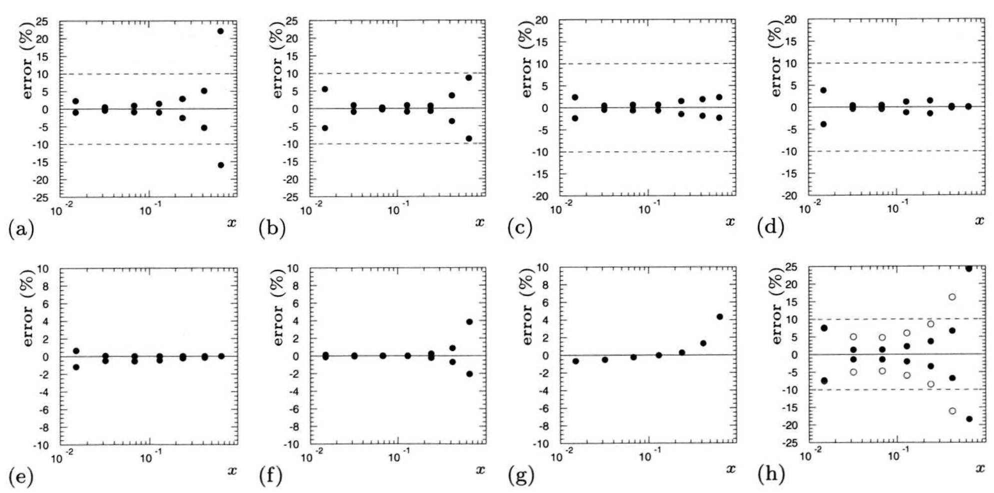

Figure B.4. Graphical representation of the uncertainties on the e^+p $\mathrm{d}\sigma^{\mathrm{CC}}/\mathrm{d}x$ *measurement. For a description of the figures see text.*

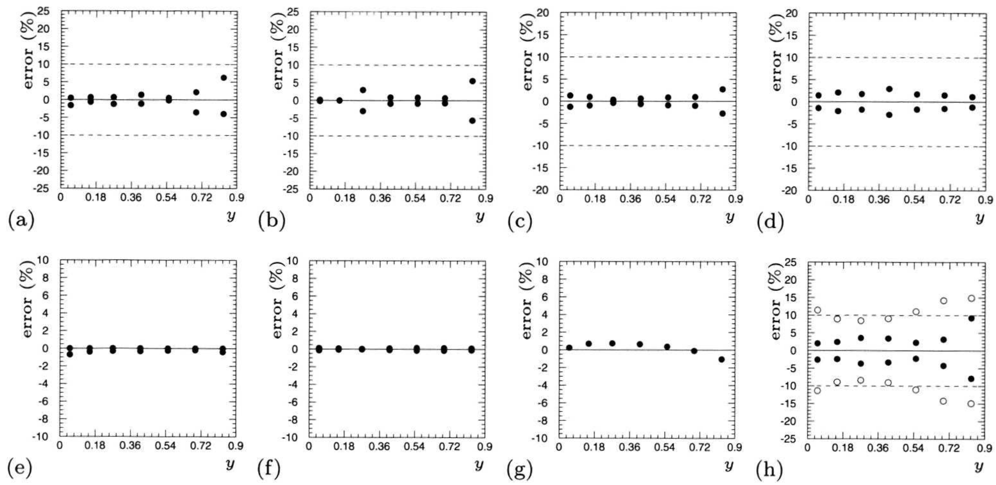

Figure B.5. Graphical representation of the uncertainties on the e^-p $\mathrm{d}\sigma^{\mathrm{CC}}/\mathrm{d}y$ *measurement. For a description of the figures see text.*

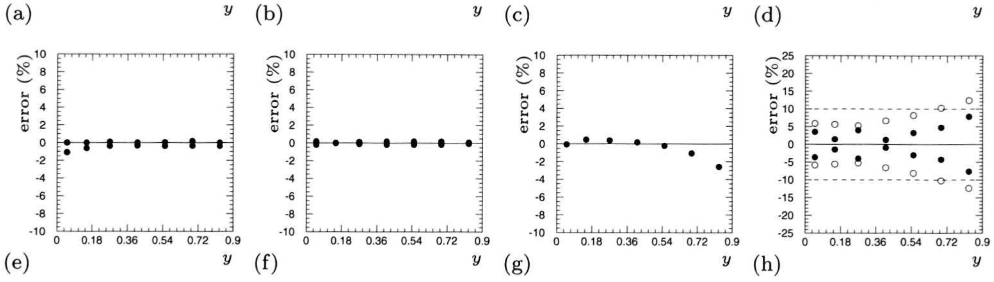

Figure B.6. Graphical representation of the uncertainties on the e^+p $\mathrm{d}\sigma^{\mathrm{CC}}/\mathrm{d}y$ *measurement. For a description of the figures see text.*

B.2. Tables with Uncertainties

Table B.1. Uncertainties on the e^-p $\mathrm{d}\sigma^{\mathrm{CC}}/\mathrm{d}Q^2$ measurement.

Q^2 range (GeV^2)	δ_{stat} (%)	δ_{syst} (%)	δ_E (%)	δ_{MEPS} (%)	δ_{T1} (%)	δ_{T2} (%)	δ_{php} (%)	δ_{PDF} (%)	δ_{QCD} (%)
200 – 400	±22	$^{+14}_{-15}$	$^{+0.8}_{-3.9}$	±7.3	±0.8	±12	$^{+0.5}_{-2.0}$	$^{+0.4}_{-0.4}$	−1.2
400 – 711	±18	$^{+6.5}_{-6.9}$	$^{+1.7}_{-2.8}$	±5.7	±1.9	±1.3	$^{+0.0}_{-1.2}$	$^{+0.5}_{-0.5}$	−1.0
711 – 1265	±11	$^{+5.9}_{-5.5}$	$^{+2.4}_{-0.9}$	±3.7	±1.2	±3.6	$^{+0.0}_{-0.5}$	$^{+0.3}_{-0.3}$	−0.4
1265 – 2249	±9.0	$^{+3.8}_{-3.9}$	$^{+0.8}_{-1.0}$	±2.8	±1.0	±2.2	$^{+0.0}_{-0.4}$	$^{+0.1}_{-0.1}$	−0.4
2249 – 4000	±8.6	$^{+2.1}_{-2.4}$	$^{+0.4}_{-1.1}$	±1.9	±0.2	±0.5	$^{+0.0}_{-0.2}$	$^{+0.1}_{-0.1}$	−0.3
4000 – 7113	±9.3	$^{+3.6}_{-3.0}$	$^{+2.0}_{-0.5}$	±2.0	±0.8	±2.0	$^{+0.0}_{-0.2}$	$^{+0.1}_{-0.1}$	−0.1
7113 – 12649	±11	$^{+2.9}_{-4.0}$	$^{+2.5}_{-3.7}$	±1.2	±0.0	±0.9	$^{+0.0}_{-0.2}$	$^{+0.1}_{-0.1}$	+0.0
12649 – 22494	±19	$^{+5.4}_{-5.6}$	$^{+5.3}_{-5.5}$	±1.0	±0.0	±0.4	$^{+0.0}_{-0.2}$	$^{+0.0}_{-0.0}$	+0.1
22494 – 60000	$^{+54}_{-37}$	$^{+13}_{-11}$	$^{+12}_{-10}$	±4.4	±0.0	±0.6	$^{+0.0}_{-0.2}$	$^{+0.1}_{-0.1}$	−0.4

Table B.2. Uncertainties on the e^+p $\mathrm{d}\sigma^{\mathrm{CC}}/\mathrm{d}Q^2$ measurement.

Q^2 range (GeV^2)	δ_{stat} (%)	δ_{syst} (%)	δ_E (%)	δ_{MEPS} (%)	δ_{T1} (%)	δ_{T2} (%)	δ_{php} (%)	δ_{PDF} (%)	δ_{QCD} (%)
200 – 400	±7.7	$^{+5.9}_{-6.4}$	$^{+1.9}_{-2.0}$	±3.8	±1.9	±3.1	$^{+1.1}_{-2.5}$	$^{+0.5}_{-0.5}$	−1.1
400 – 711	±7.1	$^{+4.2}_{-3.7}$	$^{+2.3}_{-0.8}$	±1.6	±1.4	±2.5	$^{+0.0}_{-0.7}$	$^{+0.4}_{-0.5}$	−0.8
711 – 1265	±5.8	$^{+3.2}_{-3.5}$	$^{+0.7}_{-1.3}$	±2.7	±1.0	±0.6	$^{+0.0}_{-0.5}$	$^{+0.4}_{-0.4}$	−0.7
1265 – 2249	±5.7	$^{+2.1}_{-1.8}$	$^{+1.1}_{-0.3}$	±1.6	±0.2	±0.3	$^{+0.0}_{-0.3}$	$^{+0.2}_{-0.2}$	−0.6
2249 – 4000	±6.6	$^{+2.4}_{-2.4}$	$^{+2.0}_{-2.1}$	±0.6	±0.1	±0.9	$^{+0.0}_{-0.3}$	$^{+0.0}_{-0.0}$	−0.4
4000 – 7113	±8.1	$^{+3.2}_{-2.5}$	$^{+3.0}_{-2.4}$	±0.4	±0.0	±0.6	$^{+0.0}_{-0.1}$	$^{+0.1}_{-0.1}$	−0.2
7113 – 12649	±13	$^{+7.3}_{-7.8}$	$^{+6.2}_{-6.7}$	±2.6	±0.0	±2.9	$^{+0.0}_{-0.1}$	$^{+0.1}_{-0.2}$	+0.2
12649 – 22494	$^{+40}_{-30}$	$^{+13}_{-11}$	$^{+11}_{-9.4}$	±6.5	±0.0	±0.5	$^{+0.0}_{-0.4}$	$^{+1.1}_{-1.3}$	−0.5
22494 – 60000	$^{+97}_{-54}$	$^{+28}_{-28}$	$^{+19}_{-18}$	±21	±0.0	±0.4	$^{+0.0}_{-0.5}$	$^{+3.7}_{-4.9}$	−6.2

Table B.3. Uncertainties on the e^-p $\mathrm{d}\sigma^{\mathrm{CC}}/\mathrm{d}x$ measurement.

x range	δ_{stat} (%)	δ_{syst} (%)	δ_E (%)	δ_{MEPS} (%)	δ_{T1} (%)	δ_{T2} (%)	δ_{php} (%)	δ_{PDF} (%)	δ_{QCD} (%)
0.010 − 0.022	± 17	$^{+6.0}_{-6.1}$	$^{+1.3}_{-1.8}$	± 3.2	± 3.1	± 3.7	$^{+0.0}_{-0.6}$	$^{+0.2}_{-0.2}$	-0.3
0.022 − 0.046	± 11	$^{+4.2}_{-4.4}$	$^{+1.0}_{-1.6}$	± 3.7	± 0.5	± 1.5	$^{+0.0}_{-0.7}$	$^{+0.1}_{-0.1}$	-0.3
0.046 − 0.100	± 7.8	$^{+1.7}_{-1.7}$	$^{+0.5}_{-0.2}$	± 0.5	± 0.6	± 1.4	$^{+0.0}_{-0.5}$	$^{+0.0}_{-0.0}$	-0.1
0.100 − 0.178	± 7.9	$^{+1.4}_{-1.5}$	$^{+1.0}_{-1.1}$	± 0.5	± 0.6	± 0.5	$^{+0.0}_{-0.2}$	$^{+0.1}_{-0.0}$	$+0.0$
0.178 − 0.316	± 9.1	$^{+3.1}_{-3.1}$	$^{+1.6}_{-1.6}$	± 0.2	± 2.2	± 1.4	$^{+0.0}_{-0.2}$	$^{+0.1}_{-0.0}$	$+0.2$
0.316 − 0.562	± 14	$^{+4.1}_{-4.5}$	$^{+4.0}_{-4.4}$	± 0.7	± 0.8	± 0.3	$^{+0.0}_{-0.1}$	$^{+0.1}_{-0.1}$	$+0.6$
0.562 − 1.000	$^{+97}_{-54}$	$^{+18}_{-13}$	$^{+17}_{-12}$	± 5.6	± 1.8	± 0.3	$^{+0.0}_{-0.0}$	$^{+0.2}_{-0.2}$	$+1.6$

Table B.4. Uncertainties on the e^+p $\mathrm{d}\sigma^{\mathrm{CC}}/\mathrm{d}x$ measurement.

x range	δ_{stat} (%)	δ_{syst} (%)	δ_E (%)	δ_{MEPS} (%)	δ_{T1} (%)	δ_{T2} (%)	δ_{php} (%)	δ_{PDF} (%)	δ_{QCD} (%)
0.010 − 0.022	± 7.8	$^{+7.5}_{-7.3}$	$^{+2.3}_{-1.0}$	± 5.5	± 2.4	± 3.9	$^{+0.6}_{-1.2}$	$^{+0.1}_{-0.1}$	-0.7
0.022 − 0.046	± 5.4	$^{+1.3}_{-1.4}$	$^{+0.5}_{-0.4}$	± 0.9	± 0.5	± 0.4	$^{+0.1}_{-0.5}$	$^{+0.1}_{-0.1}$	-0.5
0.046 − 0.100	± 4.9	$^{+1.4}_{-1.4}$	$^{+0.9}_{-0.9}$	± 0.3	± 0.7	± 0.5	$^{+0.0}_{-0.6}$	$^{+0.0}_{-0.0}$	-0.2
0.100 − 0.178	± 6.3	$^{+2.3}_{-2.0}$	$^{+1.5}_{-1.0}$	± 0.9	± 0.7	± 1.2	$^{+0.0}_{-0.5}$	$^{+0.0}_{-0.0}$	-0.0
0.178 − 0.316	± 7.7	$^{+3.6}_{-3.4}$	$^{+2.9}_{-2.6}$	± 0.7	± 1.5	± 1.5	$^{+0.0}_{-0.2}$	$^{+0.2}_{-0.2}$	$+0.3$
0.316 − 0.562	± 15	$^{+6.6}_{-6.8}$	$^{+5.1}_{-5.4}$	± 3.7	± 1.9	± 0.2	$^{+0.0}_{-0.2}$	$^{+0.9}_{-0.7}$	$+1.3$
0.562 − 1.000	$^{+132}_{-65}$	$^{+24}_{-18}$	$^{+22}_{-16}$	± 8.7	± 2.3	± 0.1	$^{+0.0}_{-0.0}$	$^{+3.8}_{-2.1}$	$+4.3$

Table B.5. Uncertainties on the e^-p $\mathrm{d}\sigma^{\mathrm{CC}}/\mathrm{d}y$ measurement.

y range	δ_{stat} (%)	δ_{syst} (%)	δ_E (%)	δ_{MEPS} (%)	δ_{T1} (%)	δ_{T2} (%)	δ_{php} (%)	δ_{PDF} (%)	δ_{QCD} (%)
0.00 − 0.10	± 13	$^{+2.0}_{-2.6}$	$^{+0.5}_{-1.6}$	± 0.2	± 1.3	± 1.4	$^{+0.0}_{-0.7}$	$^{+0.1}_{-0.1}$	$+0.2$
0.10 − 0.20	± 8.3	$^{+2.4}_{-2.4}$	$^{+0.7}_{-0.6}$	± 0.0	± 1.0	± 2.1	$^{+0.0}_{-0.4}$	$^{+0.1}_{-0.1}$	$+0.7$
0.20 − 0.34	± 8.2	$^{+3.6}_{-3.7}$	$^{+0.8}_{-1.2}$	± 3.0	± 0.4	± 1.8	$^{+0.0}_{-0.3}$	$^{+0.0}_{-0.0}$	$+0.7$
0.34 − 0.48	± 10	$^{+3.4}_{-3.3}$	$^{+1.4}_{-1.1}$	± 0.9	± 0.6	± 2.9	$^{+0.0}_{-0.3}$	$^{+0.1}_{-0.1}$	$+0.6$
0.48 − 0.62	± 11	$^{+2.3}_{-2.2}$	$^{+0.6}_{-0.2}$	± 0.9	± 0.9	± 1.7	$^{+0.0}_{-0.2}$	$^{+0.2}_{-0.2}$	$+0.4$
0.62 − 0.76	± 12	$^{+3.2}_{-4.2}$	$^{+2.2}_{-3.5}$	± 0.7	± 1.0	± 1.5	$^{+0.0}_{-0.2}$	$^{+0.1}_{-0.2}$	-0.1
0.76 − 0.90	± 17	$^{+9.2}_{-7.9}$	$^{+6.3}_{-3.9}$	± 5.6	± 2.7	± 1.2	$^{+0.0}_{-0.4}$	$^{+0.1}_{-0.1}$	-1.0

Table B.6. Uncertainties on the e^+p $d\sigma^{CC}/dy$ measurement.

y range	δ_{stat} (%)	δ_{syst} (%)	δ_E (%)	δ_{MEPS} (%)	δ_{T1} (%)	δ_{T2} (%)	δ_{php} (%)	δ_{PDF} (%)	δ_{QCD} (%)
0.00 – 0.10	±6.1	$^{+3.5}_{-3.7}$	$^{+0.8}_{-0.7}$	±1.7	±1.8	±2.3	$^{+0.0}_{-1.1}$	$^{+0.2}_{-0.2}$	−0.1
0.10 – 0.20	±5.3	$^{+1.4}_{-1.5}$	$^{+0.6}_{-0.4}$	±1.0	±0.6	±0.3	$^{+0.0}_{-0.6}$	$^{+0.0}_{-0.0}$	+0.5
0.20 – 0.34	±5.7	$^{+4.0}_{-4.0}$	$^{+0.8}_{-1.0}$	±3.5	±1.0	±1.4	$^{+0.1}_{-0.4}$	$^{+0.1}_{-0.1}$	+0.4
0.34 – 0.48	±6.9	$^{+1.3}_{-1.0}$	$^{+0.9}_{-0.1}$	±0.2	±0.6	±0.5	$^{+0.0}_{-0.3}$	$^{+0.2}_{-0.2}$	+0.2
0.48 – 0.62	±8.3	$^{+3.2}_{-3.0}$	$^{+1.4}_{-0.8}$	±2.2	±1.1	±1.3	$^{+0.0}_{-0.4}$	$^{+0.2}_{-0.2}$	−0.2
0.62 – 0.76	±10	$^{+4.8}_{-4.3}$	$^{+4.0}_{-3.4}$	±1.8	±0.6	±0.9	$^{+0.2}_{-0.3}$	$^{+0.2}_{-0.2}$	−1.1
0.76 – 0.90	±14	$^{+7.8}_{-7.6}$	$^{+5.3}_{-5.0}$	±1.8	±2.5	±4.0	$^{+0.0}_{-0.4}$	$^{+0.1}_{-0.1}$	−2.6

Table B.7. Uncertainties on the e^-p $\mathrm{d}^2\sigma^{\mathrm{CC}}/\mathrm{d}x\mathrm{d}Q^2$ measurement.

Q^2_c (GeV^2)	x_c	δ_{stat} (%)	δ_{syst} (%)	δ_E (%)	δ_{MEPS} (%)	δ_{T1} (%)	δ_{T2} (%)	δ_{php} (%)	δ_{PDF} (%)	δ_{QCD} (%)
280	0.032	$^{+55}_{-37}$	$^{+18}_{-19}$	$^{+0.9}_{-5.2}$	±6.1	±2.5	±17	$^{+0.9}_{-2.7}$	$^{+0.1}_{-0.1}$	+0.1
530	0.015	$^{+40}_{-30}$	$^{+11}_{-11}$	$^{+1.9}_{-2.5}$	±0.1	±0.5	±11	$^{+0.0}_{-0.3}$	$^{+0.1}_{-0.1}$	+0.2
530	0.032	$^{+38}_{-28}$	$^{+2.7}_{-4.4}$	$^{+0.3}_{-3.2}$	±2.7	±0.0	±0.0	$^{+0.0}_{-1.2}$	$^{+0.1}_{-0.1}$	+0.1
530	0.068	$^{+77}_{-47}$	$^{+11}_{-12}$	$^{+3.9}_{-3.8}$	±10	±0.4	±1.4	$^{+0.0}_{-3.6}$	$^{+0.1}_{-0.1}$	−0.2
950	0.015	±25	$^{+13}_{-14}$	$^{+2.0}_{-4.4}$	±9.3	±3.6	±8.8	$^{+0.2}_{-0.5}$	$^{+0.3}_{-0.3}$	−0.6
950	0.032	±27	$^{+5.5}_{-3.8}$	$^{+4.2}_{-1.2}$	±3.4	±0.0	±0.0	$^{+0.0}_{-1.1}$	$^{+0.0}_{-0.0}$	+0.0
950	0.068	±19	$^{+5.7}_{-5.6}$	$^{+1.7}_{-0.8}$	±2.7	±4.0	±2.6	$^{+0.0}_{-0.6}$	$^{+0.0}_{-0.0}$	+0.0
950	0.130	±25	$^{+12}_{-9.9}$	$^{+6.0}_{-0.5}$	±8.7	±3.8	±2.6	$^{+0.0}_{-0.3}$	$^{+0.1}_{-0.1}$	+0.1
1700	0.032	±18	$^{+6.7}_{-6.8}$	$^{+0.5}_{-1.3}$	±4.7	±0.1	±4.7	$^{+0.0}_{-0.3}$	$^{+0.1}_{-0.1}$	−0.3
1700	0.068	±14	$^{+4.3}_{-4.2}$	$^{+1.5}_{-1.3}$	±1.3	±0.0	±3.8	$^{+0.0}_{-0.4}$	$^{+0.1}_{-0.1}$	+0.0
1700	0.130	±19	$^{+5.3}_{-6.8}$	$^{+0.0}_{-4.2}$	±5.2	±0.6	±1.1	$^{+0.0}_{-0.3}$	$^{+0.1}_{-0.1}$	+0.0
1700	0.240	±26	$^{+7.0}_{-4.2}$	$^{+5.6}_{-0.0}$	±0.9	±4.0	±0.4	$^{+0.0}_{-0.6}$	$^{+0.1}_{-0.1}$	+0.1
3000	0.068	±14	$^{+4.1}_{-4.5}$	$^{+0.1}_{-1.7}$	±3.7	±0.0	±1.8	$^{+0.0}_{-0.3}$	$^{+0.1}_{-0.1}$	−0.1
3000	0.130	±17	$^{+4.1}_{-3.4}$	$^{+2.5}_{-0.8}$	±2.4	±0.0	±2.2	$^{+0.0}_{-0.2}$	$^{+0.1}_{-0.1}$	+0.0
3000	0.240	±19	$^{+2.3}_{-3.3}$	$^{+2.1}_{-3.2}$	±0.0	±0.2	±0.9	$^{+0.0}_{-0.2}$	$^{+0.1}_{-0.1}$	+0.1
3000	0.420	$^{+54}_{-37}$	$^{+5.3}_{-5.2}$	$^{+2.7}_{-2.6}$	±2.6	±3.7	±0.0	$^{+0.0}_{-0.0}$	$^{+0.0}_{-0.0}$	−0.1
5300	0.068	±18	$^{+10}_{-9.7}$	$^{+3.2}_{-0.1}$	±9.4	±0.0	±2.3	$^{+0.0}_{-0.3}$	$^{+0.2}_{-0.2}$	−0.3
5300	0.130	±15	$^{+3.5}_{-3.0}$	$^{+2.3}_{-1.4}$	±1.8	±0.0	±1.9	$^{+0.0}_{-0.2}$	$^{+0.0}_{-0.0}$	+0.0
5300	0.240	±22	$^{+4.8}_{-5.1}$	$^{+0.9}_{-2.1}$	±1.9	±0.0	±4.3	$^{+0.0}_{-0.1}$	$^{+0.0}_{-0.0}$	+0.0
5300	0.420	±24	$^{+4.5}_{-3.6}$	$^{+4.3}_{-3.2}$	±1.5	±0.3	±0.2	$^{+0.0}_{-0.1}$	$^{+0.0}_{-0.0}$	+0.0
9500	0.130	±17	$^{+4.8}_{-5.2}$	$^{+3.0}_{-3.5}$	±3.7	±0.0	±0.3	$^{+0.0}_{-0.2}$	$^{+0.0}_{-0.0}$	+0.0
9500	0.240	±17	$^{+3.8}_{-4.0}$	$^{+2.8}_{-3.1}$	±0.7	±0.0	±2.4	$^{+0.0}_{-0.1}$	$^{+0.0}_{-0.0}$	+0.0
9500	0.420	±28	$^{+6.4}_{-8.6}$	$^{+4.8}_{-7.5}$	±4.2	±0.0	±0.3	$^{+0.0}_{-0.0}$	$^{+0.1}_{-0.0}$	+0.1
17000	0.240	±24	$^{+6.5}_{-6.5}$	$^{+6.1}_{-6.0}$	±2.3	±0.0	±0.2	$^{+0.0}_{-0.2}$	$^{+0.0}_{-0.0}$	−0.1
17000	0.420	$^{+49}_{-35}$	$^{+6.6}_{-6.3}$	$^{+6.5}_{-6.2}$	±0.7	±0.0	±0.9	$^{+0.0}_{-0.2}$	$^{+0.0}_{-0.0}$	−0.1
30000	0.420	$^{+68}_{-43}$	$^{+12}_{-11}$	$^{+11}_{-9.5}$	±5.9	±0.0	±0.7	$^{+0.0}_{-0.3}$	$^{+0.2}_{-0.2}$	−0.8

Table B.8. Uncertainties on the e^+p $\mathrm{d}^2\sigma^{CC}/\mathrm{d}x\mathrm{d}Q^2$ *measurement.*

Q^2_c (GeV^2)	x_c	δ_{stat} (%)	δ_{syst} (%)	δ_E (%)	δ_{MEPS} (%)	δ_{T1} (%)	δ_{T2} (%)	δ_{php} (%)	δ_{PDF} (%)	δ_{QCD} (%)
280	0.008	±19	$^{+12}_{-11}$	$^{+5.3}_{-2.8}$	±5.3	±8.9	±0.4	$^{+1.8}_{-2.4}$	$^{+0.1}_{-0.1}$	-0.1
280	0.015	±14	$^{+12}_{-13}$	$^{+1.6}_{-2.4}$	±10	±6.1	±0.9	$^{+1.7}_{-2.9}$	$^{+0.1}_{-0.1}$	$+0.1$
280	0.032	±13	$^{+4.6}_{-4.0}$	$^{+2.9}_{-0.9}$	±3.1	±1.6	±0.1	$^{+0.7}_{-1.7}$	$^{+0.1}_{-0.1}$	$+0.1$
280	0.068	±19	$^{+4.3}_{-7.9}$	$^{+0.6}_{-5.3}$	±1.0	±4.0	±0.2	$^{+0.5}_{-4.1}$	$^{+0.0}_{-0.0}$	$+0.0$
530	0.015	±14	$^{+8.1}_{-7.9}$	$^{+2.3}_{-1.4}$	±7.6	±0.2	±1.5	$^{+0.1}_{-0.3}$	$^{+0.1}_{-0.1}$	$+0.0$
530	0.032	±13	$^{+4.3}_{-4.3}$	$^{+1.4}_{-1.3}$	±3.7	±0.1	±1.7	$^{+0.0}_{-0.6}$	$^{+0.0}_{-0.0}$	$+0.0$
530	0.068	±13	$^{+6.2}_{-5.4}$	$^{+3.3}_{-0.0}$	±2.4	±3.4	±3.2	$^{+0.0}_{-1.3}$	$^{+0.0}_{-0.0}$	$+0.0$
530	0.130	±20	$^{+14}_{-10}$	$^{+9.7}_{-0.3}$	±10	±1.3	±0.4	$^{+0.0}_{-1.0}$	$^{+0.0}_{-0.0}$	$+0.1$
950	0.015	±14	$^{+9.9}_{-9.7}$	$^{+2.5}_{-0.9}$	±8.5	±1.8	±3.9	$^{+0.5}_{-1.0}$	$^{+0.2}_{-0.2}$	-1.1
950	0.032	±10	$^{+5.8}_{-5.6}$	$^{+1.7}_{-0.9}$	±5.4	±0.1	±1.1	$^{+0.1}_{-0.2}$	$^{+0.0}_{-0.0}$	$+0.0$
950	0.068	±11	$^{+2.1}_{-2.9}$	$^{+0.2}_{-2.0}$	±2.0	±0.0	±0.6	$^{+0.0}_{-0.6}$	$^{+0.0}_{-0.0}$	$+0.0$
950	0.130	±15	$^{+3.8}_{-7.2}$	$^{+0.7}_{-6.1}$	±1.4	±0.1	±3.4	$^{+0.0}_{-0.7}$	$^{+0.1}_{-0.0}$	$+0.1$
950	0.240	±22	$^{+6.9}_{-6.6}$	$^{+5.2}_{-4.7}$	±4.4	±1.2	±0.0	$^{+0.0}_{-0.3}$	$^{+0.0}_{-0.0}$	$+0.0$
1700	0.032	±10	$^{+3.5}_{-3.6}$	$^{+0.8}_{-1.3}$	±3.2	±0.0	±0.9	$^{+0.0}_{-0.2}$	$^{+0.1}_{-0.1}$	-0.5
1700	0.068	±10	$^{+2.0}_{-1.1}$	$^{+1.7}_{-0.1}$	±1.0	±0.0	±0.2	$^{+0.0}_{-0.2}$	$^{+0.1}_{-0.1}$	-0.0
1700	0.130	±13	$^{+5.1}_{-4.6}$	$^{+2.2}_{-0.2}$	±3.3	±0.1	±3.1	$^{+0.0}_{-0.4}$	$^{+0.0}_{-0.0}$	$+0.1$
1700	0.240	±16	$^{+3.8}_{-5.0}$	$^{+1.4}_{-3.4}$	±3.6	±0.2	±0.1	$^{+0.0}_{-0.3}$	$^{+0.2}_{-0.2}$	$+0.2$
3000	0.068	±10	$^{+3.6}_{-3.4}$	$^{+3.1}_{-2.9}$	±1.1	±0.0	±1.1	$^{+0.0}_{-0.2}$	$^{+0.1}_{-0.1}$	-0.1
3000	0.130	±14	$^{+5.3}_{-5.2}$	$^{+2.7}_{-2.5}$	±3.2	±0.0	±3.1	$^{+0.0}_{-0.3}$	$^{+0.0}_{-0.0}$	$+0.1$
3000	0.240	±15	$^{+5.0}_{-4.3}$	$^{+3.6}_{-2.5}$	±3.0	±0.0	±1.9	$^{+0.0}_{-0.3}$	$^{+0.2}_{-0.2}$	$+0.2$
3000	0.420	$^{+54}_{-37}$	$^{+5.3}_{-4.3}$	$^{+4.1}_{-2.7}$	±3.1	±1.4	±0.2	$^{+0.0}_{-0.2}$	$^{+0.1}_{-0.1}$	$+0.2$
5300	0.068	±15	$^{+4.2}_{-5.0}$	$^{+2.7}_{-3.9}$	±2.3	±0.0	±2.0	$^{+0.0}_{-0.2}$	$^{+0.2}_{-0.2}$	-0.7
5300	0.130	±15	$^{+3.0}_{-2.1}$	$^{+2.7}_{-1.6}$	±1.2	±0.0	±0.3	$^{+0.0}_{-0.1}$	$^{+0.0}_{-0.0}$	$+0.1$
5300	0.240	±16	$^{+5.9}_{-3.3}$	$^{+5.9}_{-3.2}$	±0.7	±0.0	±0.4	$^{+0.0}_{-0.1}$	$^{+0.1}_{-0.1}$	$+0.2$
5300	0.420	±23	$^{+6.8}_{-6.4}$	$^{+5.8}_{-5.3}$	±3.6	±0.0	±0.0	$^{+0.0}_{-0.0}$	$^{+0.5}_{-0.4}$	$+0.3$
9500	0.130	±22	$^{+9.4}_{-9.9}$	$^{+8.5}_{-9.1}$	±3.9	±0.0	±0.7	$^{+0.0}_{-0.3}$	$^{+0.4}_{-0.4}$	$+0.3$
9500	0.240	±21	$^{+5.4}_{-6.9}$	$^{+4.0}_{-5.8}$	±3.6	±0.0	±0.2	$^{+0.0}_{-0.1}$	$^{+0.1}_{-0.1}$	$+0.1$
9500	0.420	$^{+49}_{-35}$	$^{+9.0}_{-9.8}$	$^{+9.0}_{-9.8}$	±0.3	±0.0	±0.2	$^{+0.0}_{-0.0}$	$^{+0.2}_{-0.1}$	$+0.1$
17000	0.240	$^{+97}_{-54}$	$^{+15}_{-12}$	$^{+13}_{-10}$	±6.5	±0.0	±0.3	$^{+0.0}_{-0.9}$	$^{+1.4}_{-1.6}$	-1.3
17000	0.420	$^{+60}_{-40}$	$^{+10}_{-11}$	$^{+9.6}_{-10}$	±2.8	±0.0	±0.9	$^{+0.0}_{-0.0}$	$^{+0.6}_{-0.8}$	-0.9

References

[1] M. Planck, Verh. Deutsch. Phys. Ges. **2**, 237 (1900).

[2] A. Einstein, AdP **49**, 54 (1916).

[3] E. Rutherford, Phil. Mag. **21**, 669 (1911).

[4] N. Bohr, Phil. Mag. **26**, 1 (1913).

[5] J. Chadwick, Proc. Roy. Soc. **A 136**, 692 (1932).

[6] R. W. Mcallister and R. Hofstadter, Phys. Rev. **102**, 851 (1956).

[7] E. D. Bloom et al., Phys. Rev. Lett. **23**, 930 (1969);
M. Breidenbach et al., Phys. Rev. Lett. **23**, 935 (1969).

[8] M. Gell-Mann, Phys. Lett. **8**, 214 (1964).

[9] TASSO Coll., R. Brandelik et al., Phys. Lett. **B86**, 243 (1979);
D. P. Barber et al., Phys. Rev. Lett. **43**, 830 (1979);
PLUTO Coll., C. Berger et al., Phys. Lett. **B86**, 418 (1979);
JADE Coll., W. Bartel et al., Phys. Lett. **B91**, 142 (1980).

[10] E. Fermi, Rev. Mod. Phys. **4**, 131 (1932).

[11] T. D. Lee and Chen-Ning Yang, Phys. Rev. **104**, 254 (1956).

[12] C. S. Wu et al., Phys. Rev. **105**, 1413 (1957).

[13] S. L. Glashow, Nucl. Phys. **22**, 579 (1961);
A. Salam. Originally printed in *Svartholm: Elementary Particle Theory, Proceedings Of The Nobel Symposium Held 1968 At Lerum, Sweden*, Stockholm 1968, 367-377;
S. Weinberg, Phys. Rev. Lett. **19**, 1264 (1967).

[14] UA1 Coll., G. Arnison et al., Phys. Lett. **B122**, 103 (1983);
UA2 Coll., M. Banner et al., Phys. Lett. **B122**, 476 (1983).

[15] R.P. Feynman, *Photon-Hadron Interactions.* Benjamin, New York, 1972.

[16] F. Halzen and A.D. Martin, *Quarks and Leptons: An Introductory Course in Modern Particle Physics.* John Wiley & Sons, Inc., 1984.

[17] R.G. Roberts, *The Structure of the Proton – Deep Inelastic Scattering.* Cambridge University Press, Cambridge, 1990.

[18] A.M. Cooper-Sarkar, R.C.E. Devenish and A. De Roeck, Int. J. Mod. Phys. **A 13**, 3385 (1998).

[19] R.P. Feynman, Phys. Rev. Lett. **23**, 1415 (1969).

[20] J.D. Bjorken, Phys. Rev. **179**, 1547 (1969).

[21] J.I. Friedman and H.W. Kendall, Annual Review of Nuclear Science **22**, 203 (1972).

[22] A.J. Buras, Rev. Mod. Phys. **52**, 199 (1980);
F.J. Yndurain, *Quantum Chromodynamics.* Springer-Verlag, 1983.

[23] Yu.L. Dokshitzer, Sov. Phys. JETP **46**, 641 (1977);
V.N. Gribov and L.N. Lipatov, Sov. J. Nucl. Phys. **15**, 438 (1972);
G. Altarelli and G. Parisi, Nucl. Phys. **B 126**, 298 (1977).

[24] G. Kramer and H. Spiesberger, *Proc. Workshop on Physics at HERA*, Vol. 2, p. 789. W. Buchmüller and G. Ingelman, Hamburg, Germany, DESY (1991).

[25] B. Heinemann, S. Riess and H. Spiesberger, *Proc. Workshop on Monte Carlo Generators for HERA Physics*, G. Grindhammer et al. (ed.), p. 530. DESY, Hamburg, Germany (1999). Also in preprint DESY-PROC-1999-02, available on `http://www.desy.de/~heramc/`.

[26] M. Bohm and H. Spiesberger, Nucl. Phys. **B 304**, 749 (1988);
H. Spiesberger, Nucl. Phys. **B 349**, 109 (1991).

[27] D.Yu. Bardin, K.C. Burdik, P.Kh. Khristova and T. Riemann, Z. Phys. **C 44**, 149 (1989).

[28] A. Arbuzov et al., Comp. Phys. Comm. **94**, 128 (1996).

[29] H. Spiesberger, *Proc. Workshop on Future Physics at HERA*, G. Ingelman, A. De Roeck and R. Klanner (eds.), Vol. 1, p. 227. DESY, Hamburg, Germany (1996), available on `http://www.desy.de/~hspiesb/eprc.html`.

[30] ZEUS Coll., U. Holm (ed.), *The ZEUS Detector.* Status Report (unpublished), DESY (1993), available on `http://www-zeus.desy.de/bluebook/bluebook.html`.

[31] LINAC-3 Coll., L. Criegee et al., Rev. Sci. Instrum. **62**, 867 (1991).

[32] ZEUS Coll., M. Derrick et al., Phys. Lett. **B 293**, 465 (1992).

[33] C. Alvisi et al., Nucl. Inst. Meth. **A 305**, 30 (1991).

[34] N. Harnew et al., Nucl. Inst. Meth. **A 279**, 290 (1989); B. Foster et al., Nucl. Phys. Proc. Suppl. **B 32**, 181 (1993); B. Foster et al., Nucl. Inst. Meth. **A 338**, 254 (1994).

[35] R. Hall-Wilton et al., *The CTD Tracking Resolution* (unpublished). ZEUS-99-024, 1999.

[36] M. Derrick et al., Nucl. Inst. Meth. **A 309**, 77 (1991); A. Caldwell et al., Nucl. Inst. Meth. **A 321**, 356 (1992).

[37] H. Tiecke. Prepared for Vth International Workshop on Instrumentation for Colliding Beam Physics, Novosibirsk, USSR, 15-21 Mar 1990.

[38] H. Abramowicz et al., Nucl. Inst. Meth. **A 313**, 126 (1992).

[39] G. Abbiendi et al., Nucl. Inst. Meth. **A 333**, 342 (1993).

[40] ZEUS Coll., M. Derrick et al., Z. Phys. **C 63**, 391 (1994).

[41] J. Andruszków et al., Preprint DESY-92-066, DESY, 1992.

[42] H. Bethe and W. Heitler, Proc. Roy. Soc. Lond. **A146**, 83 (1934).

[43] K. J. F. Gaemers and M. van der Horst, Nucl. Phys. **B 316**, 269 (1989).

[44] ZEUS Coll., R. Carlin et al., Nucl. Inst. Meth. **A 379**, 542 (1996).

[45] R. Brun et al., GEANT3, Technical Report CERN-DD/EE/84-1, CERN, 1987.

[46] E. de Wolf (editor) et al., ZGANA, ZEUS trigger simulation library.

[47] U. Fricke et al., Preprint hep-ex/0305095, 2003.

[48] H. Spiesberger, HERACLES *and* DJANGOH*: Event Generation for ep Interactions at HERA Including Radiative Processes*, 1998, available on `http://www.desy.de/~hspiesb/djangoh.html`.

[49] A. Kwiatkowski, H. Spiesberger and H.-J. Möhring, Comp. Phys. Comm. **69**, 155 (1992). Also in *Proc. Workshop Physics at HERA*, 1991, DESY, Hamburg.

[50] G. Ingelman, A. Edin and J. Rathsman, Comp. Phys. Comm. **101**, 108 (1997).

[51] Particle Data Group, D.E. Groom et al., Eur. Phys. J. **C 15**, 1 (2000).

[52] CTEQ Coll., H.L. Lai et al., Eur. Phys. J. **C 12**, 375 (2000).

[53] L. Lönnblad, Comp. Phys. Comm. **71**, 15 (1992).

[54] T. Sjöstrand, Comp. Phys. Comm. **39**, 347 (1986);
T. Sjöstrand and M. Bengtsson, Comp. Phys. Comm. **43**, 367 (1987);
T. Sjöstrand, Comp. Phys. Comm. **82**, 74 (1994).

[55] G. Marchesini et al., Comp. Phys. Comm. **67**, 465 (1992).

[56] T. Abe, Comp. Phys. Comm. **136**, 126 (2001).

[57] M. Drees, Mod. Phys. Lett. **A 2**, 573 (1987).

[58] U. Baur, J.A.M. Vermaseren and D. Zeppenfeld, Nucl. Phys. **B 375**, 3 (1992).

[59] F. Jacquet and A. Blondel, *Proceedings of the Study for an ep Facility for Europe*, U. Amaldi (ed.), p. 391. Hamburg, Germany (1979). Also in preprint DESY 79/48.

[60] S. Bentvelsen, J. Engelen and P. Kooijman, *Proc. Workshop on Physics at HERA*, W. Buchmüller and G. Ingelman (eds.), Vol. 1, p. 23. Hamburg, Germany, DESY (1992);
K.C. Höger, *Proc. Workshop on Physics at HERA*, W. Buchmüller and G. Ingelman (eds.), Vol. 1, p. 43. Hamburg, Germany, DESY (1992).

[61] U. Bassler and G. Bernardi, Nucl. Inst. Meth. **A 361**, 197 (1995);
U. Bassler and G. Bernardi, Nucl. Inst. Meth. **A 426**, 583 (1999).

[62] ZEUS Coll., M. Derrick et al., Z. Phys. **C 72**, 399 (1996).

[63] S. Kananov, *The noise study for the 1995 data in the ZEUS Calorimeter* (unpublished). ZEUS-97-018, 1997.

[64] A. Savin, *Study of Calorimeter Noise in the 1996 Data* (unpublished). ZEUS-98-007;
S. Grijpink, *Calorimeter noise reduction using the PMSTAT tables* (unpublished). ZEUS-01-031, 2001.

[65] G.M. Briskin, *Diffractive Dissociation in ep Deep Inelastic Scattering.* Ph.D. Thesis, Tel Aviv University, 1998. (Unpublished).

[66] U. Behrens et al., Nucl. Inst. Meth. **A 289**, 115 (1990);
T.C. Awes et al., Nucl. Inst. Meth. **A 311**, 130 (1992).

[67] J. Grosse-Knetter, *Energy Corrections for Islands* (unpublished). ZEUS-97-039, internal ZEUS-note, 1997.

[68] J. Grosse-Knetter, *Corrections for the Hadronic Final State* (unpublished). ZEUS-98-031, internal ZEUS-note, 1998.

[69] ZEUS Coll., Calorimeter group, A. Andresen et al., Nucl. Inst. Meth. **A 290**, 95 (1990).

[70] T. Fusayasu, *Study of Charged-Current* $e^{\pm}p$ *Deep Inelastic Scattering at* $\sqrt{s} = 318\ GeV$. Ph.D. Thesis, University of Tokyo, Tokyo (Japan), 2001.

[71] P. Billoir and S. Qian, Nucl. Inst. Meth. **A 311**, 139 (1992);
G.F. Hartner, *VCTRAK(3.07/04): Offline Output Information* (unpublished). ZEUS-97-064, internal ZEUS-note, 1997;
G. F. Hartner, *VCTRAK Briefing: Program and Math* (unpublished). Zeus-98-058, internal ZEUS-note, 1998.

[72] J. Gonçalo and K. Long, *A Minimum Bias Vertex Distribution for the 1998/99* e^-p *Data* (unpublished). ZEUS-00-027, internal ZEUS-note, 2000;
M. Moritz, *Measurement of the High* Q^2 *Neutral Current DIS cross section at HERA.* Ph.D. Thesis, Hamburg University, Hamburg (Germany), 2001.

[73] R. Pawlak, *Vertex reconstruction from FCAL timing* (unpublished). ZEUS-98-040.

[74] K. Nagano, *Measurement of Charged Current e^+p Deep Inelastic Scattering Cross Sections at $\sqrt{s} = 300GeV$*. Ph.D. Thesis, University of Tokyo, Tokyo (Japan), 1998.

[75] A. Quadt and H. Uijterwaal, *A Brief introduction to the CTD-Second Level Trigger in 1995* (unpublished). ZEUS-95-083, 1995.

[76] L. A. T. Bauerdick, A. Fox-Murphy, T. Haas, S. Stonjek and E. Tassi, Comp. Phys. Comm. **137**, 236 (2001).

[77] H. Abramowicz, A. Caldwell and R. Sinkus, Nucl. Inst. Meth. **A 365**, 508 (1995).

[78] A. Kruse, *Charged Current Interactions at HERA*. Ph.D. Thesis, Univeristy of Amsterdam, Amsterdam (the Netherlands), 1999.

[79] A. Kruse and A.I. v. Sighem, *MUFFINCUP - A Wrapper for MUFFIN* (unpublished). ZEUS-98-025, 1998;
A.I. v. Sighem, *Charged Current Deep Inelastic Scattering at HERA*. Ph.D. Thesis, Univeristy of Amsterdam, Amsterdam (the Netherlands), 2000.

[80] ZEUS Coll., S. Chekanov et al., Phys. Lett. **B 539**, 197 (2002). Erratum in Phys. Lett. **B 552**, 308 (2003).

[81] N.H. Brook et al., Preprint hep-ex/9912053, 1999.

[82] R. Barlow, Preprint hep-ex/0207026, 2002.

[83] F. James, *Minuit v94.1, CERN Program Library Long Writeup D506* (unpublished), available on `http://wwwinfo.cern.ch/asdoc/minuit/minmain.html`.

[84] ZEUS Coll., S. Chekanov et al., Phys. Rev. **D 67**, 012007 (2003).

[85] J. Pumplin et al., Preprint hep-ph/0201195, 2002.

[86] A.D. Martin et al., Preprint hep-ph/0201127, 2002.

[87] M. Derrick et al., Z. Phys. **C72**, 47 (1996).

[88] J. Breitweg et al., Eur. Phys. J. **C12**, 411 (2000).

[89] ZEUS Coll., J. Breitweg et al., Eur. Phys. J. **C 12**, 411 (2000).

[90] ZEUS Coll., S. Chekanov et al., Phys. Lett. **B 539**, 197 (2002).

[91] ZEUS Coll., S. Chekanov et al., Eur. Phys. J. **C 21**, 443 (2001).

[92] U.K. Yang and A. Bodek, Eur. Phys. J. **C 13**, 241 (2000).

Summary

Today, the proton is seen as a dynamic system with three valence quarks and a sea of quarks and antiquarks that radiate gluons and gluons that split into quark-antiquark pairs or two gluons. These processes are described by the theory of the strong force, the quantum chromo dynamics, QCD. By deep inelastic scattering of leptons on protons information about the structure of the proton can be acquired. Two types of deep inelastic processes can be distinghuished: neutral current scattering and charged current scattering. In neutral current deep inelastic scattering processes $e^{\pm}p \rightarrow e^{\pm}X$, a photon or a neutral weak boson, Z^0 particle, is exchanged between the incoming electron and a (anti)quark in the proton. The cross section of this process gives information about the contributions of all quarks and antiquarks in the proton, and can therefore be used as a direct measurement of the structure of the proton. In charged current deep inelastic scattering a charged weak boson, a W^+ or W^- particle, is exchanged between the incoming electron and one of the (anti)quarks in the proton. In this scattering process the electron (positron) changes into a neutrino (antineutrino). Due to the charge of the W boson only particular combinations of quarks and antiquarks participate in the interaction. Hence, the charged current deep inelastic process reveals information about specific quark and antiquark distributions in the proton: in $e^-p \rightarrow \nu X$ only positively charged (anti)quarks contribute to the charged current cross section and in $e^+p \rightarrow \nu X$ only negatively charged (anti)quarks contribute to it.

In this thesis the measurement is described of the cross sections of the charged current deep inelastic scattering processes $e^-p \rightarrow \nu X$ and $e^+p \rightarrow \nu X$ for $Q^2 > 200\,\mathrm{GeV}^2$ and at a centre-of-mass energy of 318 GeV. The cross sections are measured using the ZEUS detector. ZEUS is a detector at the particle accelerator HERA, an accelerator with colliding beams of electrons [1] and protons, at the DESY institute in Hamburg. The measurement of the e^-p charged current cross section is based on a data sample of $16.4\,\mathrm{pb}^{-1}$ and the e^+p charged current cross section measurement is based on a data sample of $60.9\,\mathrm{pb}^{-1}$. To

[1]Electron can be read as positron, unless otherwise stated.

build a sample of charged current interactions, one must select interactions with a neutrino in the final state. Since the neutrino will escape the detector undetected, a large measured missing transverse momentum is characteristic for these events, a property that is used on-line to identify them. But after applying this selection criteria, the vast majority of the selected events was not a charged current interaction. Background events from various sources, some of them with much larger cross sections than the cross section of the charged current interaction, had to be removed from the data sample. Special selection criteria were developed to remove the serious background of photoproduction and neutral current interactions. Although these interactions should not have missing transverse momentum, particles can escape undetected due to e.g. fluctuations in the energy measurement. Also non-ep interactions formed a considerable background. Beam-gas interactions, interactions with residual gas molecules in the beampipe, can have an imbalance in measured transverse momentum, because a lot of energy escapes through the beampipe. The selection criteria designed to remove these events were based on the quality of the reconstruction of the tracks and the vertex. Muons travelling parallel to the beam and cosmic muons which caused an imbalance in missing transverse momentum were removed by a, especially for this analysis developed, computer program, which identified halo and cosmic muons by searching for characteristic patterns caused by muons traversing the detector. After all selection criteria were applied the remaining events were subjected to a visual scan by eye which removed a few cosmic muon and halo muon events. More than a million e^-p and e^+p charged current candidate events were selected by the detector. The final data sample used for the measurements of the cross sections consisted of 627 e^-p and 1456 e^+p events.

The estimated contamination of ep background events is smaller than 2% over the full kinematic range; only at $Q^2 < 400\,\mathrm{GeV}$ the background is higher, about 10%; this is mainly due to photoproduction events.

To perform a precise measurement of the cross section it is necessary to measure the kinematic variables as precisely as possible. The kinematic variables were reconstructed using the energy, measured by the CAL, and the vertex, determined from the CTD information. Corrections were necessary since, due to detector effects, large differences can occur between the measured values of the kinematic variables and the real values. The presented reconstruction method contains energy corrections for noise in the CAL, clustering of the energy deposits in the CAL cells and corrections for energy loss of particles in inactive material in the detector. A new correction, a correction on the reconstructed vertex position was developed using the timing information of the CAL. All these corrections allowed a bias-free determination of the kinematic variables.

Measurements are presented of the single differential cross sections $d\sigma/dQ^2$, $d\sigma/dx$, $d\sigma/dy$ and the reduced double differential cross section $\tilde{\sigma}$ for both e^+p and e^-p interactions. The precision of the measured cross sections is dominated by the statistical error. To determine the systematic uncertainty many possible sources of systematic uncertainties were studied in great detail. The largest contribution to the systematic uncertainty appeared to come from the energy scale of the calorimeter and the simulation of the QCD cascade (MEPS versus Ariadne). The results for e^-p show a large improvement compared to formerly published results based on only $0.82\,\mathrm{pb}^{-1}$. For the first time it was possible to measure the e^-p cross sections in bins of x and Q^2 and to measure the reduced cross section. For the results for e^+p the statistical errors reduced considerably compared to earlier published results.

The final results are compared with the latest theoretical predictions using the most recent parametrizations of the parton distribution functions by the CTEQ, MRST and ZEUS collaborations. The parametrizations are extracted from fits to neutral current data from various experiments (the charged current data of HERA are not included in the fits). Over the whole measured kinematic range all predictions agree well with the measured cross sections. The obtained precision of the measurement allows plotting the reduced double differential cross sections for both e^+p and e^-p as function of $(1-y)^2$ in bins of x and reveals the helicity structure of charged current interactions in accordance with predictions of the Standard Model.

The work of this thesis has greatly improved the understanding of the systematic uncertainties and has shown what the experimental limits on the precision of these cross section measurements are. In the near future HERA will, after a luminosity upgrade, produce a much larger number of charged current events which will reduce the statistical error considerably, especially in the interesting region of high-Q^2 and high-x. This larger sample can be used to improve the precision of the measured cross sections, which will be an important contribution to the parameterisation of the parton density distributions.

Samenvatting

Tegenwoordig wordt het proton gezien als een dynamisch systeem van drie valentie-quarks in een "zee" van quarks en anti-quarks die gluonen afstralen en gluonen die zich opsplitsen in quark anti-quark paren of twee gluonen. De theorie die deze processen beschrijft is de theorie van de sterke wisselwerking, de quantum chromo dynamica. Via diep inelastische verstrooiing van elektronen [2] aan protonen kan informatie verkregen worden over de structuur van het proton. Er kunnen twee typen diep inelastische verstrooiing onderscheiden worden: neutrale stroom verstrooiing en geladen stroom verstrooiing. In het neutrale stroom verstrooiingsproces $e^{\pm}p \to e^{\pm}X$ wordt een foton of een Z deeltje uitgewisseld tussen het inkomende elektron en een (anti-)quark in het proton. De werkzame doorsnede van dit proces geeft informatie over alle quarks en anti-quarks tezamen in het proton, en kan daardoor gebruikt worden voor een directe meting van de structuur van het proton. In geladen stroom verstrooiing wordt een W^+ of W^- deeltje uitgewisseld tussen het inkomende elektron en een (anti-)quark in het proton en verandert het elektron (positron) in een neutrino (anti-neutrino). Doordat het W deeltje geladen is doen alleen bepaalde combinaties van quarks en anti-quarks mee in de interactie en kan er informatie worden verkregen over specifieke (anti-)quark verdelingen in het proton: in $e^-p \to \nu X$ dragen alleen positief geladen (anti-)quarks bij aan de werkzame doorsnede, in $e^+p \to \bar{\nu}X$ dragen alleen de negatief geladen (anti-)quarks bij.

In dit proefschrift worden de metingen beschreven van de werkzame doorsnede van de diep inelastische geladen stroom verstrooiingsprocessen $e^-p \to \nu X$ en $e^+p \to \nu X$ voor $Q^2 > 200\,\mathrm{GeV}^2$ bij een zwaartepuntsenergie van 318 GeV. De werkzame doorsneden zijn gemeten met de ZEUS detector. ZEUS is een detector bij HERA, een elektron-proton versneller bij DESY, in Hamburg. De metingen van de e^-p geladen stroom werkzame doorsnede zijn gebaseerd op een data verzameling van $16.4\,\mathrm{pb}^{-1}$ en de e^+p geladen stroom werkzame doorsnede metingen zijn gebaseerd op een data verzameling van $60.9\,\mathrm{pb}^{-1}$.

Om de geladen stroom werkzame doorsnede te meten worden botsingen ge-

[2] Elektron kan gelezen worden als positron, tenzij anders vermeld.

selecteerd die een neutrino, afkomstig van het inkomende elektron, in de eindtoestand bevatten. Doordat het neutrino uit de detector "ontsnapt" zonder dat het gemeten wordt, is een grote missende transversale impuls karakteristiek voor deze botsingen: deze eigenschap wordt gebruikt in de on-line selectie. Na deze selectie is echter het merendeel van de geselecteerde botsingen geen geladen stroom botsing. Deze achtergrondbotsingen afkomstig van verschillende interacties, sommige met een veel hogere werkzame doorsnede dan de werkzame doorsnede van de geladen stroom interactie, moeten verwijderd worden. Speciale selectiecriteria worden ontwikkeld om de botsingen afkomstig van fotoproductie en neutrale stroom interacties te verwijderen. In principe kunnen alle deeltjes in de eindtoestand van deze botsingen worden gemeten en zouden deze botsingen geen missende transversale impuls moeten hebben. Desondanks kan er missende transversale impuls ontstaan, bijvoorbeeld door fluctuaties in de energiemeting. Ook niet-ep interacties vormen een substantiële achtergrond. Bundel-gas botsingen, botsingen van het inkomende proton met rest gasmoleculen in de bundelpijp, kunnen een grote missende transversale impuls hebben doordat er veel energie ontsnapt via de bundelpijp. De selectiecriteria voor het verwijderen van deze achtergrond zijn gebaseerd op eigenschappen van de deeltjessporen in een botsing. Een speciaal voor dit onderzoek ontwikkeld computerprogramma wordt gebruikt om parallel aan de bundelpijp bewegende muonen en kosmische muonen te verwijderen. Deze muonen veroorzaken meestal een missende transversale impuls en worden door het computerprogramma verwijderd door te zoeken naar karakteristieke patronen van muonen die de detector doorkruisen. Na alle selectiecriteria worden de overgebleven botsingen visueel beoordeeld en zijn er nog een aantal botsingen met een muon verwijderd. Meer dan een miljoen e^-p en e^+p kandidaten voor geladen stroom botsingen zijn verzameld door de detector. De uiteindelijke verzameling botsingen die gebruikt wordt voor de metingen van de werkzame doorsneden bestaat uit 627 e^-p botsingen en 1456 e^+p botsingen. Het geschatte aantal ep achtergrondbotsingen is kleiner dan 2% in het gehele kinematische gebied; alleen voor $Q^2 < 400\,\mathrm{GeV}$ is de achtergrond groter, namelijk $\sim 10\%$; deze wordt voornamelijk veroorzaakt door fotoproductie botsingen.

Om een nauwkeurige meting van de werkzame doorsnede te kunnen doen is het nodig om de kinematische variabelen, de variabelen die een diep inelastische verstrooiingsbotsing beschrijven, zo precies mogelijk te bepalen. De kinematische variabelen worden gereconstrueerd uit de energie, gemeten door de calorimeter, en de positie van de vertex, bepaald met de centrale sporen detector. Correcties zijn nodig omdat er door detectoreffecten verschillen kunnen optreden tussen de gemeten waarden en de echte waarden. Correcties op de energiemeting zijn o.a. correcties voor ruis in de calorimeter, samenvoeging van energiedeposities in de calorimeter, en correcties voor energieverlies van deeltjes in ongeïnstrumenteerd materiaal tussen de vertex en het oppervlak van de calorimeter. Door alle correcties zijn de gemiddelde afwijkingen van de gemeten waarden van de kinematische variabelen ten op zichte van de echte waarden verwaarloosbaar klein geworden.

De metingen van de geladen stroom werkzame doorsnede worden gepresenteerd als de differentiële werkzame doorsneden $\mathrm{d}\sigma/\mathrm{d}Q^2$, $\mathrm{d}\sigma/\mathrm{d}x$, $\mathrm{d}\sigma/\mathrm{d}y$ en de gereduceerde dubbel differentiële werkzame doorsnede $\tilde{\sigma}$ voor e^-p interacties en e^+p interacties. De nauwkeurigheid van de metingen wordt gedomineerd door de statistische onzekerheid. De systematische onzekerheid in de meting wordt bepaald door veel bronnen die een systematische fout zouden kunnen veroorzaken in detail te onderzoeken. De grootste systematische onzekerheden worden veroorzaakt door de onzekerheid in de energieschaal van de calorimeter en de onzekerheid in de simulatie van de hadronisatie. De metingen van de werkzame doorsneden in e^-p botsingen zijn enorm verbeterd ten opzichte van de eerder gepubliceerde metingen gebaseerd op slechts $0.82\,\mathrm{pb}^{-1}$. Tevens is voor de eerste keer de geladen stroom gereduceerde werkzame doorsnede in e^-p botsingen gemeten. In de metingen van de werkzame doorsneden in e^+p botsingen zijn de statistische onzekerheden aanzienlijk lager in vergelijking met de eerder gepubliceerde metingen en zijn de systematische onzekerheden beter begrepen.

De resultaten worden vergeleken met de laatste theoretische voorspellingen die gebruik maken van recente parametrisaties van de parton dichtheidsvergelijkingen van CTEQ, MRST en ZEUS. De parameterisaties zijn bepaald uit fits aan diep inelastische verstrooiings data van verschillende experimenten (geladen stroom data van HERA experimenten zijn niet in de fits opgenomen). In het gehele kinematische gebied zijn de theoretische voorspellingen in goede overeenstemming met de metingen. De nauwkeurigheid van de metingen maakt het mogelijk om de gereduceerde werkzame doorsnede in e^-p en e^+p interacties te meten als functie van $(1-y)^2$. Dit laat de heliciteitstructuur van de geladen stroom interacties zien en is in goede overeenstemming met de voorspellingen van het Standaard Model.

Het werk beschreven in dit proefschrift heeft een grote bijdrage geleverd aan het begrijpen van de systematische onzekerheden in de metingen van de geladen stroom werkzame doorsneden; de totale onzekerheid in de meting kan slechts verder verkleind worden door de statistische fout te verkleinen. In de nabije toekomst zal HERA, na een luminositeitsverbetering, een veel grotere hoeveelheid geladen stroom botsingen gaan produceren en dit zal de statistische onzekerheid aanzienlijk verkleinen. De verbeterde metingen van de werkzame doorsnede in het interessante gebied van hoge-x en hoge-Q^2 zullen dan een zeer waardevolle bijdrage leveren aan de bepaling van de parton dichtheidsvergelijkingen, en daarmee aan het begrip van de structuur van het proton.

Acknowledgements

The work presented in this thesis would never have been possible without the effort of many people from around the world collaborating in the ZEUS experiment. I would like to thank all my colleagues in ZEUS for making my time as a PhD student a truly memorable one. I would like to thank Ken Long for his guidance in the analysis. Thanks to Alex Tapper and Rod Walker for introducing me to the UK style of dealing with free time.

Many thanks to all my colleagues in the NIKHEF ZEUS group for providing a highly valued and pleasant atmosphere to work in. I would like to express my gratitude towards my promoter Jos Engelen. My co-promoter and coach Els de Wolf and to Paul Kooijman who introduced me to the world of high energy physics, thought me a lot about physics and always impresses me with his broad knowledge about "everything". Also I would like to thank Niels for all his advice and Sven for the many discussions we had.

All the thanks to my family and especially to Jennifer for being there and supporting me in my work. I do not know how I would have done it without you!